Reflection Absorption Infrared Spectroscopic Studies of Surface Chemistry Relevant to Chemical and Biological Warfare Agent Defense

Joshua Robert Uzarski

Dissertation submitted to the faculty of the Virginia Polytechnic Institute and State University in partial fulfillment of the requirements for the degree of

Doctor of Philosophy

In

Chemistry

John R. Morris, Chair

Mark R. Anderson

Richard D. Gandour

Gary L. Long

Sungsool Wi

January 19, 2009

Blacksburg, Virginia

Keywords: RAIRS, self-assembled monolayers, quaternary ammonium cations, antimicrobial peptides, chemical warfare agent simulants, surface chemistry, ultrahigh vacuum

Reflection Absorption Infrared Spectroscopic Studies of Surface Chemistry Relevant to Chemical and Biological Warfare Agent Defense

Joshua Robert Uzarski

Abstract

Reflection absorption infrared spectroscopy was used as the primary analysis technique to study the interfacial chemistry of surfaces relevant to chemical and biological warfare agent defense. Many strategies utilized by the military to detect and decompose chemical and biological warfare agents involve their interaction with surfaces. However, much of the chemistry that occurs at the interface between the agents and surfaces of interest remains unknown. The surface chemistry plays an important role in efficacy of both detection and decontamination technology, and by obtaining a deeper understanding of that chemistry, researchers might be able to develop more sensitive detection devices and more effective decontamination strategies. Our efforts have focused on three different areas of surface chemistry relevant to chemical and biological warfare agent defense:

1) The development of a surface synthesis strategy to create and control the structure of antibacterial self-assembled monolayers (SAMs). Our work demonstrated a successful strategy for creating SAMs that contain long-chain quaternary ammonium groups, which were synthesized and subsequently characterized using RAIRS and X-ray photoelectron spectroscopy (XPS).

2) The determination of the surface conformation, orientation, and relative surface density of immobilized antimicrobial peptides. Our results revealed that the peptides consisted of tilted (50-60°), α-helices on the surface, regardless of solution conditions.

3) The design and construction of a new ultrahigh vacuum surface science instrument that allows for the study of gas-surface reactions with up to three gases simultaneously.

4) The study of the adsorption of chemical warfare agent simulants to silica nanoparticulate films. Our work demonstrated that the adsorbate structure was dependent on the number of hydrogen-bonding groups, and the adsorption consists of a pressure-dependent two part mechanism.

The results presented here will help increase the understanding of the surface chemistry of three interfaces relevant to chemical and biological defense. Future researchers may apply the new information to develop more effective detection and decontamination strategies for chemical and biological warfare agents.

Acknowledgements

My success in graduate school would not have been possible without the influence, help, and support of many people. I am extremely thankful for the love and support of my family. My mom, Krys, and sisters Veronica and Sarah, were always there for me during this long, arduous process. Even though we had to be separated geographically, we always made sure our family and relationships remained a priority in our lives. I am thankful for the support of my friends back in Michigan. I am grateful to my friends Tony and Kristi Smith from Roanoke, who took a risk letting a crazy Eagles fan into their home when I first arrived in Virginia. I will always be thankful for the friendship we developed in the last five years.

I'd like to thank my group members, both past and present, including Larry Fiegland, Scott Day, Mindy McPherson, Wes Gordon, Erin Davis, Leslie Adamczyk, Amanda Bolger, Wes Sanders, Will Alexander, Jessica Lu, Dimitar "Mitko" Panayotov, and many others. They were all always willing to help and a pleasure to work with. I want to thank the many professors that advised me during my time, especially Dr. Gandour for his help with synthesis, Dr. Anderson for his help with IR experiments, and Dr. Popham for his help with microbiology experiments. I especially wish to thank my advisor, Dr. John Morris, for everything he did for me during my graduate student career. His advice, guidance, patience, and understanding will always be appreciated. He truly is the best advisor I could have hoped for, and I will forever be grateful for the time I spent working with him. His support, both professionally and personally, were invaluable during some trying times.

My final acknowledgement is somewhat silly, but I must thank the actor Richard Dean Anderson for his portrayal of MacGyver. His character made a tremendous impact on me as a young child and helped spark my interest in science and in understanding how nature operates.

Dedication

Robert Steven Uzarski

October 31, 1952 – October 28, 2007

I dedicate this dissertation to my Dad, Robert "Bob" Uzarski, who sadly passed away on Sunday, October 28, 2007. I was very close to my Dad, he was my best friend, and losing him was absolutely devastating. I know he is looking down on me with a big proud smile, saying "Whoa man" to what I was able to accomplish. I miss him terribly, but I know we'll be together again someday. Until then, I hope I can continue to do him proud.

Table of Contents

List of Figures

List of Tables

List of Acronyms

CAD	Computer Aided Drafting
CD	Circular Dichroism
COOH	Carboxylic Acid
CP1_c	Cysteine-terminated Cecropin P1
DMMP	Dimethyl methylphosphonate
IR	Infrared
LED	Light Emitting Diode
MDCP	Methyl dichlorophosphate
NHS	*N*-hydroxysuccinimide
PFP	Pentafluorophenol
PGQ_c	Cysteine-terminated PGQ
PL_c	Cysteine-terminated Pleurocidin
QAC	Quaternary Ammonium Cation
RAIRS	Reflection Absorption Infrared Spectroscopy
SAM	Self-assembled Monolayer
SDS-PAGE	Sodium Dodecyl Sulfate Polyacrylamide Gel Electrophoresis
SPR	Surface Plasmon Resonance
TCEP	Tris(2-carboxyethyl) phosphine hydrochloride
TFE	Trifluoroethanol
TMP	Trimethoxy phosphate
XPS	X-ray Photoelectron Spectroscopy

Chapter 1

Introduction and Motivation

Thesis Statement

The goals of this research were to synthesize and characterize surfaces with relevance to chemical and biological warfare agent defense including: antibacterial quaternary ammonium self-assembled monolayers, surface-bound antimicrobial peptides, and chemical warfare agent simulants adsorbed to silica nanoparticulate films.

1.1 Background and Motivation

The interaction of surfaces with various molecules is a common occurrence that the majority of people give little attention to. The general population is seemingly unaware of the crucially important chemistry that takes place at an interface, such as gas exchange that occurs in the lungs, or the flow of current in crystalline semiconductor materials. Surfaces are ubiquitous and understanding of their structure and chemical properties has helped improve our understanding of Nature, as well as the lives of millions of people.

i) The chemistry that occurs at an interface is often very different from that of the bulk phase because the atoms or molecules located at the surface experience different forces than the bulk atoms. Isolating the interactions of the surface groups from the bulk is often difficult, but in the last few decades many surface-sensitive techniques have been developed that allow researchers to both create and characterize surfaces and their reactions.[1] Of particular interest to the military are the interactions of chemical and biological warfare agents with surfaces. Research focus has ranged from the initial binding or adsorption of the agents to their complete decomposition and destruction due to interactions with specific surfaces. Despite the importance of the surface chemistry of biological and chemical warfare agents, compared to bulk phase studies, relatively few studies exist that focus on the interfacial chemistry. A more detailed understanding of the fundamental chemistry that occurs when an agent

interacts with a surface may lead to improved early warning sensors, and possibly protective coatings that may kill the bacterial agents and destroy the chemical agents.

Antibacterial Surfaces

Biological warfare agents include organisms such as anthrax, ebola, *E. coli* O157:H7, and agents produced by organisms, such as ricin. A potential biological attack on a population would be devastating, not just in the number of direct casualties, but also due to the fact that the harmful organisms can self-replicate if appropriate conditions exist. A biological attack could also potentially be made on livestock animals and crops, which could catastrophically disrupt food supplies.

In order for a microorganism to cause its deleterious effects, it must first come into contact and adhere to a surface. The studies of the interaction of bacteria with various surfaces show that the surface composition,[2, 3] charge,[4] hydrophobicity,[5, 6] and surface roughness[7, 8] all affect the adhesion process. Many bacteria possess the ability to alter the surface chemistry of the substrate by releasing serum proteins and forming biofilms.[9, 10] Various researchers have shown that bacterial adhesion can be diminished, or even eliminated, by modifying the substrate surface with antimicrobial peptides,[11] pluronic surfactant coating,[12] nonsteroidal anti-inflammatory drug coating,[13] adsorbed cations,[14] amine-terminal groups,[14] and oligo-polyetheylene glycol groups.[15, 16]

Various surfaces have also been created that not only inhibit adhesion, but also kill many types of bacteria on contact. The surfaces exploit a fundamental difference in the surface chemistry of prokaryotic cells (bacteria), and eukaryotic cells (mammals, etc.). The outer surface of a bacteria cell membrane contains many anionic groups.[17], whereas the mammalian cell membranes contain more neutral species. The anionic charges are balanced by divalent cations, such as Ca^{2+} and Mg^{2+}, and the electrostatic interactions between the oppositely charged groups provides structural stability to the membranes. Antibacterial surfaces contain high densities of cationically charged groups, such as quaternary ammoniums (QAC). The QAC groups are believed to interact electrostatically with the anionic groups of the cell membrane and replace the divalent metal cations. The loss of the divalent cations causes a disruption in the integrity of the membrane, which then allows for intracellular components to leak out of the cell

nucleus, leading to the death of the cell. The majority of studies of antibacterial surfaces have used polymers,[18, 19] and relatively few have focused on antibacterial monolayers.

To improve the effectiveness of antibacterial surfaces, a more thorough understanding of the chemistry that occurs when a bacterium interacts with a lethal interface is needed. By investigating the fundamental surface chemistry that occurs, a relationship between the structure and function of the antibacterial surfaces can be developed. Knowledge of such a relationship may lead to improvements in protection from harmful organisms, which is of interest not just to the military, but to the civilian authorities as well. Common surfaces found in areas ranging from hospitals to home kitchens could all benefit from a greater protection of bacteria. In Chapter 2, we investigate a strategy, using only surface reactions, to create alkanethiol self-assembled monolayers that contain quaternary ammonium groups. By developing a relatively easy and robust method of creating monolayers with antibacterial groups, surface properties can be easily changed in a systematic way. Such properties include the surface densities of the QAC groups as well as the length of alkyl chains found in the molecule. A fundamental study performed by systematically varying the important surface properties will help reveal the relationship between surface structure and functionality.

Sensors for Bacterial Agents

Another strategy for protection from biological agents is through an early warning system. Such a system would be capable of detecting the presence of harmful microorganisms long before their concentration reached dangerous levels. The detection of biomolecules and microorganisms is achieved via the use of biosensors. A biosensor is a device that responds to the binding of a molecule- or organism-of-interest by relaying a signal that can be observed at low concentration. A typical biosensor consists of a surface functionalized with molecules that specifically bind the analyte of interest. The surface is coupled to a transducer that undergoes some type of change as a result of the binding event. Examples of transducers include a frequency change of a quartz crystal microbalance,[20] the refractive index change and resulting resonance angle shift of a surface plasmon resonance spectrometer,[21] or a change in capacitance or resistance of an electrochemical cell.[22] The most important part of a biosensor is the surface where the binding event occurs. The functionalized surface must bind specifically to the analyte of interest; otherwise false positive results will occur.

One strategy for the selective detection of pathogenic bacteria is through the use of antimicrobial peptides. Antimicrobial peptides are produced by a multitude of animals, ranging from insects to humans, and serve as the organisms' first line of defense against harmful bacteria. One class of antimicrobial peptides is the α-helices, and in their active α-helical conformation, the peptides possess amphiphilic properties. The α-helix contains two distinct faces: one face contains non-polar amino acids with hydrophobic side groups, and the other face contains polar amino acid with cationic side chains. When a minimum peptide concentration is reached, the cationic residues are thought to disrupt the electrostatic binding of the cellular membrane, similar in manner as the quaternary ammonium molecules described above. However, before the minimum inhibitory concentration is reached, the peptides bind to the bacterial membranes without causing death.

The binding of the peptides to the bacterial membranes has been explored for use in biosensors for pathogenic strains of bacteria. The peptides are immobilized to a substrate and exposed to both pathogenic and non-pathogenic strains of bacteria. Using both enzyme-linked immunosorbent assays (ELISA) and surface plasmon resonance, Soares and Mello demonstrated the specific binding of pathogenic *Escherichia coli* O157:H7 to the immobilized antimicrobial peptides cecropin P1 and PGQ relative to the non-pathogenic strain, ML35.[23] In the SPR study, the peptides were immobilized to gold substrates via the addition of the thiol-containing amino acid cysteine. The study included the investigation of non-physiological conditions, such as at high and low ionic strength, and at acidic and basic pH, but minimal was put forth to characterize the immobilized peptides. The conformation, orientation, or surface densities were unknown, and these surface structural properties may play an important role in the binding mechanism and efficacy of the antimicrobial peptides.

In Chapter 3, we investigate the surface structure of three α-helical antimicrobial peptides, cecropin P1, PGQ, and pleurocidin immobilized to gold via terminal cysteine residues. The conformation and average orientation of the surface-bound peptides were deduced from reflection-absorption infrared spectra, and the relative surface densities were determined using X-ray photoelectron spectroscopy and surface plasmon resonance. For cecropin P1, the effects of the solution conditions on the peptide surface structure were investigated. The different conditions included pH, peptide concentration, solution conformation, and dimerization state of

the peptides. This study serves as one of the first to investigate the structure of immobilized naturally-occurring peptides, and our results lay the foundation for future peptide surface studies. The ultimate goal of the peptide project is to develop a sensor array capable of detecting multiple strains of pathogenic bacteria. To accomplish this goal, scientists will need a firm understanding of how peptides assemble at solid interfaces as well as the ability to control the peptide adsorption.

Surface-bound Chemical Warfare Agent Decontamination via Highly Oxidizing Gases

Chemical warfare agents are a class of molecules that are used only to incapacitate and kill people. Due to their similarity of their molecular structure to organophosphate-containing pesticides, they were discovered by scientists attempting improve the protection of crops and livestock from insects. It was discovered that some versions of the pesticides were lethal to mammals, and upon discovery, militaries around the world became interested in their use as agents of war. Many large stockpiles of the harmful agents exists, both home in the US and abroad, and due to their relatively easy synthesis, rogue organizations might be able to obtain them. Despite their supposed worldwide ban, chemical warfare agents still pose a threat to both the military and civilian populace.

Due to the persistent threat of a chemical warfare agent attack, much effort has been given to the study of their detection[24] and destruction. Recently Talmage *et al.* published a review of the environmental fate and decomposition pathways of the agents HD, GA, GB, GD, and VX.[25] They also reviewed many of the decomposition strategies and formulas currently used by various agencies. Most common CWA's are subject to hydrolysis and will break down to less toxic chemicals in days to weeks.[26] The CWA's also undergo oxidation, and the P-S bond found in HD and VX is highly subject to oxidation. For VX, oxidation is the preferred decontamination strategy because hydrolysis can result in the formation of a toxic byproduct. In general, decontamination formulas are designed to oxidize or hydrolyze HD, hydrolyze nerve agents, and oxidize VX. Despite the similar types of decomposition reactions the CWA's undergo, the reaction byproducts as well as agent persistence are remarkably different.

The hydrolysis half-life of the agents VX, GA, GB, and GD differ from 5 ¼ hours to 41 days under ambient conditions. The persistence appears to depend on a combination of low

vapor pressure, low water solubility, and the presence of hydrolysable functional groups. GD, which has a water solubility of 21 g/L and a vapor pressure of 0.40 mm Hg, contains a hydrysable P-F bond and has a hydrolysis half life of 5.25 hours. VX, which has a water solubility of 30 g/L and a vapor pressure of 0.0007 mm Hg, has a hydrolysis half life of 41 days. The hydrolysis reaction is highly dependent on pH, with higher hydrolysis rates observed at both acidic and basic pH. An extreme pH can also be a detriment to hydrolysis, as seen for VX which has a much lower solubility at highly basic pH. For some agents, the hydrolysis products remain toxic and other strategies are needed for their safe decontamination.

The oxidation of CWA's has been explored using hydrogen peroxide. H_2O_2, along with the addition of activators such as molybdate, carbonate, and bicarbonate, as well as cosolvents such as alcohols, and surfactants can rapidly oxidize CWA's to produce non-toxic products.[27] Combinations of hydrogen peroxide and sodium hydroxide are currently used to decompose stockpile amounts of VX, and the reaction does not result in the generation of toxic products.[28] The importance of activators and cosolvents was demonstrated in the study of GB degradation via H_2O_2. GB in neutral peroxide and t-butanol had a half life of 67 hours, but the addition of bicarbonate dramatically reduced the half life to less than one minute.[27] Activated H_2O_2 with cosolvents has also been shown as fast decontamination strategy for VX and HD without the formation of toxic products.[27, 29]

For many decontamination situations, the application of a solution based formula is not feasible. For example, the decontamination of a building or remote personnel and equipment using solution based hydrogen peroxide is unrealistic. In addition, the liquid decontamination formulas may not penetrate into all contaminated surfaces and leave live agents present in the immediate environment. One possible solution to the problem is the use of vaporous hydrogen peroxide (VHP). The technology is currently employed to disinfect surfaces, but it has recently been tested as a possible decontamination agent.[30] Ammonia gas has been mixed with VHP to form a modified VPH (mVHP). It was shown that after 24 hours contact with 250 ppm mVHP, the CWA GD was decomposed to pinacoyl methyl phosphonic acid.[30] This promising result is being further explored for other agents.

Despite the successful demonstration of CWA-contaminated-surfaces with modified VHP, there is currently very little knowledge about the surface chemistry that occurs from the

point of view of both the agent and the substrate material. Many important questions remain that require attention. What are the reaction mechanisms and rates? What are the gas-phase and surface-bound reaction products? Are they harmful? How does the mVHP interact with the substrate material? Does the material change? Is it structurally compromised? These questions must be answered if mVHP and other oxidizing vapors are to be used as large-scale decontamination formulas.

In order to address the important questions mentioned above, a new surface science instrument was designed and constructed in our lab that allows for the study of gas-surface reactions. The instrument is centered around an ultrahigh vacuum chamber that is capable of achieving pressures lower than 1 x 10^{-9} Torr, which is necessary to keep a surface clean for the duration of an experiment. The chamber is coupled to a number analytical surface instruments, including a reflection absorption infrared spectrometer, used to monitor surface-bound reaction products, a mass spectrometer, used to monitor gas phase reaction products, and an X-ray photoelectron spectrometer that can provide elemental analysis of the surfaces-of-interest before and after a reaction. The reactant gases, such as mVHP, are directed to the surface-of-interest using three separate capillary array dosers. The multiple doser arrangement will allow us to test various gas combinations simultaneously to determine the most effective formula. Chapter 4 describes the design and construction of the new surface science instrument.

Chemical Warfare Agent Simulants

The study of chemical warfare agents is a hazardous endeavor thanks to their highly toxic nature. To avoid the risks and health problems associated with the study of CWA's, organophosphate molecules with similar structures to the live agents, but with reduced health risks, have received a great deal of study. A table of the select CWA's along with commonly used simulants is shown below. The simulants all posses the phosphoryl group (P=O) found in the majority of the nerve agents, but each simulant possesses one or more additional functional groups found on the various live agents. These groups include esters, isopropyl groups, P-X bonds, and P-CH_3 bonds. The selection of a particular agent depends on what functional group(s) of the real agent one wishes to investigate.

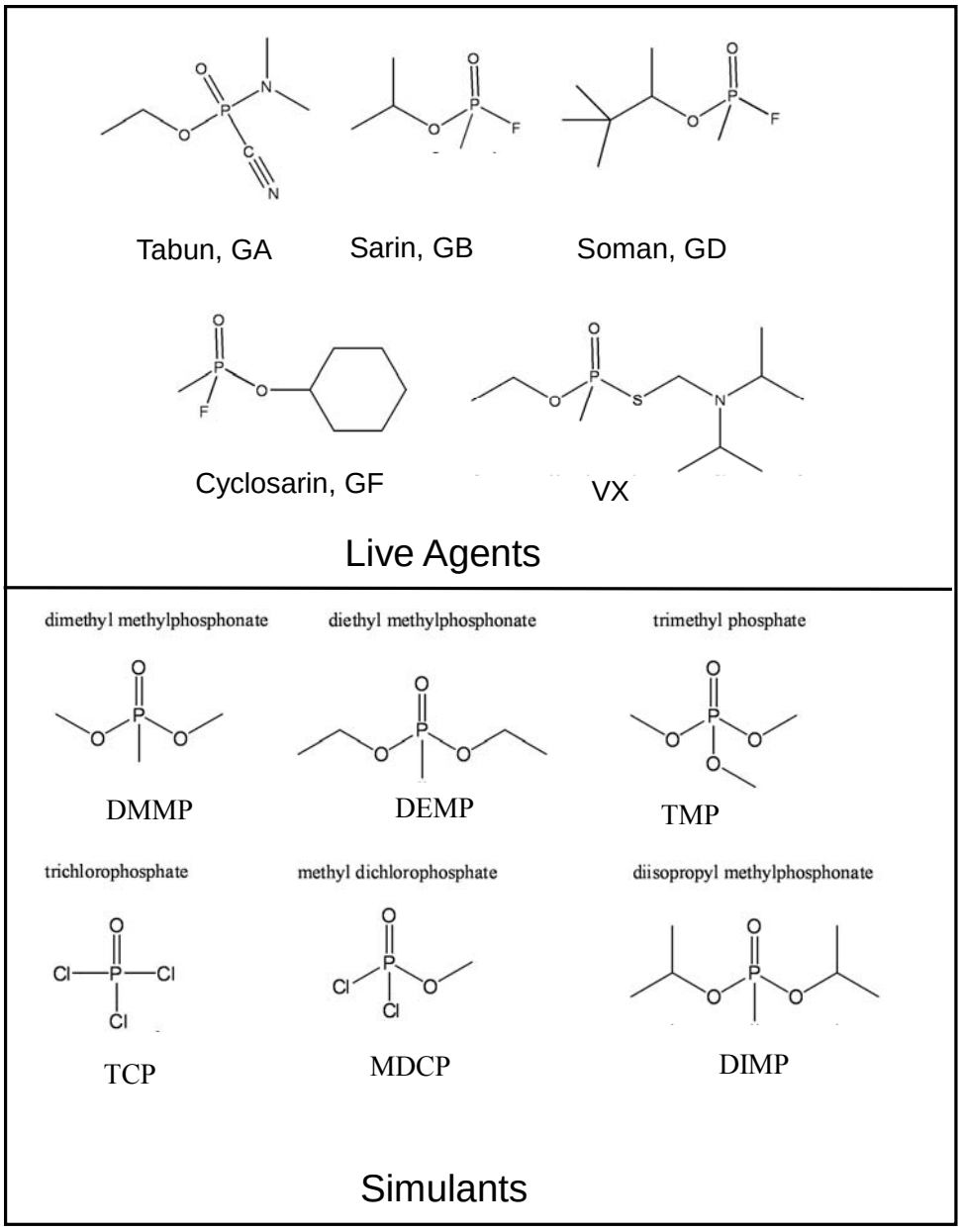

Figure 1-1: A schematic showing a selection of chemical warfare agents and their non-toxic simulant analogues.

The adsorption and decomposition of the simulant DMMP metal oxides has been investigated previously in our group and elsewhere.[31-41] On most of the metal oxides, the DMMP adsorbs to the surface via biding to Lewis acid sites or Brønsted base sites.[42, 43] The adsorbed molecules then undergo a surface hydrolysis or oxidation reaction that results in a surface bound O-P- O species and either a gas phase or surface bound methoxy group.[32]

In contrast to most metal oxides, DMMP does not decompose after adsorption to silicon oxide surfaces. DMMP was observed to desorb molecularly upon evacuation at room temperature[44] with no degradation products detected on the surface or in the gas phase. Because of the non-reactive and excellent adsorbent properties of silica, it has received attention as a potential pre-filtering agent in the development of a potential CWA sensor.[44] Silica may serve as a potential substrate and sorbent material used to study the reactions of CWA simulants with the oxidizing gases mentioned above. Because the silica does not react with the simulants, any possible reaction products could be attributed to a reaction with the decontamination vapors.

Prior to studying the reaction of silica-bound CWA simulants with oxidizing gases, the adsorption of the simulants to the silica should be well characterized. Both the adsorption mechanism and binding structure of the simulants may play a crucial role in its reactivity with the decontamination vapors. In Chapter 5, we investigate the adsorption of the simulants DMMP, TMP, and MDCP to silica nanoparticulate films prepared on gold substrates. We utilize RAIRS to determine both the binding structure of the adsorbed molecules as well as the adsorption mechanism via the analysis of adsorption isotherms.

Summary and Overview of Thesis

The reactions that occur at the surface of materials are important in a multitude of areas that span topics from the large scale atmospheric chemistry down to nanoscale electronics. Understanding of the fundamental chemistry that occurs at surfaces allows scientists to predict properties of new materials and utilize them for new applications. One area of surface chemistry that has received much attention from the military is interfaces with relevance to chemical and biological warfare agent defense. By developing a greater understanding of the chemistry that occurs when chemical and biological warfare agents interact with a surface, the military hopes to develop and improve detection and decontamination devices and strategies that will offer enhanced protection from a possible chemical and biological attack.

In the work presented here, we investigate a number of surfaces relevant to both biological and chemical warfare agent defense. Each part of our study utilizes reflection-absorption infrared spectroscopy to characterize the surfaces-of-interest and serves to demonstrate the tremendous power of infrared spectroscopy to surface analysis. In Chapter 2,

the surface synthesis of alkanethiol self-assembled monolayers that contain long-chain quaternary ammonium groups is presented. Surfaces that contain quaternary ammonium cations are known for their antimicrobial activity, and the goal of our study was to develop a relatively easy and fast way to systematically change the surface structure to develop a structure/function relationship. The surfaces were characterized via RAIRS before and after each reaction of the surface synthesis. In Chapter 3, the surface structure of immobilized antimicrobial peptides is investigated in an effort to better understand how their interfacial structure relates to their ability to selectively bind the pathogenic bacteria *E. coli* O157:H7. RAIRS was used to determine both the peptide conformation and average orientation of the surface-bound peptides. Our efforts are part of a larger collaborative effort designed to develop peptide arrays for use in a biosensor for biological agents.

The next two chapters change the focus from biological to chemical agent relevant surfaces. The goals are two-fold. First, the design, construction, and function of a new surface analysis chamber is described. The chamber combines the ability to achieve an ultrahigh vacuum, to characterize surfaces and reaction products via RAIRS, mass spectrometry, and X-ray photoelectron spectroscopy, and the ability to dose a surface-of-interest with up to three vapors simultaneously. The chamber was designed and constructed to enable the study of the reaction of militarily-relevant bare and chemical-warfare-agent-simulant-covered surfaces with vaporous decontamination formulas, including modified vaporous hydrogen peroxide and chlorine dioxide.

One goal of the study of the reactions of the decontamination vapors with chemical warfare agent simulants is to elucidate a reaction mechanism. Many of the surfaces that bind the simulant molecules can react with the simulants, and these reactions would make it very difficult to identify a reaction mechanism between the oxidizing gas molecules and the simulants. To isolate the gas-simulant reactions, a surface that is both adsorbent and inert to the simulant molecules is needed. Nanosize silicon dioxide (silica) is shown in the literature to adsorb, but decompose, CWA simulants.[44] In Chapter 5, we describe the adsorption of the simulants DMMP, TMP, and MDCP to silica nanoparticulate films formed on gold substrates. RAIRS is used to determine both the structure of the adsorbed molecules as well as the adsorption mechanism via the analysis of adsorption isotherms.

The studies presented here clearly demonstrate both the importance of fundamental surface chemistry to chemical and biological warfare agent detection, and the application of reflection-absorption infrared spectroscopy to a wide range of surface chemistry problems. By obtaining a greater understanding of the chemistry that occurs when biological and chemical warfare agents interact with a surface, scientists may one day be able to develop better devices and strategies for the detection of and protection from the persistent threat of an agent attack.

Chapter 2

Surface Synthesis of Long-chain Quaternary Ammonium Self-Assembled Monolayers

2.1 Introduction

The control and elimination of bacterial infection has been an ongoing battle since the first sterilization techniques developed by Louis Pasteur and Joseph Lister in the 19th century. More recently, research on the sterilization process has focused on developing self-sterilizing surfaces which are capable of killing harmful microorganisms on contact. Such surfaces have tremendous utility in locations that require a sterile environment, such as a hospitals or food production facilities. Self-sterilizing surfaces are also important for medical implants as well as every day locations such as household kitchens and bathrooms.

Many self-sterilizing surface compounds incorporate surface active amphiphilic cations in their structure. The antibacterial action of surface active cations was reported in 1928 by Hartmann and Käig.[45] In 1940, Kuhn and Bielig suggested that quaternary ammonium cation (QAC) containing detergents might act on the bacterial membrane, resulting in leakage of intercellular components.[46] The hypothesis was proved by Hotchkiss in 1944 when he detected nitrogen and phosphorus containing compounds leaking from *Staphylococcus aureus* upon treatment with a wide range of QAC-containing molecules.[47] Further studies using a variety of methods additionally supported the hypothesis.[48]

Many surface-bound antimicrobial molecules have analogous structures to the solution-based molecules. For example, structures of two common solution-based antimicrobial compounds, cetyltrimethylammonium bromide (CTAB) cetylpyridinium chloride are shown in Figure 2-1. Both molecules contain a long alkyl chain bonded to a quaternary nitrogen atom. In Figure 2-2, the structures of two surface-bound antimicrobial molecules are shown. Note the similar structure relative to the solution-based molecules. The most noteworthy difference is the

alkyl chain length of the pyridinium QAC molecules; the solution-based molecule has a fifteen carbon alkyl chain but the surface-bound pyridinium QAC has a six carbon chain. The surface-bound species were incorporated into polymers where it was hypothesized that the longer alkyl chains crosslink and shield the quaternary ammonium group from bacterial membranes.[18]

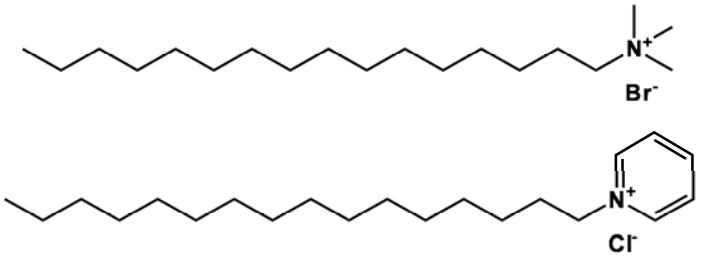

Figure 2-1: Molecular structure of two antibacterial solution-based quaternary ammonium molecules, cetyltrimethylammonium bromide (top) and cetylpyridinium chloride (bottom).

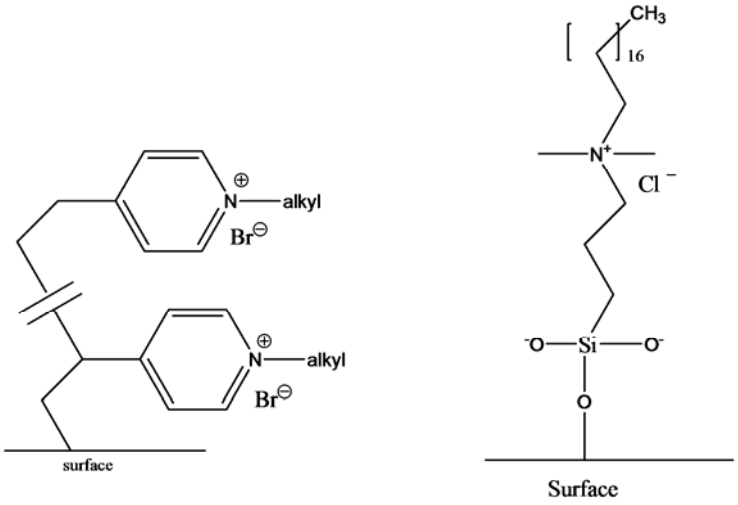

Figure 2-2: Molecular structures of surface-bound antimicrobial molecules analogous to those in Figure 2-1.

The accepted mechanism of cell death imparted by quaternary ammonium molecules is a general membrane disruption caused by the interaction of the cationic quaternary ammonium molecules and the anionic outer cell membranes of bacteria. The complicated structures of both Gram positive and Gram negative bacteria contain anionic moieties. Some molecular structures of these groups are shown in Figure 2-3. The binding of the antimicrobial compounds begins through the electrostatic attraction between the cationic quaternary ammonium moieties and the

anionic membrane groups. The long alkyl chains then insert into the hydrophobic interior of the lipid bilayer. The result of these interactions is the loss of membrane integrity which can lead to the leakage of intercellular material, eventually causing cell death.[46-48]

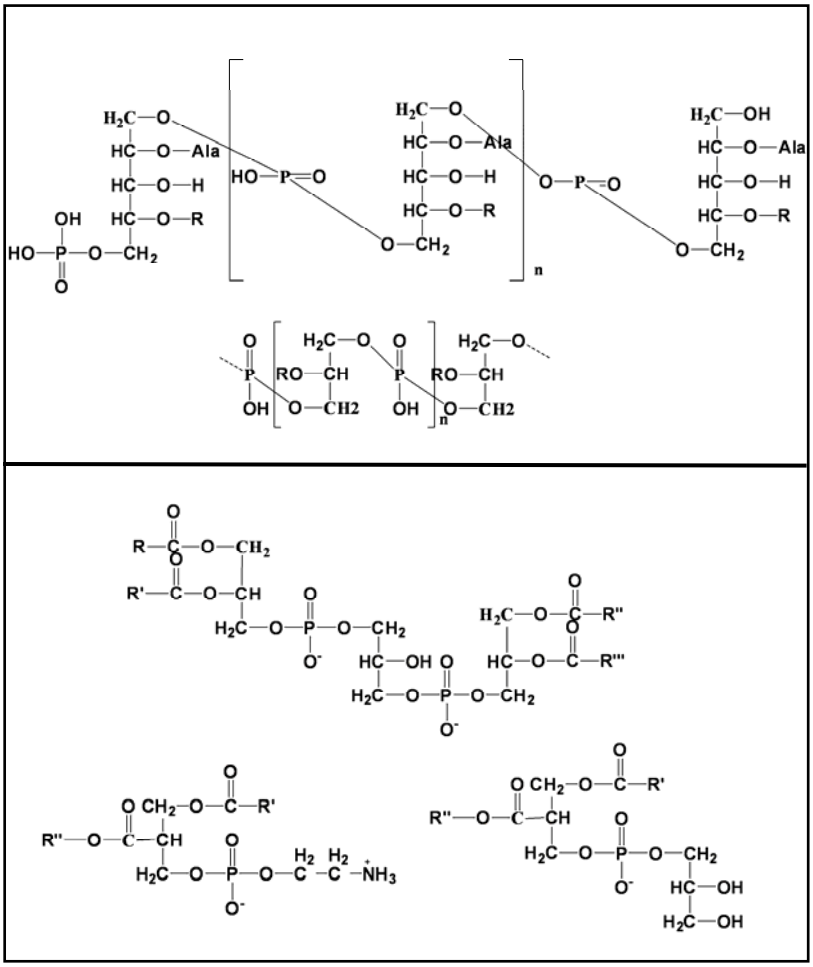

Figure 2-3: The molecular structures of several molecules found in the outer cell envelope of Gram negative bacteria. In the top frame are teichoic acid molecules and the bottom frame are phospholipids.

With the tremendous interest in self-sterilizing surfaces and their current commercial availability, it is quite surprising that relatively little work has been done to investigate the mechanism of cell death on non-polymeric surfaces. The molecular structure of antimicrobial monolayers is not well-understood and fundamental structure-function relationships remain unknown. The goal of our work presented here was to develop antimicrobial monolayers via facile surface synthesis techniques that would allow us to control the molecular surface structure. Such control would allow us to investigate important surface structure properties like surface

density, alkyl chain length, and surface order. To create surfaces with the desired properties, we used the well-known alkanethiol self-assembled monolayers.

Alkanethiol SAMs have been used as model surfaces since their initial discovery in the 1980's and have been employed in studies ranging from cell binding[49-54] to molecular electronics.[55, 56] Alkanethiol SAMs are formed due to the strong (~40 kcal/mol) interaction between sulfur and gold surface atoms and the establishment of favorable van der Waal's interactions between adjacent alkane chains.[57] The strong gold-thiolate interaction causes thiol molecules to spontaneously chemisorb to the gold surface. Over time, the alkane chains of the neighboring thiol molecules align themselves in a titled, all-trans configuration to maximize their van der Waal's interactions. The final structure is a quasi-crystalline arrangement of alkane chains with the sulfur atoms chemisorbed to the gold at the bottom of the chain and a terminal group on the opposite end at the interface. The general structure of an alkanethiol SAM is shown in Figure 2-4.

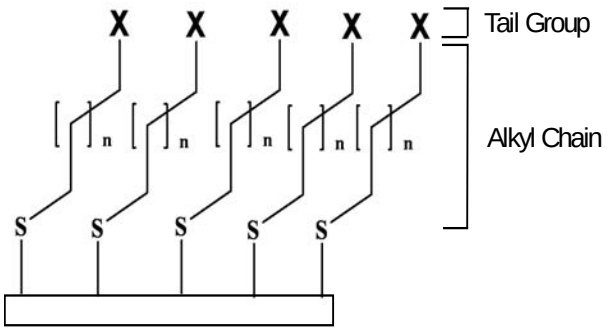

Figure 2-4: The basic structure of an alkanethiol self-assembled monolayer. The thiolate species binds to the gold substrate and the alkane chain, between 6 and 18 methylene units, form an ordered all-trans structure. The terminal group, X, is found at the interface and is responsible for the surface properties.

One important advantage of using alkanethiol SAMs on gold substrates as model surfaces is that they are amenable to a large number of surface characterization techniques including reflection-absorption infrared spectroscopy, X-ray photoelectron spectroscopy, ellipsometry, surface plasmon resonance, and many others. These surface sensitive techniques provide data about the molecular orientation, packing density, crystalline structure, monolayer thickness, atomic oxidation states, and more. By using a combination of these techniques, one can determine the molecular structure of an alkanethiol monolayer.

Alkanethiol SAMs have been used in a wide range of applications, and their versatility results from the fact that terminus of the alkane chain can be varied. Such variations include simple methyl moieties to large, protein resistant polyethylene glycol species.[15, 58] It has been found that the general underlying crystalline alkane chain structure is nearly identical for different of terminal groups.[59] A number of terminal groups can undergo surface reactions which can change their interfacial chemistry. A great deal of research has been performed on surface reactions involving alkanethiol SAMs. For an extensive review of the applications and surface reactions of alkanethiol SAMs, see the reviews by Love et al.[60] and Sullivan.[61]

We have shown in a previous study that alkanethiol SAMs can be rendered antibacterial. We reacted a carboxylic acid terminated SAM with silver nitrate to form a silver carboxylate terminated SAM that was antibacterial towards *E. coli.*.[62] The carboxylic acid terminated SAMs were immersed in a 1 mM ethanolic solution of silver nitrate for approximately 15 minutes, and after removal from solution, the surface had a monolayer of silver ions at the interface bound electrostatically to the carboxylate groups. Both RAIRS and XPS measurements confirmed the near quantitative conversion of carboxylic acid to silver carboxylate, and the spectra are shown in Figures 2-5 and 2-6.

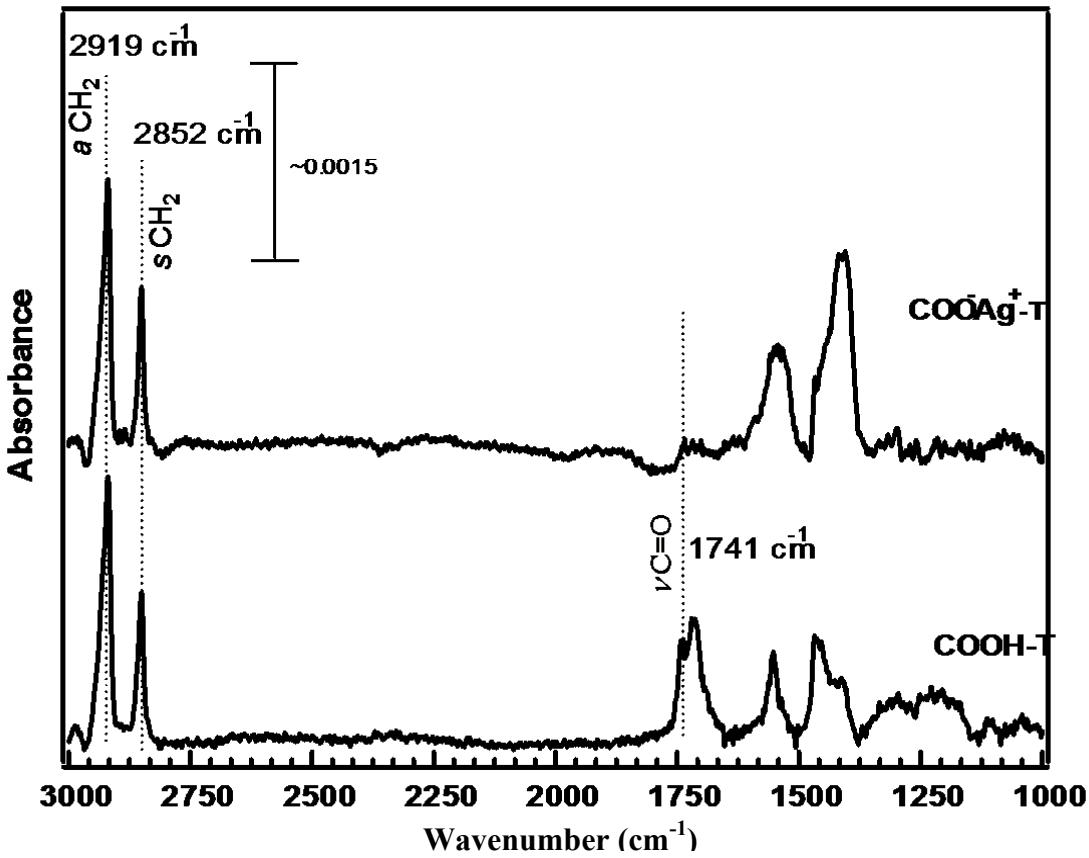

Figure 2-5: RAIR spectra of a carboxylic acid terminated SAM before (bottom) and after (top) immersion in a 1 mM solution of silver nitrate.

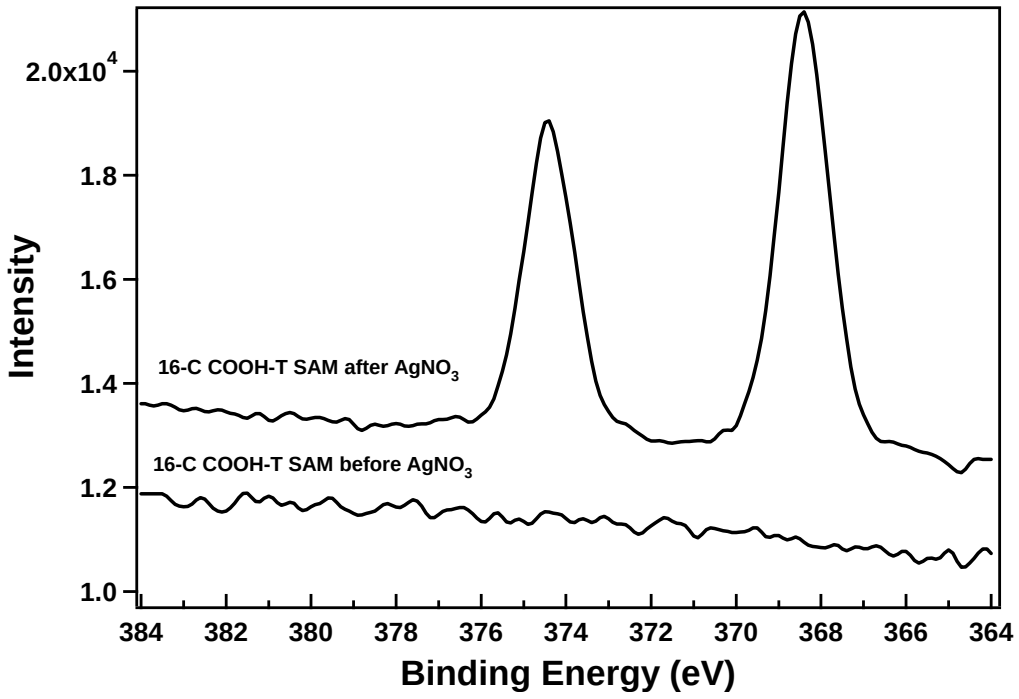

Figure 2-6: XP spectra of the Ag3d^5 region of a carboxylic acid terminated SAM before and after immersion in a 1 mM solution of silver nitrate.

In the RAIR spectrum, the disappearance of the carbonyl stretching mode at 1741 cm^{-1} and the appearance of the carboxylate stretching modes at lower wavenumbers are indicative of the formation of the silver carboxylate complex. The Ag 3d^5 region of the XP spectrum clearly shows the presence of silver ions after immersion in the silver nitrate solution. The atomic percentages, as determined via XPS and shown in Table 2-1, indicate a near 1:1 conversion of COOH to COO^-Ag^+.

Element	Predicted	Experimental
C	84.2	82.0 ± 5.0
Ag	5.3	3.9 ± 1.4
O	10.5	12.5 ± 3.9

Table 2-1: Comparison of the predicted and experimentally determined atomic percent composition of a 16Ccarboxylic acid terminated SAM after immersion in silver nitrate.

The silver carboxylate SAMs were assayed for antimicrobial activity towards both airborne and waterborne *E. coli*. In the airborne assay, a suspension of *E.* coli was sprayed onto the surfaces using a chromatography sprayer. Melted growth agar was then poured over the slide and incubated overnight. In the waterborne assay, the slides were placed in contact with a bacterial suspension for one hour. Aliquots were taken from the suspension before and after contact with the surface, serially diluted, plated out on agar growth media plates, and incubated overnight. As shown in Figure 2-7, the SAMs were

completely antibacterial as there were no viable colonies present. The assay for airborne bacteria showed a zone of inhibition in the immediate vicinity of the surface. Such a zone is indicative of the leakage of the antimicrobial constituents from the surface.[63] The leakage of the antimicrobial constituents, in this case silver ions, normally renders the surface non-antibacterial. Such was the case for the silver carboxylate SAMs because a second airborne assay, as shown in Figure 2-8, showed very little to no antibacterial activity.

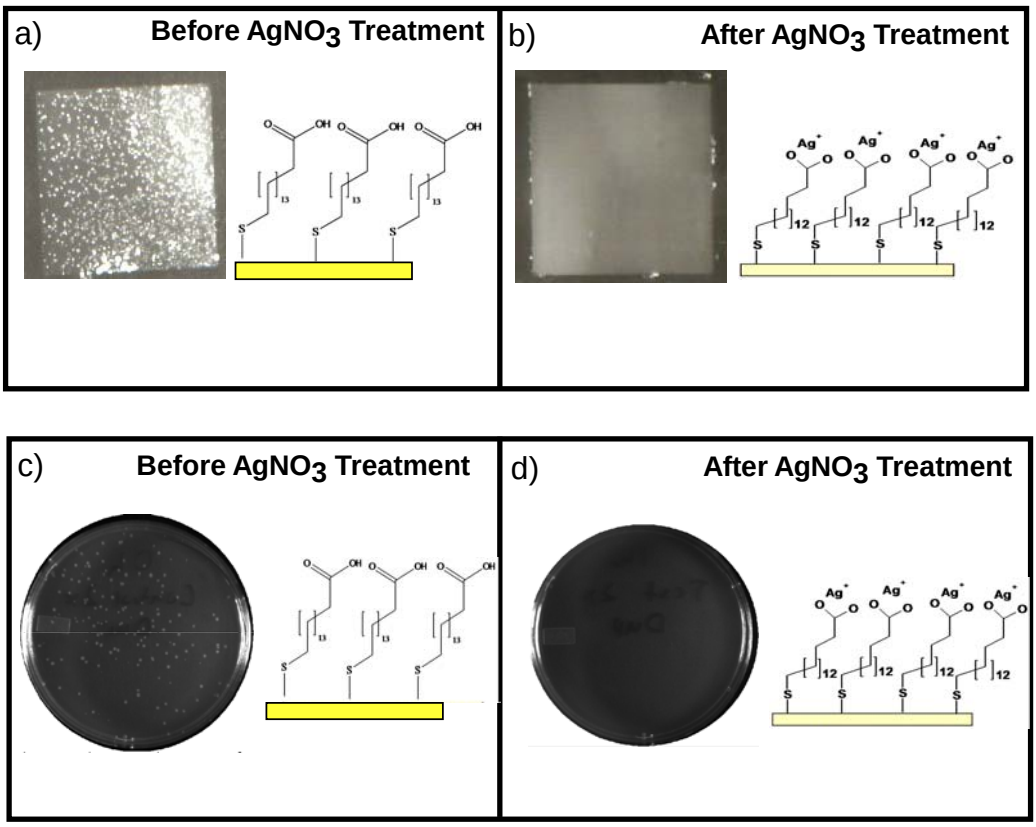

Figure 2-7: Images recorded after antibacterial assays of a carboxylic acid SAM before and after immersion in silver nitrate. The top images are for an airborne assay and the bottom are for a waterborne assay. The lack of viable bacterial colonies is indicative of high antimicrobial activity.

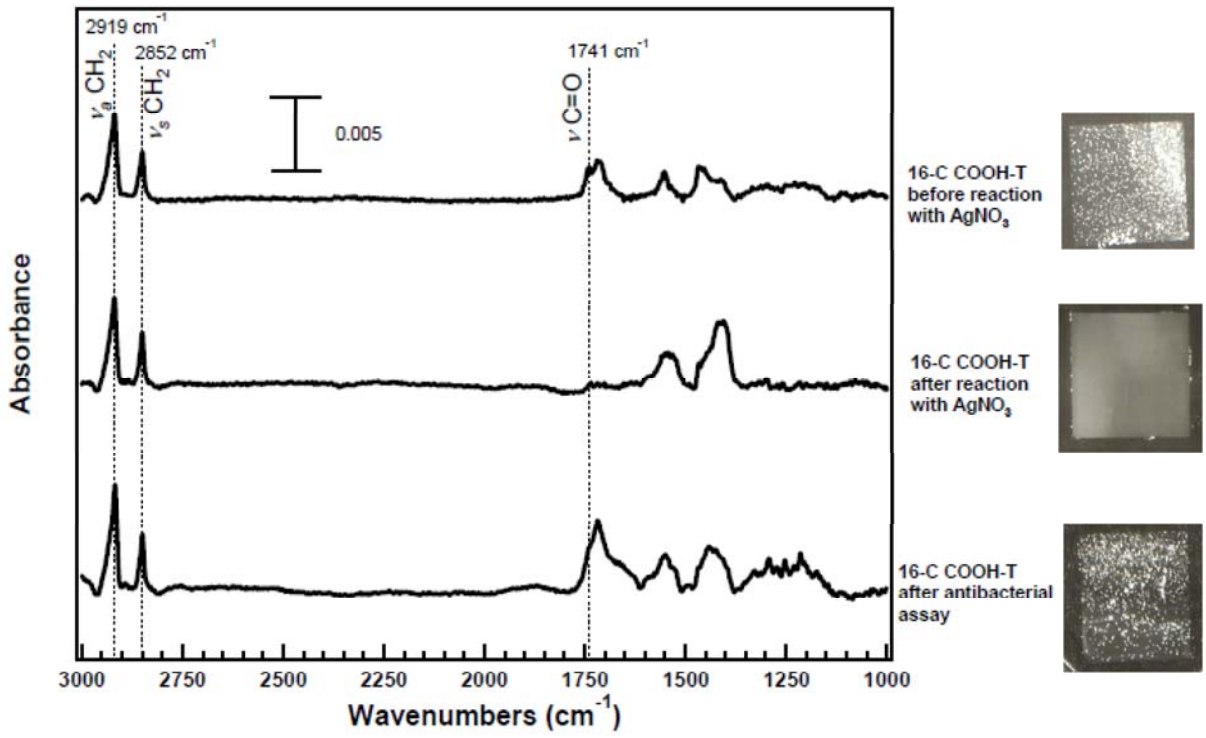

Figure 2-8: RAIR spectra recorded before and after immersing a carboxylic acid SAM in 1 mM silver nitrate along with a spectrum of the same surface recorded after an antibacterial assay. The images on the right are from antibacterial assays performed on the surfaces after the RAIR spectra were recorded.

The RAIR spectrum recorded after the initial airborne assay shows evidence for the reformation of the carboxylic acid groups. In the spectrum recorded before the assay, the carbonyl stretching mode at 1741 cm^{-1} is absent, however after the assay, the mode reappeared. As should be expected, without the presence of the silver ions, the SAM was rendered non-antibacterial as observed in the second airborne assay. The silver carboxylate groups could be regenerated by a second immersion in a silver nitrate solution. The resulting SAM was antibacterial, however there were a few viable colonies visible on the surface suggesting that there was not as high of a concentration of silver ions present after the second silver nitrate reaction.

To summarize, the silver carboxylate SAMs helped show that a carboxylic acid monolayer could be rendered completely antibacterial with a simple and fast treatment with silver nitrate. The surface was, however, not permanently antibacterial because the silver ions did not remain bound to the surface. The loss of the silver ions from the surface was necessary though for cell death to occur because the antibacterial mechanism of silver ions does not occur

at the cell membrane as observed for quaternary ammonium molecules. Silver ions act inside the cell where they disrupt the function of enzymes[64, 65] and bind to thiols[66, 67] and DNA.[68-72] Despite the fact the silver carboxylate SAMs were not permanently antibacterial, our study did help lay the foundation for using alkanethiol SAMs to study the fundamental importance of surface structure and functionality on antimicrobial activity.

The goal of our work in this study was to develop a facile method to create antimicrobial self-assembled monolayers that would allow us to control the molecular surface structure to investigate the structure-function relationships. In the work presented here, we used carboxylic acid-terminated alkanethiol SAMs and surface reactions to create surfaces with long chain quaternary ammonium groups. Each reaction was optimized to obtain the highest surface density of the quaternary ammonium groups. Briefly, terminal carboxylic acid groups were linked to a diamine group via the formation of an amide bond. The subsequent tertiary amine terminal group was then reacted with a 1-bromo-2-alkanone species to form the quaternary ammonium species. The optimum reaction conditions for each step of the surface modification was investigated and included the reactant concentration, solvent, temperature, time, and reaction intermediates. The surfaces were characterized after each step of the reaction via reflection-absorption infrared spectroscopy and X-ray photoelectron spectroscopy. These studies have provided initial insights into reactivity of self-assembled monolayers and the practicality of using surface reactions to form long-chain quaternary ammonium groups.

2.2 Experimental Methods and Approach

2.2.1 Chemicals and Reagents

11-mercaptoundecanoic acid (95%), 16-mercaptohexadecanoic acid (90%), pentafluorophenol (99+%), *N,N*-dimethylethylenediamine (95%), *N*-hydroxysuccinimide (98%), 1-ethyl-3-[3-(dimethylamino)propyl]carbodiimide (>97%), and anhydrous toluene (99.8%) were purchased from Sigma-Aldrich and used as received. Thionyl chloride was purchased from Fluka and used as received. 200 proof ethanol was purchased from Aaeper Alcohol and Chemical Company and used as received. 1-bromooctadeca-2-one was synthesized and kindly provided by the research group of Professor Richard D. Gandour group at Virginia Tech.

2.2.2 Substrate Preparation

All gold substrates used in this study were purchased from EMF Corp. (Ithaca, NY) and consist of 100 nm gold evaporated on top of a 50 nm titanium adhesion layer evaporated on glass slides. Prior to use, all gold substrates were cleaned in fresh piranha solution which consists of 70% concentrated sulfuric acid and 30% hydrogen peroxide. Extreme care should be undertaken when using piranha solution. It is a very highly oxidizing solution and can be explosive when not properly vented. After immersion in piranha for 15 to 60 minutes, the slides were removed, rinsed with copious amounts of MilliQ deionized water (18.3 MΩ) and dried with ultrahigh purity nitrogen. The substrates were then immediately placed into the desired thiol solution. Further surface reactions will be detailed in later sections.

2.2.3 Surface Characterization

Reflection-Absorption Infrared Spectroscopy (RAIRS)

Reflection infrared spectroscopy is a well-established tool to study surface-bound species and reactions.[73, 74] Using gold as the substrate for the SAMs permits the use of reflectance methods due to the high reflectivity of IR light from the gold surface. Infrared light induces vibrational transitions in molecular bonds, and by measuring the frequency and intensity of the absorbed infrared light, information such as chemical environment, structure, and functional group identity can be elucidated.

In a typical RAIRS experiment, infrared radiation is directed from the source through a series of gold coated mirrors towards the surface. The impinging photons interact with the surface molecules and reflect from the gold substrate where they are directed and focused into the detector through another series of gold coated mirrors. The raw signal is then Fourier transformed into the familiar frequency domain.

The mathematical basis of reflection infrared spectroscopy was developed by Greenler in the 1960's.[73] He investigated both the effects of the polarization of the light and the angle of incidence in which the light strikes the surface. Figure 2-9 shows the effects of polarization on the reflected light intensity.

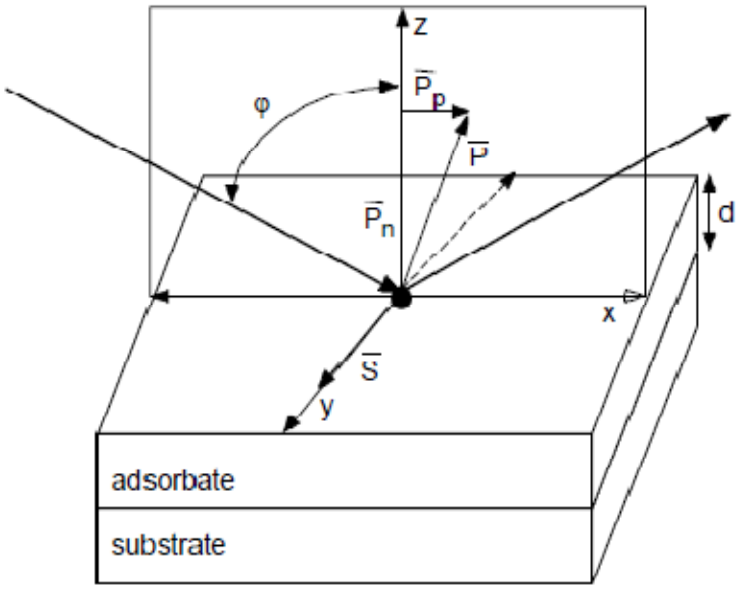

Figure 2-9: Schematic showing the S and P components of linearly polarized light. Upon reflection, the S component undergoes a 180° phase shift, but the P component undergoes a 90° phase shift that results in an increase in amplitude.

Impinging light that is linearly polarized can be separated into two different components, S and P. The S component is parallel to the surface in the y direction and perpendicular to the plane of incidence, while the P component is perpendicular to the S component; that is it is parallel to the plane of incidence and perpendicular to the surface. When the S polarized light is reflected form the surface, it undergoes a 180° phase shift that results in a near total cancellation of the amplitude at the surface. The P polarized light undergoes a 90° phase shift that results in amplitude addition. Installing a polarizer into the infrared beam path allows one to select only the P polarized light. The result is a significant increase in the detected signal-to-noise ratio.

Greenler also found, by using Maxwell's equations, that the amplitude of the P-polarized light reaches a maximum at a grazing angle of incidence (φ). He established that the absorption factor increases by a factor of 10^7 for 89° incidence compared to normal incidence.[73] By using the same approach, the critical angle of RAIRS experiments using gold substrates is found to be 86°.

The *p* component of linearly polarized light is used to take advantage of the surface selection rule. This rule states that only absorption modes that have a component of their dipole moment perpendicular to the surface will be excited. Modes that are completely parallel to the surface normal do not interact with p-polarized light and are not vibrationally excited. The

surface selection rule can be demonstrated with Equations 2-1 and 2-2. In equation 2-1, the intensity of the absorbance mode, *I*, is equal to the square of the dot product of the scalar product of the electric field, $\vec{E}$ and the intensity of the transition dipole moment, $\vec{\mu}$. The intensity of the transition dipole moment is dependent on the angle between it and the surface normal, $\vec{z}$. If that angle, θ, is 90°, signifying a perpendicular orientation of the transition dipole moment relative to the surface normal, then $\cos^2\theta$ is equal to zero. It then follows that the intensity of the absorbance mode will also be equal to zero.

$$\boldsymbol{I = \left|\vec{E} \cdot \vec{\mu}\right|^2}$$

Equation 2-1

$$\boldsymbol{\left|\overrightarrow{\mu \cdot \vec{z}}\right|^2 = |\vec{\mu}|\left|\vec{E}\right| \cdot \cos^2\theta}$$

Equation 2-2

X-ray Photoelectron Spectroscopy (XPS)

XPS work was performed on a Perkin Elmer 5400 X-ray Photoelectron Spectrometer equipped with a non-monochromatized Mg(Kα) radiation source (1253.6 eV) and a positron sensitive, multi-channel plate detector. The measurements were taken at a pressure of less than 5 x 10^{-7} Torr and a take-off angle between 15 and 90°. Exact take-off angles will be provided where necessary. Binding energies were referenced to the Au $4f^{7/2}$ peak at 83.9 eV. Survey spectra were collected with a pass energy of 89.45 eV for 10 minutes on a 1 mm x 3.5 mm spot size and 250 W electron beam power.

X-ray photoelectron spectroscopy, also known as electron spectroscopy for chemical analysis (ESCA), is a powerful analytical tool that allows for the determination of the surface atomic composition, formal oxidation state of the atoms, and the local physical and chemical environment. In addition, the atomic percent composition of a surface can also be determined from XPS data. Experimental percent composition can be compared to the predicted percent

composition to help determine the extent of surface reactions. In an XPS experiment, the samples are placed in a high vacuum environment and irradiated with photons in the energy range of 0 to 2000 eV. The basis of the technique relies on the exchange of energy between the incoming photons and the core energy level electrons of the surface atoms. X-ray photons have sufficient energy to cause core level electrons to be ejected from the atom, as shown in Figure 2-10 The kinetic energy (E_k) of the escaping electrons can be calculated, as shown in Equation 2-3, where (hv) is the X-ray photoelectron energy, (E_b) is the electron binding energy, and (E_w) is the work function of the spectrometer.

$$\boldsymbol{E_k = h\nu - E_b - E_w}$$

Equation 2-3

Each type of core level electron from a different atom has a different binding energy. The identity and atomic composition of the surface can be determined from the different binding energies. Different chemical environments of the core electrons cause small changes in the binding energies. The small binding energy shifts allow for the determination of specific oxidation states of the atoms.

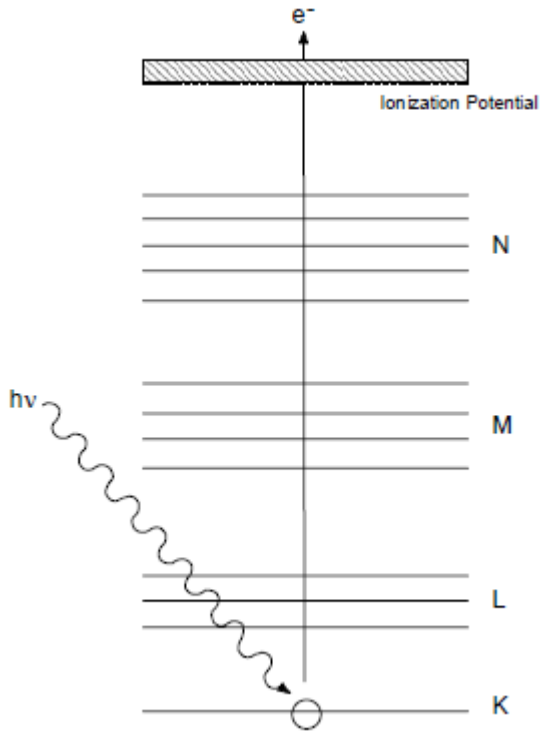

Figure 2-10: Example energy diagram for the photoelectric effect in XPS. X-ray photons cause core level electrons to be ejected from the atom.

XPS can be used to determine the relative atomic concentrations of the surface constituents of interest and is based on the following relationship:[75]

For a homogeneous sample, the number of photoelectrons per second in a specific spectral peak is given by:

$$\boldsymbol{I = nf\sigma\phi y\lambda AT}$$

Equation 2-4

Where n is the number of atoms of the element per cm^3 of the sample, f is the X-ray flux in photons/cm^2/sec, σ is the photoelectric cross-section for the atomic orbital of interest in cm^2, ϕ is an angular efficiency factor for the instrumental arrangement based on the angle between the photon path and the detected electron, y is the efficiency in the photoelectric process for formation of photoelectrons of the normal photoelectron energy, λ is the mean free path of the photoelectrons in the sample, A is the area of the sample from which the photoelectrons are detected, and T is the detection efficiency for electrons emitted from the sample.

Rearranging Equation 2-4 to solve for the number of atoms of the element in question gives:

$$n = \frac{I}{f\sigma\phi y\lambda AT}$$

Equation 2-5

The denominator of Equation 2-5 can be defined as the atomic sensitivity factor, *S*, and can be determined for every element and is specific to each spectrometer system. The percent concentration of a specific atom can then be determined using the following ratio:

$$C_x = \frac{n_x}{\sum n_i} = \frac{I_x/S_x}{\sum I_x/S_x}$$

Equation 2-6

To ensure accurate results using this technique, it is important to check the spectrometer operation frequently to ensure that the analyzer response is consistent.

2.3 Results

2.3.1 General Surface Reaction Scheme

The most important goal of our study was to develop a facile way to create self-assembled monolayers containing antibacterial long-chain quaternary ammonium groups. Total organic synthesis of thiol molecules containing these groups is undoubtedly a many step process that necessitates protecting the reactive thiol moieties and many product separation steps. We chose to use surface synthesis techniques whereby we begin by forming a surface first, followed by modification of the surface structure via surface reactions. This strategy eliminates the need for thiol protection as well as product separation because the thiols are inherently protected when bound to the gold, and reaction bi-products remain non-bound to the surface and can be removed easily.

The formation of the quaternary ammonium SAMs is a three step process that involves:

1. Forming a carboxylic acid-terminated SAM
2. Converting the carboxylic acid group into an amide group which has a tertiary amine terminus

3. Quaternizing the tertiary amine by reacting it with a long-chain 1-bromo-2-ketone group.

The general scheme is outlined in Figure 2-11.

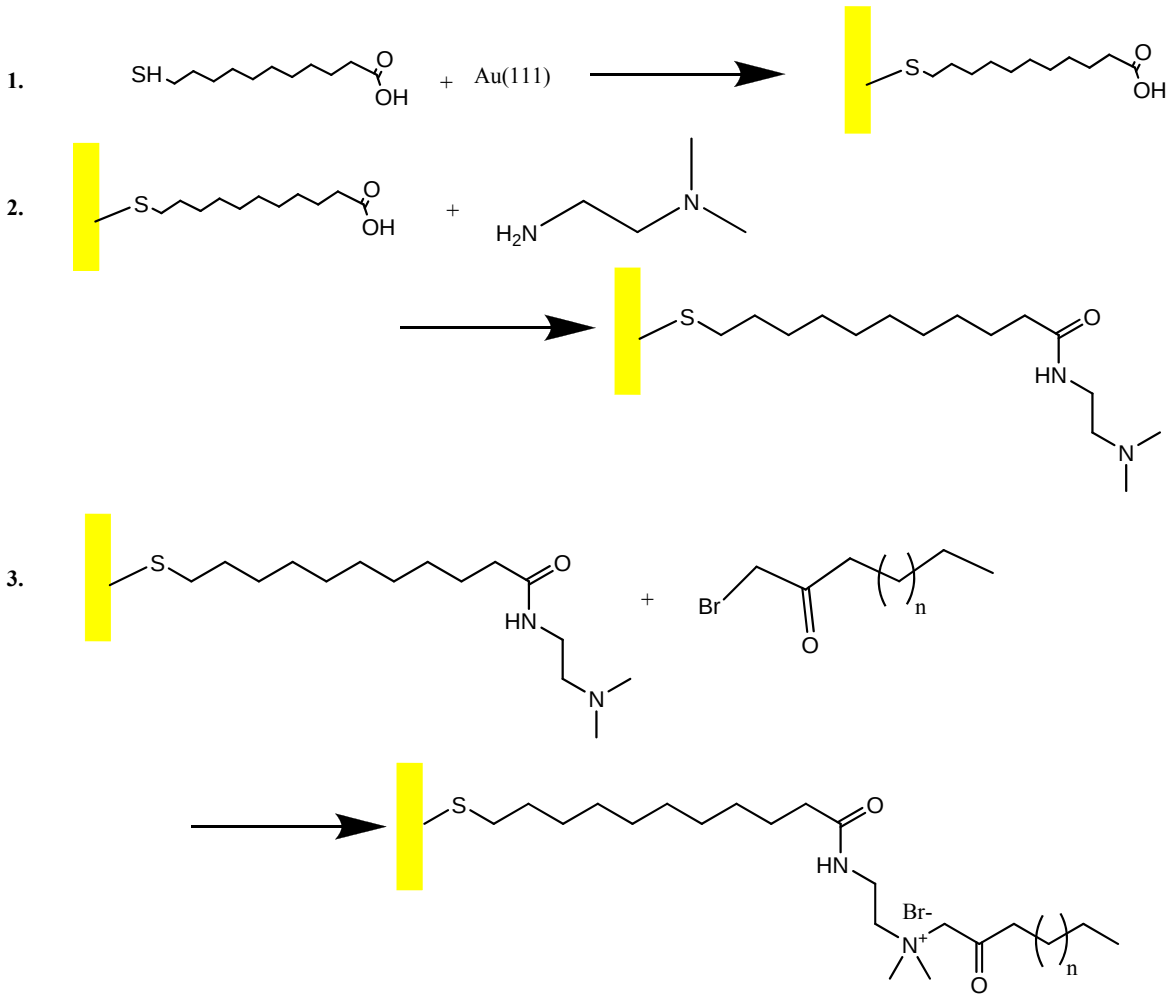

Figure 2-11: Overall scheme of our stepwise surface reactions approach used to form long-chain QAC SAMs.

The goal of this study was to optimize the reaction conditions of steps 2 and 3 of the reaction scheme to maximize the reaction rate and to achieve the highest possible surface density of quaternary ammonium groups. The following sections present data and offer discussion for the different methods attempted to synthesize quaternary ammonium SAMs using surface-based reactions.

2.3.2 Vapor Phase Surface Reactions

We considered two strategies for creating self-assembled monolayers with tertiary amine terminal groups that could later be quaternized. The first strategy we employed was to use vapor phase reactions to convert terminal carboxylic acid groups to the tertiary amino species. We decided to initially use vapor phase reactions because they are less prone to form side products and previous work by our group has shown that the well-ordered structure of the SAM is not disrupted when vapor phase reactions are utilized.[76]

The terminus of a carboxylic acid SAM is a reactive moiety that can be converted into a number of different chemical species. In the second step of our strategy to form a QAC SAM, the carboxylic acid group is converted into an amide via substitution of the hydroxyl moiety with a nitrogen atom. The conversion into the amide group can be greatly enhanced by first converting the hydroxyl moiety to a more reactive and better leaving group. One such reactive leaving group is the chlorine atom of an acid chloride species. In the first surface synthesis reactions described here, the carboxylic acid species is converted into an acid chloride via the vapor phase reaction with thionyl chrloride. The acid chloride is then immediately reacted with a diamine in the vapor phase which provides the final amide species.

Use of the acid chloride intermediate to convert a terminal carboxylic acid group was first reported by Duevel and Corn in 1992.[77] They converted the terminal groups of an 11-mercaptoundecanoic acid SAM into acid chlorides via reaction with vaporous thionyl chrloride. They then converted the acid chloride intermediate into either an amine or an ester via a second vapor phase reaction. The reactions were monitored with Polarization Modulation RAIRS. In the work presented here, the same experimental approach was used. The experimental details are outlined next.

Experimental

The carboxylic acid SAMs were prepared by immersing a freshly cleaned gold slide in a 1.0 mM ethanolic solution of 11-mercaptoundecanoic acid. After approximately 18-24 hours, the slides were removed from the thiol solution, rinsed with 200 proof ethanol, dried with ultrahigh purity nitrogen, and either analyzed or used for further reactions.

The vapor phase surface reactions, as shown schematically in Figure 2-12, were performed in a three-neck round bottom flask. One neck was attached to a mechanical pump which obtained a pressure below 10^{-2} Torr, another neck was attached to a supply of ultrahigh purity nitrogen for use as a purge gas, and the third neck was sealed with a rubber septum. The temperature was controlled by using a sand bath on top of a hot plate. Reagents were introduced into the flask via a syringe through the rubber septum. Before the introduction of the thionyl chloride, the reaction flask was purged with nitrogen for 5-10 minutes and then evacuated for 2-3 minutes. Approximately 25 μL of thionyl chloride was injected into the flask with careful consideration to avoid adding the reagent directly on top of the surface. After reacting for 10 minutes, the reaction flask was evacuated again for 15-30 minutes. Approximately 25 μL of *N,N*-dimethylethylenediamine was then injected into the flask and allowed to react for 10 minutes. The flask was then evacuated again for ten minutes followed by a short nitrogen purge. The functionalized surface was removed from the reaction flask, rinsed with 200 proof ethanol, and immediately used for analysis.

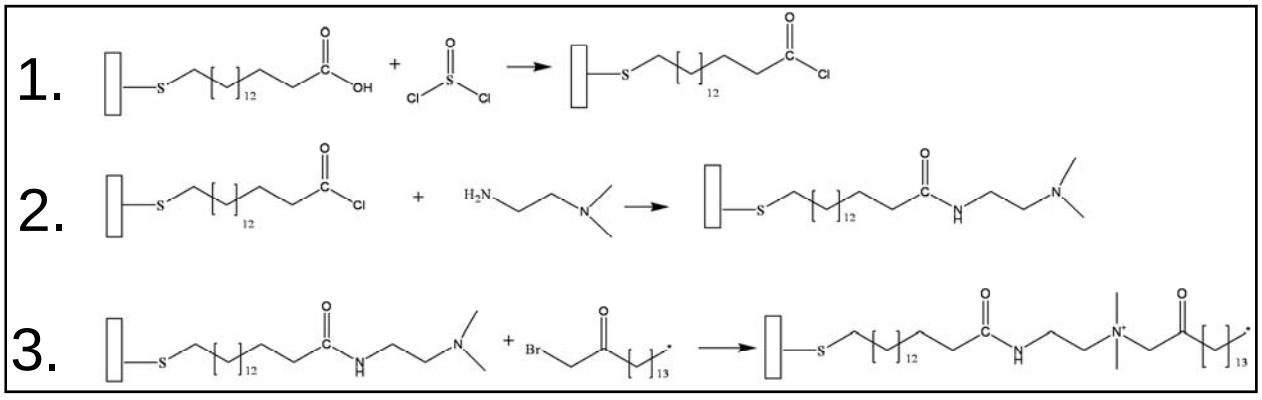

Figure 2-12: Reaction scheme for the vapor phase reaction of a carboxylic acid SAM with thionyl chloride followed by reaction with *N,N*-dimethylethylenediamine.

Results

Surface Characterization

RAIRS

The formation of the carboxylic acid-terminated SAMs was verified with RAIRS. The typical spectrum is shown in Figure 2-13. The characteristic carbonyl stretching modes are clearly evident at 1741 and 1718 cm^{-1}; the splitting is the result of intramolecular hydrogen bonding of the carbonyl groups.[59] Due to the highly reactive nature of the acid chloride intermediate, the surface was not removed from the reaction flask for characterization. The surface was next analyzed after reaction with the vapor phase diamine. The resulting spectrum is also shown in Figure 2-13. The most important observation is the change in the carbonyl stretching peaks. In the amine spectrum, the carbonyl mode has broadened and red shifted nearly 140 cm^{-1} to 1600 cm^{-1}. This region of the spectrum is characteristic of carbonyl stretches associated with an amide group. In addition, the methylene stretching modes near 3000 cm^{-1} are larger in the amine spectrum, which is consistent with the addition of two methylene groups from the ethylene diamine moiety. The IR spectral changes clearly provide evidence supporting the conversion of the carboxylic acid group to an amide group. Further confirmation is provided by XPS.

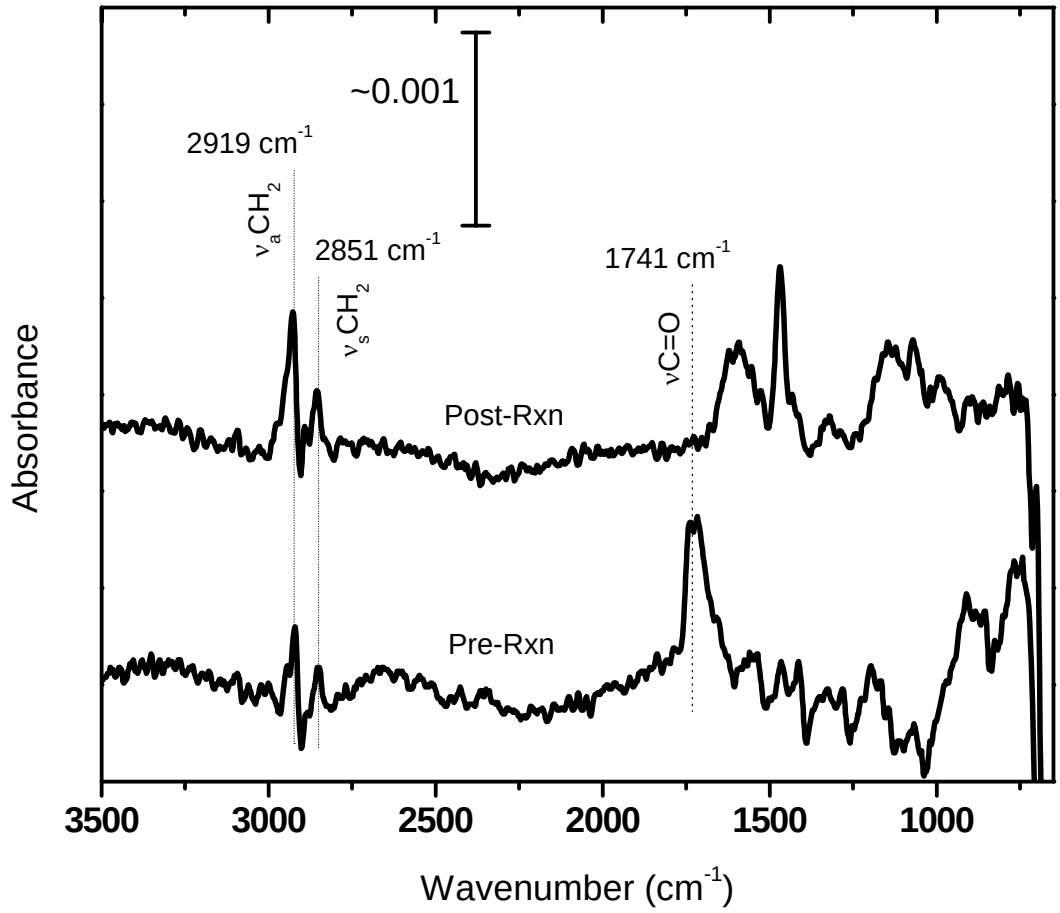

Figure 2-13: Vapor phase surface reaction RAIR spectra. The bottom trace is a 16 COOH SAM and the top is the same SAM after reacting with vaporous thionyl chloride and *N,N*-dimethylethylene diamine.

XPS

While RAIRS provides information about the introduction and disappearance of surface-bound functional groups as well changes to surface structure, a more complete understanding of the surface chemistry requires elemental analysis and determination of atomic percent composition. This additional information can only be provided by X-ray photoelectron spectroscopy. XPS can help determine both the atomic percentages and oxidation states of each element on a surface. Changes to the chemical composition of a monolayer can easily be detected and quantified via XPS. For the vapor phase reactions performed to convert the carboxylic acid groups into amide groups, the gold, carbon, oxygen, and nitrogen regions were monitored XPS. The XP spectral regions characteristic of the constituent atoms of the surface are presented in Figure 2-14.

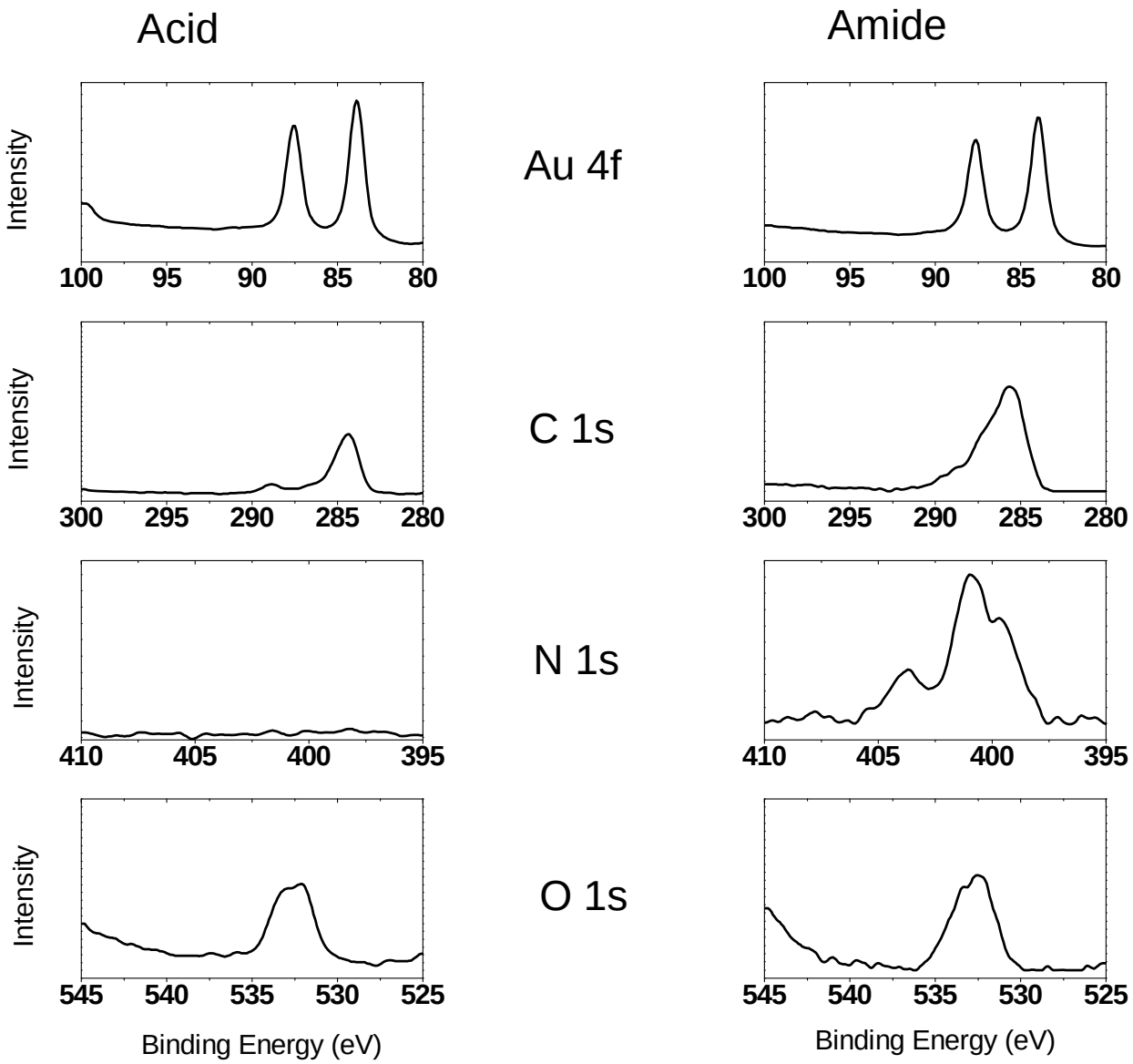

Figure 2-14: XP Spectra of a 16 COOH SAM before (left panels) and after (right panels) reaction with vaporous thionyl chloride and *N,N*-dimethylethylene diamine. The corresponding figures of each element are drawn at the same intensity scale.

The analysis of all four elements surveyed provides evidence of amide bond formation. First, the Au $4f^{7/2}$ peak intensity diminishes after the amide reactions, which is the result of photoelectron attenuation. The addition of the diamine, which includes an ethylene spacer and terminal dimethyl amino group, to the monolayer terminus creates a thicker overlayer for the low-lying gold photoelectrons to travel through before reaching the detector. The C 1s spectra also show evidence of amide bond formation. On the carboxylic acid spectrum, there is a small peak at 289 eV which is assigned to the carbonyl carbon of the acid group.[78] On the C1s region

of the amide spectrum, this small peak is absent and a new shoulder is present at 287 eV, which is assigned to the carbonyl of the amide group. The overall intensity of the C 1s peak is larger for the amide spectrum, which is consistent with an increase in the number of carbon atoms on the molecular chain. The N 1s spectra provide the most obvious evidence for the formation of the amide bond. In the carboxylic acid spectrum, no nitrogen is present, as should be expected. In the amide spectrum, there is a large broad peak, suggesting that a number of different nitrogen containing species contribute to the signal in this region. The shoulder near 398 eV is assigned to the tertiary nitrogen at the monolayer terminus, the peak near 400 eV is assigned to the amide nitrogen, and the smaller peak near 402 eV is assigned to tertiary nitrogen that may have been protonated or quaternized.[79] In contrast to the C1s and N1s spectra, the O 1s spectra do not show significant change. The amide O 1s spectrum is slightly more intense than the carboxylic acid C 1s spectrum, which is unexpected. We contribute this increase in oxygen to additional atmospheric contamination which can occur during sample transfer to and from the analytical instruments.

Both RAIRS and XPS provided evidence for the successful formation of the desired amide groups which resulted in a monolayer with tertiary amine groups at the interface. However, we often observed that other side reactions were occurring when the thionyl chloride was introduced. A significant loss of the surface bound molecules was detected via both RAIRS and XPS and was attributed to the highly reactive thionyl chloride molecules diffusing to the thiolate groups where they were oxidized. The results of the vapor phase reactions that caused the loss of the monolayers are presented and discussed next.

Vapor Phase Reactions Resulting in Loss of Monolayer

The most common result of the vapor phase amide synthesis was a disordered surface with a significant loss of monolayer. The RAIR spectrum of such a surface is shown in Figure 2-15. There is some evidence of the red shift of the carbonyl stretch as observed previously, however the methylene stretching modes almost completely disappear, which highly suggests a significant loss of surface coverage. The loss of monolayer was the most common result obtained for the vapor phase surface synthesis of amide SAMs. A multitude of different conditions were investigated including temperature, time, and pressure and each change in

variable ultimately led to the same result: loss of monolayer. The reasons for the observed loss of monolayer are discussed next.

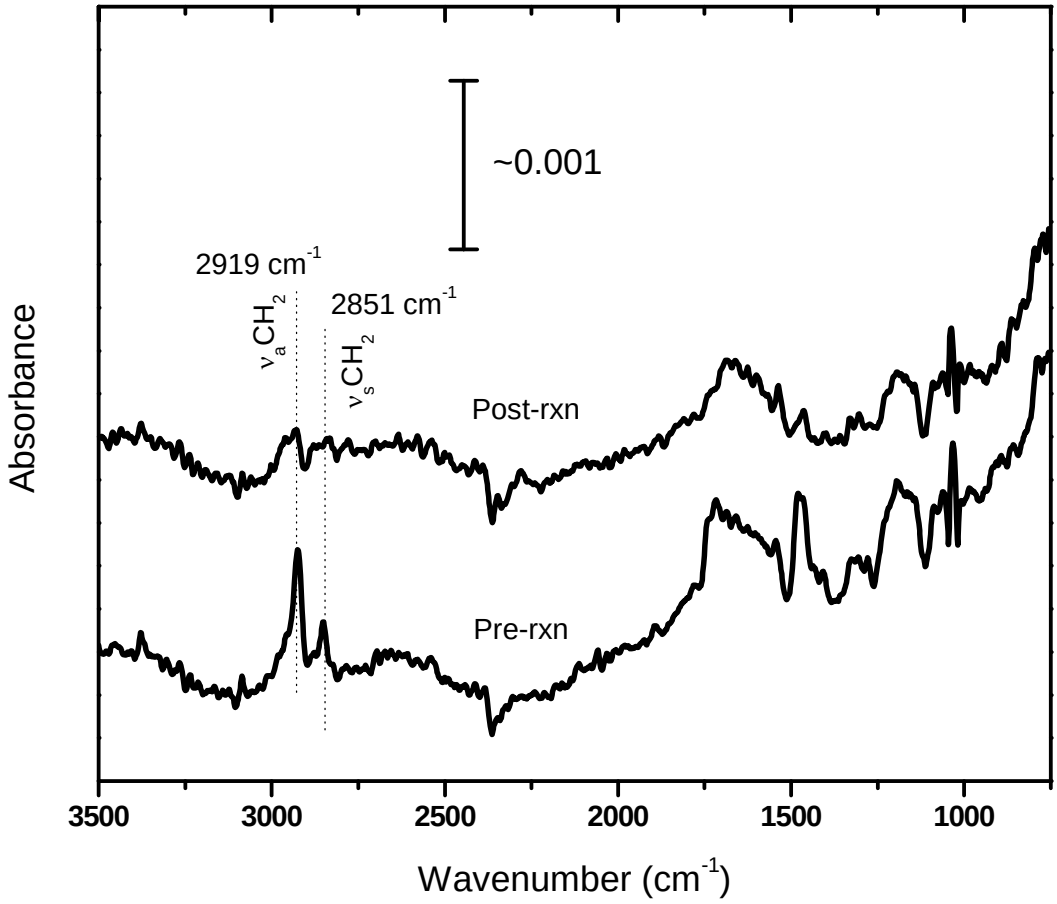

Figure 2-15: RAIR spectra of a 16 COOH SAM after the vapor phase surface reactions in which there was significant loss of surface coverage. The bottom spectrum is before the reaction and the top spectrum is after the reaction.

Discussion of the Vapor Phase Reactions Leading to Loss of Monolayer

Thionyl chloride is a highly oxidizing and reactive molecule which is most commonly used to convert carboxylic acids into acid chlorides[77, 80, 81] and alcohols to alkyl chlorides.[80] The thiol moiety has similar chemical properties to the hydroxyl group and can undergo similar reactions with oxidizing agents. The spectral observations of the vapor phase amide synthesis reactions revealed that there was often a significant loss of monolayer surface coverage, which suggests that the gold-thiolate bond had been broken and the unbound molecule was rinsed away from the surface. An 11-mercaptoundecanoic acid monolayer is not as well-packed as a similar

length methyl terminated SAM.[82, 83] Because of this disorder, it is possible that thionyl chloride molecules could diffuse to the gold-thiolate bond and react with the thiolate. Without the covalent bond to the gold surface atoms, the reacted thiolate molecule would be easily rinsed away prior to characterization. While this hypothesis was not directly tested, it is the most probable cause of the observed loss of monolayer. The slightly elevated temperature used (50°C) perhaps contributed to the desorption, however previous studies have shown that an hexadecanethiol monolayer did not desorb from the surface at temperatures below 170°C.[84]

The loss of monolayer was the most commonly observed result of the vapor phase amide surface synthesis. The reactivity of the thionyl chloride towards the surface-bound thiolates made the vapor phase reactions unfeasible. We next turned our attention towards another strategy for creating SAMs with tertiary amine groups via solution phase reactions. .

2.3.3 Functionalizing SAMs Via Condensed Phase Surface Chemistry

The structure of the long-chain quaternary ammonium alkanethiol molecule, synthesized via surface reactions, contains a very common linking group for biomolecules: the amide bond. The amide bond is the key linker group of proteins as the connection between each amino acid of the peptide sequence is made via an amide bond, which connects a carboxylic acid moiety to a primary or secondary amine group. The amide bond has also been utilized extensively to covalently bind biomolecules to surfaces[85] as well as to modify alkanethiol self-assembled monolayers to add desired properties to the surface, such as electro-active groups[86] and hydrogen bonding groups[76] which can increase the stability of the monolayers. The formation of the amide bond on monolayer surfaces was facilitated by the use of a catalyst, 1-[3-(dimethylamino)propyl]-3-ethylcarbodiimide (EDC).[85] The following sections describe the solution phase reaction of the carboxylic acid terminated SAMs with the *N,N*-dimethylethylenediamine to form an amide bond and a tertiary amine terminated interface.

Direct Reaction of a COOH SAM with a Free Amine via EDC Catalysis

Experimental

The carboxylic acid terminated SAM was created by immersing a clean gold slide in an ethanolic 1.0 mM solution of 11-mercaptoundecanoic acid for 18-24 hours. The slide was then

removed from the solution, rinsed with 200 proof ethanol, dried with ultrahigh purity nitrogen, and either immediately analyzed or used for further surface derivatization.

The newly formed carboxylic acid SAM was placed into an aqueous solution containing 0.002 M of the EDC catalyst and 0.005 M *N,N*-dimethylethylenediamine. The solution was stored in the dark at room temperature for 24 to 48 hours. The slide was then removed from the solution, rinsed with deionized water, and used immediately for analysis.

Results

RAIRS

Figure 2-16 shows the reaction scheme used to convert the carboxylic acid terminated SAM into an amide SAM with tertiary amine groups.

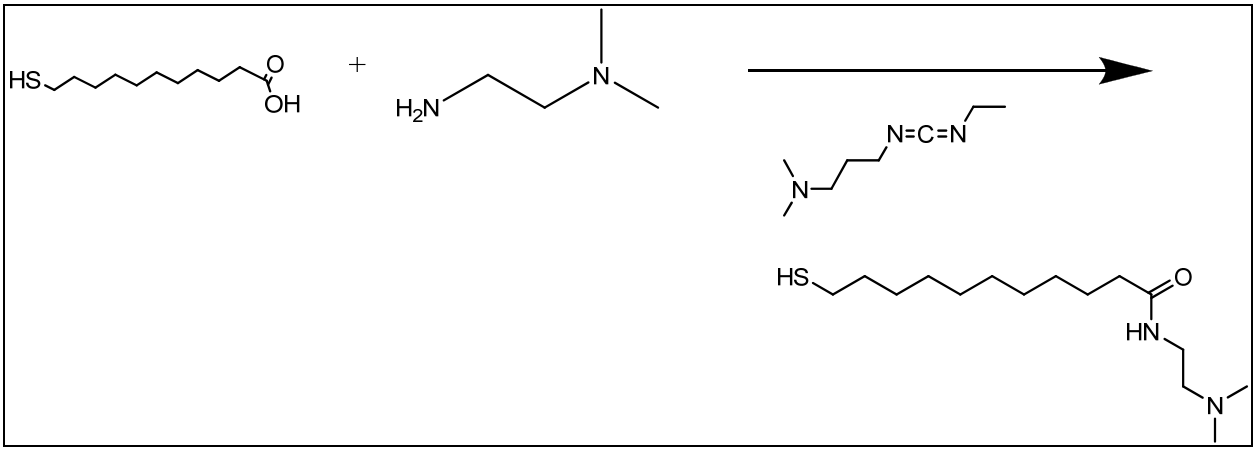

Figure 2-16: Reaction scheme of an 11 COOH SAM with *N,N*-dimethylethylenediame in solution using the EDC catalyst.

The surface was characterized both before and after the amide forming reaction with RAIRS and XPS. Figure 2-17 shows the RAIR spectra of the carboxylic acid terminated SAM and after the EDC catalyzed reaction with the diamine. The vibrational mode assignments are provided in Table 2-2.

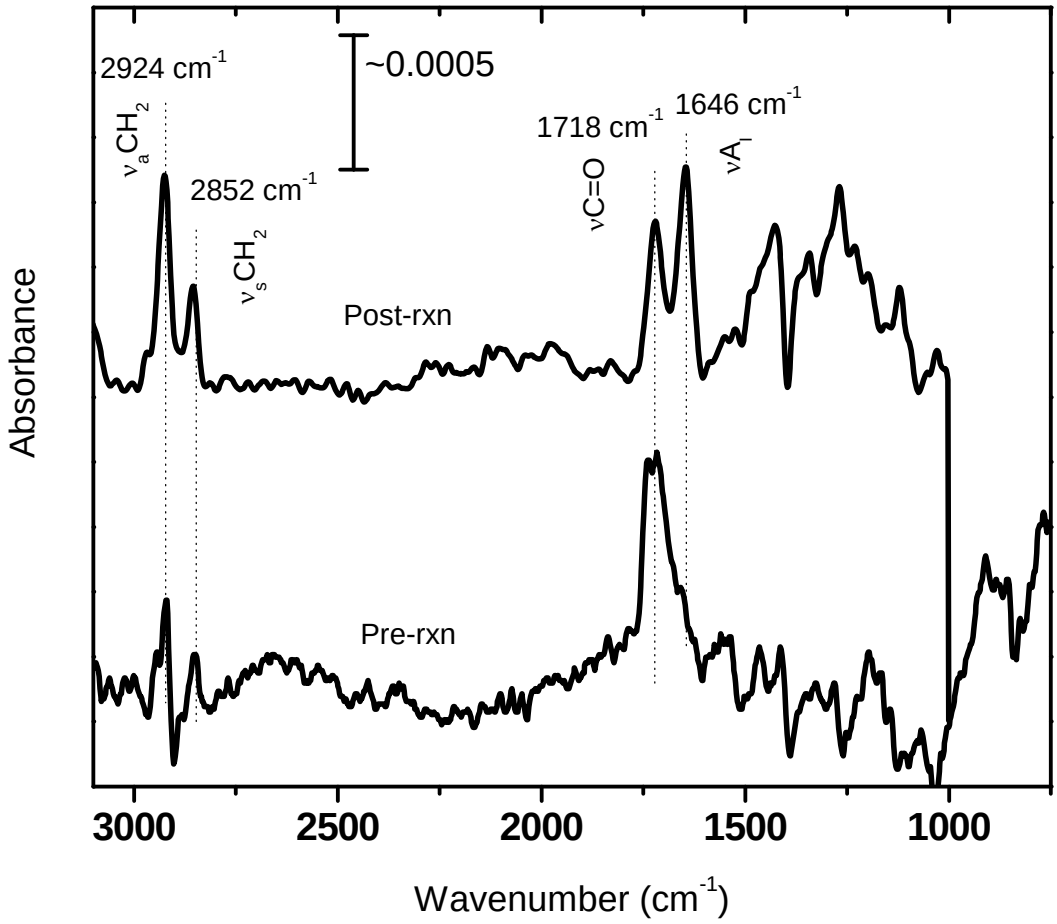

Figure 2-17: RAIR spectra of a 11 COOH SAM recorded before (bottom) and after (top) solution reaction with *N,N*-dimethylethylenedieamine using the EDC catalyst.

The RAIR spectrum recorded after the amide reaction suggests that the reaction occurred to form new amide bonds. In the amide SAM spectrum, there is a new peak at 1648 cm^{-1} which is characteristic of the carbonyl stretch of an amide group.[59] There is also a small, broad peak near 1545 cm^{-1} which is characteristic of the N-H bending mode of the amide group. The low intensity may be due to a mostly horizontal orientation of the amide moieties.[76] The methylene stretching modes at 2920 cm^{-1} and 2852 cm^{-1} are larger for the amide spectrum, which is the primarily result of the additional methylene groups added to the molecular chain. Interestingly, there is a strong absorption mode in the amide spectrum present at 1723 cm^{-1}. This frequency is

Position	Mode
2966 cm^{-1}	ν_a-CH_3
2920 cm^{-1}	ν_a-CH_2
2875 cm^{-1}	ν_s-CH_3
2852cm^{-1}	ν_s-CH_2
1723 cm^{-1}	νC=O acid
1648 cm^{-1}	Amide I (νC=O)
1545 cm^{-1}	Amide II (δN-H)

Table 2-2: Vibrational mode assignments of RAIR spectra from Figure 2-17.

commonly associated with a hydrogen bonded carbonyl stretch of a carboxylic acid, as can be seen on the spectrum of the acid-terminated SAM. The occurrence of this acid carbonyl stretch on the spectrum of the amide SAM suggests that the acid-to-amide conversion was not quantitative; there are still some carboxylic acid groups left on the surface. Further evidence for the formation of amide bonds on the surfaces was provided by XPS.

XPS

The carboxylic acid terminated surface was analyzed via XPS before and after the reaction with the diamine to form the amide bonds. High resolution spectra were recorded for Au 4f, C1s, N1s, and O1s regions. Both the C1s and N1s spectra support the RAIR spectra observations that the amide forming surface reactions did take place and are shown in Figures 2-18 and 2-19 respectively.

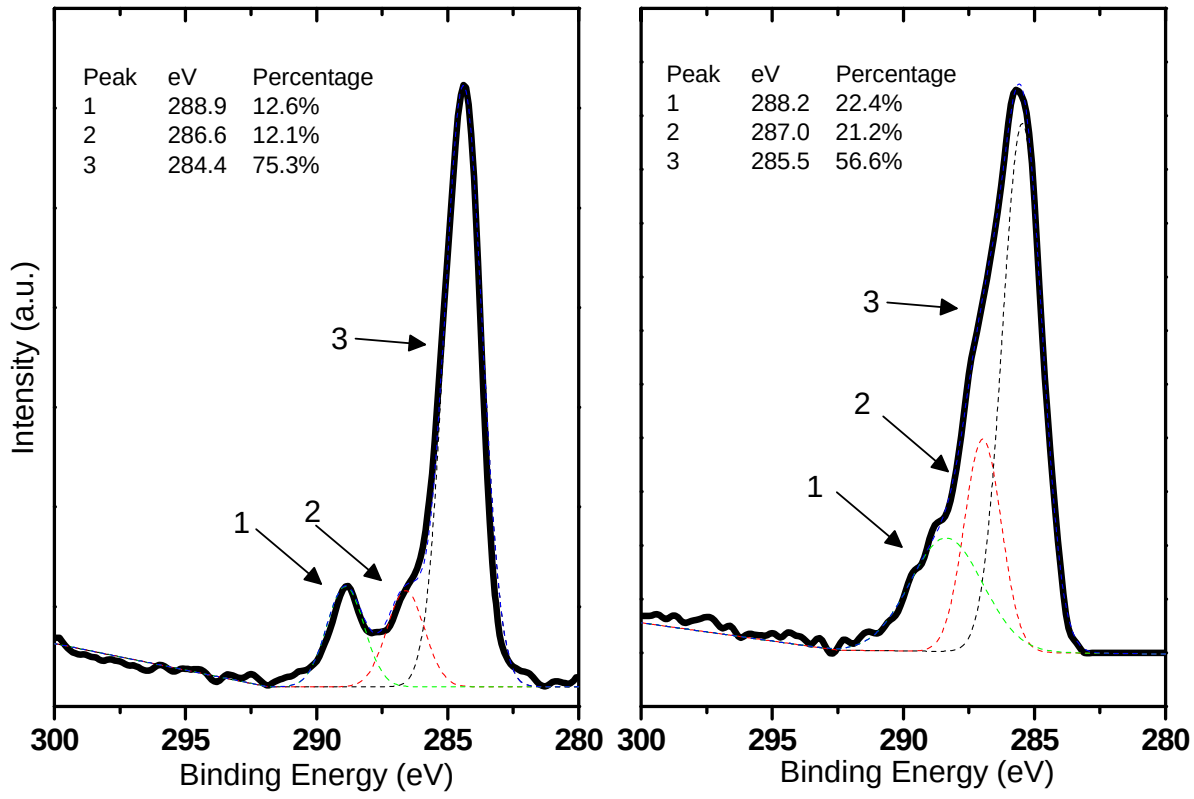

Figure 2-18: C1s region of XP spectra for a 11 COOH SAM recorded before (left) and after (right) solution reaction with *N,N*-dimethylethylenedieamine and EDC catalyst.

The XP spectrum of the C1s region for the carboxylic acid SAM contains characteristic features. The peak contains contributions from at least three components that can be fit using a sum of Gaussian curves. There is a well defined peak at 288.9 eV which is assigned to the highly oxidized carbon of the carboxylic acid moiety. The shoulder at 286.6 is assigned to the carbon alpha to the carbonyl carbon and the largest peak at 284.4 eV is assigned to the carbons of the alkyl chain.[75] The C1s spectrum of the surface after the amide-forming reactions show features characteristic of the amide species. There are again three prominent peaks that can be identified. The largest peak at 285.5 eV is from the carbon atoms of the alkyl chain, and the now larger peak at 287.0 eV is assigned to the carbons of the amide group. The third peak is found at 288.2 eV and is assigned to the carbon of unreacted carboxylic acid groups. This observation is in agreement with the RAIR spectra recorded after the amide reactions. There were two peaks present in the carbonyl stretching, one assigned to the amide (~1650 cm^{-1}) and the other to the unreacted carboxylic acid moieties (~1723 cm^{-1}).

The N1s XP spectra clearly reveal the addition of nitrogen to the surface after the amide reactions. As should be expected, no nitrogen is detected in the N1s spectrum of the carboxylic acid SAM. For the amide N1s XP spectrum, three peaks are identified: one at 401 eV, which is assigned to the amide nitrogen atom, one at 399 eV, which is assigned to the terminal tertiary nitrogen, and one at 403 eV which is most likely a protonated ammonium nitrogen.

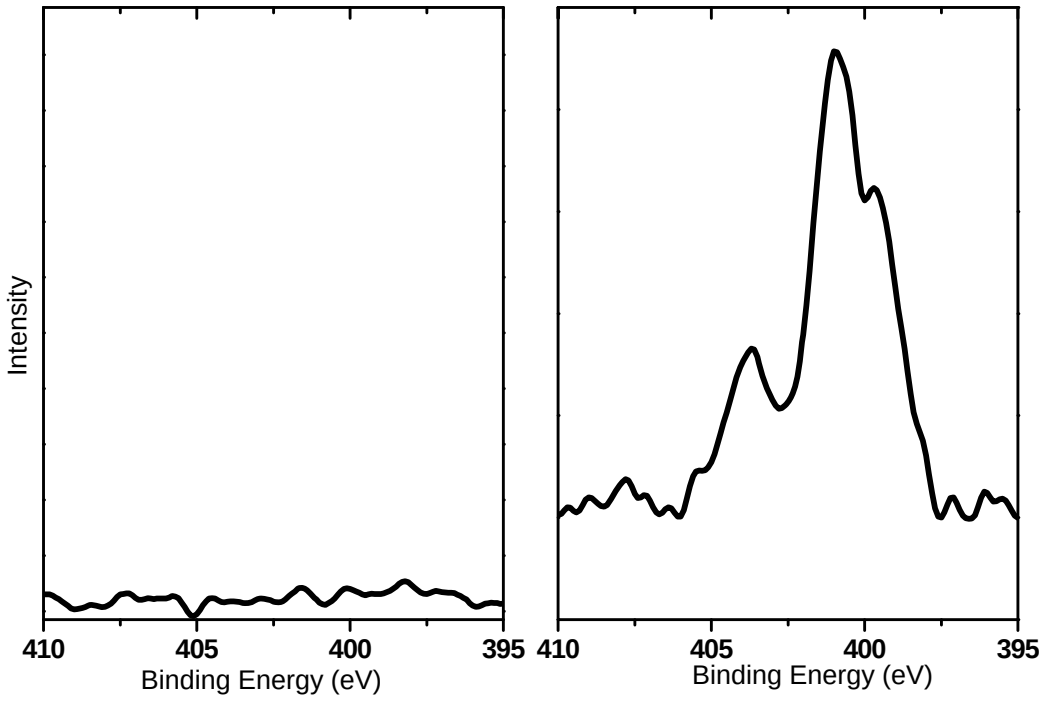

Figure 2-19: N1s region of XP spectra for a 11 COOH SAM recorded before (left) and after (right) solution reaction with *N,N*-dimethylethylenedieamine and EDC catalyst.

The remaining carbonyl stretching mode for a carboxylic acid after the amide forming reactions as seen in the RAIR spectrum revealed that the carboxylic acid moieties were not converted into amide groups in a 1:1 ratio. The most definitive evidence that reactions were not quantitative is provided by measurement of the atomic percentages of each surface. In Table 2-3, the atomic percentage of carbon, nitrogen, and oxygen is provided and compared to the expected percentage values. The experimental data was obtained by measuring the area of each elemental XPS peak and dividing by the elemental sensitivity factor. The expected values were calculated by assuming a surface containing either 100% 11-mercaptoundecanoic acid molecules or 100 % *N*-(2-(dimethylamino)ethyl)-11-mercaptoundecanamide molecules.

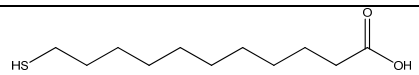 Acid	Atoms	Expected Percent	Experimental Percent
C	11	84.62%	84.75%
N	0		0.00%
O	2	15.38%	14.82%

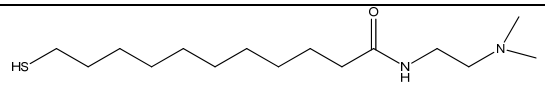 Amide	Atoms	Expected Percent	Experimental Percent
C	15	83.33%	84.75%
N	2	11.11%	7.68%
O	1	5.56%	15.25%

Table 2-3: Comparison of experimentally determined and predicted atomic percent composition for a 11 COOH SAM before (top) and after (bottom) reaction with *N,N*-dimethylethylenediamine with EDC catalyst.

The experimentally determined atomic percentage for the carboxylic acid SAM agrees very well with the predicted values, which are based on a SAM composed of molecules with 11 carbon and two oxygen atoms per molecule. This should be expected as the SAM was prepared from a pure ethanolic solution of the thiol. For the amide surface, however, the experimental percentages do not agree well with the expected percentages, which suggest that the conversion from carboxylic acid groups into amide groups was incomplete.

Conclusions

It is clear that the direct reaction of the carboxylic acid groups with the primary amine of *N,N*-dimethylethylenediame in the presence of the EDC catalyst is not quantitative. Using this reaction to provide the necessary tertiary amine moieties will effectively limit the maximum surface density of the quaternary ammonium groups that can be produced via reaction of the tertiary amines. A modification of the amide surface reaction scheme was necessary to move the reaction equilibrium more towards the product side and create a larger surface concentration of tertiary amines. Therefore, in the next section, the use of a reactive intermediate, *N*-hydroxysuccinimide as a method to promote the conversion of the carboxylic acid groups into amide moieties is explored.

Conversion of a COOH terminal group to an amide via a reactive intermediate, *N*-hydroxysuccinimide

The reaction between a carboxylic acid terminated SAM and primary amine using EDC catalyst result in a 1:1 conversion. The reaction of carboxylic acid groups with primary amines to form amide groups is a substitution reaction where the primary nitrogen attacks the carbonyl carbon of the carboxylic acid group. The hydroxyl group leaves with a pair of electrons and abstracts a lone proton from the primary amine to form water. The nitrogen forms a bond with the carbonyl carbon to form the amide group. One of the most important factors affecting the equilibrium of a substitution reaction is the stability of the leaving group. In the direct reaction of the carboxylic acid with the primary amine, the leaving group was the hydroxyl moiety of the acid, which is a stable leaving group under optimum conditions. Previous studies have shown that the reaction yield of the amide synthesis reaction can be greatly increased by using a reactive intermediate. *N*-hydroxysucciniimide (NHS) can react with a carboxylic acid group to form an ester intermediate. The NHS ester serves as a much better leaving group than the hydroxyl group and can provide a greater yield of amide moieties.

The NHS intermediate has been used extensively to create amide bonds.[87] Biomolecules such as DNA[88] and proteins[54], and even whole cells[16, 54] have been immobilized on surfaces using amide bonds formed from the NHS intermediate. The goal of the work presented next was to increase the yield of the amide surface synthesis reactions resulting in an increased surface density of the terminal tertiary amine groups.

Experimental

11-Mercaptoundecanoic acid and 16-mercaptohexadecanoic acid SAMs were prepared as described previously. The carboxylic acid terminated SAMs were then placed in an aqueous solution of 0.1 M NHS and 0.4 M EDC for ten minutes. The slides were removed from the solution, rinsed with deionized water, dried with ultrahigh purity nitrogen, and either analyzed or used for further reaction. The NHS-terminated SAMs were placed into an aqueous solution of 0.1 M *N,N*-dimethylethylenediamine for at least 2 hours. The slides were then removed from the amine solution, rinsed with DI water, and dried with ultrahigh purity nitrogen. The surfaces were immediately used for analysis.

Results

RAIRS

The amide surface synthesis was a two step process as outlined in Figure 2-20. The surface was characterized after each step of synthesis with RAIRS and XPS. The full RAIR spectra are shown in Figure 2-21 and the carbonyl region (1950-1350 cm^{-1}) is shown in Figure 2-22.

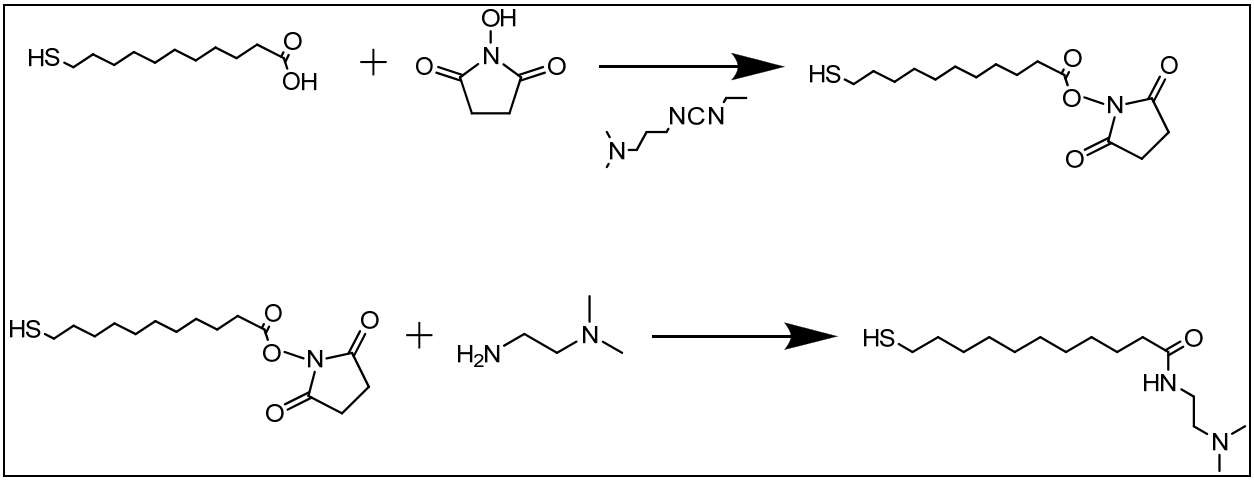

Figure 2-20: Reaction scheme of an 11 COOH SAM with *N*-hydroxysuccinimide intermediate using EDC catalyst followed by reaction with *N,N*-dimethylethylenediame in solution.

The carbonyl stretching region provides the most direct evidence of successful surface reactions. The carboxylic acid terminated SAM shows the characteristic carbonyl stretching mode at 1741 cm^{-1}. After reaction with the NHS/EDC, there are two new modes associated with the NHS moiety. The small peaks at 1821 and 1787 cm^{-1} are assigned to the C=O stretch of the activated ester carbonyl and the symmetric stretch of the imide C=O groups, respectively.[89] The large peak near 1650 cm^{-1} has been previously assigned to the C=O stretch of carboxylic acid grous.[89] The spectrum recorded after reaction with *N,N*-dimethyletheylenediamine has two modes associated with the amide group. The broad peak at 1650 cm^{-1} is assigned to the amide I C=O stretch and the peak at 1545 cm^{-1} is assigned to the amide II N-H bend. There is also a broad peak near 1720 cm^{-1} along with a corresponding shoulder at 1741 cm^{-1}. These modes are

typically assigned to the hydrogen and non-hydrogen bonded C=O stretch of a carboxylic acid. [59] This observation suggests that even with the inclusion of the NHS ester intermediate, the conversion of the carboxylic acid moieties into amide groups is not quantitative. Further evidence for the incomplete conversion into amide groups is provided by XPS.

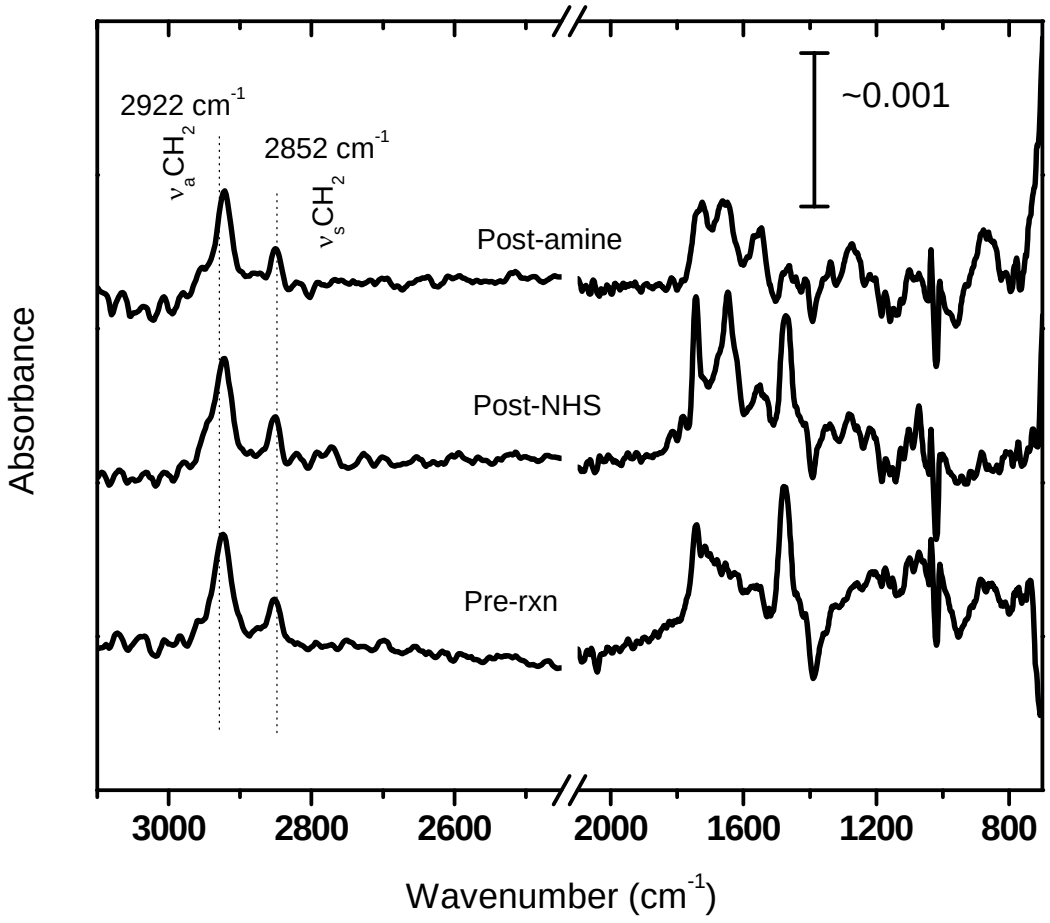

Figure 2-21: RAIR spectra of a 11 COOH SAM before reaction (bottom), after reaction NHS intermediate (middle), and after reaction with *N,N*-dimethylethylenediamine in solution (top).

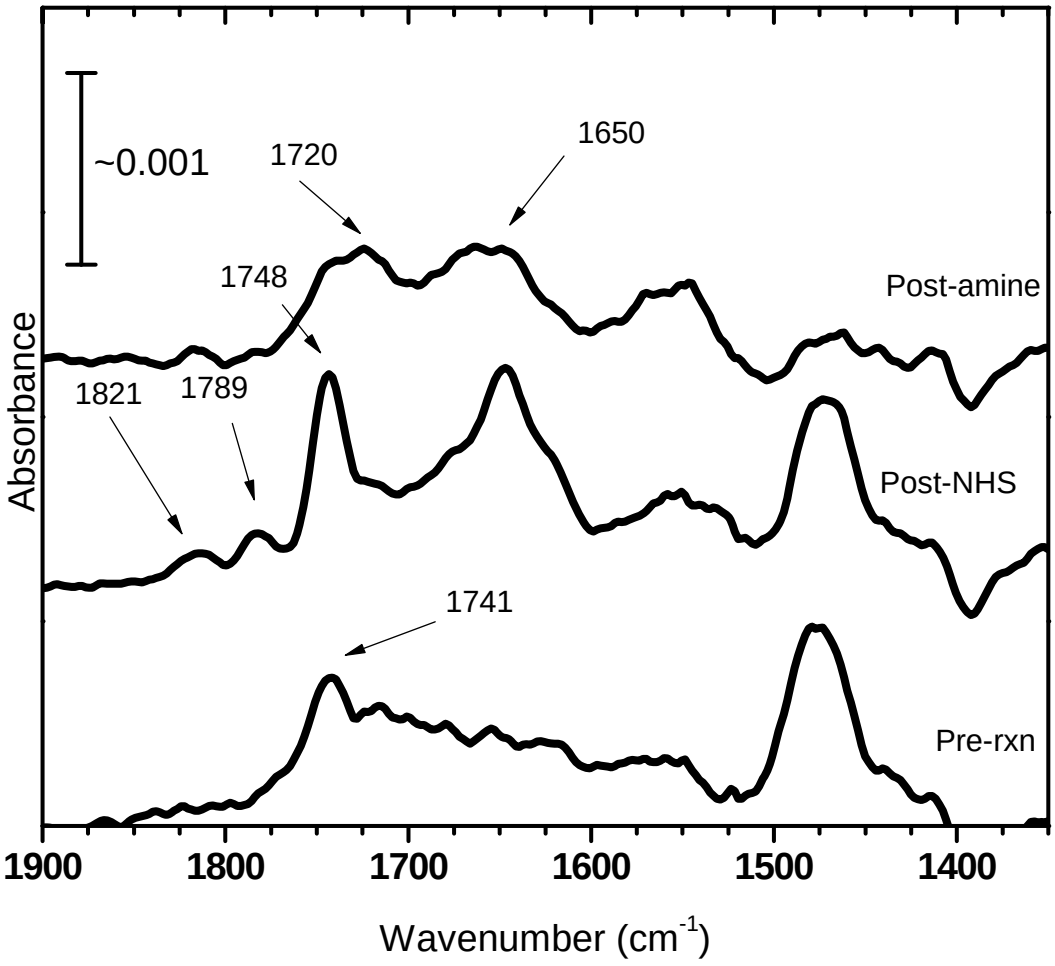

Figure 2-22: RAIR spectra of the carbonyl stretching region of a 11 COOH SAM before reaction (bottom), after reaction with NHS intermediate (middle), and after reaction with *N,N*-dimethylethylenediamine (top) in solution.

XPS

The surface was analyzed via XPS after each step of the surface synthesis. Multiplex spectra were recorded for the C1s, N1s, and O1s regions. The C1s XP spectra are shown in Figure 2-23.

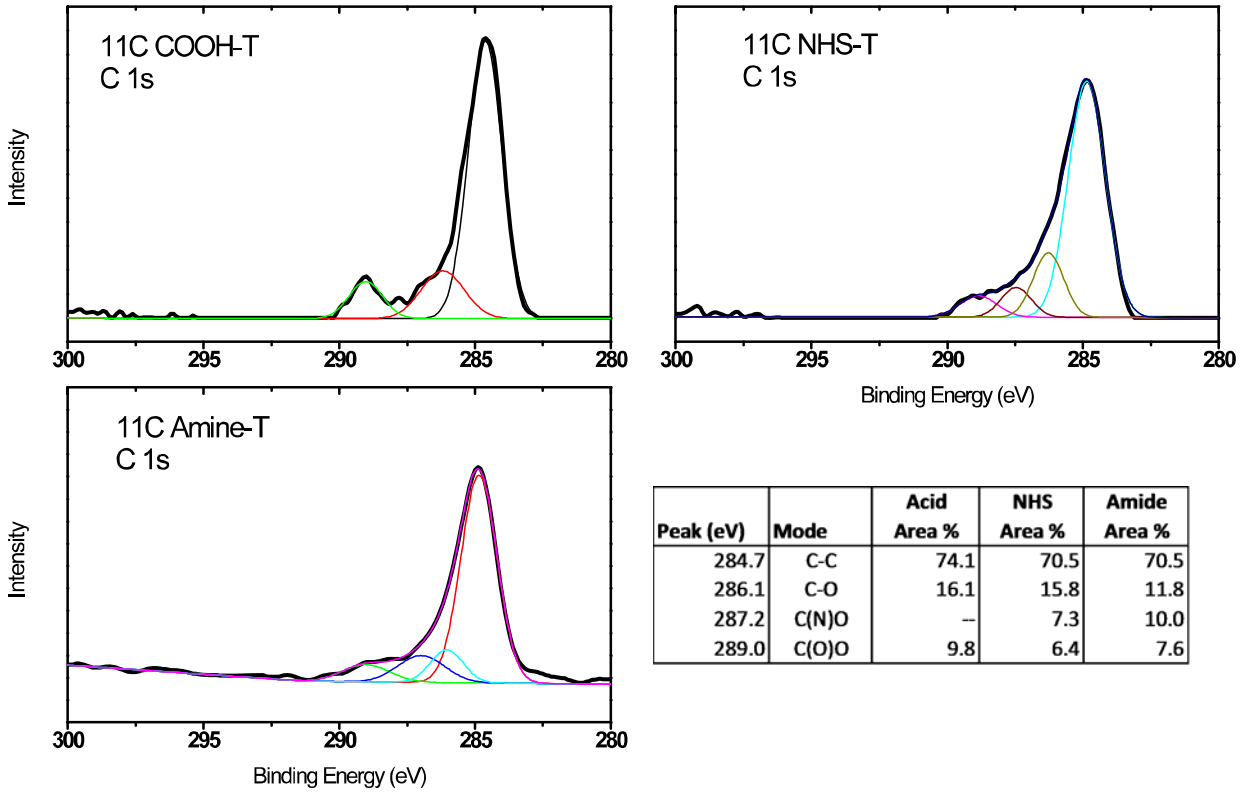

Peak (eV)	Mode	Acid Area %	NHS Area %	Amide Area %
284.7	C-C	74.1	70.5	70.5
286.1	C-O	16.1	15.8	11.8
287.2	C(N)O	--	7.3	10.0
289.0	C(O)O	9.8	6.4	7.6

Figure 2-23: C1s region of XP spectra for a 11 COOH SAM after reacting with NHS intermediate and *N,N*-dimethylethylenediamine. The table presents the percent area of each Gaussian curve comprising the total peak area for each spectrum.

For the carboxylic acid spectrum, the main peak contains contributions from three peaks that can be fit with Gaussian functions. The highly oxidized carbonyl carbon of the acid moiety is found at 289.0 eV, the carbon alpha to the carbonyl is at 286.1 eV, and the aliphatic backbone chain carbons are found at 284.6 eV. The C1s spectrum recorded after the NHS reaction has contributions from four peaks. The peak at 289.0 eV is assigned to a highly oxidized carbon (C(O)O), 287.2 eV is assigned to a C(N)O species, 286.1 eV is from a C-O species, and 284.7 is the alkyl chain backbone. These mode assignments are in good agreement with the literature.[88] The C1s spectra recorded after the NHS-terminated surface reacted with the diamine also shows evidence that the reaction took place. The peak at 286.1 eV is associated with the carbon of the

amide group and the peak at 284.7 eV is again associated with the aliphatic carbons. There is a more oxidized peak found at 287.2 eV which is most likely from the carbon adjacent to an unreacted carboxylic acid carbon (C(O)O), which also observed at 289.0 eV. The presence of carbon atoms from carboxylic acid groups is similar to what was observed from the direct reaction of the amine with the carboxylic acid groups. This suggests that the acid-into-amine conversion by using the NHS intermediate was not quantitative. In fact, the area percent of the carboxylic acid carbon increases for the amine surface relative to the NHS surface. This observation suggests that some of the NHS moieties underwent hydrolysis to reform the carboxylic acid groups. The incomplete reaction was also evidenced in the RAIR spectra as there was a significant absorption peak present normally associated with the carbonyl stretch of an acid group.

Discussion of the NHS Surface Reactions

As was observed in the direct amine reaction with the carboxylic acid terminated SAMs, using reactive NHS ester intermediate also led to an incomplete conversion into the amide groups. The reason for the non-quantitative reaction is most likely because of the steric hindrance of the carboxylic acid groups at the interface. Even though an 11-mercaptoundecanoic acid SAM is not as well-ordered as a similar length methyl-terminated SAM, there is still significant steric hindrance that prevents many carboxylic acid groups from reacting with the NHS/EDC species.

We observed that the conversion of a carboxylic acid terminated SAM into a tertiary amine terminated SAM via the formation of amide bonds did not occur in a quantitative manner. The most likely reason for the incomplete conversion of the carboxylic acid groups to amide groups is the steric hindrance surface bound species. The effect of steric hindrance on the reactivity of the NHS ester was observed by Dordi et. al.[90] They found definitive chain length dependence for the NHS reactivity, with the longer chain lengths showing less reactivity due to the higher degree of surface order of the longer alkane chains. The NHS groups of the more disordered monolayers had a smaller degree of steric hindrance. Our results are similar to theirs; the more ordered 16C SAMs showed a lower conversion to NHS groups than the less ordered 11C SAMs.

Lahiri et. al achieved a quantitative reaction using the NHS/EDC system in their investigation into the selective and specific bonding of proteins to PEG-terminated SAMs.[89] However, they used a series of mixed monolayers where the surface density, and there by the intramolecular spacing, of the carboxylic acid groups was controlled. The decreased surface density resulted in the reduction of the steric hindrance and promoted the quantitative NHS/EDC reactions.

Frey and Corn also observed the incomplete conversion from carboxylic acid groups into amides via the NHS ester intermediate reactions.[85] In their study, the EDC/NHS reactions were repeated up to four times and the maximum NHS surface coverage obtained was around 80 percent. They also observed the residual acid carbonyl stretching mode at 1715 cm^{-1}. The non-quantitative conversion was attributed to two main factors: the steric hindrance of the NHS ester when confined to a surface, and the propensity for the NHS ester to hydrolyze on the surface.[90] The hydrolysis reaction results in the loss of the NHS moiety from the surface and the generation of a terminal carboxylate species. In a slightly acidic environment, the carboxylate species could protonate and create the original carboxylic acid groups. The IR spectra and the XP spectra shown here both support the persistence of the carboxylic acid species.

As with the direct reaction of *N,N*-dimethylethylenediamine with carboxylic acid-terminated SAMs, the addition of the NHS ester intermediate did not result in a quantitative conversion from acid into amide moieties. The reasons for the incomplete reactions are the steric hindrance of the surface-bound NHS esters that prevents them from reacting with the diamine groups, and from the competing NHS hydrolysis side reaction. While an 80 percent conversion to amide groups may seem high, a higher conversion percentage would allow for a higher surface density of subsequent quaternary ammonium groups to be attached to the terminal tertiary amines. The density of quaternary ammonium groups on polymer films was found to be an important variable of their antimicrobial activity[91], and we suppose that the same density dependence exists for antibacterial monolayers.

One possible way to increase the conversion of acid into amide groups is to use a more stable intermediate that is less prone to hydrolysis. A fluorinated ester intermediate, formed using pentafluorophenol, is less reactive towards hydrolysis and shows an increase in stability in

basic solutions compared to *N*-hydroxysuccinimide. In the next section, the acid-tino-amide surface reactions using the pentafluorophenol intermediate are presented.

Conversion of a COOH terminal group to an amide via a reactive intermediate, pentafluorophenol

Pentafluorophenol (PFP) has been used previously as a reactive intermediate to convert surface-bound carboxylic acid groups into amide moieties. Relative to the NHS ester, the PFP ester is less apt to undergo hydrolysis, which increases the probability of the ester reacting with an amine to form the desired amide bond.[92, 93] The increased reactivity of PFP in solution reaction was first documented in the 1970's by Kovacs et. al.[94] They found that the PFP ester reacted approximately 10 times faster than the corresponding NHS ester. The Whitesides group was one of the first to demonstrate that the PFP ester can be used as a reactive intermediate for surface reactions.[89] Following this precedent, we used pentafluorphenol in place of NHS as a reactive intermediate to convert carboxylic acid groups into amide groups.

Experimental

The amide surface reactions utilizing the pentafluorophenol intermediate are shown in Figure 2-24. The surface reactions were performed as follows: 11-mercaptoundecanoic acid and 16-mercaptohexadecanoic acid SAMs were prepared as described previously. After rinsing with ethanol and drying with ultrahigh purity nitrogen, the surface was immersed in an ethanolic solution of 0.1 M EDC and 0.2M pentafluorophenol for 15 minutes. The surface was then removed from solution, rinsed with ethanol, and immediately placed into an ethanolic solution of 0.1 M *N,N*-dimethylethylenediamine for 20 minutes to 3 hours. The surface was then removed, rinsed with ethanol, dried with nitrogen, and immediately used for analysis or further reaction.

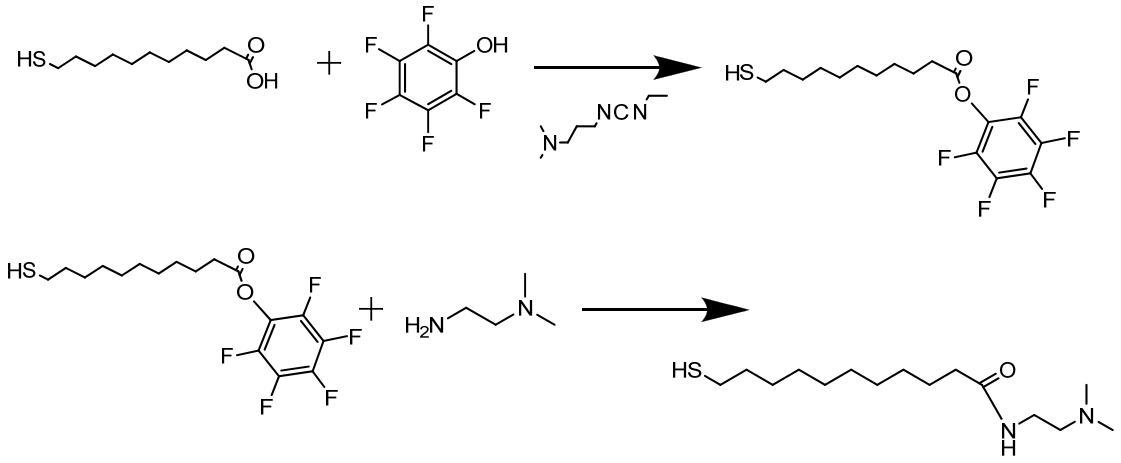

Figure 2-24: Reaction scheme of an 11 COOH SAM with pentafluorophenol intermediate using the EDC catalyst followed by reaction with N,N-dimethylethylenediame in solution.

Results

RAIRS

As with the previously described surface reactions, the surfaces were characterized before and after the reactions via RAIRS and XPS. Because of the high reactivity of the pentafluorphenol moieties, the surfaces were not characterized after the reaction between the carboxylic acid terminated SAMs and PFP. The SAMs were analyzed after the subsequent reaction with the diamine. Figure 2-25 shows the RAIR spectra of the 11 COOH-terminated SAM before the surface reactions and after the reaction with the diamine.

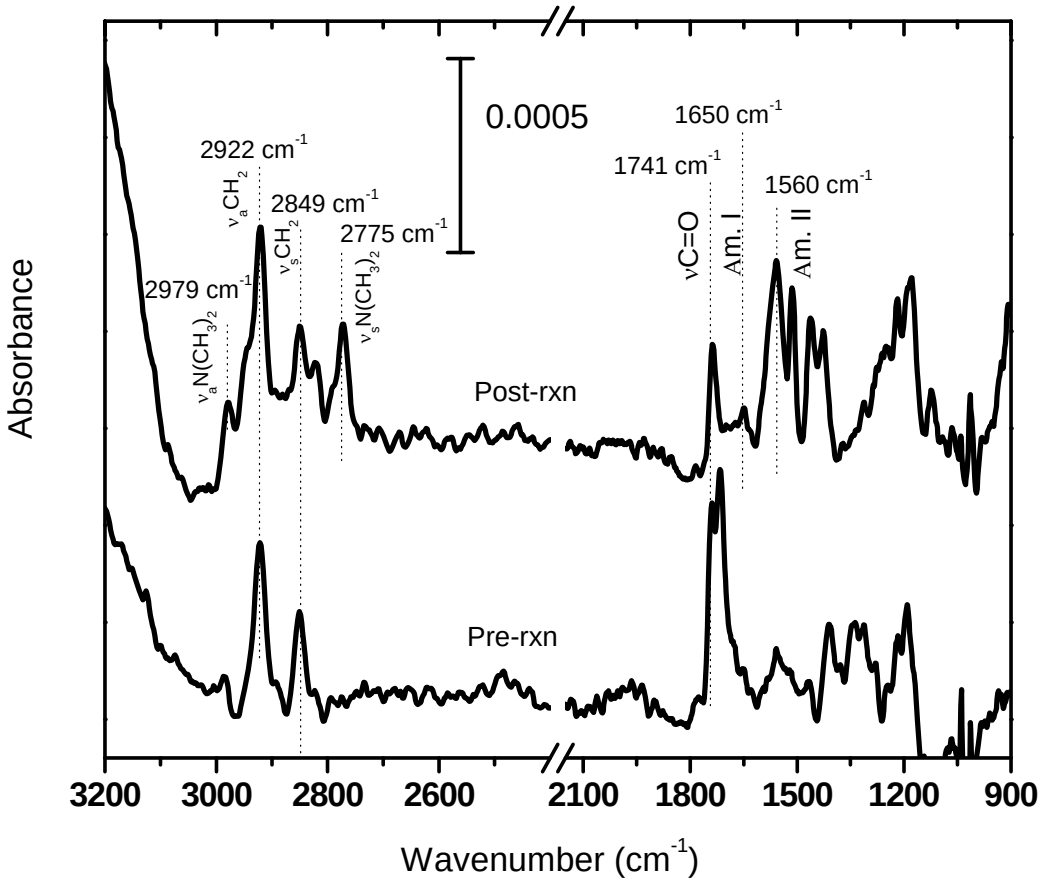

Figure 2-25: RAIR spectra of a 11 COOH SAM before (bottom) and after reaction PFP intermediate followed by reaction with *N,N*-dimethylethylenediamine (top) in solution.

The spectra for the 11C SAM shows clear evidence of the formation of the amide groups as well as the terminal tertiary amine species. The peak at 1552 cm^{-1} is assigned to the amide II mode and the smaller peak at 1662 cm^{-1} is assigned to the amide I mode. Several new peaks are present in C-H stretching region in the post-reaction spectra. The peaks at 2979 and 2894 cm^{-1} are assigned to the asymmetric and symmetric C-H stretches of the methyl groups of the terminal tertiary amine. These modes were not observed in the surface reactions by using NHS which suggests that the reaction with PFP is converting more of the carboxylic acid groups into amide moieties. There is, however, a peak at 1737 cm^{-1} in the post-reaction spectrum which is characteristic of the carboxylic species. Despite the appearance of the C-H stretching modes of the tertiary amino methyl groups, the remaining carboxylic acid carbonyl stretch strongly suggests that the conversion into the amide species was not quantitative.

The spectra of the 16-C SAMs, shown in Figure 2-26, do suggest a near quantitative reaction. The C=O stretching mode of the carboxylic acid at 1738 cm^{-1} is nearly absent in the post-reaction spectrum, which highly suggests a near quantitative conversion from carboxylic acid groups into amide moieties. Lahiri et al. observed a similar near quantitative conversion using the pentafluorophenol intermediate.[95] It is interesting to note that the frequency of the methylene stretching modes does not change as a result of the surface reactions. The static frequencies suggest that the monolayer retains a highly-ordered structure after the reaction. The C-H stretching modes characteristic of the methyl groups on the terminal tertiary amine are also present and are assigned to the asymmetric methyl C-H stretch at 2979 cm^{-1} and the corresponding symmetric stretch at 2771 cm^{-1}.

The relative intensities of the amide I and amide II modes can allow one to infer significant information about the orientation of the amide-containing molecules. The transition dipole moments of the amide I and amide II modes are nearly orthogonal to each other in an all-trans configuration.[96] The amide I transition dipole moment results from the stretch of the carbonyl group and is pointed parallel along the backbone of the bond. The amide II transition dipole moment results from the bending of the N-H bond and points perpendicular to the direction of the backbone of the bond. In accordance with the surface selection rule, the molecular orientation of the amide groups of the surface molecules can be determined.[97]

In both the 11C and 16C post-reaction spectra, the amide II mode is much larger than the corresponding amide I mode. One possible explanation for this observation is that the transition dipole moment of the amide II N-H bend might be larger than that of the amide I carbonyl stretch. However, a theoretical study by Kubelka et al. demonstrates that that amide I dipole is stronger both in the gas phase and aqueous solution.[98] The more likely explanation of the observed larger amide II intensity stems from the orientation of the amide groups on the surface. The intense amide II mode suggests that the N-H bond lies mostly parallel to the surface as the dipole moment of the N-H bend is perpendicular to the direction of the bond, putting the N-H bend dipole moment perpendicular to the surface where it interacts most strongly with the p-polarized infrared radiation. On the other hand, the amide I carbonyl stretching mode, which is orthogonal to the amide II mode, has a very small intensity, suggesting a weak interaction with

the p-polarized light. The C=O stretching vibration has a significant transition dipole moment and the small absorbance of this mode must be due to a parallel orientation of the bond.

Previous studies have investigated the effects of sub-terminal amide groups on surface order for alkanethiol self-assembled monolayers.[96, 99-101] In their investigations, the amide groups were introduced into the thiol molecules prior to the formation of the SAMs. It was found that the amide groups form an intramolecular hydrogen bonding network established by an all-trans configuration amide moieties. The formation of the hydrogen bonding network is energetically favorable enough to increase the normal 4.98 Å spacing between thiolate molecules to 5.1 Å. The increased lattice spacing achieves a nominal N-O distance 2.8 Å of the N-H···O hydrogen bond. The configuration results in 18° tilt of the molecules relative to surface normal and a 0° N-H···O bond angle which results in the N-H bending mode to be parallel to the surface normal. The proposed surface structure was supported by their RAIR spectra that showed very intense amide II modes and very weak amide I modes. Our IR results are in good agreement with these previous studies and we propose a structure for the surfaces after the amide forming reactions in Figure 2-27.

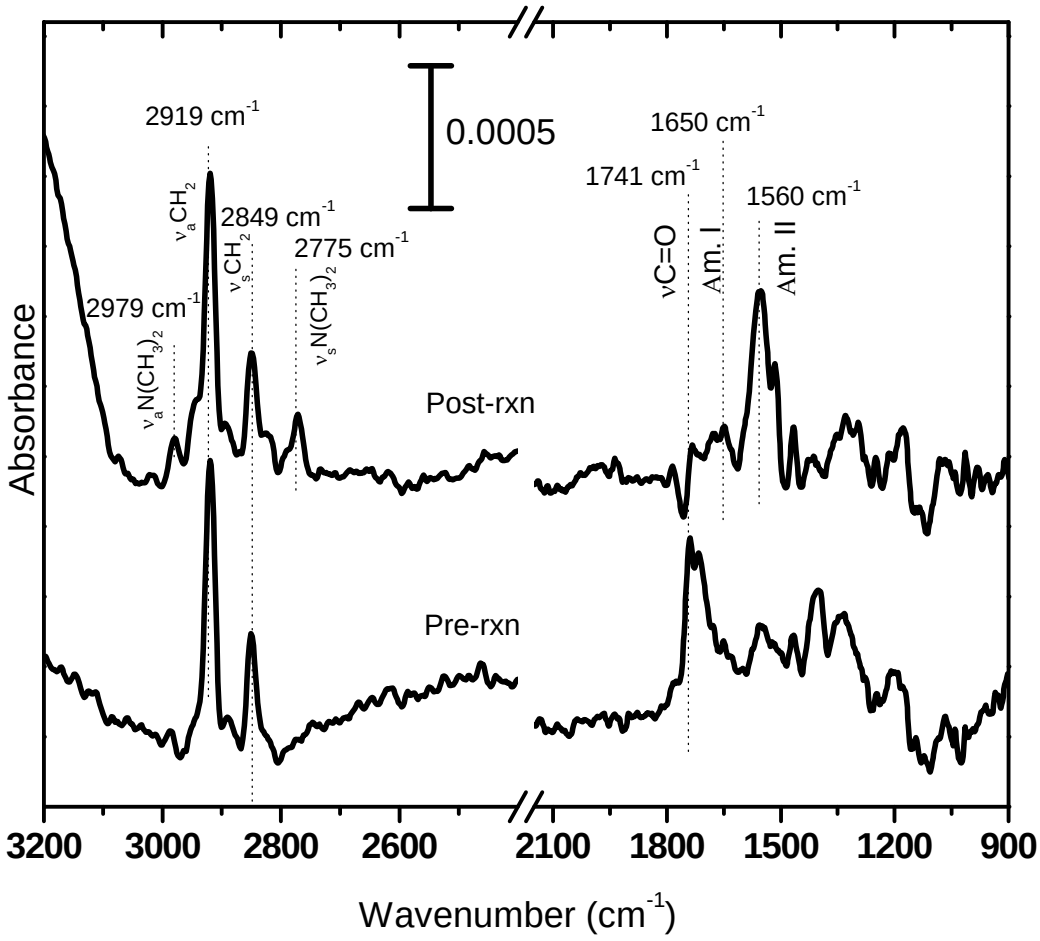

Figure 2-26: RAIR spectra of a 16 COOH SAM before (bottom) and after reaction of PFP intermediate followed by reaction with *N,N*-dimethylethylenediamine (top) in solution.

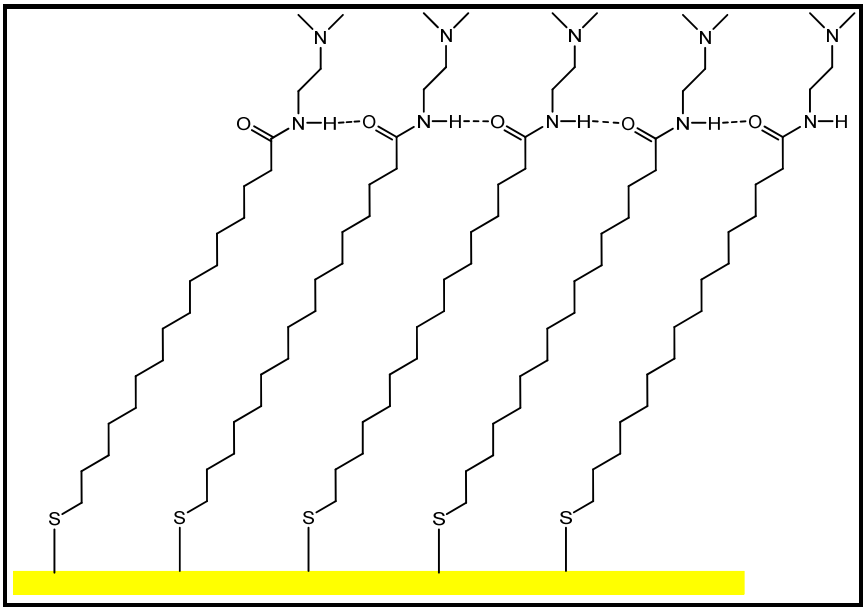

Figure 2-27: Possible surface structure of a well-ordered N-(2-(dimethylamino)ethyl)-11-mercaptoundecanamide SAM demonstrating the nearly parallel orientation of the C=O bonds. The proposed configuration supports the IR spectra which have strong amide II (N-H bend) absorbance modes and weak amide I (C=O stretch) modes.

XPS

The PFP and amide surface reactions were monitored via XPS with particular focus on the C1s region. The spectra of the 11C and 16C carboxylic acid terminated SAMs before and after the surface reactions are shown in Figure 2-28. For both SAMs, the height of the alkyl carbon signal post reaction increases in agreement with the addition of four new carbon atoms to the chain. A new carbon signal, centered at 286.1 eV, can be found and is assigned to the carbon of the newly formed amide moiety.[102] Both the 11 and 16C surfaces show a highly oxidized carbon species at 289.2 eV which is assigned to COO carbon of non-reacted carboxylic acid groups.[78]

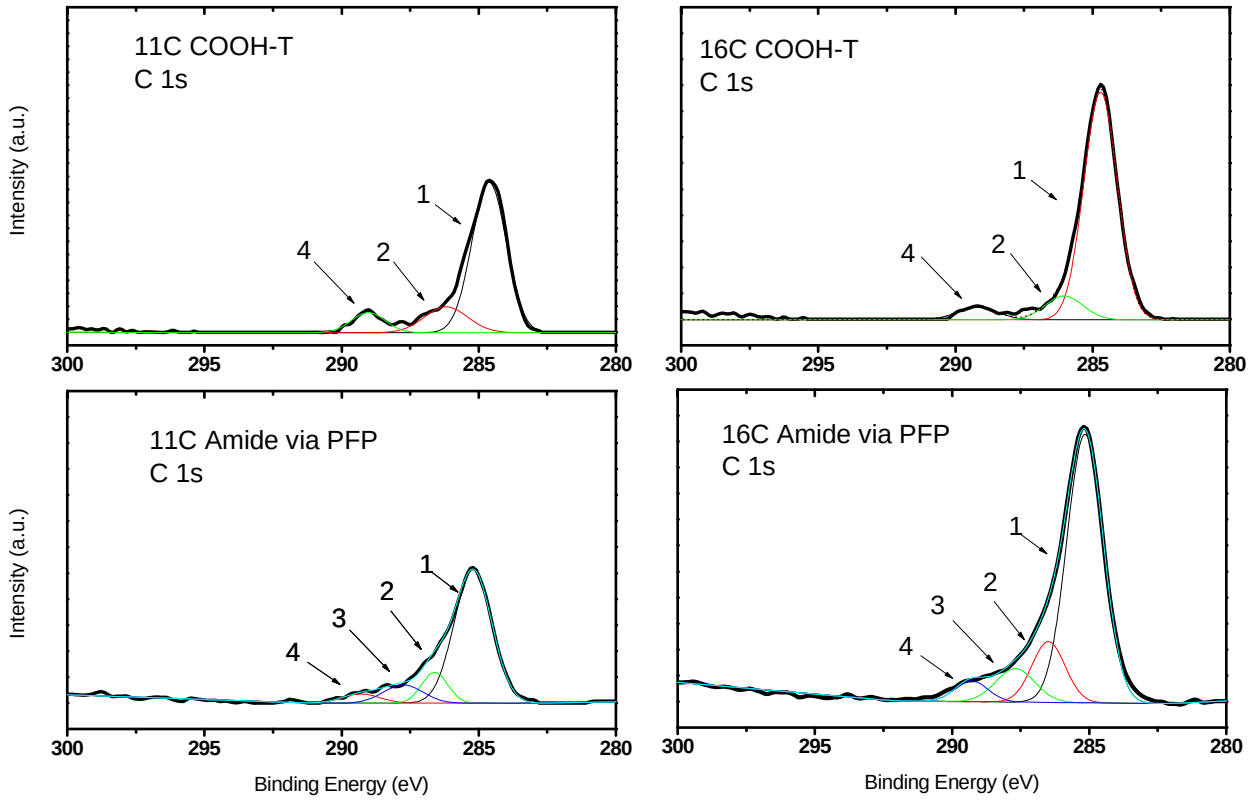

Figure 2-0-28: C1s region of XP spectra for an 11 COOH (left) and 16 COOH (right) SAM before (top) and after (bottom) reaction with PFP intermediate followed by *N,N*-dimethylethylenediamine.

	11C Peak (eV)	Mode	Acid Area %	Amide Area %
1	284.7	C-C	74.1	12.7
2	286.1	C-O	16.1	11.6
3	287.9	C(N)O	--	10.6
4	289.2	C(O)O	9.8	5.1

	16C Peak (eV)	Mode	Acid Area %	Amide Area %
1	284.7	C-C	84.3	71.0
2	286.1	C-O	10.0	14.6
3	287.9	C(N)O	--	9.5
4	289.2	C(O)O	5.7	4.9

Table 2-4: Comparison of the experimental and theoretical atomic percent composition for 11 and 16 COOH SAMs before and after reaction with PFP intermediate followed by *N,N*-dimethylethylenediamine.

Discussion and Conclusions of the Pentafluorophenol Catalyzed Surface Reactions

Both RAIR and XP spectra showed that conversion of carboxylic acid terminated 11C and 16C SAMs was not 100 percent quantitative. The C1s region of the XP spectra for both SAMs showed evidence of a highly oxidized carbon species that mostly comes from a carbonyl carbon of unreacted carboxylic acid groups. The RAIR spectra, based on the persistence of the carboxylic acid carbonyl stretching mode, showed that the reaction was less complete for the 11C SAM than for the 16C SAM. The carbonyl stretching peak, found at 1741 cm^{-1}, is much more intense on the 11C spectrum than it is on the 16C spectrum. If the two SAMs have the same molecular orientation and structure, then their respective RAIR spectra should be nearly identical. The spectra are clearly different which suggests that the two SAMs with different chain lengths have different structures after the formation of the amide bonds.

Mendoza et al. have shown via scanning tunneling microscopy, X-ray photoelectron spectroscopy, and cyclic voltammetry that an 11-mercaptoundecanoic acid SAM forms a less ordered monolayer than a 16-mercaptohexadecanoic acid SAM.[103] The latter SAM is more ordered because of the extra five methylene groups that increase the attractive van der Waal's forces between adjacent alkyl chains. A consequence of the larger disorder found in the 11C SAMs is that the neighboring carboxylic acid groups do not have a consistent intramolecular spacing. The inconsistent spacing may prevent the formation of a strong hydrogen bonding network. A consequence of the formation of a surface hydrogen bonding network is that the hydrogen bonded groups are often found in mostly horizontal orientations, as is seen in hydroxyl terminated monolayers.[104, 105] A parallel dipole moment orientation is "invisible" in reflection IR due to the surface selection rule.[73] If the carbonyl moieties are present in a well-ordered monolayer with a regular hydrogen bonding network, the carbonyl stretching vibration would occur in a parallel orientation.

Figure 2-30 shows the probable surface structure of a well-ordered 16C and a less-ordered 11C after the amide reactions. For the longer chain SAM, the amide and carboxylic acid groups can obtain a more regular intramolecular distance than the corresponding shorter chain SAM. The regular spacing allows for the formation of a hydrogen bonding network which encourages the carbonyl stretching vibration to adopt a mostly parallel orientation. The post-reaction RAIR spectrum of the 16C SAM supports this hypothesis because both the carboxylic

acid (1740 cm^{-1}) and amide I (1650 cm^{-1}) modes are small in intensity. The amide II mode, however, is very intense, which is in agreement with a mostly perpendicular orientation of the amide II N-H bending vibration. The shorter chain carboxylic acid-terminated SAM forms a more disordered surface and a possible post-reaction structure might look like that shown in Figure 2-29. The carbonyl moieties are found in many different orientations, including perpendicular. Such perpendicular orientations would show a strong absorbance in the RAIR spectrum and that is exactly what we observe in Figure 2-25.

.

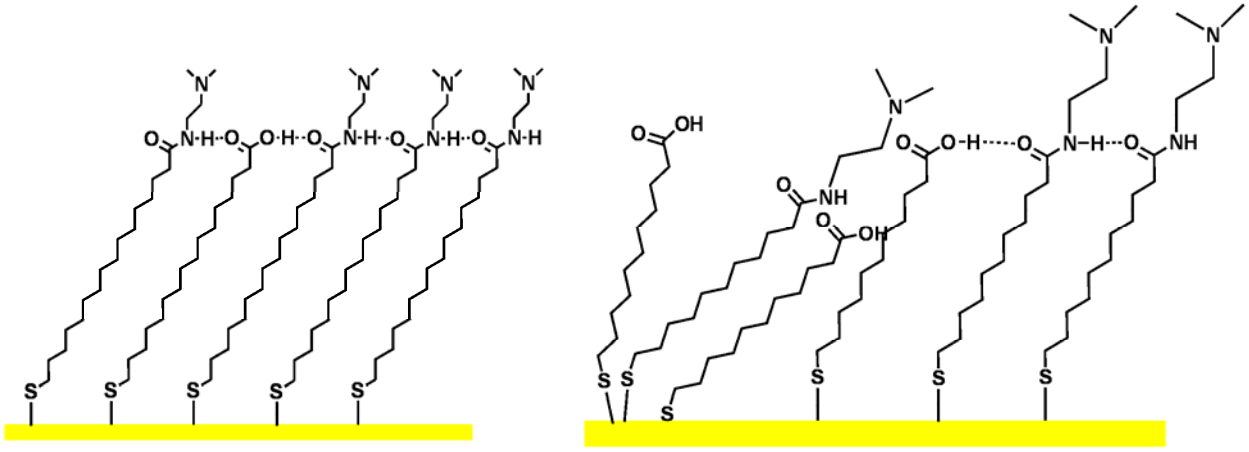

Figure 2-29: Schematic representation of the hypothesized surface structures of a well-ordered 16C (left) and non well-ordered (right) 11C COOH terminated SAM after reaction with PFP and *N,N*-dimethylethylenediamine. The non well-ordered structure has carbonyl moieties in a vertical orientation whereas the well-ordered structure does not.

The most significant difference between the 11 and 16C post-reaction RAIR spectra is the carbonyl stretch of the carboxylic acid groups which is present in the 11C spectrum but not in the 16C spectrum. In contrast to the RAIR spectra, the post-reaction XP spectra show evidence for carbonyl moieties in both the 11 and 16C SAMs. We hypothesize that the seemingly incongruent results can be explained by the difference in surface order between the 11 and 16C monolayers and the subsequent effect on dipole moment orientations. The 16C SAMs form a more well ordered surface than do the 11C SAMs because of the increased van der Waals interaction between the additional five methylene units. The increased surface order is evidenced by the frequency of the asymmetric methylene stretching modes. For the 11C SAM, this mode is found at 2922 cm^{-1} which is characteristic of a somewhat disordered arrangement of the alkyl chains.[59] The 16C SAM asymmetric methylene stretch appears at 2919 cm^{-1} and the

relatively lower energy of the vibration is indicative of a higher degree of crystalline-like packing of the alkyl chains.[59] After the surface reactions, the asymmetric methylene stretching modes of both SAMs appear at the same frequency which means that the degree of surface order was not altered as a result of the surface reactions.

Our goal for using the pentafluorophenol intermediate was to achieve a higher conversion of carboxylic acid into amide groups than the 80 percent conversion obtained using the NHS intermediate. Both the shorter and longer chain SAMs react non-quantitatively to form a mixture of amide and carboxylic acid terminal groups in ratio close to 9:1 which is similar results reported previously in the literature.[95] The pentafluorophenol intermediate reactions did result in a higher surface concentration of terminal tertiary amino groups than did the reactions by using the *N*-hydroxysuccinimide intermediate. For the final step of the quaternary ammonium surface synthesis, all the tertiary amine-terminated surfaces were prepared by using the pentafluorphenol intermediate.

2.3.4 Formation of Quaternary Ammonium Cations

The goal of our study was to develop a simple method of creating SAMs with long-chain quaternary ammonium groups. The new method would allow us to control surface properties, such as alkyl chain length and quaternary ammonium group density, to study the relationship between antimicrobial activity and surface structure. We adopted a step wise surface synthesis approach to build our surface molecule, which involved forming a carboxylic acid terminated SAM followed by attaching terminal tertiary amino groups. The tertiary amino groups were attached by converting the carboxylic acid groups into amide moieties via the use of a pentafluorophenol intermediate species.

The final step our surface synthesis approach is to form the quaternary ammonium groups by reacting the terminal tertiary amino groups with long-chain bromoketone groups. We chose to perform the quaternization using 1-bromooctadecan-2-one rather than 1-bromohexadecane (structures found in Figure 2-30) because previous work of the Gandour group at Virginia Tech found that the quaternary ammonium groups containing the ketone moieties increased the spermicidal and anti-HIV activity relative to the straight alkane chain species.[106] The ketone-functionalized bromoalkane offers another, perhaps, more important advantage over the straight

chain bromoalkanes. The quaternization reaction occurs via an S_N2 replacement reaction when the lone pair of the tertiary nitrogen attacks the carbon atom alpha to terminal bromine. The bromine atom leaves with an extra electron to form a bromide ion and the alpha carbon forms a bond with the tertiary nitrogen to create quaternary ammonium. The rate of S_N2 reactions depends on the stability of the leaving group and a 2-ketone species forms a more stable reaction transition state than does the corresponding straight alkyl chain. We hypothesize that the functionalized bromoalkanes would react with the tertiary amines to a greater extent and under milder conditions than corresponding non-functionalized bromoalkanes.

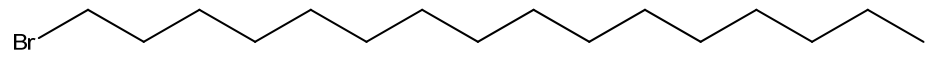

1-bromohexadecane

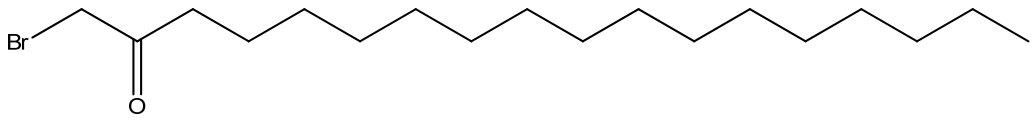

1-bromooctadecan-2-one

Figure 2-30: Structures of long-chain bromine terminated molecules used to quaternize tertiary amine groups.

Experimental

1-Bromooctadecan-2-one (hereto after referred to as the bromoketone) was synthesized and kindly provided by the Gandour group. The fluffy white powder was dissolved in various solvents to form solutions ranging from 0.01 to 0.25M. Tertiary amine terminated SAMs prepared as described earlier were placed into the bromoketone solution and stored in the dark for various intervals. Reaction temperatures were varied via use of a sand bath placed on a hot plate. After differing reaction times, the surfaces were removed from solution, rinsed with toluene, ethanol, and deionized water and dried with ultrahigh purity nitrogen. The surfaces were then immediately used for analysis or antimicrobial assays.

Room Temperature Reaction

Results

As in previous work, the SAMs were characterized via RAIRS and XPS after reaction with the bromoketone molecules. Characterization was performed at different reaction time intervals ranging from one hour to several weeks. The extent of the reaction was monitored with RAIRS by observing both the frequency and intensity of the methylene stretching modes. In addition, the use of the bromoketone molecules as opposed to alkyl bromides provides an additional IR signature as the carbonyl moiety has a strong absorbance due to the stretching mode at 1732 cm^{-1}. Both the C1s and N1s XP spectra were used to monitor the quaternization reaction.

RAIRS

We followed the quaternization reaction as a function of time and the time-dependent RAIR spectra recorded at room temperature are shown in Figure 2-31. After analysis, the surfaces were immediately placed back into the original bromoketone solution.

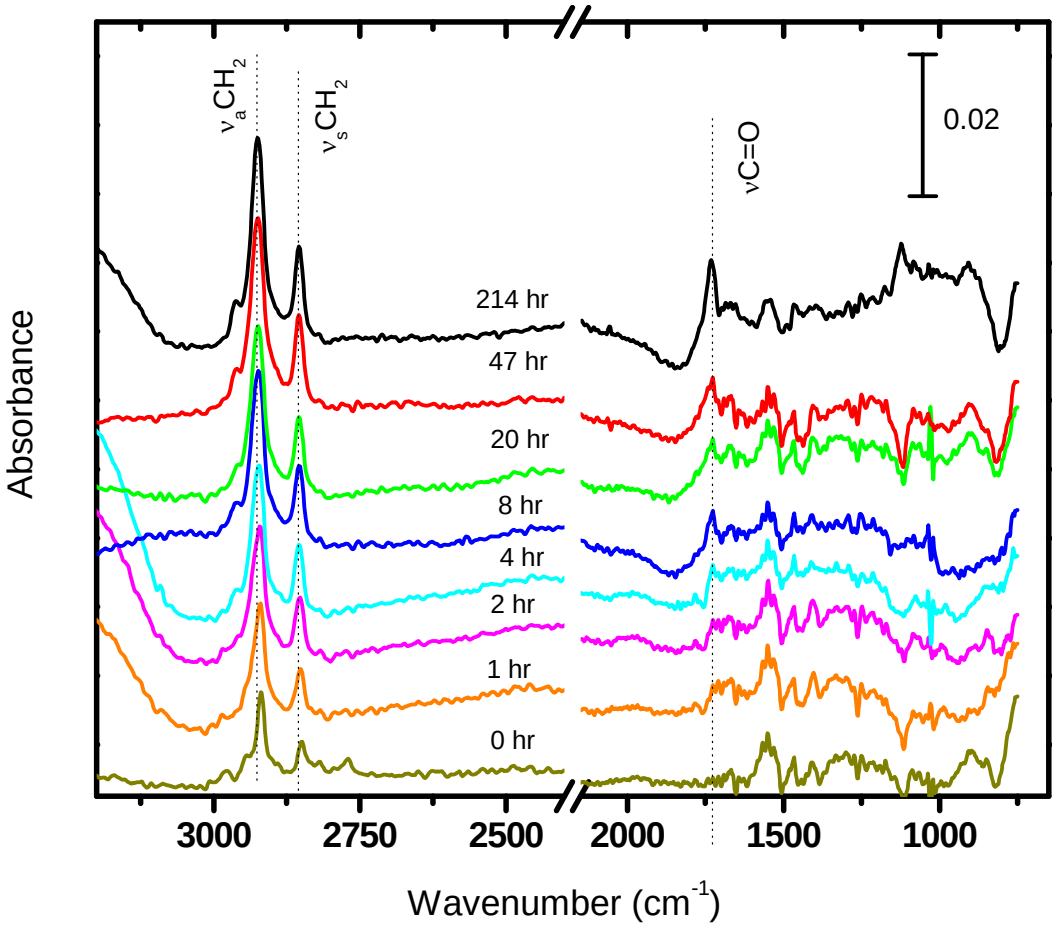

Figure 2-31: RAIR spectra of the room temperature reaction between a tertiary amine SAM prepared via the PFP intermediate and 1-bromooctadeca-2-one recorded at different reaction times

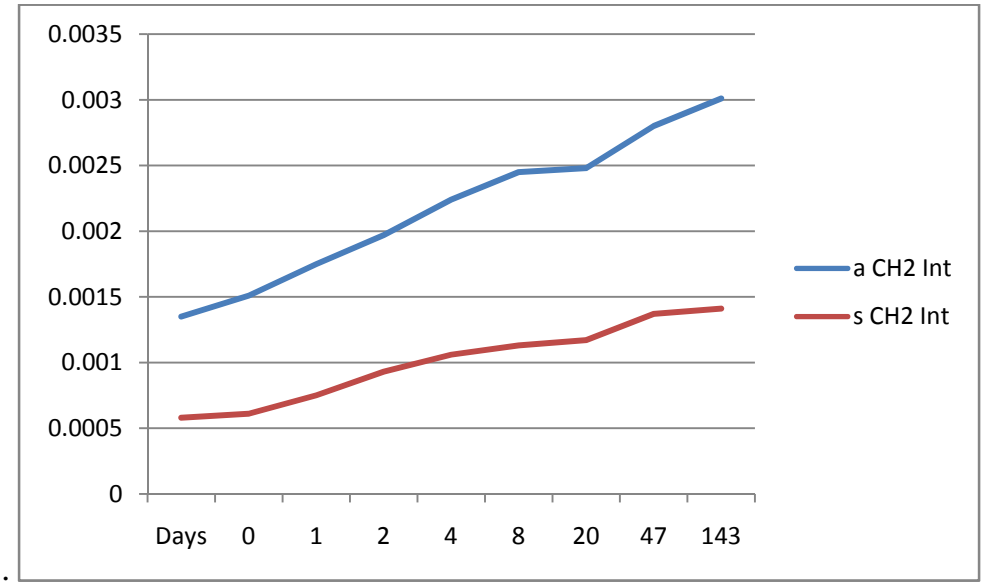

Figure 2-32: Methylene stretching mode intensities as a function of time for the reaction of a teritary amine terminated SAM and 0.025 M 1-bromooctadeca-2-one in toluene at room temperature.

The bottom dark green colored spectrum is the tertiary amine terminated SAM prepared via the PFP intermediate. The next spectrum, recorded at two hours, already shows evidence of reaction as the methylene stretching modes have both increased in size, which is consistent with the attachment of a 15 methylene-containing molecule. In addition, the frequencies of the modes have blue-shifted slightly in accordance with the formation of a more disordered alkyl chain. At the 8 hour mark, a new peak begins to grow in at 1732 cm^{-1} which is assigned to the carbonyl stretching vibration of the newly attached ketone moieties. The intensity of the ketone carbonyl peak increases over time with the largest increase occurring from 143 to 214 hours.

The methylene stretching modes also increase in intensity as function of time as shown in Figure 2-32. Increased absorbance intensity can stem from an increased surface density of the absorbing species or from a change to a more vertical orientation of the transition dipole moment, or a combination of both. A change in orientation is not likely because if this were to occur, the ratio of the asymmetric and symmetric methylene stretching modes would change as well. A change in ratio was not observed which suggests that the increased intensity of the methylene stretching modes is the result of an increased surface density of the long-chain quaternary ammonium groups as a function of time.

The RAIR spectra provide evidence that the surface density of the long-chain quaternary ammonium groups increases over time, however RAIRS cannot help identify the quaternary ammonium nitrogen species, nor can it provide quantitative surface density data. To determine the existence and concentration of quaternary ammonium groups, we used XPS with emphasis on the N1s region.

XPS

As with the time-dependent RAIR spectra, the reaction of the bromoketone molecules was followed using XPS to monitor quaternary ammonium surface density as a function of time. The quaternary ammonium surface density was determined by calculating the ratio of the nitrogen signal from the quaternary ammonium nitrogen atoms and the tertiary nitrogen atoms. To help facilitate the proper assignment of the different nitrogen oxidation states, an XP spectrum of the N1s region of a solution cast film of *N*-(2-dodecanamidoethyl)-*N,N*-dimethyltetradecan-1-aminium bromide was recorded and is shown in Figure 2-33. There are

two distinct peaks present in the N1s region that can be assigned, based on literature precedent, to the amide nitrogen at 399.3 eV and the quaternary nitrogen at 401.8 eV.[107]

The N1s XP spectra after reaction of the tertiary amine-terminated SAMs with bromoketone and recorded at different time intervals is shown in Figure 2-34. As the reaction time increases, the peak at 402.4 eV increases in intensity, which indicates that the quaternary ammonium moieties continue to form. After 23 days, the N1s spectrum was not changed, which suggests that the reaction had reached equilibrium. To determine the extent of the quaternization reaction, the ratios of the quaternary nitrogen peak and the amide nitrogen peak were determined. In this manner, a ratio of 1.00 suggests a quantitative reaction. At 23 days reaction time, the quaternary-to-amide nitrogen intensity ratio was 0.84, which suggests that approximately 84% of the tertiary amines reacted with a bromoketone to form a quaternary ammonium.

Based on the conversion percentage of each synthesis step, we can estimate the surface concentration of quaternary ammonium groups. The first reaction step converted 90 percent of the terminal carboxylic acid groups into tertiary amines and the second reaction step converted 84 percent of the tertiary amine groups into quaternary ammoniums. Based on the conversion percentage of the two synthesis steps, approximately 76 percent of the carboxylic acid groups were converted into quaternary ammoniums. A well-ordered close packed SAM has a typical surface density of around 4.5 x 10^{14} molecules/cm^{2}[57] and based on a 76 percent conversion rate, the quaternary ammonium surface density was 3.4 x 10^{14} molecules/cm^{2}. The final QAC surface concentration is close to that reported for long chain QAC molecules immobilized to glass which were found to be highly antibacterial.[108] The quaternization reaction was, however, very slow taking close to four weeks to reach completion. In an effort to decrease the reaction time and possibly increase the QAC surface concentration, we increased the reaction temperature from room temperature to 50°C.

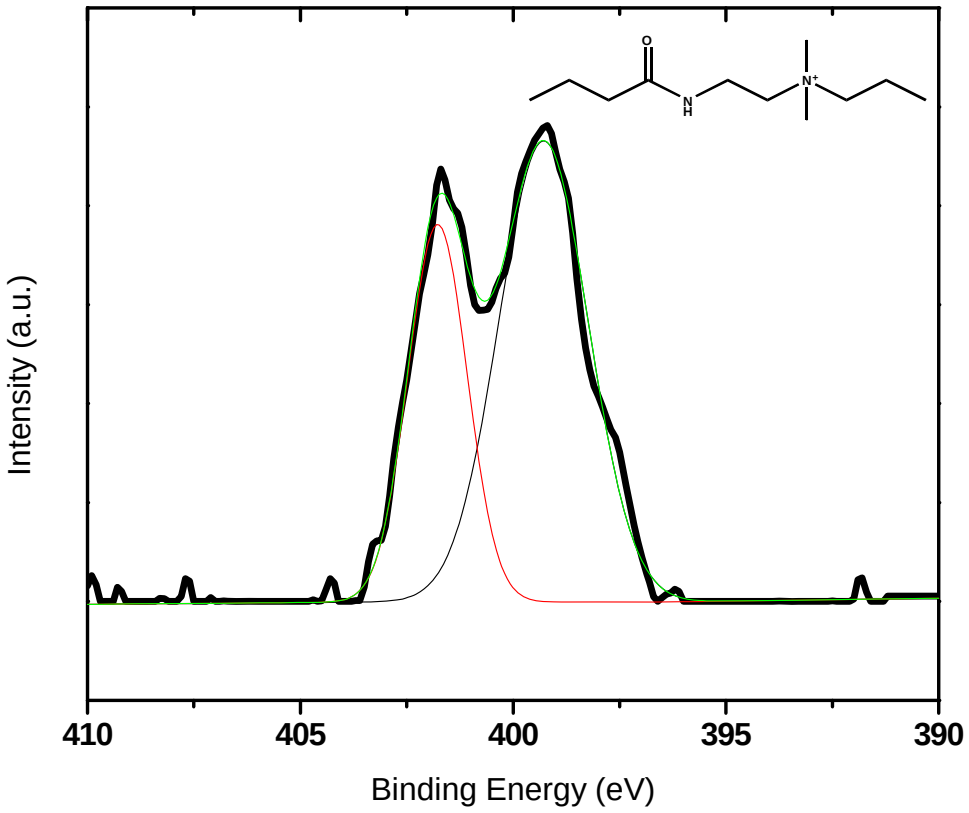

Figure 2-33: N 1s region of the XP spectrum of *N*-(2-dodecanamidoethyl)-*N,N*-dimethyltetradecan-1-aminium bromide prepared as a solution cast film.

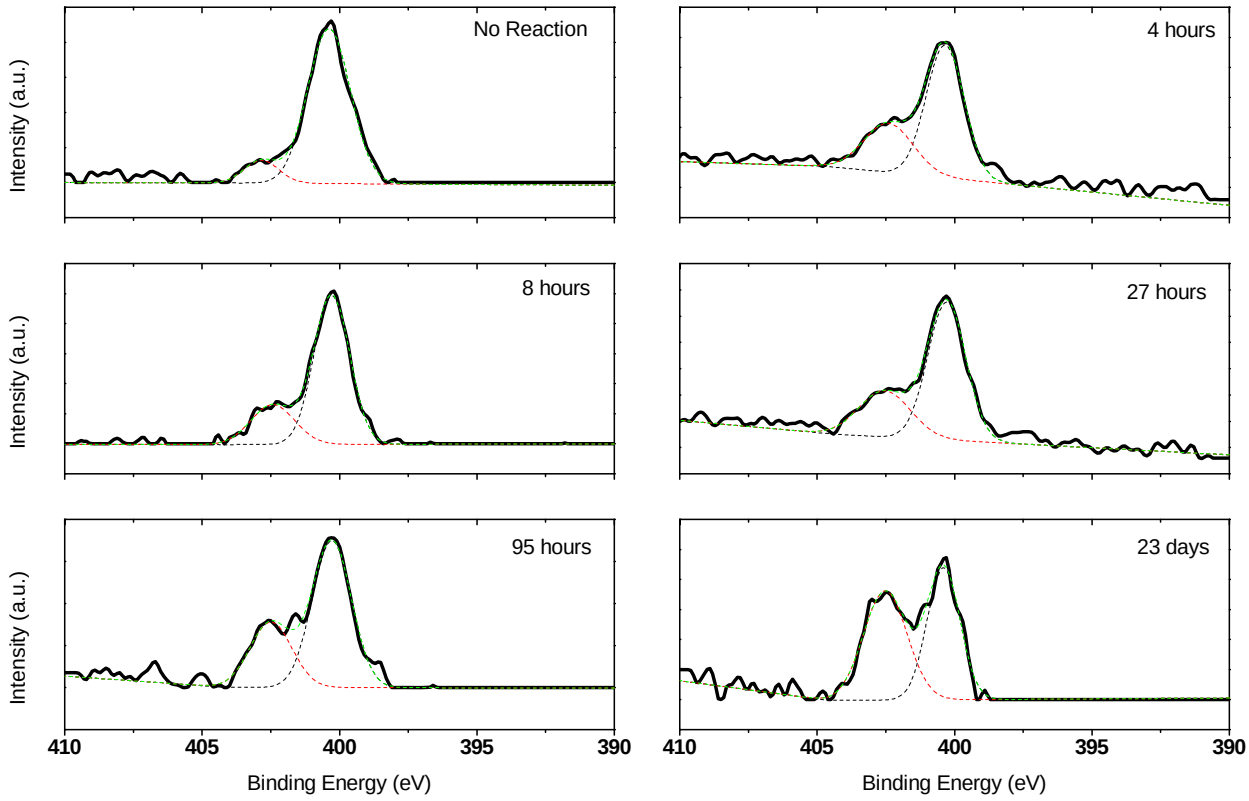

Figure 2-34: N1s region of XP spectra recorded at different time intervals of the room temperature reaction between a tertiary amine SAM prepared via the PFP intermediate method and 1-bromooctadeca-2-one.

The quaternary ammonium forming surface reactions between the terminal tertiary amine groups and the long-chain bromoketones were performed in the same manner as described earlier except at a temperature of 50 °C. The reactions were again monitored at different time intervals with RAIRS and XPS.

The C-H stretching region of RAIR spectra collected as a function of time for the 50 °C reactions are shown in Figure 2-35 and the asymmetric methylene stretching mode intensities for both 50 °C and room temperature reactions are shown in Figure 2-36. The intensity of the asymmetric methylene stretching mode can be used as an indication of surface coverage. During the first two hours, the 50 °C $\nu_a CH_2$ mode increases at a higher rate than the room temperature mode, 5.49 x 10^{-4} abs/hr compared to 2.44 x 10^{-4} abs/hr. Clearly within the first few hours the 50°C reaction occurs at a faster rate than the room temperature reaction, however at 8 hours the $\nu_a CH_2$ mode intensities are nearly the same. After 8 hours, a rather interesting observation can be made. With the room temperature reactions, the methylene peak intensities continued to increase for up to 23 days. Beyond 8 hours the 50°C methylene peak intensities diminish, which suggests

that the surface density is actually decreasing at longer reaction times. We further investigated the 50 °C reactions with XPS.

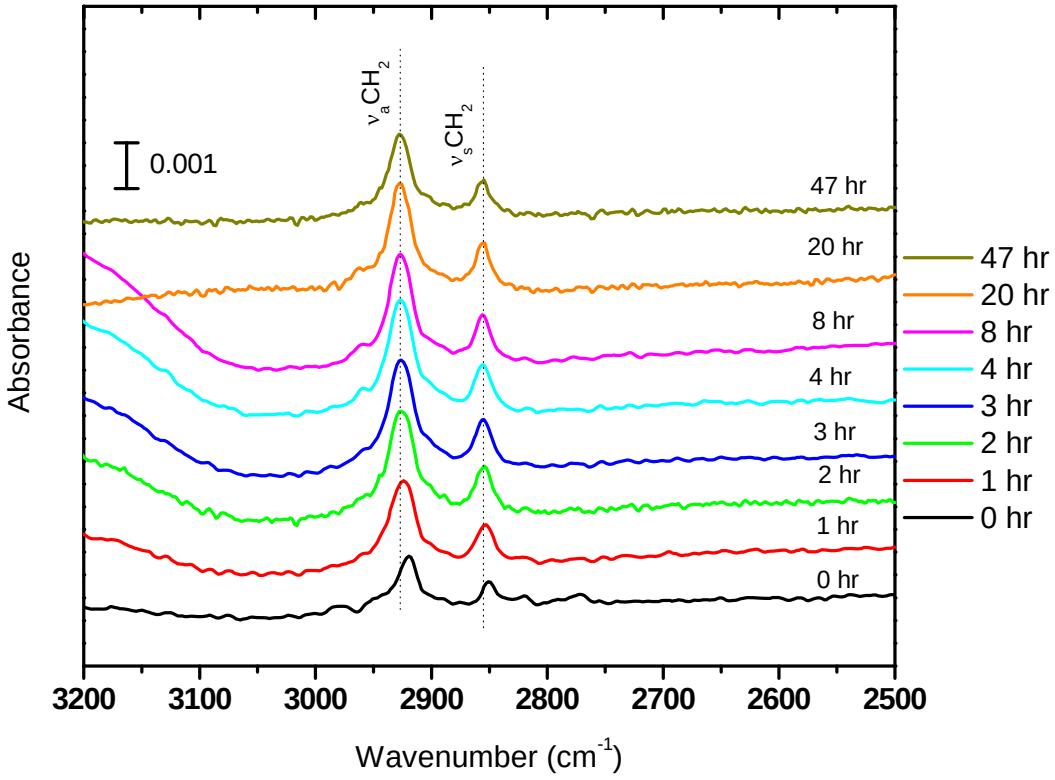

Figure 2-35: C-H stretching region of the RAIR spectra recorded for the 50°C reaction between a tertiary amine SAM prepared via the PFP intermediate and 0.025 M 1-bromooctadeca-2-one in toluene recorded at different reaction times.

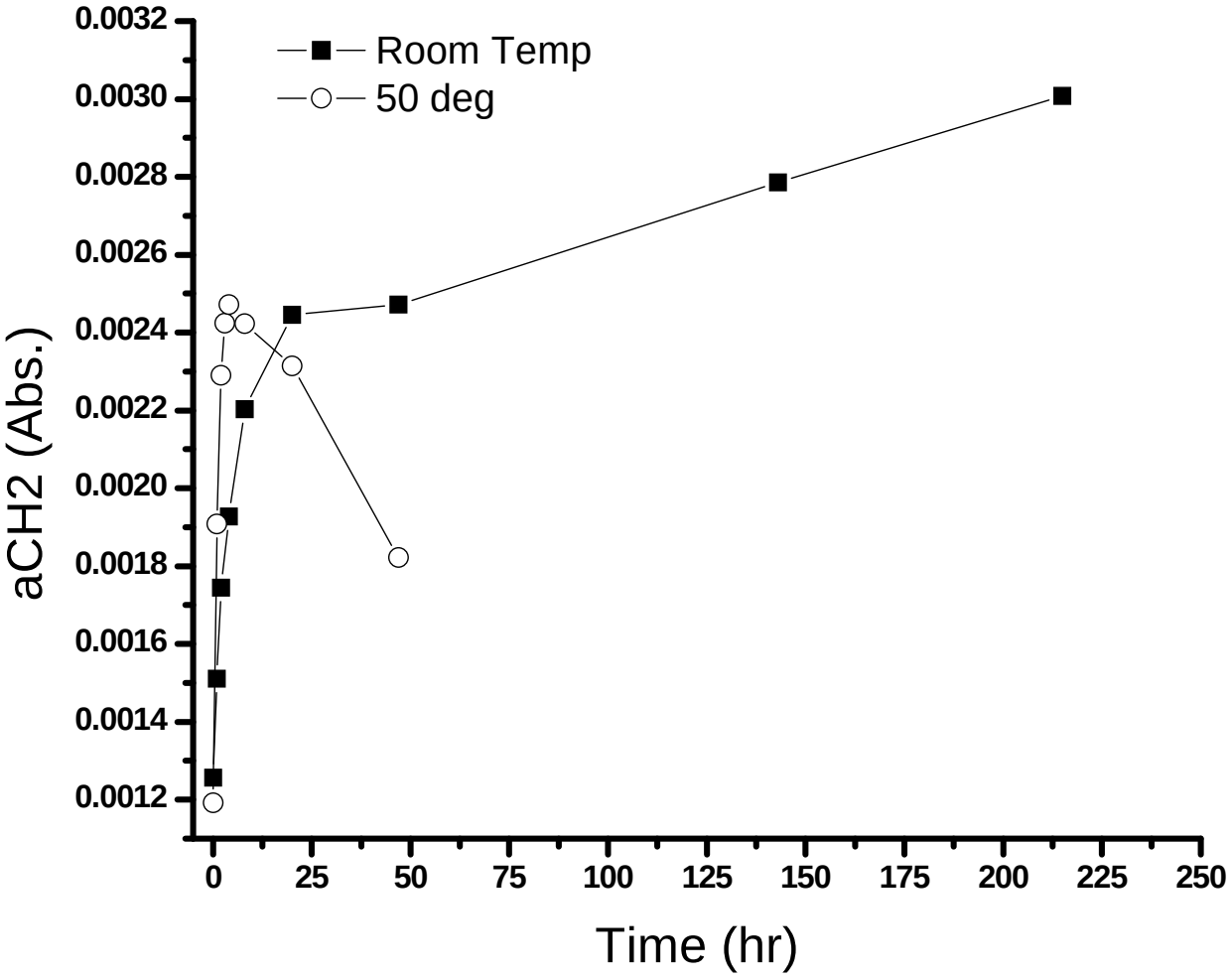

Figure 2-36: Plot of asymmetric methylene stretching mode intensities versus time for the room temperature and 50°C reaction between a tertiary amine terminated SAM prepared via the PFP intermediate and 0.025 M 1-bromooctadecan-2-one in toluene.

We focused the XPS study on the carbon-gold ratio, which is an excellent indicator of changes in surface coverage. For the gold photoelectrons to reach the detector, they must travel through the overlaying monolayer without any collisions. The intensity of the gold signal can become attenuated as a result of collisions between the gold photoelectrons and the overlayer molecules. The extent of the attenuation effect is dependent on the thickness of the overlayer and a measurement of the gold attenuation is a good indicator of relative surface density. We determined the extent of gold signal attenuation by calculating the ratio of the C 1s and Au $4f^{7/2}$ signals. A larger ratio suggests that that gold signal is more attenuated by a thicker overlayer with higher surface density.

The carbon-gold ratios for both the room temperature and 50 °C reactions as a function of time are shown in Table 2-5. At 4 hours, the 50 °C ratio is larger than the room temperature ratio and remains so up to 8 hours. The larger ratio suggests a higher surface density and this observation agrees with the prior RAIR spectra. Beyond 8 hours, the 50 °C ratio decreases significantly, suggesting a decrease in surface density which is again consistent with the RAIRS observations. The room temperature ratio continues to increase beyond 8 hours, which yet again agrees with the RAIRS observations. Both the RAIRS and XPS data support the conclusion that while the increased reaction temperature initially increases the quaternization reaction rate, after a certain time the higher temperature leads to a loss of surface density.

Time (hr)	Room Temp	50 deg
0	20.9	20.9
4	19.7	27.2
8	18.8	27.8
27	21.4	12.0
95	25.3	

Table 2-5: Comparison of the C 1s : Au $4f^{7/2}$ ratios for the room temperature and 50°C reaction between a tertiary amine SAM and 1-bromooctadeca-2-one as determined via XPS peak area integration.

Discussion and Conclusions

In this final step of the surface synthesis of long chain quaternary ammonium self-assembled monolayers, the tertiary amine terminated monolayers, prepared via the pentafluorophenol intermediate, reacted with long-chain 1-bromooctadeca-2-one under different conditions to maximize the surface concentration of quaternary ammonium groups. We found that the highest QAC surface density was achieved using 0.025 M bromoketone in toluene at room temperature for up to three weeks with a maximum QAC surface concentration of near 4 x 10^{-14} mol/cm^2, which corresponds to approximately 75 percent monolayer coverage.

The fact that full monolayer coverage of QAC groups was not achieved was not surprising due to a number of detrimental factors that can hinder the long-chain QAC forming reactions. First is the steric hindrance often found with surface reactions, especially if the reactant molecules are large. The 1-bromooctadeca-2-one molecules are rather large with a fully-extended all-trans length of 23.3 Å. For a full monolayer of QAC groups to form, the 23.3 Å long bromoketone molecules must react with surface-bound molecules that are only 4.97 Å

apart. Not only must the bromoketone molecules diffuse to the surface-bound tertiary amines, they must also adopt an orientation that puts the bromine end of the molecule closest to the surface groups. Both the diffusion and reorientation of the bromoketone molecules must occur in the presence of other long-chain bromoketone molecules in solution. Clearly steric constraints can hinder the reaction between the surface-bound tertiary amine groups and the long-chain bromoketone molecules in solution.

The other detrimental factor that deters the formation of a high density quaternary ammonium SAM is electrostatic repulsion. A full monolayer of quaternary ammonium groups would require the cationic quaternary nitrogen atoms to be only approximately 4.97 Å away from other cationic nitrogens. Electrostatic repulsion would prevent such a close proximity of like charged species, and a similar observation was made by Yokokawa and co-workers who found that cationic disulfide molecules do not form complete monolayers.[109]

A number of variables that can affect a condensed phase surface reaction are dependent on temperature, including solvent mobility, diffusion, and surface residence time. We found that at 50 °C, the reaction between the tertiary amine terminated SAMs and long-chain bromoketones in toluene initially occurred at a faster rate than at room temperature, but beyond eight hours significant loss of surface coverage was observed. The initially faster reaction at the higher temperature agrees with the temperature dependence of an increased solvent mobility and diffusion rate, but desorption of the surface-bound molecules after eight hours does not follow the same trend. The desorption of the covalently bound surface molecules cannot be caused by the increase in temperature alone as increasing the temperature from 20 to 50 °C imparts only an additional 0.25 kJ/mol to the system. The small additional thermal energy alone is not nearly enough to break the 167 kJ/mol energy of the gold-thiolate bond, but it may have a significant effect on diffusion and solvent mobility and both of these factors may affect the solubility of the surface-bound long-chain quaternary ammonium molecules.

The solubility of the surface-bound quaternary ammonium molecules might have a significant impact on the decreased surface coverage observed at the 50 °C reactions. The reactions were performed in toluene, which is a non-polar solvent. The formation of the quaternary ammonium groups on the surface also adds a seventeen methylene unit alkyl chain which increases the hydrophobic character of the surface molecules. The more hydrophobic

surface-bound quaternary ammonium molecules might be more soluble in toluene than the unreacted tertiary amine terminated molecules. A similar observation was made by Kertes et al. who found that the solubility of alkyl amine hydrochlorides in non-polar solvents increased as a function of increasing hydrophobic character of the alkyl group.[110] The total energy of solvation might be large enough to overcome the energy needed to break the gold-thiolate bonds.

Based on the solubility arguments alone, one might expect the room temperature and 50°C reactions to have the same loss of surface coverage. However, not only is solubility larger at higher temperatures, the diffusion and solvent mobility are also increased. At higher temperatures, the long-chain quaternary ammonium thiols become more soluble and the increased diffusion rate and solvent mobility allows the desorbed surface molecules to diffuse away from the interface more easily than at lower temperatures.

To conclude, by using a series of only surface reactions, we were able to create a self-assembled monolayer containing long-chain quaternary ammonium groups. The three step synthesis resulted in an estimated QAC surface density of 3.4×10^{14} molecules/cm^2, which corresponds to an approximately 75 percent monolayer coverage. The primary goal of our study was to develop a synthetic route that would allow us to easily control important surface properties that are known to influence antimicrobial activity such as QAC surface density and chain length. The QAC SAMs prepared here comprise the most likely highest attainable long-chain QAC surface density by using only surface reactions. The next part our study was to determine if the QAC SAMs were antimicrobial towards *E. coli.*

2.3.5 Antibacterial Activity of QAC-containing SAMs: Dynamic Contact Assay

Determination of the antimicrobial activity of surface-bound molecules is inherently more difficult than for solution antimicrobial molecules. In solution, the active molecules are spread throughout the medium and have a high probability of interacting with microbes in solution. With surface-bound antimicrobial molecules, because the active compounds are located only at the surface, interaction with microbes in solution can only occur if the microbes diffuse to the surface. To determine the antimicrobial activity of our surfaces, we used a dynamic assay that to maximized the contact between *E. coli* in solution and the surface of interest. Details of the dynamic assay and the subsequent results are described next.

Experimental

Reagents and Microorgansims

Escherichia coli (strain JM109) was purchased from New England Bio Labs. Tyrptone and yeast extract were purchased from Difco. Sodium chloride, sodium dodecyl sulfate (99%), ammonium sulfate, potassium hydrogen phosphate, potassium dihydrogen phosphate, and sodium citrate dehydrate were purchased form Fisher Scientific and used as received. Growth media used in the preparation of bacteria had the following compositions:

2XYT: 16 g tryptone, 10 g yeast extract, 5 g NaCl in 1L deionized H_2O

LB: 10 g tyrptone, 5 g yeast extract, 10 g NaCl in 1 L of deionized H_2O

Dynamic Contact Assay Procedure

The dynamic antibacterial assay protocol is based on the method, ASTM E2149-01, from ASTM International provided in reference 64. The assay measures the bacteria viability before and after one hour of contact between the surface of interest and an aqueous bacterial suspension. Two control assays, which consist of a surface with no known antimicrobial activity and an assay container with no surface, are run concurrently with the test assay to ensure that any measured antimicrobial activity can be attributed to only the test surface.

The assay is initiated by growing an inoculum of *E. coli* (strain JM109) in 2XYT growth media to a concentration of 1.3-3.0 x 10^5 colony forming units (CFU)/mL as determined via optical density at 600 nm. The inoculum is then diluted 10-fold and 10% sodium dodecyl sulfate is added as a wetting agent to ensure contact between the aqueous bacteria suspension and hydrophobic surfaces. The test containers consist of one inch cubed plastic boxes with sealable lids. The bacterial viability before contact with the surface of interest is determined by adding 3 mL aliquots of the diluted a bacteria suspension to each of the three test containers. The containers are then placed onto a wrist-action rotary shaker and shaken for one minute. 100 µL aliquots are taken from each of the three test containers and diluted 10 fold in 2XYT media. 50 µL aliquots from each 10-fold dilution are taken and plated out in duplicate onto LB agar plates. The plates are then inverted and placed into a 37°C incubator overnight. The surface of interest and the control surface, consisting of a 16C carboxylic acid terminated SAM, are then placed

into the test containers. The third container is used without a surface to serve as an additional control to ensure that any possible antimicrobial activity does not result from contact with the test containers. The three test containers are placed onto the rotary shaker and shaken for one hour. After shaking, 3 mL aliquots are taken from each of the three test containers and diluted 10-fold in 2XYT media. 50 µL aliquots are then plated out in duplicate on to LB agar plates which are subsequently inverted and placed into the 37 °C incubator overnight.

On the following day, the plates are removed from the incubator and the visible colony forming units are counted manually. The counts of the duplicate samples are averaged and the percent difference between the duplicate counts is determined. If the difference is larger than 15 percent, the samples are discarded and the test is repeated. The antimicrobial activity is given as a percent reduction in colony forming units determined by calculating the percent difference between the average colony counts of the initial and post one hour contact times. If the surface of interest has a reduction in viable colonies, one must ensure that it is in fact the surface that is responsible for the antimicrobial activity. The percent reduction of the surface of interest is compared to the percent reduction for both the control surface and the empty test container. If the percent reduction for either the control or empty test container after one hour contact time is greater than 15 percent different than that of the sample of interest, the results are discarded because the reduction observed for the surface of interest cannot be solely attributed to the antimicrobial activity of the surface.

Results and Discussion

The dynamic contact assays were performed with the long-chain QAC containing SAMs prepared using the surface synthesis route described previously. Figure 2-37 shows the images recorded after one of the assays. The left-hand image shows the viable colonies before contact with the surface of interest and the right-hand image shows the viable colonies after one hours contact with the surface. For the dynamic assay shown in images, the number of viable colonies after one hour of contact with the surface was 37 percent lower than before contact and the average reduction of all the successful dynamic assays was 12.3 ± 7.0 percent. The percent reduction is rather low, especially when compared to the antimicrobial assay results of similar monolayers. Previously we showed that a silver carboxylate terminated SAM was totally antibacterial towards both airborne and water-borne *E. coli* where the water-borne antimicrobial

assay was determined using the same dynamic contact procedure described here. A better comparison can be made to the results of Isquith et al. who showed that a monolayer of 3-(trimethoxysilyl)-propyldimethyloctadecyl ammonium chloride bound to silicon substrates was nearly 100 percent antimicrobial.[111] Both the silver carboxylate and organosilicon monolayers had antimicrobial active functional groups with concentrations close to the surface density of the QAC groups of our monolayers. Clearly there is an important factor that is limiting the antimicrobial activity of our SAMs, and to get a better understanding of the low activity, we must consider the requirements for a QAC-containing surface to exhibit antimicrobial activity.

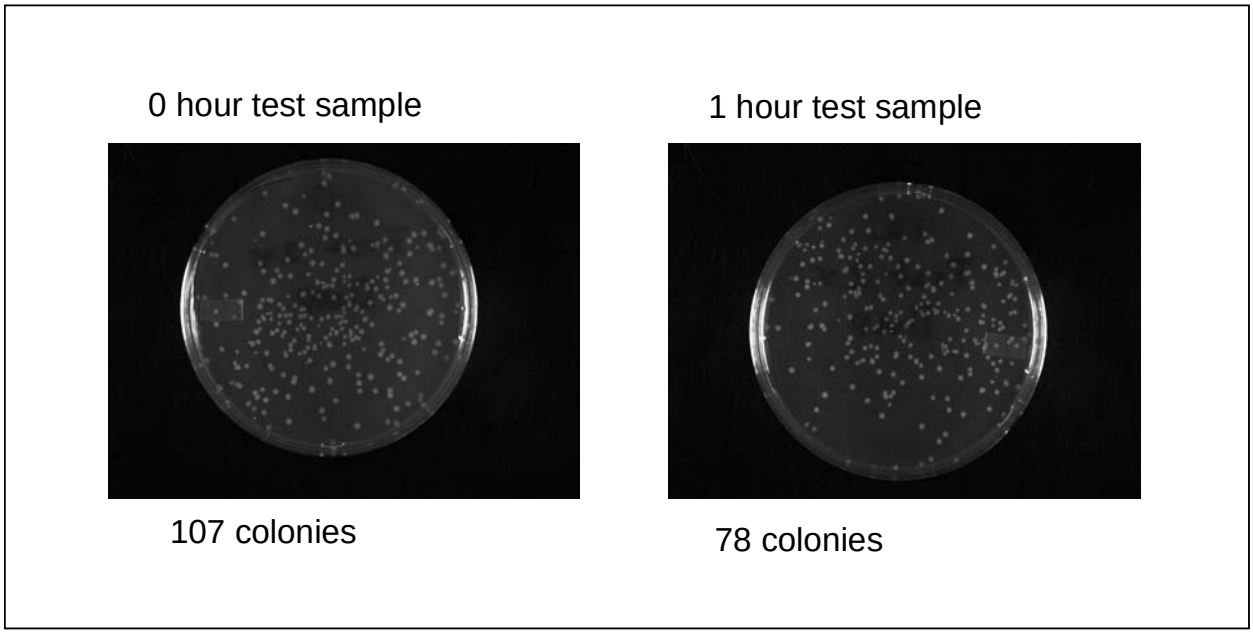

Figure 2-37: Example images from the dynamic contact antibacterial assay of viable colonies taken at 0 and 1 hr contact time. The surface of interests contained an etimated 75 percent coverage of long-chain quaternary ammonium groups.

The currently accepted interaction mechanism between long-chain quaternary ammonium molecules and the outer membrane of a bacterium involves the electrostatic biding of the cationic QAC groups and the anionic moieties found in the outer membranes. The anionic charges of the bacterial membrane are normally stabilized by divalent metal cations such as Mg^{2+} and Ca^{2+}, and the cationic QAC groups are thought to displace the metal cations upon interaction with the membrane. The loss of the stabilizing metal ions causes the membrane to become unstable and can lead to the death of the cell due to an increase in membrane permeability. The entire membrane destabilization process is dependent on the bacteria making contact the surface.

The initial electrostatic interaction between the QAC groups and the cell membrane can only occur if the bacterium is sufficiently close to the surface for electrostatic forces to become

important. This particular distance is described by the Debye-Hückel screening length and is typically in the range of 1 nm depending on the salt concentration of the liquid medium. The first requirement, therefore, that must be satisfied for a long-chain QAC SAM to cause the death of a bacterium is that the cell must be within approximately 1 nm of the surface. Over course of one hour, the Brownian motion of a bacterium in water results in a displacement of only 40 μM, and any bacterium that is initially more than that distance away from the QAC surface has a small chance of naturally diffusing to the interface. The dynamic assay procedure attempts to increase the mobility of the bacteria by agitating the bacterial suspensions with the rotary shaker.

Once the bacterium is close enough to the surface for the electrostatic interactions to occur, the number of surface-bound QAC groups interacting with one bacterium must be high enough to cause the destabilization of the membrane. The number of charges found at the outer membrane of a typical bacterium is on the order of 10^5, which corresponds to a surface density of approximately 10^{15} anionic charges/cm^2.[17] Murata and co-workers found that for antimicrobial surfaces with molecular lengths insufficient to penetrate the entire cell envelope, the surface density of the QAC groups must be on the order of 10^{15} molecules/cm^2.[91] Our long-chain QAC SAMs fall into the category of being insufficiently long to penetrate the cell envelope, which is 46 nm thick,[112-114] which implies that for our SAMs to be highly antimicrobial the need to have a QAC surface density of at least 10^{15} molecules/cm^2. Using XPS, we estimated the surface density of the QAC groups in our SAMs to be 3.4×10^{14} charges/cm^2, which is nearly an order of magnitude less than the suggested necessary surface density needed for activity. In fact, the number of QAC groups accessible to the bacteria may be significantly less than what was estimated from XPS measurements.

The estimated surface density determined via XPS was for all of the QAC groups irrespective of their accessibility to bacteria. Each of the QAC groups has a 16 methylene unit alkyl chain covalently bonded and RAIR spectra showed that the alkyl chains are very disordered. A significant quantity of the surface-bound QAC groups may be buried below a disordered network of alkyl chains that effectively shield them from interacting with the bacteria. We hypothesize that this may be occurring with our surfaces, and that the number of accessible QAC groups is sufficiently less that the amount required for significant antimicrobial activity. If the hypothesis is true, the low effective QAC concentration may be the sole reason for the low antibacterial activity the SAMs.

2.4 Future Work

The goal of our study was to develop a facile method to create long-chain quaternary ammonium SAMs that also allows us to easily control the surface structure to help elucidate the relationship between structure and antibacterial activity. Our synthesis strategy focused on building the QAC SAMs using surface reactions rather than normal organic solution reactions. Using surface reactions provided two advantages over solution reactions: reaction side products could be separated by a simple surface rinse rather than a laborious silica gel column separation, and the reactive thiol groups, when bound to the gold substrates, are naturally protected from unwanted side reactions. Our stepwise surface synthesis strategy was successful as we were able to form SAMs containing long-chain quaternary ammonium groups with surface densities as high as 3.4×10^{14} molecules/cm^2, however none of our surface exhibited significant antibacterial activity. Despite the lack of activity, our study helped reveal new insight into using a surface synthesis approach to build long-chain cationic monolayers and helped focus the direction of future work.

One of the first key factors observed in our surface synthesis study was the importance of the surface bond. We used alkanethiols bound to gold which have bond strengths of 167 kJ/mol.[57] Even though alkanethiols do not thermally desorb at temperatures below 170 °C,[84] we observed significant loss of surface density at temperatures well below the desorption temperature, which suggests that other factors, including thiolate oxidation and solvation, were contributing to the loss of the gold-thiolate bonds. One focus area of future work will be to explore the use different surface bonds that are both stronger and less reactive than the thiolate species.

The surface density of quaternary ammonium groups has been shown in previous studies to be a crucial factor of surface antimicrobial activity, especially for surface with molecular lengths less than the length of the bacterial cell envelope.[91] Our SAMs have a maximum end-to-end molecular length of around 4.5 nm, which is an order of magnitude less than the 46 nm cell envelope thickness, and this means that the QAC surface density is a crucial parameter for any possible antimicrobial activity. The current standing hypothesis explaining the antimicrobial activity of such surfaces is that the surface density of the cationic QAC groups must be very close to the surface density of anionic groups in the cell membrane, which have been found to be

between 5 x 10^{14} and 5 x 10^{15} charges/cm^2 depending on the growth stage of the bacteria.[17] The QAC surface density of our SAMs was estimated to be 3.4 x 10^{14} molecules/cm^2, which in itself is less than the hypothesized lower limit for antibacterial activity. The number of accessible QAC groups may be even lower because the groups are bound to long alkyl chains that most likely form a disordered network which may shield the QAC moieties from the bacterial membranes. The primary focus of future work will be to increase the QAC surface density at least two-fold.

Using our surface synthesis approach, we were unable to achieve a 1:1 ratio of QAC groups to surface molecules. If the 1:1 ratio were achieved, the QAC surface density would be approximately 5 x 10^{14} molecules/cm^2, which is still less than the hypothesized minimum density needed for thin films to exhibit antimicrobial activity. Increasing the QAC surface density using methods described earlier is futile because the electrostatic repulsion of cationic groups in close proximity will limit the maximum attainable QAC density. One possible way to diminish the effects of electrostatic repulsion is to put a covalent linker group between the two quaternary nitrogens. Yokokawa and co-workers compared the surface densities of SAMs formed from gemini surfactants composed of QAC-terminated thiols linked at covalently at the QAC-terminal end of the molecule and at the thiol end to form a disulfide.[109, 115] They found that the SAMs formed with the linker group at the QAC end had a much higher surface density owing to the reduction in electrostatic repulsion of the cationic groups. An example of this type of dithiol molecule is shown in Figure 2-38.

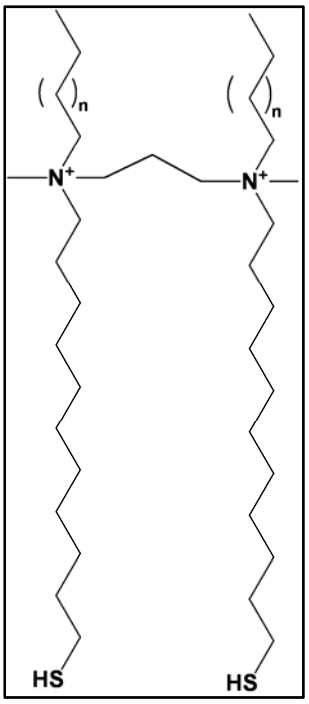

Figure 2-38: Molecular structure of a gemini dithiol that may limit electrostatic repulsion of close-packed QAC groups due to the covalent linker.

While linking adjacent quaternary nitrogen atoms with alkyl spacer groups may reduce electrostatic repulsion, it does not help to increase the surface density of the QAC groups because the QAC-per-thiol ratio is still 1. One way to increase the QAC ratio is to use branched thiol molecules that have two or more functionalized alkane chains per thiol. One example of a branched thiol is shown in Figure 2-39. A SAM composed of branched thiols would increase the QAC-thiol ratio to 2, however careful

consideration must be given to the ability of the branched thiols to form a close-packed structure. Chechik and co-workers studied the SAMs formed from branched thiols containing straight alkane chains and found that they adopted a more closely packed structre than the analgous non-branched thiols.[116] They also found that branched thiols that contain groups capable of favorable intermolecular interactions, such as hydrogen bonding or aromatic groups, are more stable than non-functionalized branched alkanethiols. To our knowledge, no studies have been done on branched thiols containing ionic species, and it is rather safe to assume that our proposed branched thiol molecules which contain two QAC groups will be affected by electrostatic reupulsion. The construction of a close-packed SAM composed of branched thiols containing multiple QAC groups will require careful consideration of the design of the total molecular structure. A careful balance between the repulsive electrostatic force and the attractive intramolecular forces, such as van der Waals, hydrogen bonding, and pi-pi interactions, must be achieved, otherwise the electrostatic repulsion of the close-packed QAC groups will prevent the formation of a close-packed high density SAM.

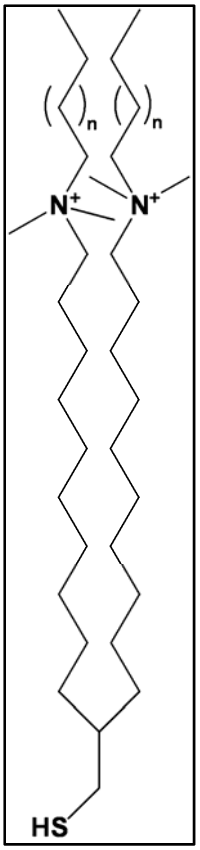

Figure 2-39: Molecular structure of a possible branched thiol containing two long-chain QAC groups.

In conclusion, our work has shown that long-chain quaternary ammonium self-assembled monolayers can be constructed using only surface reactions. The maximum surface density of QAC groups achieved was estimated to be 3.4×10^{14} /cm^2, which is an order of magnitude lower than the density threshold needed for significant antimicrobial activity. Our SAMs showed very little antimicrobial activity, killing, on average, only 12 percent of viable bacteria, and we attributed the lack of activity to a low surface density of accessible QAC groups which may in fact be lower than the estimated total QAC density. Our future work will be focused on creating SAMs with an at least two-fold increase in QAC surface density. Despite the low antimicrobial activity of our SAMs, our work has laid the foundation for future studies using SAMs to investigate the structure/function relationship of antimicrobial activity.

Chapter 3

Surface Structure of Linear Amphipathic Antimicrobial Peptides

3.1 Introduction

In the previous chapter, potentially antimicrobial long-chain quaternary ammonium cations were synthesized via various surface reaction schemes after initial immobilization to gold substrates. The goals of the previously described study were to develop a relatively simple procedure to synthesize the QAC-containing SAMs, which would allow us to systematically change the properties of the surface. By systematically changing the alkyl chain lengths and QAC surface density, we hoped to reveal the relationship between surface structure and antibacterial activity. We discovered, however, that the highest attainable QAC surface density using surface reactions was insufficient to impart antibacterial activity. We next turned our attention to another class of antibacterial molecules; naturally occurring antimicrobial peptides.

The structure of proteins and peptides are described by their primary, secondary, and tertiary structures. The primary structure is simply the sequence of the amino acids that comprise the peptide or protein chain. The secondary structure is the physical shape that the peptide chain adopts, and is commonly defined as α-helix, β-sheet, and random coil. The tertiary structure is important only for the larger protein molecules, and is defined as the three-dimensional space occupied by the multiple secondary structures that can be found in one protein. With the smaller peptide molecules, the secondary structure is most often responsible for the functionality of the peptide.

The number of antimicrobial peptides discovered is in excess of 500, and they are generally classified according to their secondary structure. Common to all the peptides are separate regions of hydrophobic and cationic amino acids that, when folded into helical conformation, instill amphipathic properties. The β-sheet peptides, including the defensins and bactetencin,[117] form a rigid anti-parallel arrangement of hydrophobic and cationic regions constrained by disulfide bonds. The linear antimicrobial peptides, including the cecropins and magainins, assume an amphipathic α-helical conformation upon interaction with a bacterial membrane. The same primary peptide structure is rarely found in different animal species;

however, significant structural conservation of specific amino acid sequences has been found on different peptides.[118]

Antimicrobial peptides, due to their amphipathic nature, are surface active molecules. The mechanism by which they kill microbes is based upon the interaction of the peptides with the microbial cell outer membranes. The peptides exploit a key difference between prokaryotic and eukaryotic cell membranes. The outer membrane of prokaryotic cells, which include bacteria, have many anionic charges at the outer membrane where they often interact with the external environment. Eukaryotic cells, such as animal cells, do not have the anionic moieties located at the outermost portion of the cell membrane, and instead have many more neutral phospholipids. The Shai-Matsuzaki-Huang model explains the mechanism of most antimicrobial peptides.[119-121] The peptides first interact with the membrane, which causes displacement of the lipids followed by alteration of the membrane structure. In certain cases, membrane alteration is followed by peptide entry into the interior of the cell. The actual kill mechanism is still debated, as there are a number of different hypotheses including fatal depolarization of bacterial membrane,[122] creation of membrane holes that cause the leakage of intercellular constituents,[121] the activation of lethal processes such as cell wall degradation,[123] disordering of the distribution of membrane lipids, and damage to intercellular components after the peptide has entered the cell.[124]

Outer membrane binding is the first step in the lethal mechanism of antimicrobial peptides, and the initial binding action of the peptides has been exploited for use in biosensors and biosensor arrays.[125-127] In such devices, the peptides are generally immobilized on a substrate that serves as a transducer to measure binding behavior. Mello and coworkers,[128] Gregory and Mello,[129] Mello and Soares,[130] and Sores et al.[23] showed that the α-helical peptide cecropin P1 exhibits discriminatory binding behavior towards pathogenic versus non-pathogenic *Escherichia coli.* The studies found that the discriminatory binding behavior is influenced by ionic strength and pH, which suggests that electrostatic interactions play a large role in binding to the non-pathogenic *E. coli* strain.

While much effort has been undertaken to investigate the binding behavior immobilized antimicrobial peptides and the effects of solution parameters, such as pH, concentration, and solvent polarity, surprisingly little work to determine the surface structure of the immobilized

peptides exists. Important variables such as secondary structure, orientation, and density of the surface-bound peptides are largely unknown, as well as any effects these parameters may have on the efficacy of the peptides towards binding. Previous studies of *de novo* designed peptides have demonstrated the effects of ionic strength,[131] solution concentration,[132, 133] and solvent composition[134-136] on the surface structure of immobilized peptides. Substrate properties such as hydrophobicity[137] and surface conjugation scheme[138] have also been shown to influence the peptide surface structure.

The majority of investigations into peptide surface structure have focused on relatively short, rationally designed helix forming peptides. There are very few studies investigating the surface structure of naturally occurring helix forming peptides. The interfacial structure of immobilized peptides may have a significant influence on binding capacity and may ultimately determine their utility as pathogen sensor transducers. The goal of the investigations presented here focused on determining the surface structure of three helix forming peptides, along with the effects of solution properties such as pH, concentration, and solvent polarity. Our studies will help lead to a better understanding of how antimicrobial peptides assemble at a solid interface and may lead to improvements in pathogenic bacteria biosensors.

Our work described here is one part of a collaboration lead by Dr. Charlene Mello of the US Army Natick Soldier Center. The goal of the overall collaborative project is to develop a biosensor comprised of peptide arrays that can detect specific pathogenic bacterial strains. Such a device will serve as an early warning system of a possible biological weapon attack. Dr. Mello's group has focused on the biochemical and microbiological aspects of the study, including characterizing the peptides in solution and performing the bacteria binding assays. Our focus has been on the characterization of the peptides after immobilization to a surface. Another collaborator at the University of Michigan has focused on characterizing the immobilized peptides when the surfaces are in solution. The combined collaborative effort, we, and the Army, hope will lead to an efficient and reliable pathogen sensor.

3.1.1 Antimicrobial Peptides: PGQ, Pleurocidin, and Cecropin P1

To date, over 500 antimicrobial peptides have been discovered, and choosing appropriate molecules to study requires a detailed selection criteria. The Mello Group chose a group of peptides for the initial binding studies based on the following properties:[23] 1) the lack of post-translational modification, 2) the absence of any cysteine residues, and 3) activity for *E. coli*. The selection criteria were motivated by the desire for rapid synthesis and the need to control the peptide orientation during immobilization for the cell binding assays. The peptides selected for the binding study were cecropin P1, cecropin A, pleurocidin, PGQ, ceratoxin A, and SMAP-29, and the assay results revealed that cecropin P1 and PGQ showed a strong binding preference for pathogenic *E. coli* O157:H7 relative to *E. coli* ML35. Three of the peptides, cecropin P1, PGQ, and pleurocidin, were used in a surface plasmon resonance (SPR) study to further investigate binding selectivity. The binding selectivity of cecropin P1 was further investigated under non-physiological conditions including acidic and basic pH and low and high ionic strengths. In the SPR experiments, the three peptides were covalently linked to a gold coated sensor surface, however the information acquired from an SPR sensorgram reveals nothing about the molecular structure of the immobilized peptides. In our work, we investigated the same peptides used in the SPR study to reveal their surface structure, including the secondary conformation, as well as average orientation relative to surface normal.

The antimicrobial peptides PGQ, pleurocidin, and cecropin P1 investigated here are all of the linear α-helix forming variety. As in the quaternary ammonium alkanethiol surface synthesis studies described in chapter 2, we employed the covalent Au-S interaction to immobilize the peptides. The naturally occurring peptides do not contain any thiol moieties, therefore in order to facilitate binding to the gold substrates, a cysteine residue, which contains a thiol moiety, was added to the C-terminus of each peptide. While all three peptides share the α-helical structure upon interaction with a bacterial membrane, they differ in their net charge and hydrophobic content. PGQ, found in the stomach of the African clawed frog, is a 45 percent hydrophobic, 24 residue peptide with a net charge of +3.[139] Pleurocidin, found in the skin secretions of the winter flounder, is a 44 percent hydrophobic, 25 residue peptide with a net charge of +7.[140] Cecropin P1, found in the parasitic worms of the small intestines of pigs, is a 35 percent hydrophobic, 31 residue peptide with a net charge of +5.[141] All three peptides adopt a random coil structure in

polar solution and fold into helical conformation upon interaction with a non-polar medium, such as a bacterial membrane. The ability of the peptides to fold into an active conformation only under appropriate conditions imparts structural stability not often observed for proteins and peptides, as many can be denatured in solution under mild conditions.

The helical conformations of the three peptides are shown in helical wheel diagrams found in Figures 3:1-3. A helical wheel diagram shows the arrangement of amino acid residues as viewed in a top down perspective. Beginning with residue #1, residue #2 is found 100° clockwise, followed by each successive residue 100° clockwise to the previous. The wheel diagram reveals the arrangement of hydrophobic and hydrophilic residues in the helix. Table 3-1 provides the single letter abbreviations and structures of the twenty natural amino acids that comprise all peptides and proteins.

The helical wheel diagram for each of the three peptides reveals the amphipathic nature of the α-helices as there are distinct polar and hydrophobic faces. As will be shown, the amphiphilicity has as large influence on the resulting surface structure.

Alanine	Arginine	Asparagine	Aspartic Acid	Cysteine
A	R	N	D	C
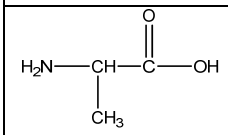	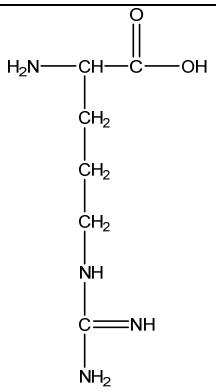	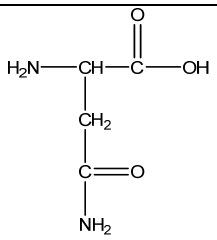	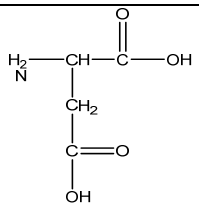	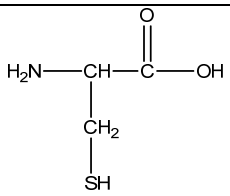
Glutamic Acid	Glutamine	Glycine	Histidine	Isoleucine
E	Q	G	H	I
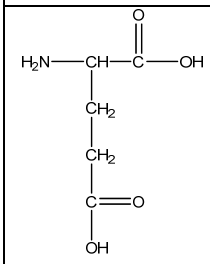	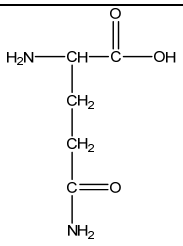	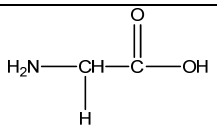	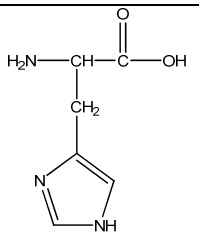	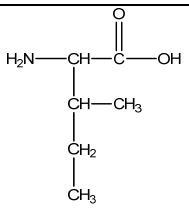
Leucine	Lysine	Methionine	Phenylalanine	Proline
L	K	M	F	P
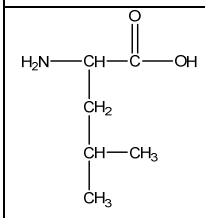	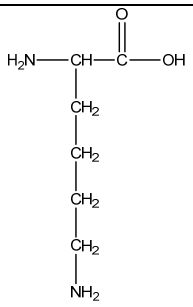	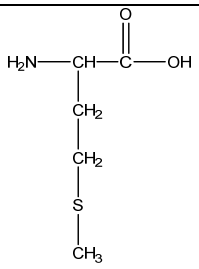	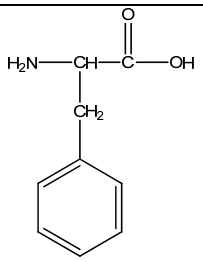	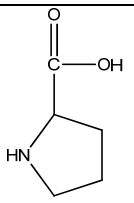
Serine	Thronine	Tryptophan	Tyrosine	Valine
S	T	W	Y	V
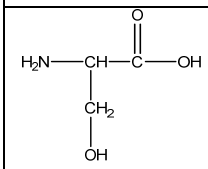	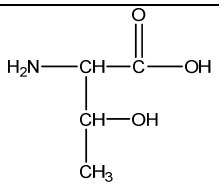	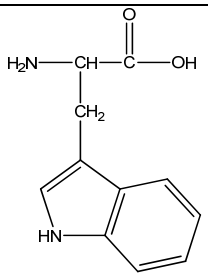	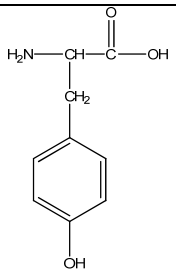	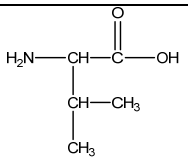

Table 3-1: The molecular structures and one-letter abbreviations of the twenty naturally occurring amino acids.

Anionic	Cationic	Aromatic	Non-polar, aliphatic	Polar (OH), aliphatic
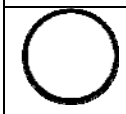				

Table 3-2: Symbols representing the types of amino acids in the helical wheel diagrams.

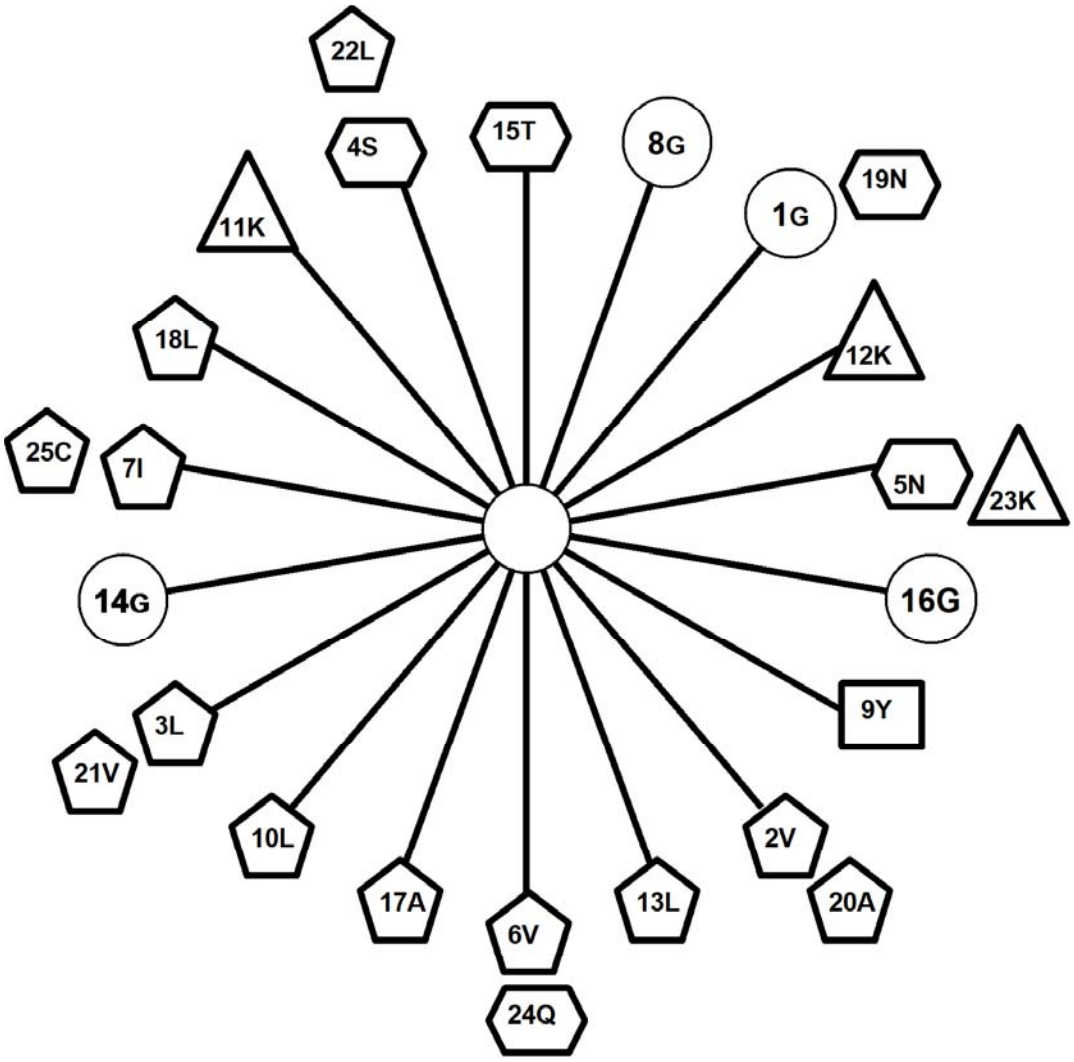

Figure 3-1: PGQ helical wheel diagram.

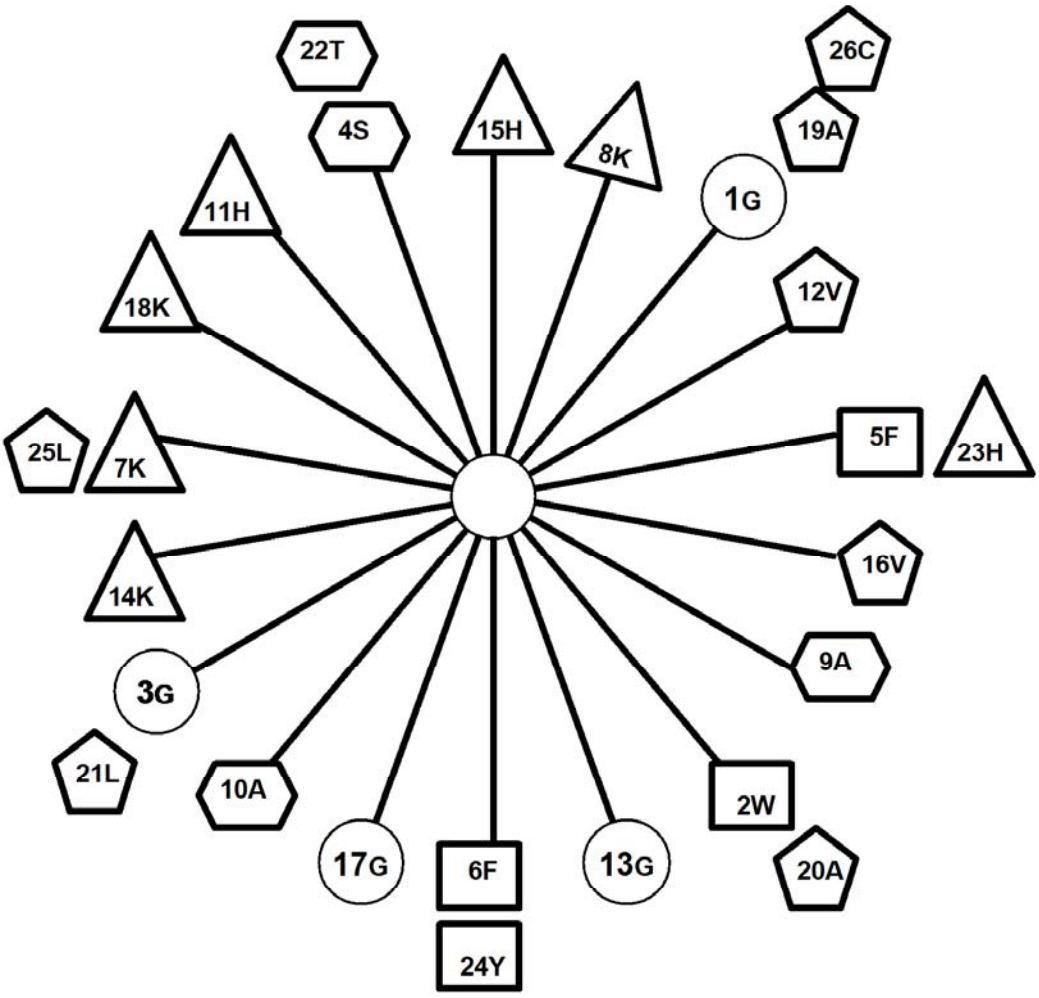

Figure 3-2: Pleurocidin helical wheel diagram.

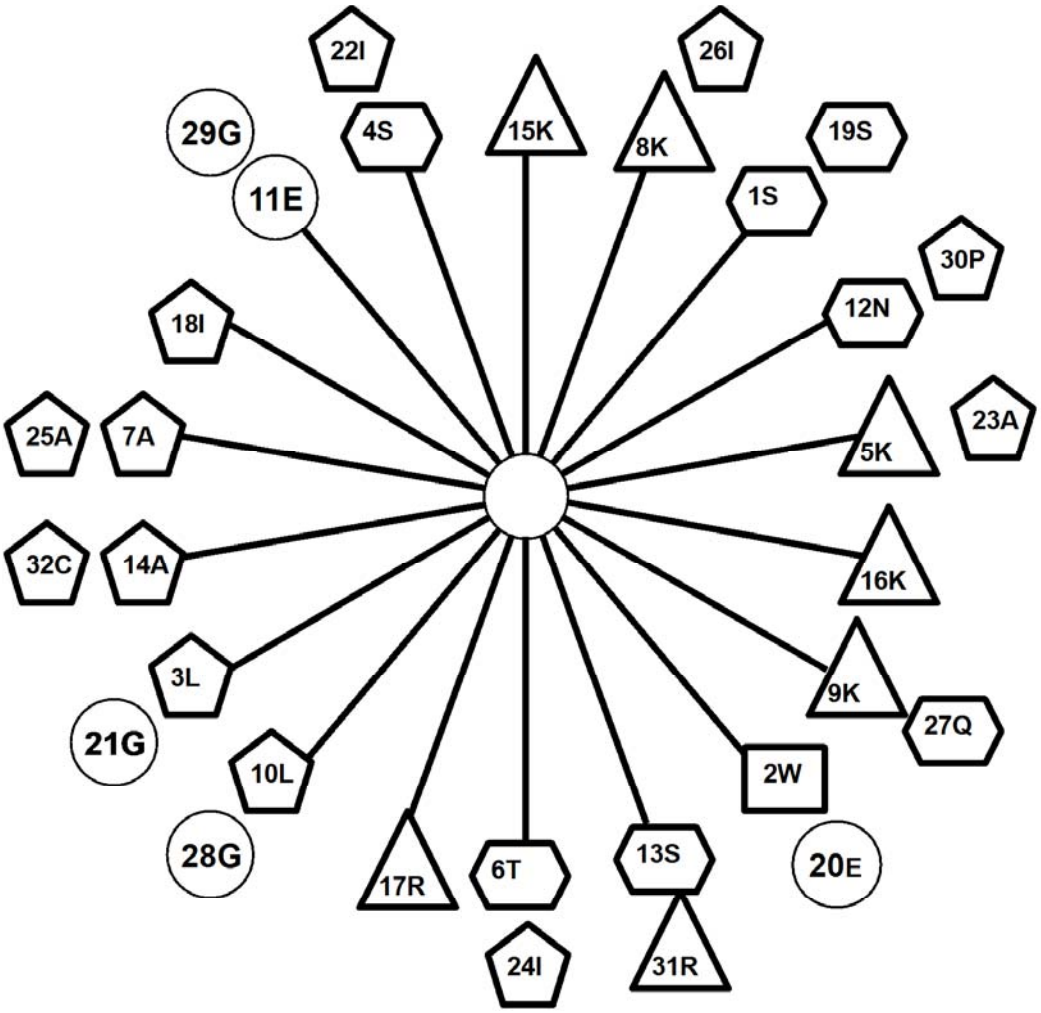

Figure 3-3: Cecropin P1 helical wheel diagram.

3.2 Experimental

3.2.1 Chemicals and Reagents

Cysteine-terminated antimicrobial peptides PGQ (PGQ_c sequence NH_2-GVLSNVIGYLKKLGTGALNAVLKQC-OH, M_W = 2578), Pleurocidin (PL_c sequence NH2-GWGSFFKKAAHVGKHVGKAALTHYLC-OH, M_W = 2855), and cecropin P1 (CP1_c sequence NH2-SWLSKTAKKLENSAKKRISEGIAIAIQGGPRC-OH, M_W = 3442) were synthesized using standard FMOC-solid phase methods by Synprep (Dublin, CA) and purified to 85%+ by RP-HPLC. The lyophilized powders were reconstituted in pH 7.4 phosphate buffer and diluted to the desired concentrations. 2,2,2-Trifluoroethanol (TFE), sodium phosphate dibasic heptahydrate (98%+), sodium phosphate monobasic monohydrate (98%+), and N-

cyclohexyl-3-aminopropanesulfonic acid (CAPS, 98%+) were purchased from Sigma-Aldrich. Tris(2-carboxyethyl) phosphine hydrochloride (TCEP) was purchased from Pierce Biotechnology Inc. (Rockford, IL). Gold substrates were purchased from EMF Corp. (Ithaca, NY) and contain glass substrates with 10 nm Ti adhesion layer followed by 100 nm Au evaporated on top. Ti was used as the adhesion rather than the more common Cr layer because chromium is toxic to many bacteria species,[142] which may affect the results of any future binding assays.

3.2.2 Surface Preparation

Gold slides (1 cm x 1 cm x 0.1 cm) were cleaned by immersion in fresh piranha solution for at least 15 minutes. The substrates were removed, rinsed with copious deionized water, dried with ultrahigh purity nitrogen, and placed into the desired peptide solution, which were prepared in glass vials with plastic tops. 600 μL of solution was found to be sufficient to cover the entire gold surface upon immersion. After immersion in peptide solution for at least 18 hours, the gold substrates were removed, rinsed with buffer and deionized water, dried with ultrahigh purity nitrogen, and immediately used for analysis.

3.2.3 Peptide Solutions

The lyophilized peptide powders were reconstituted in 0.1 M phosphate buffer at pH 7.4 and the stock peptide solutions were stored at 4 °C prior to use. Working solutions of the desired peptide concentrations were prepared from the stock solutions and diluted with buffer. Trifluoroethanol (TFE), which is a non-polar solvent used to induced peptide conformation change in solution, and tris 2-(carboxyethyl) phosphine (TCEP), which is a disulfide specific reducing agent, were added to the buffer immediately before sample preparation. Both the TFE and TCEP were added to change the peptide structure in solution prior to immobilization, and more details regarding their usage will be provided shortly. All of the peptide sample volumes were 600 μL.

3.2.4 Surface Analysis Methods

Reflection Absorption Infrared Spectroscopy (RAIRS)

In Chapter 2, RAIRS was shown to be a very powerful analytical technique for the study of surface chemical reactions. From the infrared spectra, the appearance of new functional groups, the average surface order, and relative surface concentration could be ascertained. RAIRS is also a very powerful analytical technique that can be used to study the surface structure of immobilized biological molecules, such as peptides. In our study of immobilized antimicrobial peptides, RAIRS was used to determine the secondary conformation and average orientation of surface bound peptides. All peptides contain amide bonds that are formed when the carboxyl end of one amino acid condenses with the primary amine end of another amino acid along with the loss of a water molecule. The amide bond gives rise to two important vibrational modes labeled amide I and amide II. The amide I mode is comprised primarily of the stretching motion of the C=O bond and the amide II mode is comprised of the bending motion of the N-H bond.[143]

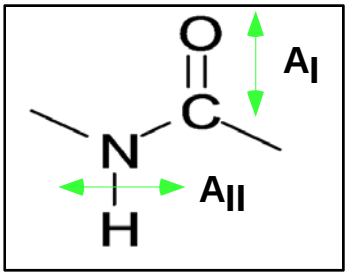

Figure 3-4: Schematic showing the amide I and amide II vibrational mode orientations.

The secondary structure of peptides and proteins is the physical three dimensional shape the molecules adopt in a particular environment, and is dependent on inter and intramolecular hydrogen bonding. The carbonyl oxygen and amine hydrogen can participate in hydrogen bonding with both solvent molecules and adjacent groups found along the peptide, and these bonds can have a large impact on the amide I vibration frequency. The hydrogen bonding present in peptides can range from significant intermolecular hydrogen bonding, as observed with β-sheets and α-helices, to hydrogen bonding with solvent molecules, as seen in random coil structures, and the extent of H-bonding has a significant effect on the absorption energy of the C=O stretching vibration. The absorption energy is directly proportional to the frequency (and wavenumber) of the absorbed photon, and the frequency is related to the bond strength in the following equation:

$$\nu = \frac{1}{2\pi}\sqrt{\frac{k}{\mu}}$$

Equation 3-1

where k is the "spring constant" of the chemical bond and can be considered analogous to bond strength, and μ is the reduced mass of the atoms that comprise the bond. When hydrogen bonding occurs, the electron density of the covalent bond that participates in the additional hydrogen bond is decreased, which results in a decrease in the "spring constant" of the bond. As shown in Equation 3-1, the frequency of the absorbed photon is directly proportional to the bond strength, therefore the extent of hydrogen bonding by the carbonyl moieties of the peptide significantly impacts the frequency of the amide I vibrational mode.

The frequency of the amide I mode is proportional to the extent of hydrogen bonding within the peptide molecules on the surface. Table 3-3 shows the different frequency ranges of the amide I vibration for a variety of peptide secondary structures, recorded by using transmission FTIR.

Secondary Structure	Amide I Frequency (cm^{-1})
Antiparallel β-sheet	1675-1670
3_{10}-helix	1660-1670
α-helix	1648-1660
Unordered, random coil	1640-1648
β-sheet	1625-1640
Aggregate strands	1610-1628

Table 3-3: Table showing the most common protein secondary structures and their respective amide I absorption frequencies.

In addition to the solution environment, RAIRS can be used to determine the secondary structure of surface-bound peptides. The gold substrate, however, can influence the frequency of the IR absorption and affect the assignment of secondary structures. The interaction of the infrared photons with the gold surface atoms causes a blue shift of the absorption frequency, generally between 15 and 40 cm^{-1}, that is independent of secondary structure.[144] The magnitude of the blue shift depends on the absorbance intensity and the orientation of the amide I vibrational mode relative to the surface.[145-147] Significant work is reported on the RAIR spectra of immobilized synthetic peptides on gold, and the literature precedents are used to make secondary structure assignments in this study.[143, 148-153]

In Chapter 2, the RAIRS surface selection rule was presented, which states that only the component of the transition dipole moments that is oriented perpendicular to the surface plane absorbs the p-polarized incident IR radiation. Absorption modes that have a more perpendicular orientation (or normal to the surface plane) are more intense than those that are parallel. The amide I and amide II modes found in peptides are nearly orthogonal to each other, and because of the surface selection rule, can be used to determine the average orientation of a thin peptide film immobilized on gold. Figure 3-5 shows the coordinate system that is used to calculate the average peptide orientation based on the intensities of the amide I and II absorption modes. **Z** is defined as the surface normal, **H** is the axis along the helix backbone, $\mathbf{A_I}$ is he amide I mode, $\mathbf{A_{II}}$ is the amide II mode, $\boldsymbol{\theta_I}$ is the angle between the helix backbone and the amide I mode (79°), $\boldsymbol{\theta_{II}}$ is the angle between the helix backbone and the amide II mode, and $\boldsymbol{\theta}$ is the angle between the helix backbone and the surface normal.

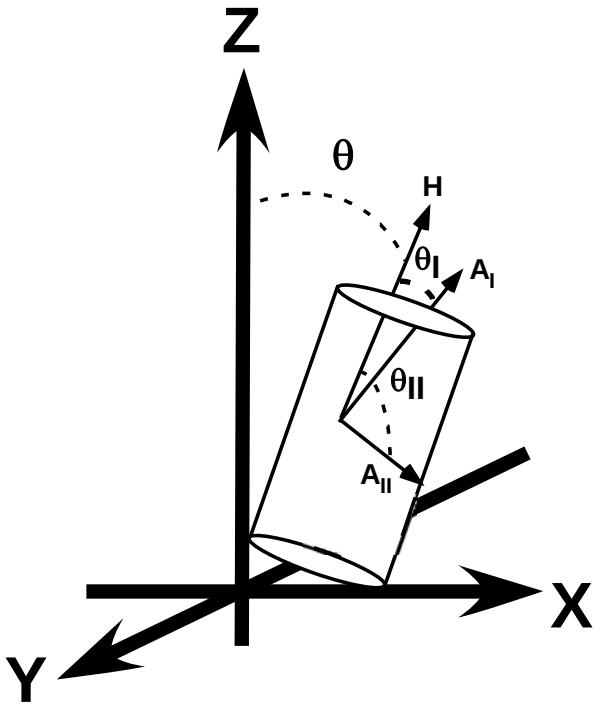

Figure 3-5: Diagram of the molecular coordinate system used to determine the average peptide helix tilt angles. Z is defined as the surface normal, H is the axis along the helix backbone, A_I is the amide I mode, A_{II} is the amide II mode, Θ_1 is the angle between the helix backbone and the amide I mode, θ_{II} is the angle between the helix backbone and the amide II mode, θ is the angle between the helix backbone and the surface normal.

By using the molecular coordinate system described in Figure 3-5, the average orientation of the immobilized peptides with respect to surface normal can be calculated. A similar type of molecular coordinate system was used in the study of synthetic surface-bound peptides.[148-150, 153] Equation 3-2 shows the relationship between the intensity ratio of the amide I and amide II absorbance modes and the tilt angles described by the coordinate system. D_{obs} is the calculated ratio of the amide I and amide II absorbance intensities, θ_I is the angle between the amide I mode and the helix backbone (79°), θ_{II} is the angle between the amide II mode and the helix backbone, K is a proportionality constant defined as the amide I:II ratio calculated from transmission spectra, typically taken to be 1.50, and θ is the angle between the surface normal and the helix backbone.

$$D_{obs} = K \frac{2\left(\frac{1}{2}\left(3\cos^2\theta - 1\right)\right)\left[\frac{1}{2}\left(3\cos^2\theta_I - 1\right)\right] + 1}{2\left(\frac{1}{2}\left(3\cos^2\theta - 1\right)\right)\left[\frac{1}{2}\left(3\cos^2\theta_{II} - 1\right)\right] + 1}$$

Equation 3-2

From the work of Boncheva and Vogel, Figure 3-6 shows IR spectra expected for the extreme cases of peptide helix orientation on a surface. If a peptide helix is oriented vertically, or perpendicular to the surface plane, the amide I mode exists in a mostly perpendicular orientation, which results in an intense IR absorption. The nearly orthogonal amide II mode exists in a nearly parallel orientation, which leads to a weak IR absorption. The spectrum shown reflects this configuration as the amide I mode is much more intense than the amide II. In the opposite case of a peptide helix lying nearly flat on the surface, the amide I mode is mostly parallel and the amide II mode is nearly perpendicular. This configuration results in the amide II absorbance being more intense than the amide I and is reflected by the example spectrum shown.

The dependence of the amide I:II intensity ratio has been demonstrated previously in our group.[76] Highly ordered alkanethiol self-assembled monolayers containing terminal carbamate groups with varying alkane chain lengths were formed on gold substrates. The all-trans configuration of the adjacent alkane chains along with the hydrogen bonding interaction of the carbamate groups constrained the amide I vibration to a mostly parallel orientation relative to the surface plane. The RAIR spectra of the amide region supported a parallel orientation as the amide I:II ratio was less than 1.0.

The previous work described above provided the foundation for using RAIRS in our investigation of the surface structure of immobilized antimicrobial peptides. In the study presented here, of PGQ, pleurocidin, and cecropin P1, the RAIR spectra of the peptide thin films were collected in order to ascertain the secondary structure and average orientation of the peptide monolayers. Primary focus was on the amide mode region of the spectra between 1800 and 1400 cm^{-1}.

Reflection absorption infrared spectroscopy (RAIRS) measurements were performed by using a Nicolet Nexus 670 FTIR spectrometer. The samples were positioned on an 80° reflection stage available from Thermo Scientific. The *P* component of the linearly polarized light was selected by using a zinc-selenide polarizer that was placed in front of the reflection stage. A mercury-cadmium-telluride (MCT-A) detector was used which had a spectral range of 4000-650 cm^{-1}. A clean gold surface was used as the background reference spectrum.

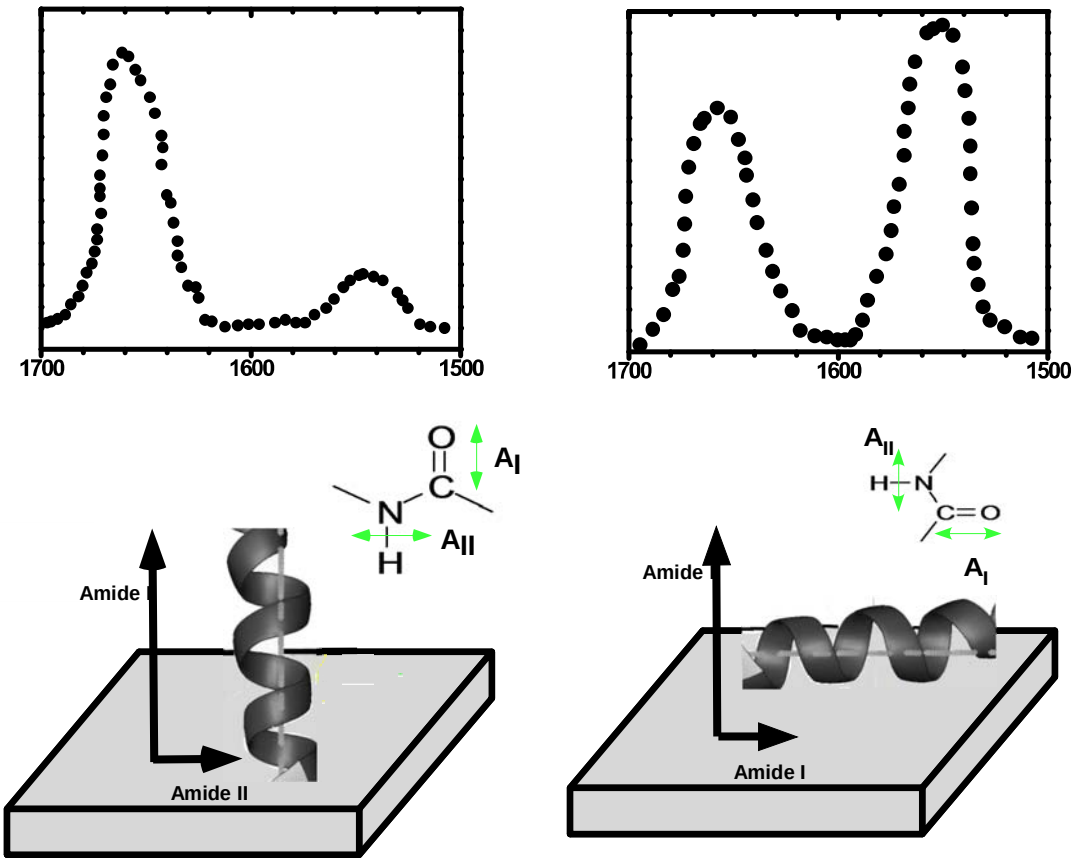

Figure 3-6: Diagram presenting examples of the two extremes of peptide orientation on a surface along with the corresponding IR spectra. Spectra figures were reproduced from *Biophys. J.* 1997, *73* (2), 1056-1072.

X-ray Photoelectron Spectroscopy (XPS)

X-ray photoelectron spectroscopy is another powerful technique that provides information about the oxidation states and atomic concentrations of surface-bound molecules. XPS is quite useful for systems that use Au-S binding because it allows for the determination of the oxidation state(s) of the terminal sulfur moieties, including the distinctive binding energy of a gold-bound thiolate species. In our study, XPS was used to verify that the peptides had covalently bonded to the gold through the desired Au-S interaction, and that carbon, nitrogen, and oxygen were present.

XPS work was performed on a Perkin Elmer 5400 X-ray Photoelectron Spectrometer equipped with a monochromatized Mg(Kα) radiation source (1253.6 eV) and a positron sensitive, multi-channel plate detector. The measurements were taken at a pressure of less than 5 x 10^{-7} Torr and a take-off angle of 15° with respect to the surface normal. Binding energies are referenced to the Au $4f^{7/2}$ peak at 83.9 eV. Survey spectra were recorded with a pass energy of 89.45 eV for ten minutes on a 1mm x 3.5 mm spot size and 250 W electron beam power. High resolution multiplex scans were recorded with an average scan time of 10 minutes per element, except for sulfur which required a longer scan time of 30 minutes.

Surface Plasmon Resonance (SPR)

Surface plasmon resonance is a surface analysis technique that is used to determine the extent to which a particular surface sample adsorbs an analyte of interest. The technique is based on the resonance that occurs when impinging electromagnetic radiation of the correct energy and angle couples with the electromagnetic field of the oscillating free electrons in the conduction band of a metallic substrate, such as silver or gold. The surface plasmons create an evanescent wave that propagates along the surface and the associated electric field decays exponentially away from the surface up to approximately 300 nm into the adjacent phase.[154] The intensity of the reflected radiation is measured as a function of reflection angle, and when the correct phase matching conditions are met, the incident photons resonate with the free electrons of the metal, which causes a minimum in the reflected light intensity. If a material is adsorbed to the surface of the metal overlayer, optical properties such as the refractive index are altered. The change in optical properties of the system results in a change in the resonance angle, and the change in resonance angle is directly proportional to the mass of the adsorbate material.

Figure 3-7 outlines the setup of a surface plasmon resonance experiment. The impinging light is focused from the source into the prism, which is coupled to the metal layer. The light reflects off of the metal layer towards the detector, and if resonance occurs, the detector measures a minimum in reflected light intensity.

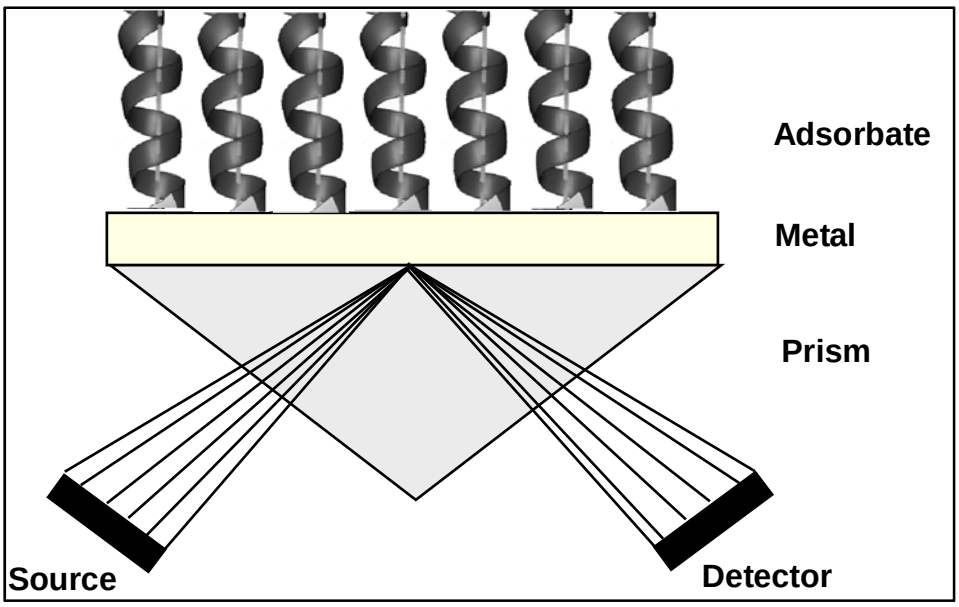

Figure 3-7: Schematic representation of the setup of a surface plasmon resonance experiment. The optical properties of the system vary as result of a change in the adsorbate layer.

The resonance angle shift is related to the change in refractive index and the change in adsorbed layer thickness by the following equation:

$$\Delta\theta(\lambda) = c_1\Delta n + c_2\Delta d$$

Equation 3-3

where c_1 and c_2 constants.[155-158] The change in refractive index (Δn) caused by a binding event can be predicted by the Lorentz-Lorenz relation[155]:

$$\Delta n = -\frac{1}{6n}\left(n^2+2\right)^2\left(\frac{n^2-1}{n^2+2} - \frac{n_w^2-1}{n_w^2+2}\frac{V_p}{V}\right)\frac{\Delta d}{d}$$

Equation 3-4

Where n is the refractive index of the adsorbate, n_w is the refractive index of water, V_p is the volume of the adsorbate and V is the volume of the adsorbed layer ($V = V_p + \mathrm{V_w}$).

The data obtained during an SPR experiment is displayed as a sensorgram, which shows the resonance angle shift as a function of time. The shift in the resonance angle is converted into a response unit (RU), where 1 RU is equivalent to a 0.0001° resonance angle shift. The plot of response units versus time is called a sensorgram and Figure 3-8 demonstrates the relationship

between the resonance angle shift and a corresponding sensorgram. One response unit is equivalent to adsorbed mass density of 1 pg/mm^2. For a peptide of average molecular weight of 3000 g/mol, SPR is sensitive to changes in surface density of 3.33 x 10^{-14} mol/cm^2. In our study, we employed SPR to quantify the immobilization of the antimicrobial peptides to the gold substrates. SPR allowed us to determine if different adsorption solution conditions such as pH, solvent polarity, and concentration had an effect on adsorption rate and density of the immobilized peptides.

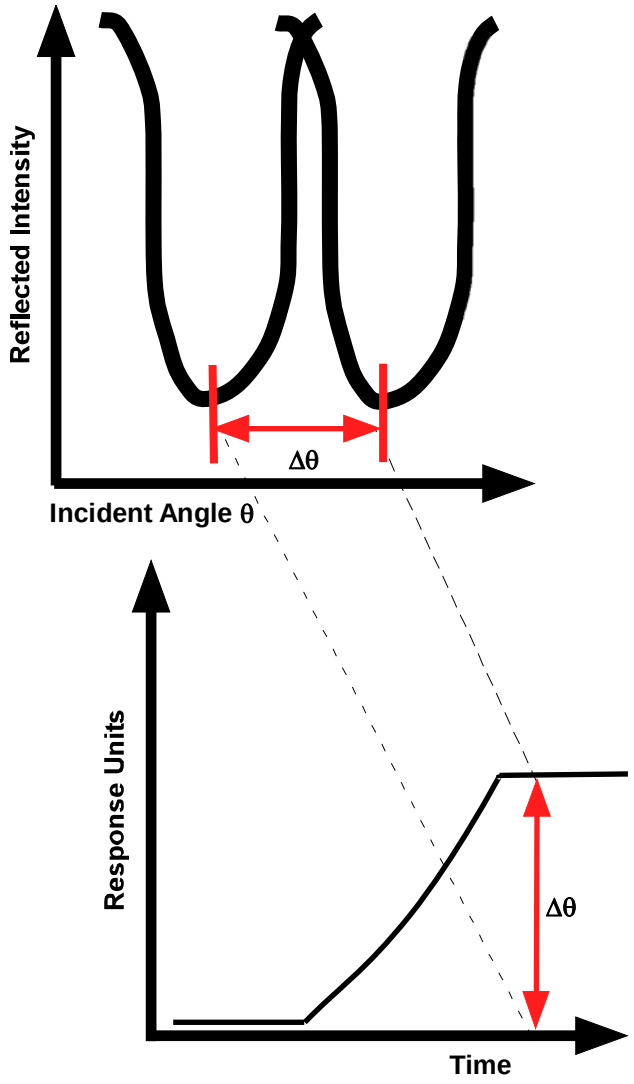

Figure 3-8: A schematic demonstration how the resonance angle shift caused by an adsorbed mass is converted to the response unit of an SPR sensorgram.

The SPR spectra were collected using a T100 system from Biacore, Inc. (Piscataway, NJ). Bare gold sensor chips were purchased from Biacore and consist of four independent flow channels. One limitation of SPR measurements is the occurrence of non-specific binding to the substrates. The resonance shift is only sensitive to adsorbed mass changes and different chemical species cannot be distinguished. To minimize the interference of non-specific binding during the adsorption of the peptides, each flow channel was passivated prior to the introduction of peptide by flowing buffer over the surfaces for 50 minutes at a rate of 30 µL/min. Even with the passivation step, some non-specific binding was detected. To further address the non-specific binding, during each SPR experiment, one of the four flow channels was used as a blank

in which the solution contained everything except for the peptide. The remaining three flow channels used solutions containing the peptide, and the final SPR response was calculated by subtracting the reference blank response from the trial response. Each experiment was performed at a flow rate of 1 μL/min.

3.2.5 Peptide Solution Characterization

Circular Dichroism (CD)

In our study of the surface structure of antimicrobial peptides, we hypothesized that the structure of the peptides in solution would affect the subsequent surface structure. Therefore, it was important that the peptides were characterized in solution as well as on the surface. One of the most useful spectroscopic techniques used to characterize the secondary structure of proteins and peptides is circular dichroism, which is an optical technique that measures the difference in the response of chiral molecules to right and left-handed circularly polarized light.[159] The technique is especially amenable to the study of biological molecules because many of them are composed of chiral units, such as amino acids.[159-161] For example, naturally occurring peptides and proteins are composed of all L-amino acids which form only right-handed α-helices. The left and right-handed circularly polarized light interacts differently with the α-helices, as well as other protein structures. The difference between the absorbance of the left and right-handed polarized light is shown as the circular dichroism spectrum, which displays the molar ellipticity as a function of wavelength. The molar ellipticity is given by equation 3-5 where Δε is the difference between the left and right-handed absorbance.[162]

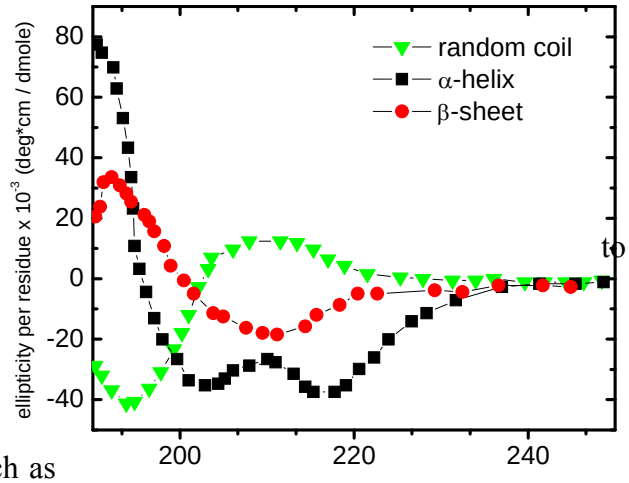

Figure 3-9: Example CD spectra of different peptide secondary structures. Spectra were reproduced from reference 1.

$$[\theta] = 3298.2\Delta\varepsilon$$

Equation 3-5

Different types of secondary structures in proteins and peptides give different types of circular dichroism spectra and examples of each are shown in Figure 3-9. The double minimum spectral profile is characteristic of the α-helical secondary structure. The percent alpha helix for the peptides were determined using equation 3-6 which uses the mean residue contributions of -39000 deg cm^2/dmol for alpha helix and -3000 deg cm^2/dmol for random coil.[162]

The CD spectra were recorded using a JASCO J-715 spectrapolarimeter at 25°C. For each sample, five scans at wavelengths of 250-190 nm were collected with capped quartz cell with 0.1 cm path length.

$$\%\ \alpha\text{-helix} = \left(-[\theta_{222}] + 3000\right)/39000$$

Equation 3-6

3.3 Data and Results

The goal of the study presented here was to determine the surface structure, including secondary conformation, average orientation relative to surface normal, and relative surface densities of three selected antimicrobial peptides along with the effects of the solution conditions. In brief, we found that the surface structure of the immobilized peptides was mostly independent of the solution conditions. The peptides were always α-helical on the non-solvated surfaces, and they adopted a highly titled (~50°) orientation relative to the surface normal. In the next section we provide the data and resulting observations that led to our conclusions.

3.3.1 Effect of Peptide Solution Secondary Conformation on Surface Structure

In an aqueous environment, most amphipathic α-helical antimicrobial peptides exist in a random coil configuration.[163] In a polar medium, it is more energetically favorable for the polar amino acid residues of the peptide to hydrogen bond with solvent molecules than it is to form intermolecular hydrogen bonds. Upon interaction with the lipid containing outer membrane of bacteria, the peptides fold into the active α-helical form because it is more energetically favorable for the polar amino acid residues to form intermolecular hydrogen bonds than it is to

interact with the non-polar lipid membrane. Interestingly, the random coil-to-helix transition can also be induced by introducing a less polar solvent to the aqueous solution. Trifluoroethanol has been shown to induce the helix transition of antimicrobial peptides in aqueous buffer.[164-166] In our study, we used TFE to induce the peptides to adopt α-helical conformations in aqueous buffer.

We hypothesized that the conformation of peptides in solution affects their resulting structure when immobilized to a gold surface. Helical peptides may be able to form higher density surface films because they might have larger diffusion rates than the random coil peptides. In addition, peptides immobilized as α-helices may form a film with a more vertical average orientation, as opposed to peptides adsorbed from solution as random coils. To test this hypothesis, the three peptides were prepared in phosphate buffer with and without 25 percent trifluoroethanol at pH 7.4.

Cecropin P1

The first peptide we investigated was cecropin P1 because it is the peptide that was most thoroughly studied by the Mello group for discriminatory binding behavior.[23, 128-130] Cecropin P1 differs from both PGQ and pleurocidin as it is longer than the other peptides (31 vs 24 and 25 residues, respectively) and is less hydrophobic (35% vs 45 and 44%, respectively). In the study of cecropin P1, we investigated the effects of solution secondary structure (section 3.3.2), peptide solution concentration (section 3.3.3), solution pH (section 3.3.4), and the addition of a disulfide specific reducing agent (section 3.3.5). The initial experiment focused on examining the effect, if any, of the additional cysteine residue on the secondary structure in solution. Circular dichroism is a technique commonly used to determine protein and peptide secondary structure in solution, and the results of those experiments are presented next.

Circular Dichroism for Peptide Solution Structural Characterization

Circular dichroism data was especially important in our study of peptide structure for two reasons: 1) CD can verify the secondary structure of the peptides in solution prior to immobilization on the gold substrates, and 2) CD can verify that that addition of the terminal cysteine group did not alter the ability of the peptides to fold into α-helices upon the addition of TFE.

Circular dichroism spectroscopy was used to determine the α-helical content of the peptides. The peptides consisted of cecropin P1 with and without the additional terminal cysteine residue in pH 7.4 phosphate buffer, with 50% trifluoroethanol, and with 50% TFE and the reducing agent TCEP (the effects of TCEP will be explained in more detail later).

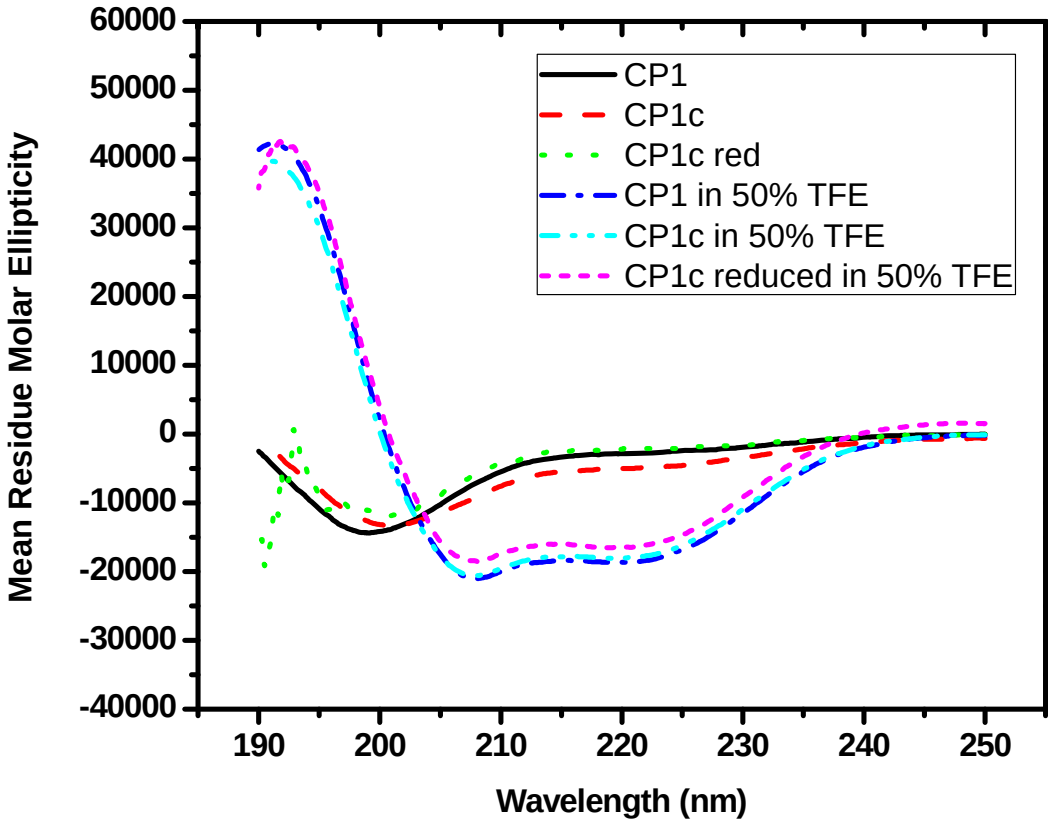

Figure 3-10: Circular dichroism spectra of cecropin P1 (CP1) and cysteine-terminated cecropin P1 (CP1_c) under reducing and non-reducing conditions with and without 50% trifluoroethanol.[167]

A peptide with significant α-helical content exhibits a characteristic double minimum profile in the CD spectra. In Figure 3-10, all of the peptides prepared with TFE exhibited the characteristic double minimum profile associated with a mostly α-helical conformation. The addition of the terminal cysteine group, as well as the presence of the reducing agent, had minimal effect on the secondary structure in the phosphate buffer at pH 7.4. The percentage of α-helical content was calculated as described in the experimental section, and is given in Table 3-4. All three of the peptides prepared with TFE had nearly 50 percent α-helical content. The minimal influence of the terminal cysteine residue is important as it allows us to compare the

experimental results to unmodified naturally produced cecropin P1 which does not contain a cysteine residue.

Following initial characterization at pH 7.4, circular dichroism was also used to investigate the effect of buffer pH on the α-helical content of the peptides in the presence of TFE. Cysteine-terminated cecropin P1 was prepared in phosphate buffer with 50% TFE at pH 5, 7.4, and 9.2 and the CD spectra are shown in Figure 3-11 along with calculated α-helical content in Table 3-4. Both acidic and basic pH led to a reduction in the α-helical content with pH 5 having nearly 34 percent α-helical content and pH 9.2 having 33 percent. The pH dependence of the α-helical content demonstrates the importance of electrostatic interactions in the formation of the helices in solution. The formation of the α-helix requires a delicate balance of inter- and intramolecular forces, and the addition or reduction of external charged species, as such is the case at acidic and basic pH, can have a large effect on the ability of a peptide to fold into the compact helix form. The polar face of cecropin contains five cationic species and for these charges to come in to close proximity, as is the case in the α-helix, the electrostatic repulsion must be properly balanced. At physiological pH (7.4), apparently there is sufficient charge balance in solution and the peptides contain the highest helical content. At the other pH's, the charge balance might be insufficient and the peptides cannot fold into the helices as effectively.

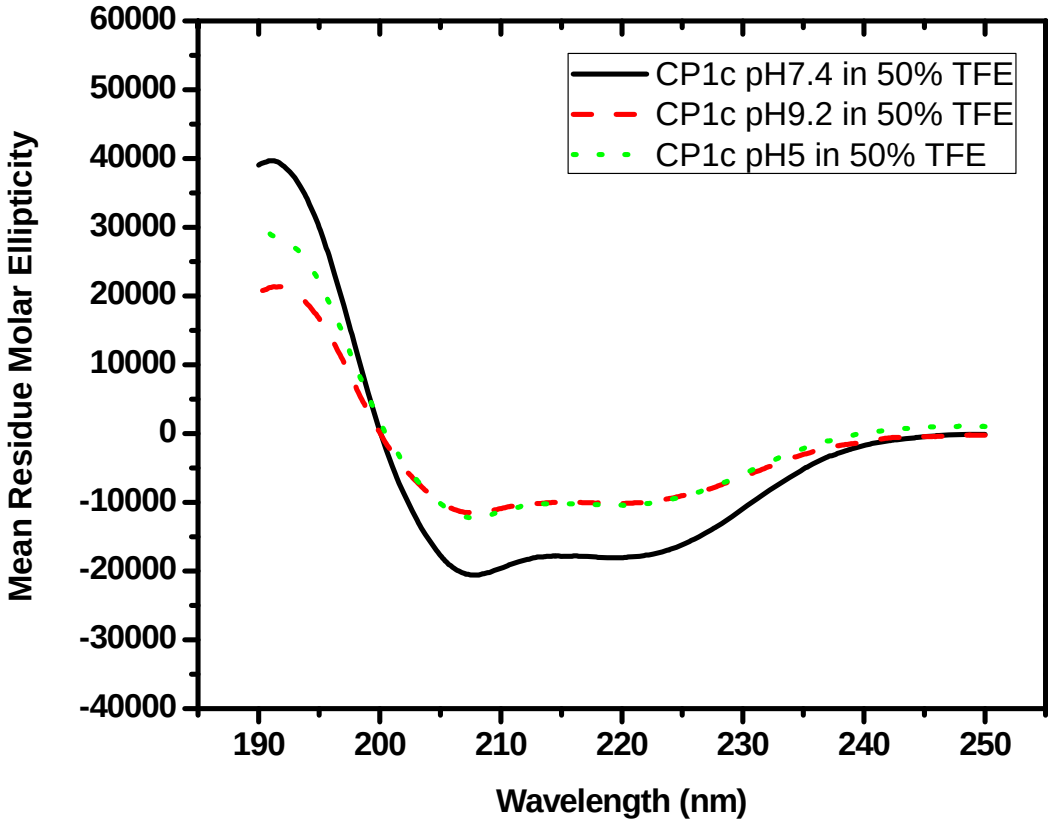

Figure 3-11: Circular dichroism spectra of CP1_c at pH 5, 7.4, and 9.2 with 50% trifluoroethanol.[167]

	CP1	CP1_c Reduced	CP1_c Non-reduced
pH 5 Buffer	--	--	9.49%
50% TFE	--	--	33.90%
pH 7.4 Buffer	14.80%	13.10%	20.20%
50% TFE	54.79%	49.04%	54.41%
pH 9.2 Buffer	--	--	12.32%
50% TFE	--	--	33.29%

Table 3-4: α-helical content of cecropin P1 (CP1) and cysteine-terminated cecropin P1 (CP1_c) under different conditions as determined from circular dichroism.[167]

3.3.2 Cecropin P1 Solution Effects: Secondary Structure in Solution

RAIRS

The circular dichroism experiments verified that the secondary structure of cecropin P1 depends on the polarity and pH of the buffer, and that the additional cysteine residue does not alter the folding characteristics. We next began a systematic investigation on the effects of solution conditions such as buffer polarity, pH, peptide concentration, and cysteine oxidation state on the immobilized peptide surface structure. To our knowledge, our study is one of the first to systematically investigate the effects of solution factors on the surface structure of immobilized natural peptides.

The systematic study began by investigating the effects of solution secondary. 9.7 μM cysteine-terminated cecropin P1 was prepared in pH 7.4 phosphate buffer with and without 25 percent trifluoroethanol. RAIR spectra were collected after overnight immersion, and the amide region of the spectra are shown in Figure 3-12. The full RAIR spectra are provided in Appendix A.

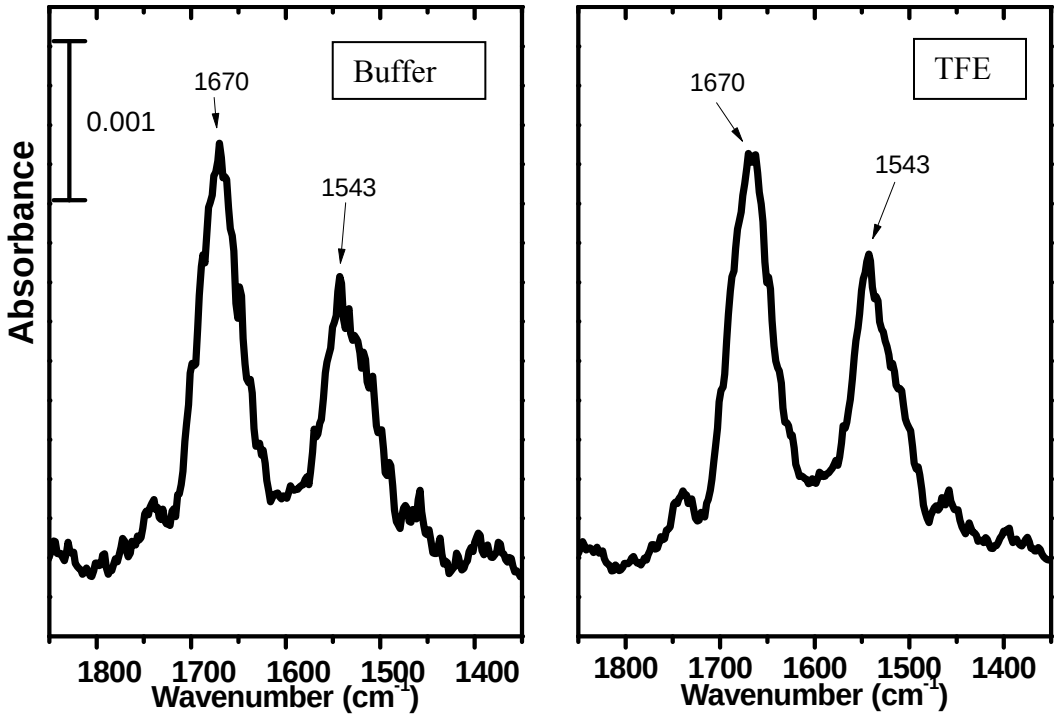

Figure 3-12: Amide vibration region of the RAIR spectra of cecropin P1 immobilized with and without 25% TFE in the buffer. The peptide solution concentration was 9.7 μM in pH 7.4 phosphate buffer.

The amide regions of the spectra are remarkably similar to those of other peptides investigated by our group (see sections 3.4 and 3.5). The surfaces prepared with and without 25 percent TFE are also very similar; both amide I modes appear at 1670 cm^{-1} and the intensities are nearly equal within standard error $(1.64 \pm 0.18) \times 10^{-3}$ and $(1.44 \pm 0.37) \times 10^{-3}$, respectively, see Table 3-5). The amide ratios are 1.79 ± 0.34 and 1.52 ± 0.24 for the non- and with-TFE spectra, respectively, which result in tilt angles of 50.7 ± 4.2 and 54.2 ± 3.8. Within error, it appears that the secondary structure in solution has minimal effect on the surface structure of cecropin P1.

Proteins and peptides in the bulk phase are randomly oriented, and their corresponding amide ratio is typically between 1.5 and 2.0.[168-170] The calculated amide ratios of the CP1_c spectra fall within this range, which suggests that the immobilized peptides are also are randomly oriented. While a tilt angle value can be calculated from the amide ratios, if the ratio falls between 1.5 and 2.0, a random immobilized peptide distribution must also be considered. Both random coil and α-helical secondary structures in phosphate buffer at pH 7.4 form surfaces with titled, randomly oriented α-helical peptides.

XPS

XPS was utilized to identify the constituent atoms of the peptides and compare the relative surface densities by comparing the carbon-gold ratios. A relatively larger carbon-gold ratio is indicative of a higher peptide surface density. The XP survey spectra are provided in Appendix A and show that the constituent carbon, nitrogen, and oxygen atoms were all detected. Figure 3-13 shows the C1s and Au4d$^{5/2}$ XP multiplex spectra that were used to determine the carbon-gold ratios and, subsequently, the relative surface densities. The carbon-gold ratio for the CP1_c surface prepared with TFE had a slightly larger ratio, 1.42, than the surface prepared in only pH 7.4 phosphate buffer, 1.37. The somewhat larger ratio suggests a slightly higher surface density for the peptides immobilized to the surface in α-helical conformation.

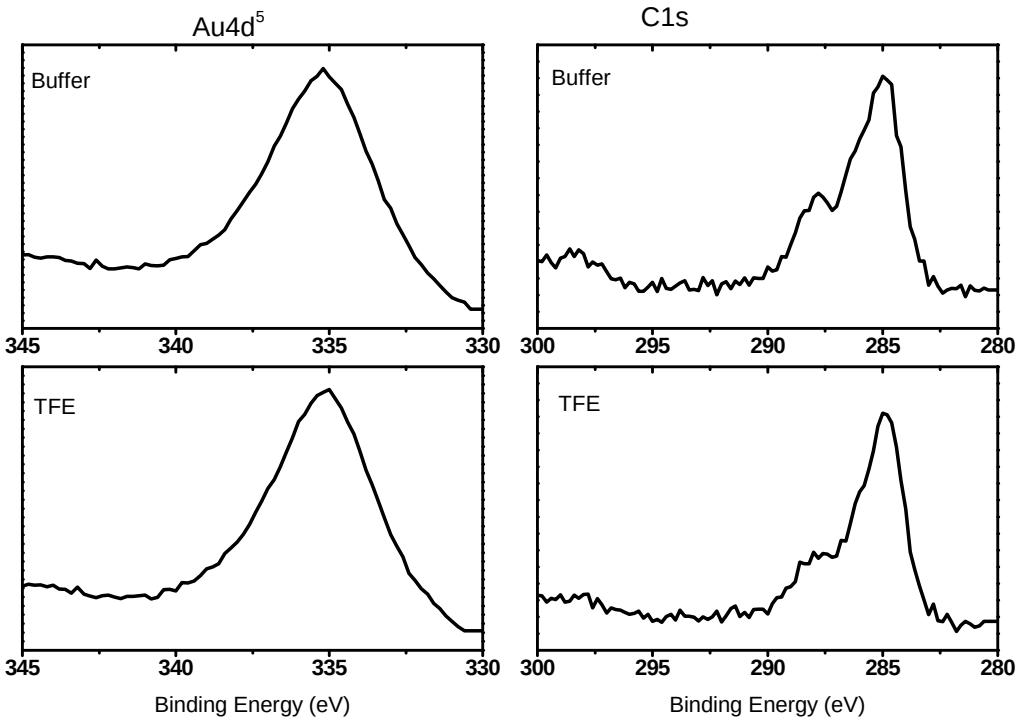

Figure 3-13: XP spectra of the C1s and Au4d^5 regions for 9.7 μM CP1_c immobilized in pH 7.4 phosphate buffer with and without 25 percent TFE.

Extended Peptide Adsorption Time

The adsorption of biological macromolecules from solution is normally identified by high affinity isotherms.[171] The isotherms are typically characterized by a very fast initial adsorption due to the high affinity of the molecules towards the surface. The surface density increased at a

much slower rate after the initial fast adsorption until equilibrium was reached. We hypothesized that the surface density of CP1_c would continue to increase as a function of adsorption time. We tested this hypothesis by returning the peptide samples to solution after RAIRS analysis for up to 23 days. We did not collect XP spectra for the extended adsorption time study in order to avoid any possible X-ray induced damage to the samples. Figure 3-14 shows the amide regions of the RAIR spectra collected for both samples from 1 to 23 days.

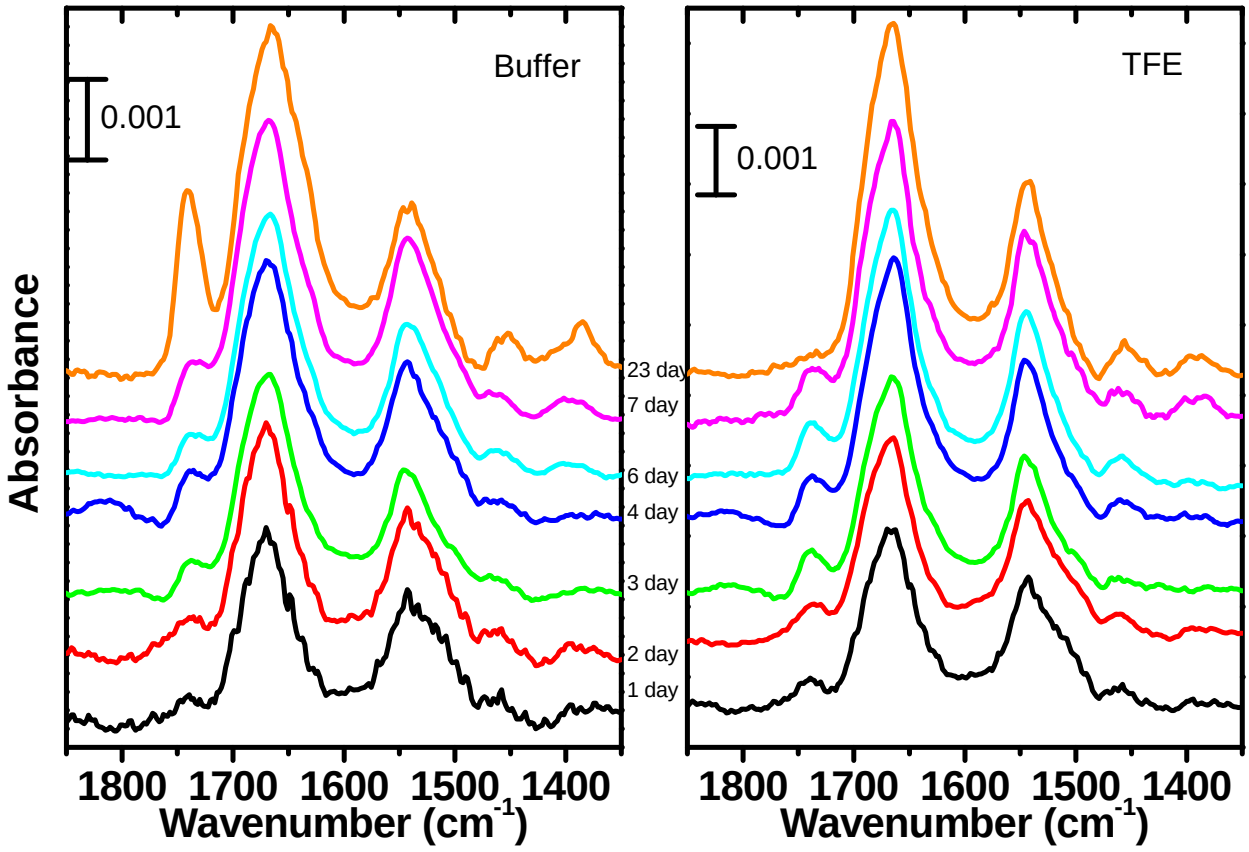

Figure 3-14: The amide vibration region of cecropin P1 immobilized with and without 25% TFE recorded at increasing adsorption time.

For the two samples, both the amide I intensities and the amide I:II ratios increase over time, suggesting that the surface density increases and the average orientation becomes more parallel to the surface normal. Figure 3-15 shows the amide I intensities for both surfaces as a function of time along, with the respective tilt angles.

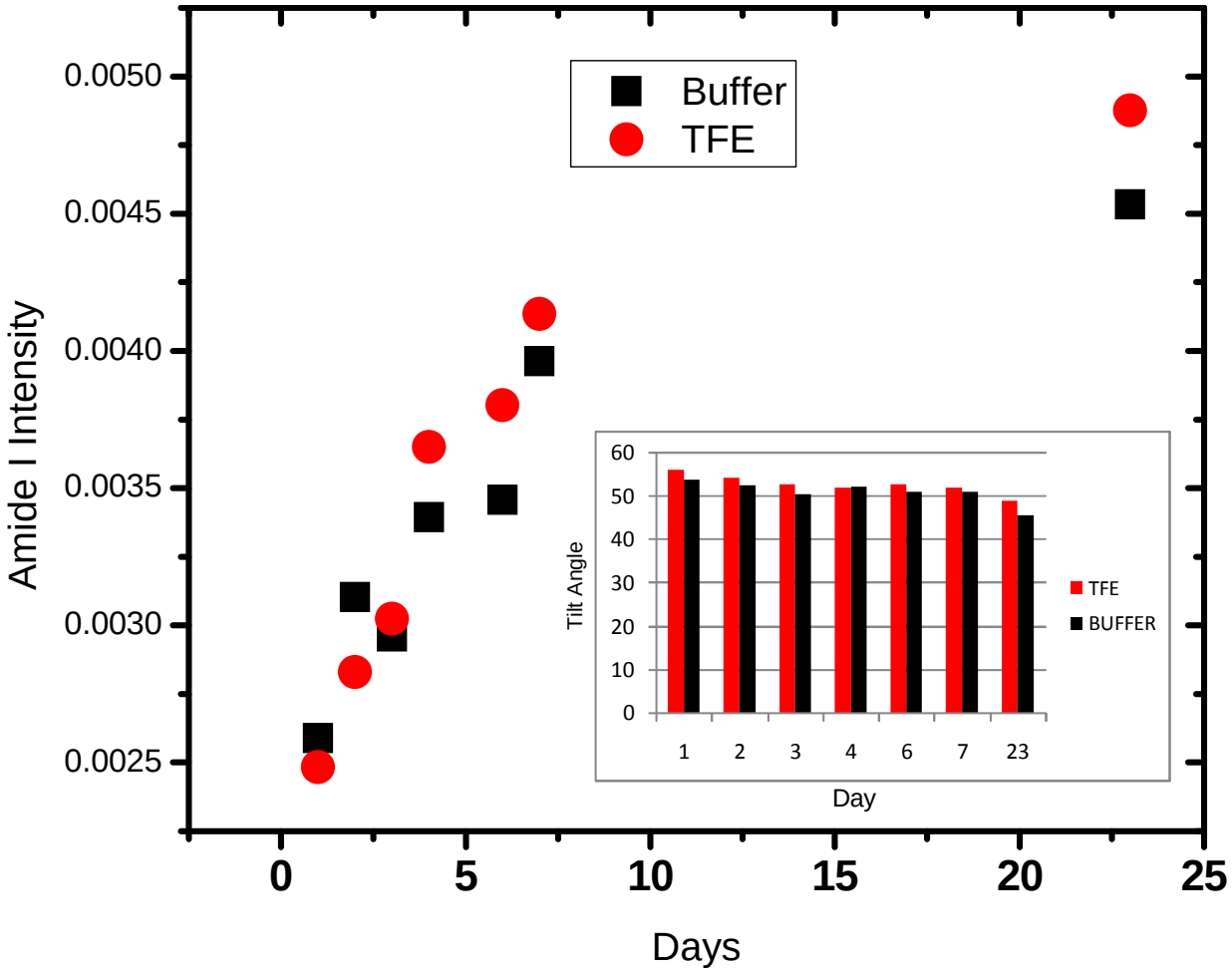

Figure 3-15: Plot of the amide I mode absorbance intensity as a function of time for cecropin P1 immobilized with and without 25% TFE. The inset plot is of the calculated average peptide tilt angles relative to surface normal.

Figure 3-15 shows the integrated intensities of the amide I mode as a function of adsorption time. Clearly the amide I intensities of both surfaces increase over time, even after three weeks of adsorption. The inset plot of the average tilt angles as a function of time suggests that while the angles do decrease over time, the change is slight with a near 5 degree change from day 1 to day 23. This small decrease in average tilt angle suggests that the peptides remain flat on the surface, even at higher surface densities.

3.3.3 Cecropin P1 Solution Effects: Solution Concentration

RAIRS

Adsorption to a surface is affected by time, as well as adsorbate solution concentration, and the influence of peptide solution concentration was investigated by increasing the cecropin P1 concentration from 9.7 to 29.1 μM. The peptides were prepared in pH 7.4 phosphate buffer with and without 25 percent TFE. The amide regions of the RAIR spectra are shown in Figure 3-16.

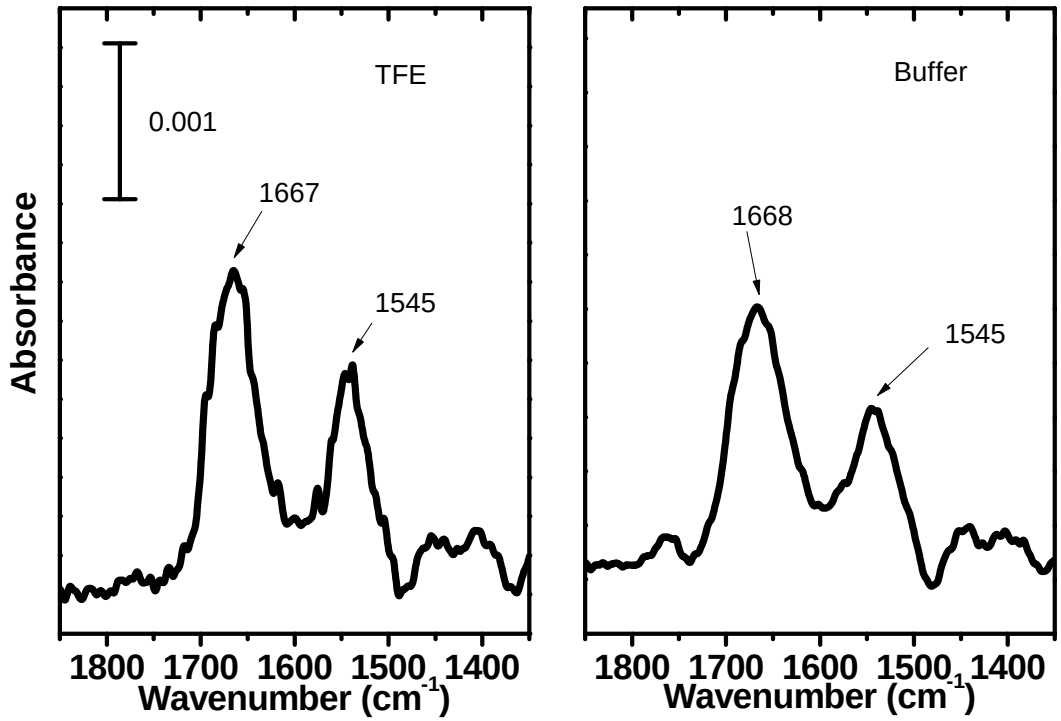

Figure 3-16: Amide vibration region of the RAIR spectra recorded for cecropin P1 immobilized with and without 25% TFE at a peptide solution concentration of 29.1 μM in pH 7.4 phosphate buffer.

The amide I modes of both spectra again appear near 1670 cm^{-1}, which is characteristic of mostly α-helical peptides. The amide I mode intensities are (2.07 ± 0.15) x 10^{-3} and (1.65 ± 0.078) x 10^{-3} for the spectra with and without TFE, respectively. Both of the amide I intensities are larger than the corresponding intensities of the surfaces prepared at a lower surface concentration (9.7 μM), which suggests a higher surface density of immobilized peptides. Within error, the two peptide films had the same average tilt angles, 53.2° ± 1.3 and 52.9° ± 0.2 for the TFE and non-TFE conditions, respectively. The amide ratios are within the 1.5-2.0 range

and the calculated tilt angles should be considered part of a random distribution of the peptides on the surface.

XPS

XP spectra of the peptide surface were again collected to identify the constituent atoms and ascertain the relative surface densities via the carbon-gold ratios. The XP survey spectra are provided in Appendix A and the constituent carbon, nitrogen, and oxygen atoms of the peptides can clearly be identified. The XP multiplex spectra of the C1s and $Au4d^{5/2}$ regions are shown in Figure 3-17. As was observed using the lower peptide solution concentration, the peptide surface prepared with TFE had a larger carbon-gold ratio, 1.94, than did the surface prepared without TFE, 1.57.

The higher peptide solution concentration appears to have a small effect on the surface structure of immobilized CP1_c, with the only observable difference being a slightly higher surface density compared to a lower solution concentration. There was very little dependence on the peptide secondary structure in solution, outside of a small increase in surface density for the peptides immobilized as α-helices with TFE.

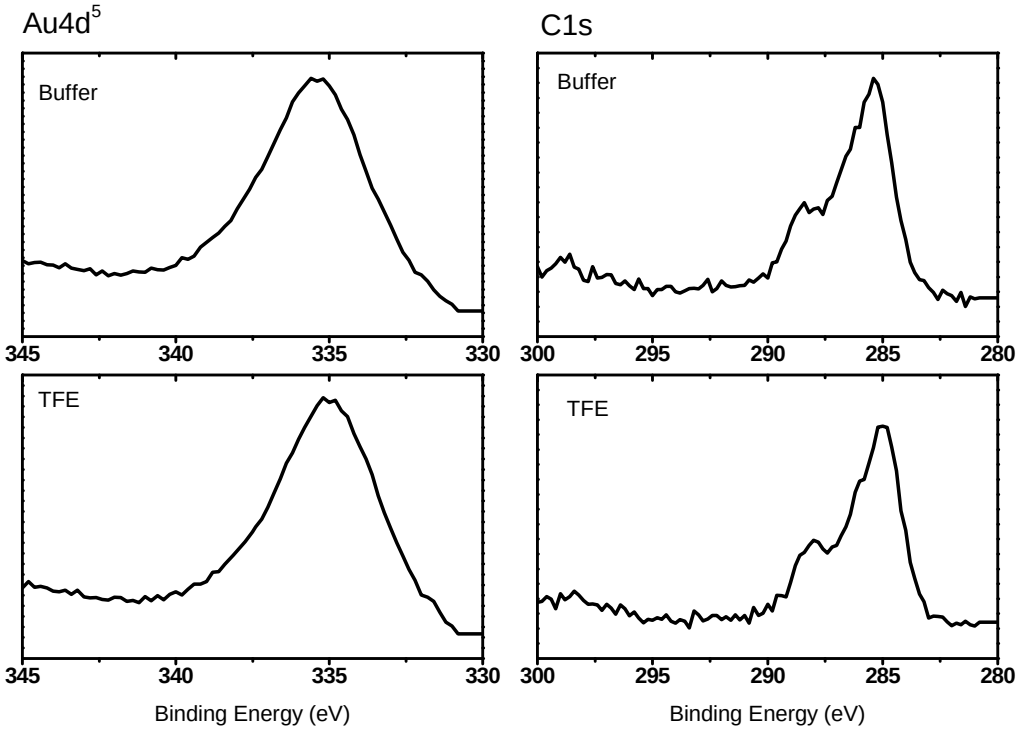

Figure 3-17: XP spectra of the C1s and Au4d^5 regions for 29.1 µM CP1_c immobilized in pH 7.4 phosphate buffer with and without 25 percent TFE.

3.3.4 Cecropin P1 Solution Effects: Buffer pH

The solution pH can have a large effect on the solution structure of proteins and peptides because both inter- and intramolecular binding phenomena, such as secondary and tertiary protein structures, are influenced by electrostatic interactions. The effect of a more basic pH on the secondary structure of cecropin P1 in solution was demonstrated in Section 3.3.1 via circular dichroism spectroscopy. In phosphate buffer containing 50 percent TFE at pH 9.2, the α-helical content of the peptides was reduced from 54 percent at pH 7.4 to 33 percent at pH 9.2.

The adsorption of CP1_c to gold may be different at a more basic pH because of the charged residues found in the peptide. The polar face of the cecropin P1 helix contains five cationic residues at physiological pH. At higher pH, the charged residues can become deprotonated, which affects the intermolecular non-covalent bonding and reduces the ability of the peptides to fold into helices. At pH 7.4, the proximity of the immobilized helical peptides is limited due to electrostatic repulsion of the cationic groups of neighboring molecules. At higher pH, the cationic charges are deprotonated and we hypothesized that electrostatic repulsion of

neighboring immobilized peptides might be diminished. This hypothesis was tested by preparing CP1_c with and without 25 % TFE in phosphate buffer at pH 9.2 and CAPS buffer at pH 11.

RAIRS pH 9.2

RAIR spectra were collected for CP1_c with and without 25 percent TFE at both pH 9.2 and 11.0, which are slightly below and above the isoelectric point of cecropin (10.56).[172] At the isoelectric point pH, all amino acid residues of the peptide are neutral. The amide regions of the pH 9.2 spectra are shown in Figure 3-18. The amide I frequencies of both spectra are near 1670 cm^{-1}, which is again characteristic of α-helical conformation. The calculated amide ratios and corresponding tilt angles are again within the range of the randomly distributed peptides. The non-TFE sample spectrum had an amide I intensity of (1.57 ± 0.035) x 10^{-3} with an average tilt angle of 54.6 ± 0.9 whereas the TFE-containing sample spectrum had an amide I intensity of (1.44 ± 0.042) x 10^{-3} with an average tilt angle of 53.2 ± 1.3. Within error, there was no observable difference between the samples prepared at pH 9.2 with and without 25 percent TFE. The results were not unexpected since a pH of 9.2 is still below the pI of cecropin P1, which means that peptide most likely still contained ionized species, and the charged residues would prevent close packing. In the next experiment, the pH was increased to 11.

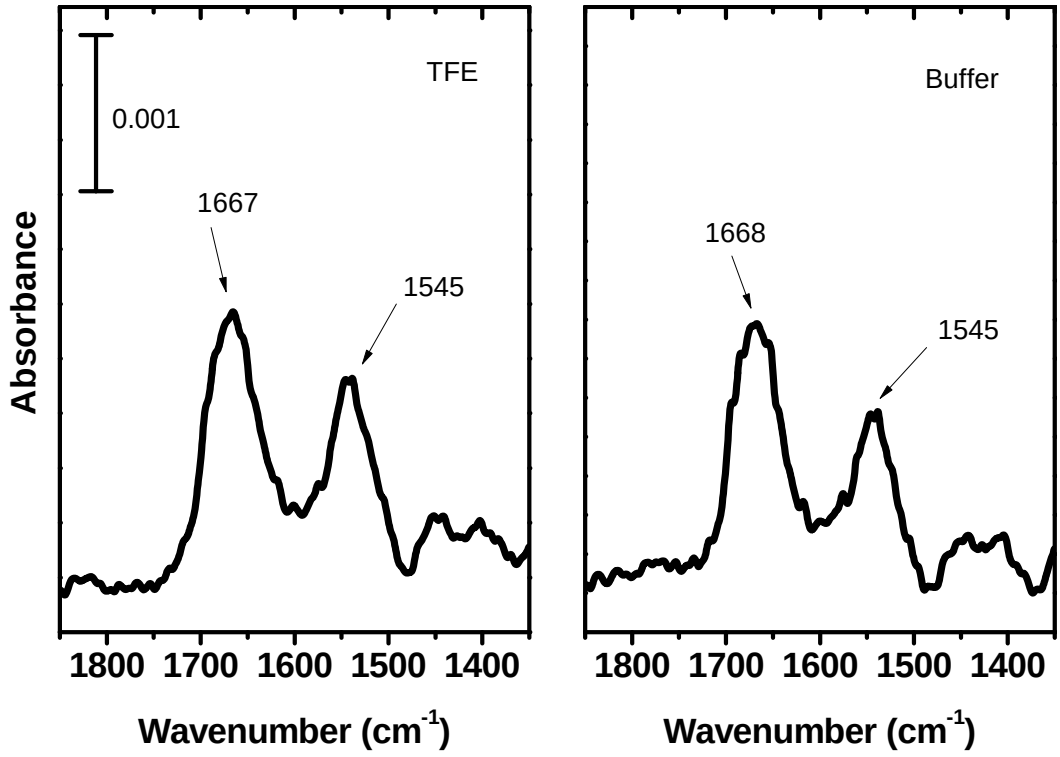

Figure 3-18: Amide vibration region of the RAIR spectra recorded for cecropin P1 immobilized with and without 25% TFE at a peptide solution concentration of 9.7 μM in pH 9.2 phosphate buffer.

RAIRS pH 11

The highest attainable pH with a phosphate buffer is approximately 9.2, and in order to increase the pH to a more basic level, a different buffer was needed. We used *N*-cyclohexyl-3-aminopropanesulfonic acid, or CAPS, to prepare a 0.1M buffer at pH 11. The surfaces were prepared at concentrations of 9.7μM in pH 11 CAPS buffer with and without 25 percent TFE. The amide regions of the RAIR spectra are shown in Figure 3-19 and appear very similar to those recorded at pH 9.2. The amide I intensity of the surface prepared with TFE is 1.92 x 10^{-3} and has a tilt angle of 51.37° and the surface prepared without TFE has an amide I intensity of 1.63 x 10^{-3} with a tilt angle of 51.69°. The overall intensities of the amide I modes at pH 11 were slightly higher than those at pH 9.2, but the average orientation was again tilted with respect to surface normal. The decreased electrostatic repulsion achieved by deprotonating the cationic residues in basic pH does not appear to have a significant effect on the surface structure of the immobilized peptides.

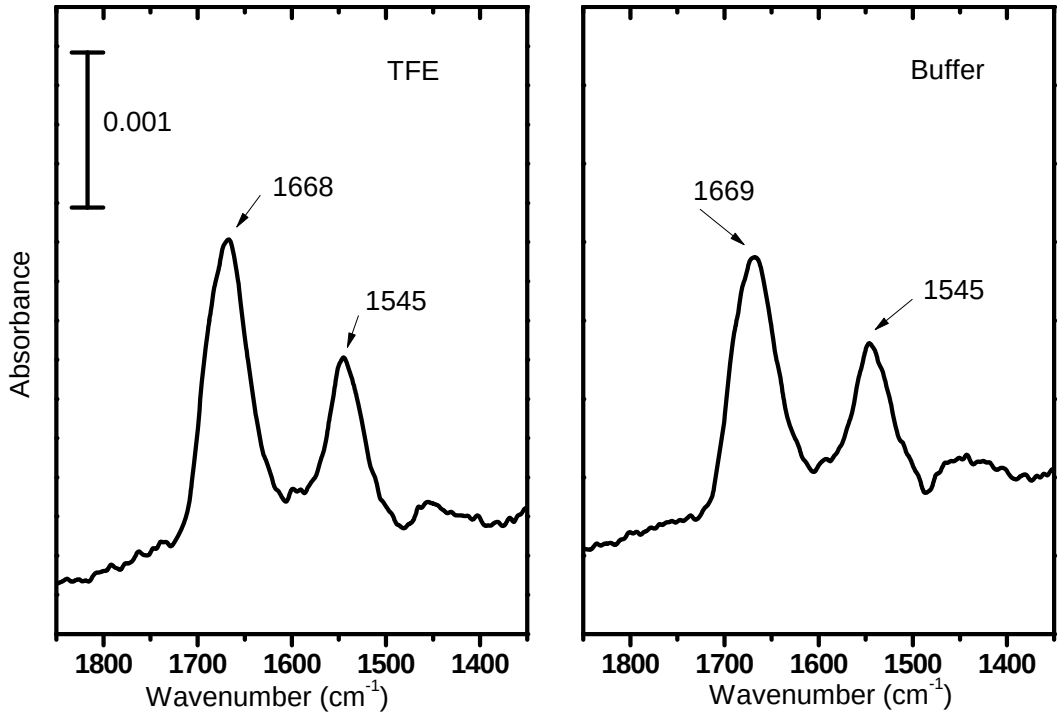

Figure 3-19: Amide vibration region of the RAIR spectra recorded for cecropin P1 immobilized with and without 25% TFE at a peptide solution concentration of 9.7 μM in pH 11 CAPS buffer.

3.3.5 Cecropin P1 Solution Effects: Sulfur Oxidation State and Peptide Aggregation

Peptides and proteins that contain cysteine residues can form disulfide bonds that link two molecules together to form a dimer. We hypothesized that the size difference between modified cecropin P1 monomers and dimers might affect their adsorption behavior. The adsorption of biological macromolecules to surfaces is largely mass transport controlled, which means that smaller molecules can diffuse to the surface more easily than can larger molecules. In addition, due to diffusivity differences, the adsorbed dimers and monomers may have different effects on the equilibrium surface density and structure. The results presented so far have shown that the peptides adopt a highly tilted, random like orientation on the gold surfaces. When a peptide lies flat on the surface it can block other gold binding sites from being available. A peptide dimer can occupy up to twice the two dimensional space of a peptide monomer and, therefore, can block twice as many gold binding sites. Blocking of the gold binding sites can diminish the adsorption rate and lower the equilibrium surface density of the adsorbate molecules.

Peptides and proteins, along with non-biological polymers, can form aggregates in solution with sizes ranging from dimers to large polymers.[173] Many of the aggregates form from non-covalent interactions, such as hydrogen or electrostatic bonding. In some cases, dimers are formed from covalent bonds, with one example being a disulfide bond formed via the oxidation of two thiol moieties. Disulfide bond formation is found extensively in large peptides and proteins; in fact disulfide bonds are an integral part of the tertiary structure of proteins as they link together different structural domains of a peptide.[174]

The thiol moiety found on the terminal cysteine residue of the modified cecropin P1 is readily oxidized by oxygen, metal ions, and other agents. Typically, two oxidized forms of the thiol are found; sulfonic acids and disulfides. The disulfides form from the oxidation and binding of two thiol groups on neighboring cysteine residues of two modified cecropin P1 molecules. The formation of the peptide dimers can be shown by using sodium dodecyl sulfate polyacrylamide gel electrophoresis (SDS-PAGE) because the larger peptide dimers have less electrophoretic mobility than do the peptide monomers.[175] SDS-PAGE images of reduced and non-reduced CP1_c are shown in Figure 3-20. Lanes 4, 7, and 10 contain peptide not treated with TCEP and these lanes show a shorter migration than the other lanes suggesting that the non-TCEP treated peptides contain significant dimerized species. The higher molecular weight dimer has migrated less than the monomer, which is a clear indication that the TCEP has reduced the peptides to monomers.

Figure 3-20: Image of a SDS-PAGE experiment demonstrating the effects of TCEP on cecropin P1 dimers. Lane 1: marker; Lanes 2 and 3: reduced CP1_c pH 7.4; Lane 4: non-reduced CP1_c pH 7.4; Lanes 5 and 6: reduced CP1_c pH 10; Lane 7: non-reduced CP1_c pH 10; Lanes 8 and 9: reduced CP1_c pH 11; Lane 10: non-reduced CP1_C pH 11.

The cecropin P1 molecules used in this study were not treated with any type of reducing agent to diminish or eliminate disulfide bonds. We wanted to test our hypothesis that the dimerization state of the peptide molecules did in fact affect the subsequent surface structure. To do so, all of the terminal cysteine residues of the peptides were converted into free thiols by using the disulfide-specific reducing agent Tris(2-carboxyethyl) phosphine to the buffer. The specificity of TCEP towards the reduction of disulfides has been shown in the literature.[176] TCEP is advantageous compared to other disulfide reducing agents such as trialkyl phosphines because it has very high water solubility and a high stability in air. TCEP is also compatible with biomolecules because it does not react with other functional groups, is effective over a large pH range, and is can be used at millimolar concentrations.

To investigate the effect of disulfide reduction on the surface structure of cysteine-terminated cecropin P1, 5 mM TCEP was added to the peptide solutions, which consisted of 9.7 μM peptide in pH 7.4 phosphate buffer with and without 25 percent trifluoroethanol. The surfaces were again characterized with RAIRS and XPS as well as surface plasmon resonance.

SPR was employed to acquire a quantitative comparison of the surface density of the immobilized peptides under reducing and non-reducing conditions via the introduction of TCEP.

RAIRS

Figure 3-21 shows the amide regions of the RAIR spectra for CP1_c prepared with 5 mM TCEP with and without 25 percent TFE. Figure 3-21 also contains the RAIR spectra recorded for CP1_c under equivalent conditions without the TCEP. The effects of the reducing agent are clearly evident as the amide peak intensities of the reduced CP1_c spectra are much larger than the non-reduced spectra. The amide I intensity of the spectrum prepared with TFE is (3.34 ± 1.74) x 10^{-3} with a corresponding tilt ratio of 48.6 ± 2.2 and the non-TFE spectrum has a amide I intensity of (2.75 ± 1.66) x 10^{-3} with a corresponding tilt angle of 52.2 ± 0.3. The much higher peak intensities suggest that there is a higher peptide surface density. Under reducing conditions, the presences of TFE in the buffer resulted in a statistical difference in tilt angle, which suggests that the reduced peptides, in monomeric form having α-helical conformation in solution, form a slightly closer packed structure upon immobilization to the gold. The closer packing might be due to the fact that peptides in α-helical form occupy a smaller solution volume than the random coil peptides, and after immobilization to the surface, occupy a corresponding smaller surface area.

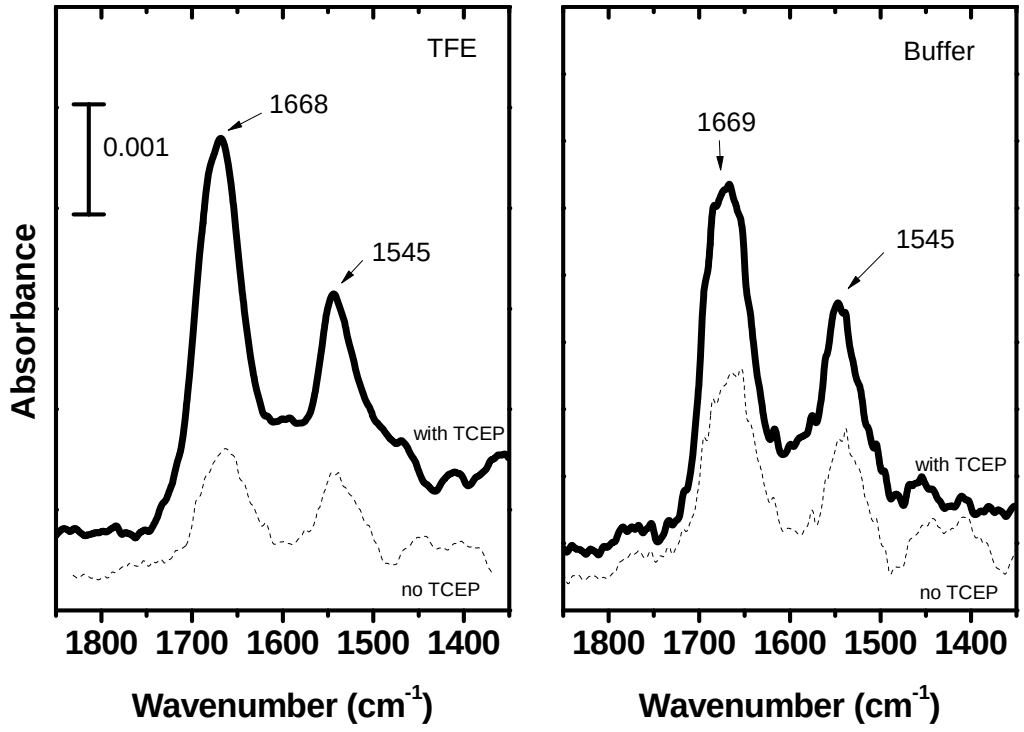

Figure 3-21: Amide vibration region of the RAIR spectra recorded for cecropin P1 immobilized with and without 25% TFE and 5 mM TCEP at a peptide solution concentration of 9.7 µM in pH 7.4 phosphate buffer. The dotted line spectra are those from Figure 3-18 and are shown for comparison.

XPS

XP spectra were recorded to identify the constituent atoms and to compare the relative surface densities via the carbon-gold ratios. The survey spectra are shown in Appendix A and the constituent carbon, nitrogen, and oxygen atoms can be clearly identified. Figure 3-22 shows the C1s and $Au4d^{5/2}$ regions of the XP multiplex spectra. The carbon-gold ratios for the reduced peptides are 3.00 with TFE and 2.44 without TFE. Under reducing conditions, the adsorption of both the solution α-helical and random coil peptides resulted in a larger carbon-gold ratio than all the other peptide solution conditions investigated. Clearly reducing the dimer peptides in solution prior to adsorption is having a significant effect on the surface density.

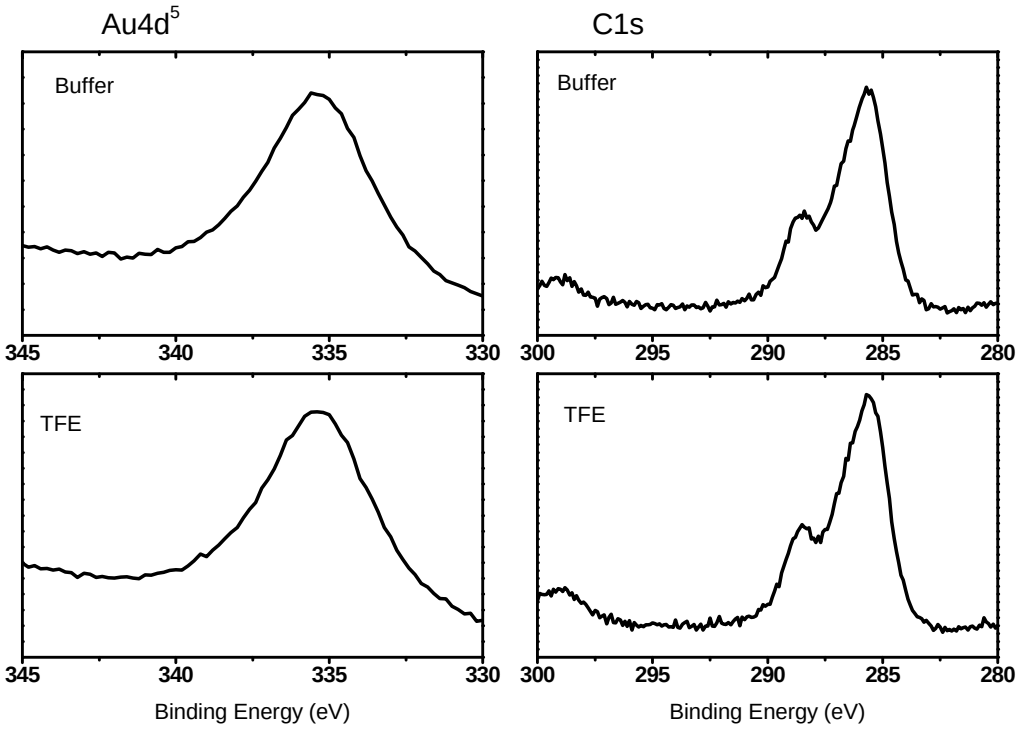

Figure 3-22: : XP spectra of the C1s and Au4d^5 regions for 9.7 µM CP1_c immobilized in pH 7.4 phosphate buffer with and without 25 percent TFE

Further evidence for increased surface density is shown in the sulfur region of the XP multiplex spectra. The S 2p region of the XP spectra for the peptide surfaces prepared with TCEP are shown in Figure 3-23 along with those prepared without TCEP with all other conditions equivalent. The spectra collected under reducing conditions have much larger sulfur signals than the spectra collected under non-reducing conditions. The results again agree with the XP survey and RAIR spectra which also showed evidence of a higher peptide surface density obtained under reducing conditions.

Thiol groups, as with hydroxyl moieties, are readily oxidized in atmosphere as well as by oxygen dissolved in aqueous solutions.[177] We observed a higher energy sulfur peak present in every sulfur region of the XP spectra. The lower energy thiolate-gold peak is found at 162 eV[178, 179] along with a shoulder at 164 eV. The shoulder peak can be attributed to free thiols,[180] which indicates that some of the peptide molecules have not covalently bonded to the gold. The peptides might be non-covalently bound to the gold through other interactions, as it is known that cationic peptides bind to gold substrates electrostatically via the interaction of the cationic lysine residues and the gold.[181, 182] In addition, we observe a significant peak at 167 eV, which is

characteristic of a higher oxidation state. The peak at 167 eV can be attributed to highly oxidized sulfur atoms found in a sulfate group, SO_3.[183] The sulfur atoms probably become oxidized due to reaction with oxygen dissolved in the buffer and from reaction with atmospheric oxygen. Even though oxidized sulfur was observed, the presence of the gold-thiolate photoelectron peaks clearly demonstrate the peptides do covalently bond to the gold surface.

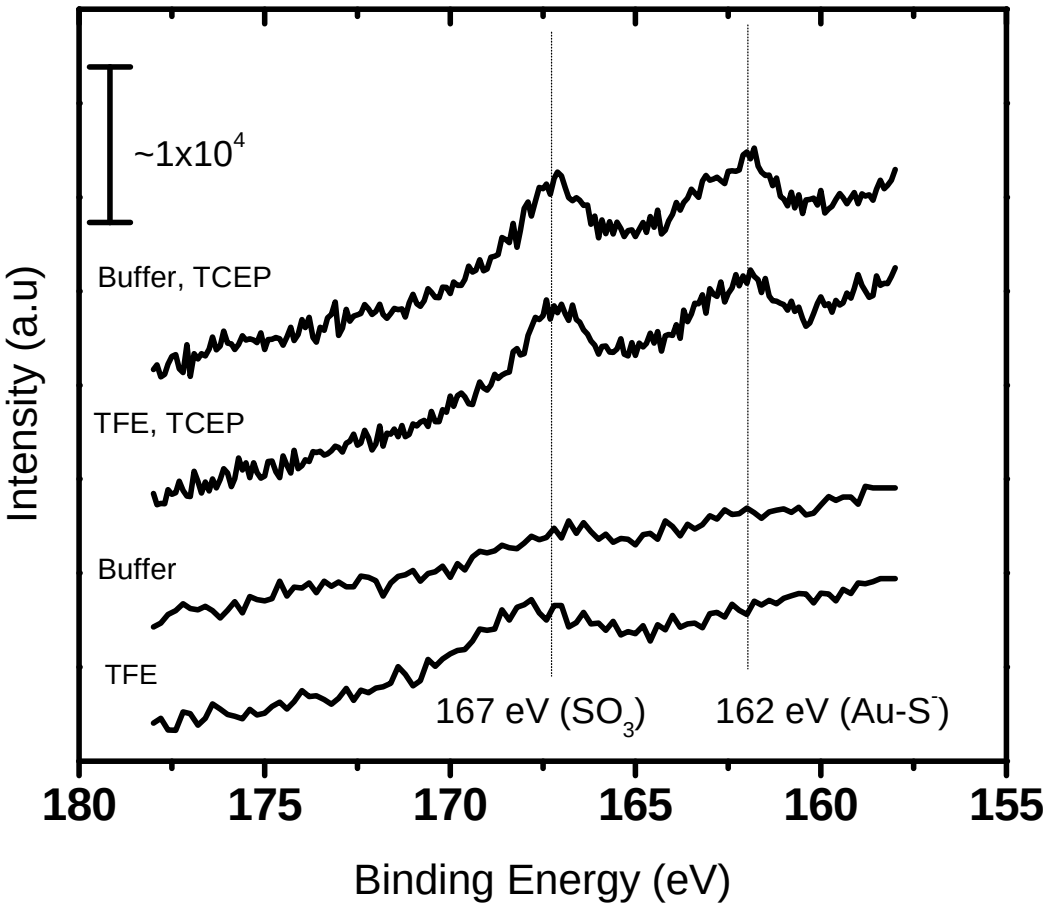

Figure 3-23: XP multiplex spectra of the S $2p^3$ region for cecropin P1 immobilized with and without TFE and TCEP in pH 7.4 phosphate buffer.[167]

Surface Plasmon Resonance

Surface plasmon resonance experiments were performed to obtain a quantitative measurement of the effects of TCEP on CP1_c adsorption to gold. We hypothesized that the conversion of peptide dimers into monomers would influence the adsorption rate as well as the

equilibrium peptide surface density. SPR experiments were performed under reducing conditions and non-reducing conditions via the addition of TCEP. The sensorgrams shown in Figure 3-24 are the difference between the sample (which contained peptide) and blank (which contained everything except peptide) experiments. The difference sensorgram eliminates the effects of non-specific binding from buffer constituents as well as the effects of bulk refractive index changes.

The sensorgrams are characterized by a very fast initial binding phase that occurs within the first 90 to 120 seconds. The non-reduced sensorgram then begins to level off with only a minor increase in response over the next 28 minutes. The reduced sensorgram response, on the other hand, continues to increase up to 200 seconds and also begins to level off. However, in contrast to the non-reduced sensorgram, the response continues to increase over the duration of the experiment. At the end of the experiment, the reduced sensorgram is still increasing as the slope has not yet plateaued, suggesting that adsorption continues after 30 minutes.

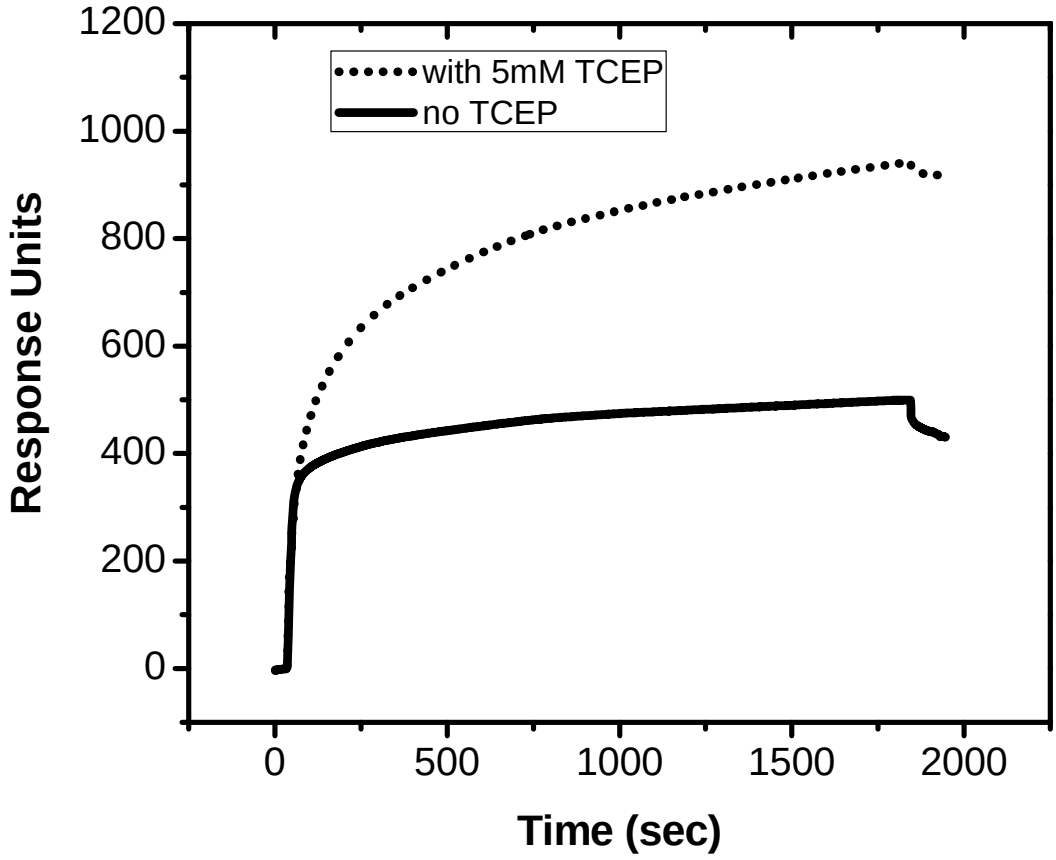

Figure 3-24: SPR sensorgrams for cecropin P1 immobilized with and without 5 mM TCEP in pH 7.4 phosphate buffer.

The response unit value of the sensorgrams is directly related to the surface density with one response unit equivalent to 1 pg/mm^2. The non-reduced sensorgram had a final RU value of 453 ± 8 and the reduced sensorgram was 814 ± 110 RU. These data most clearly demonstrates that the addition of TCEP to the peptide solutions results in a higher surface density. It is interesting to note that the RU value of the reduced samples had a much higher standard deviation than the non-reduced samples. This can be attributed to non-specific binding of the TCEP molecules to gold, a phenomenon that has been observed previously.[184]

3.4 Surface Structure of PGQ and the effect of solution secondary conformation

We followed our study of immobilized cecropin p1 by investigating the surface structure of the antimicrobial peptide, PGQ. Like cecropin P1, PGQ demonstrated binding selectivity for the pathogenic bacteria strain *E. coli O157:H7*.[23] However, the physical structure of PGQ is different that cecropin P1 as it is shorter (31 vs 24 residues), contains more non-polar residues (45 percent vs 35 percent) and fewer cationic residues (3 vs 5) than cecropin P1. We wanted to determine if PGQ adopted a similar surface structure after immobilization to gold, which would provide additional insight into the importance of surface structure on binding selectivity.

Two 13 μM 600 μL solutions of PGQ were prepared in pH 7.4 phosphate buffer. Twenty five percent TFE was prepared by adding 150 μL of neat TFE to 450 μL of buffer. Gold slides measuring one square centimeter were added to each solution. After 18-24 hours of immersion, the substrates were removed, rinsed with phosphate buffer (without TFE), deionized water, and dried with ultrahigh purity nitrogen. The samples were immediately analyzed via RAIRS, followed by XPS.

RAIRS

RAIR spectra were collected of PGQ_c immobilized to gold to determine the secondary structure and average orientation of the surface-bound peptides. The full RAIR spectra of

PGQ_c immobilized with and without 25 percent TFE are shown in Appendix A. The most important information from the RAIR spectra is found in the carbonyl stretching region near 1600 cm^{-1}, where the amide I and amide II modes are located. Figure 3-25 focuses on the amide mode region of the spectra.

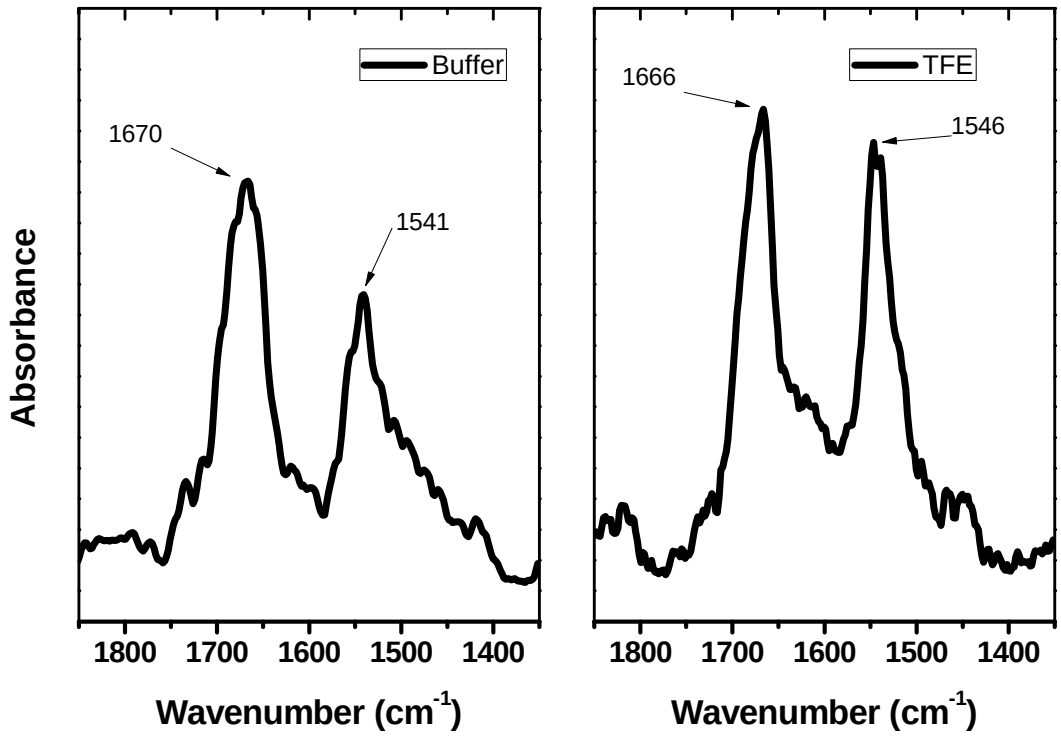

Figure 3-25: Amide region of the RAIR spectra collected for PGQ immobilized in pH 7.4 buffer with and without 25 percent TFE at a solution concentration of 13.0 µM.

The amide I mode of both spectra was centered near 1670 cm^{-1}, which, according to the literature, is characteristic of an α-helical peptide conformation.[143, 168, 185, 186] The intensity of both amide modes was slightly larger for the peptide solution with TFE, which suggests a slightly higher surface density. The ratios of the amide modes for each spectrum were slightly different; the spectrum recorded without TFE had an amide ratio of 1.39 and the spectrum recorded with TFE present had a ratio of 1.14. The ratios, according to equation 3-2, correspond to average tilt angles of 56.2 and 60.9°, respectively. For PGQ, the secondary structure in solution appears to have had little effect on the surface structure, as both systems were composed of highly titled α-helical peptides.

XPS

While RAIRS spectra can provide important information pertaining to the structure of the immobilized peptides, it cannot provide information about the identity and bonding of the constituent atoms that comprise the peptide molecules. X-ray photoelectron spectroscopy can be used to both identify and quantify different atomic species present on the surface. XP survey spectra were recorded for immobilized PGQ_c with and without 25 percent TFE and are shown in Appendix A. The characteristic carbon, nitrogen, and oxygen signals were detected. 3- 26 shows the C1s and Au $4d^5$ regions of the XP spectra, and by calculating the ratio of the integrated areas of the C1s and Au $4d^{5/2}$ signals, a qualitative peptide surface density can be determined. The spectrum recorded without TFE had a C1s:Au $4d^{5/2}$ ratio of 2.44 and the spectrum recorded with TFE had a ratio of 3.02. The larger ratio suggests that there is an increased amount of carbon, which is indicative of a larger surface density.

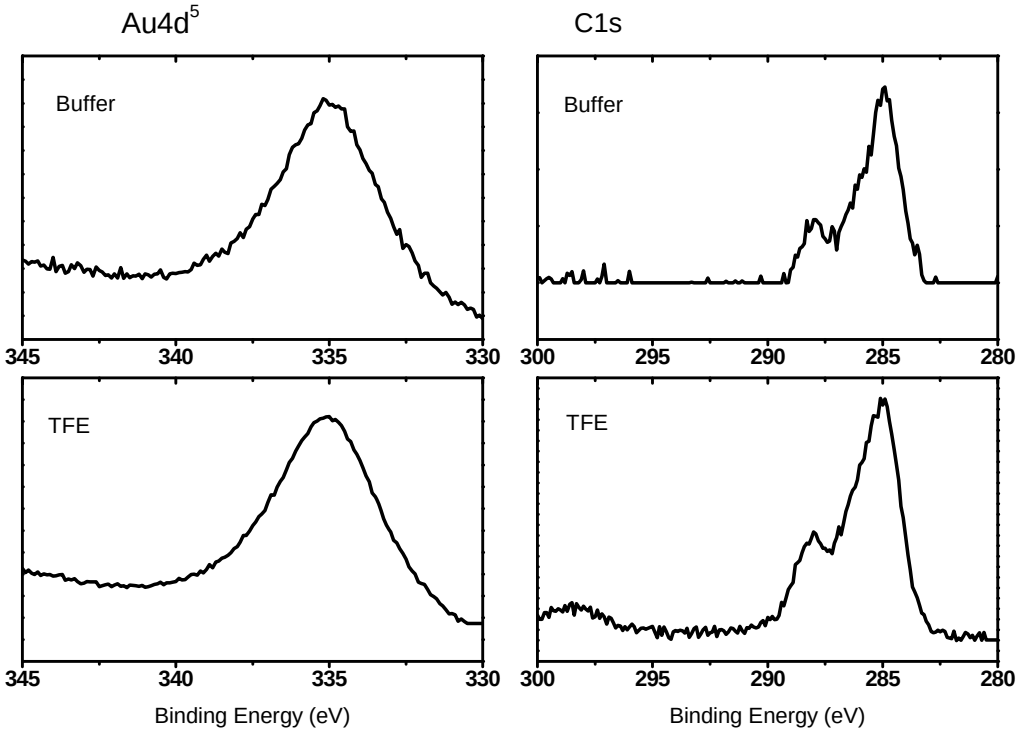

Figure 3-26: XP spectra of the C1s and Au$4d^5$ regions for 13.0 μM PGQ_c immobilized in pH 7.4 phosphate buffer with and without 25 percent TFE

The relative surface density of covalently bound thiol-containing molecules can be determined from the amount of sulfur detected via XPS. Figure 3-27 shows the sulfur $2p^3$ region of the multiplex XP spectra for PGQ with and without TFE. Clearly, the peaks for the spectrum with TFE are larger than those without TFE, which are indistinguishable from the noise. The sulfur XP data agrees with the other observations regarding the increased surface coverage because a higher amount of sulfur is the direct consequence of a higher peptide surface density.

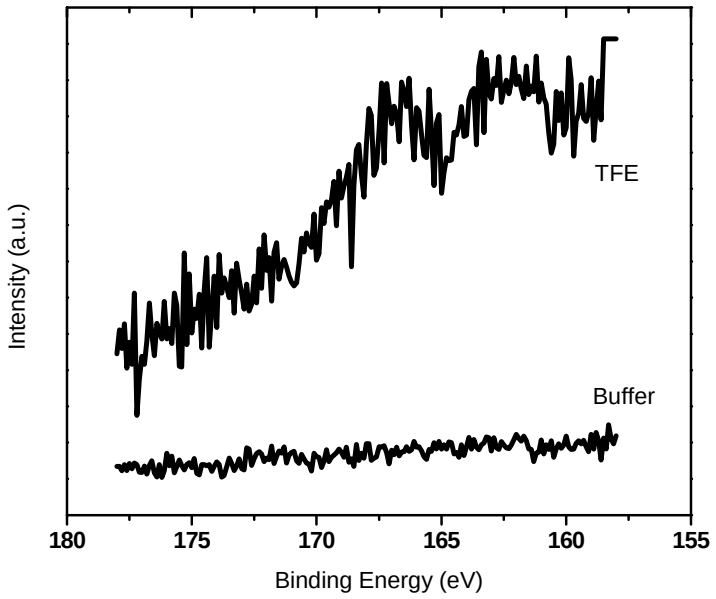

Figure 3-27: XP spectra of the S 2p region for 13.0 µM PGQ_c immobilized in pH 7.4 phosphate buffer with and without 25 percent TFE

From RAIR and XP spectra, the basic surface structure of covalently bonded cysteine-terminated PGQ on gold can be inferred. After removal from solution and drying with nitrogen, the peptides form a layer consisting of primarily highly titled α-helices, oriented parallel to the surface. The surface structures were very similar, regardless of the secondary structure in solution, which suggests that the TFE-induced α-helical structure in solution has little influence on surface orientation or secondary structure; however both RAIRS and XPS data suggest that the peptides immobilized in the presence of TFE had a slightly larger surface density. The observations agree with those of the cecropin P1 that the peptides immobilized in α-helical conformation, rather than random coil, form slightly denser surface layers.

3.5 Surface Structure of Pleurocidin and the effect of solution secondary conformation

We next turned our attention to the antimicrobial peptide, pleurocidin. In the whole cell binding assays performed by the Mello group, pleurocidin, along with PGQ and cecropin P1, were investigated for selective binding of pathogenic *E. coli O157:H7*. Unlike PGQ and cecropin P1, pleurocidin showed very little binding specificity, which might be caused by a different surface structure of immobilized pleurocidin relative to PGQ. Pleurocidin and PGQ have a nearly identical percentage of hydrophobic amino acid residues (44 and 45 percent, respectively), but differ in the number of cationic residues (7 and 3, respectively). We hypothesized that the larger number of cationic charges on pleurocidin may cause it to adopt a different surface structure than PGQ. The hypothesis was tested by recording both RAIR and XP spectra of cysteine-terminated pleurocidin to determine the surface structure.

Pleurocidin samples were prepared similarly to PGQ with one sample containing 25% TFE and the other only phosphate buffer at pH 7.4. The Pleurocidin concentration in each solution was 11.0 μL. RAIR and XP spectra were recorded by using the same parameters utilized for PGQ.

RAIRS

RAIR spectra were recorded for PL_c to help determine both the secondary structure and average orientation of the immobilized peptides. The full RAIR spectra of immobilized pleurocidin, recorded with and without 25 percent TFE, are shown in Appendix A. The most important structural information is found in the amide region near 1600 cm^{-1}, and that area of the spectra is shown in Figure 3-28.

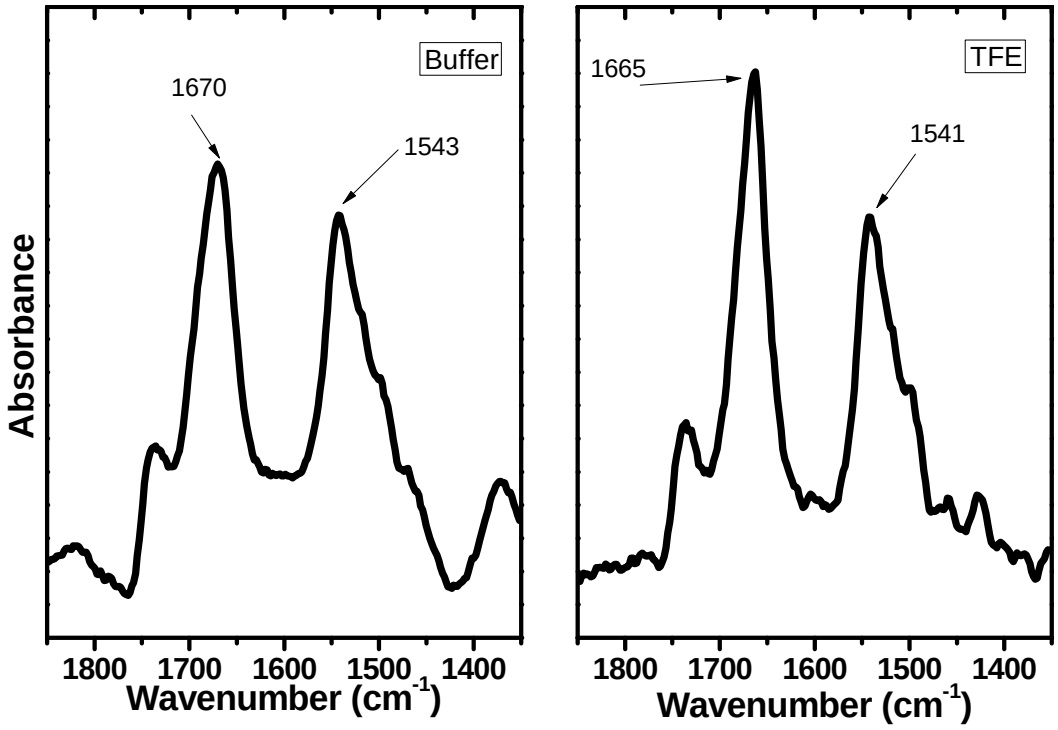

Figure 3-28: Amide region of the RAIR spectra collected for PL_c immobilized in pH 7.4 buffer with and without 25 percent TFE at a solution concentration of 11.0 μM.

The amide regions of the pleurocidin spectra are very similar to those of PGQ. Both spectra recorded with and without TFE have an amide I mode centered near 1670 cm^{-1}, which is again indicative of a mostly α-helical conformation of the immobilized peptides. The ratio of the amide I and II intensities are 1.12 for the non-TFE spectra and 1.55 for the with-TFE spectra, respectively. The average tilt angles, determined by using equation 3-2 were 61.34° non-TFE surface, and 53.65° for the with-TFE surface. The intensity of the amide modes on the TFE containing spectrum are larger (see Table 3-5) than those without TFE, suggesting a slightly higher surface density.

XPS

XP spectra were recorded for PL_c to again identify the constituent atoms of the peptide and to get a qualitative comparison the quantity of gold-thiolate bonding. The XP survey spectra of pleurocidin with and without 25 percent TFE are provided in Appendix A. The constituent atoms, carbon, nitrogen, and oxygen, were all detected. Figure 3-29 shows the C1s and $Au4d^{5/2}$ regions of the XP multiplex spectra, which were used to determine the relative surface densities. The C 1s:Au $4d^{5/2}$ ratio with TFE is 3.85 compared to 2.98 for the non-TFE spectrum. Figure 3-

30 shows the sulfur $2p^3$ region of both spectra, which revealed that the pleurocidin immobilized with TFE had a higher amount of sulfur. The larger sulfur signal suggests that the PL_c immobilized with TFE had a larger surface density.

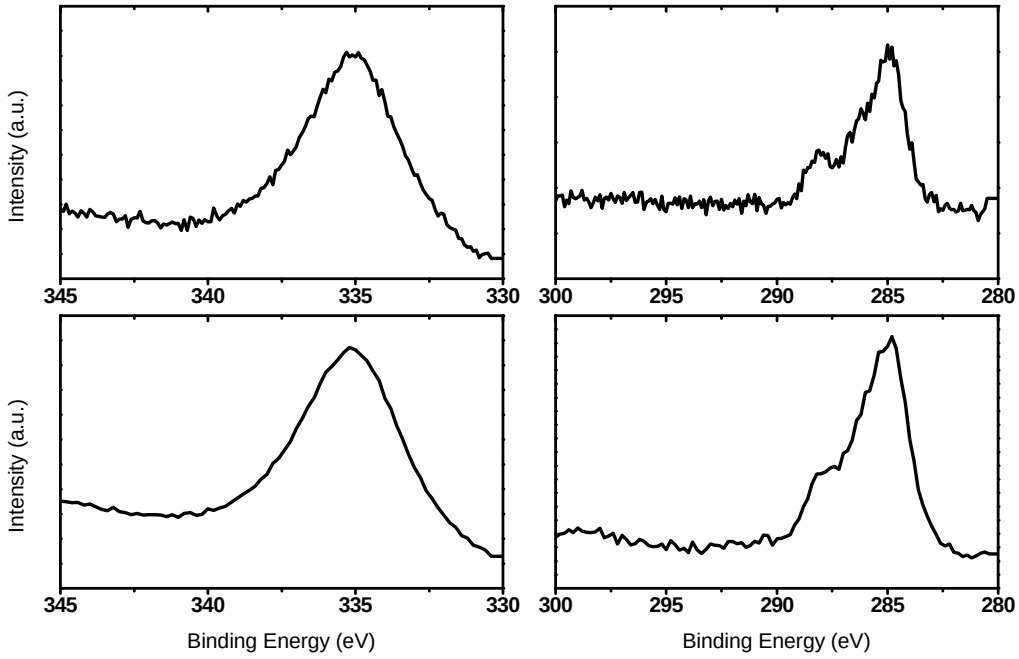

Figure 3-29: XP spectra of the C1s and Au4d[5] regions for 11.0 µM PL_c immobilized in pH 7.4 phosphate buffer with and without 25 percent TFE

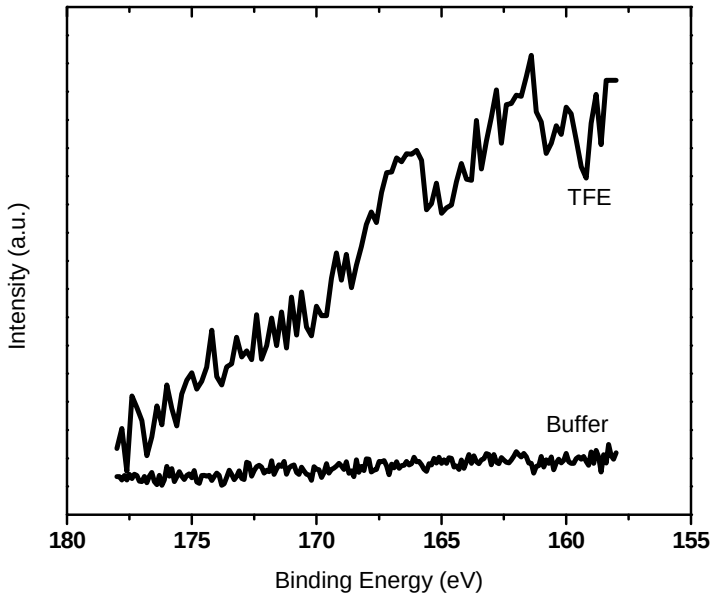

Figure 3-30: XP spectra of the S 2p region1 for 11.0 µM PL_c immobilized in pH 7.4 phosphate buffer with and without 25 percent TFE

The RAIR and XP spectra for the pleurocidin samples are very similar to those of PGQ, which suggests that pleurocidin adopts a similar surface structure, and is influenced by TFE in the same manner as PGQ. The immobilized PGQ molecules form a highly titled layer of α-helices on the gold surface, and the peptides adsorbed as α-helices in solution form a slightly denser layer on the surface. The similar surface structures of PGQ and pleurocidin disprove our hypothesis that the four additional cationic residues found on pleurocidin would affect the immobilized peptides. The conformation and average orientation adopted by the peptides appears to be independent of the primary structure of the peptides. As long as the peptides are amphipathic in nature, the number of non-polar or cationic residues does not affect the surface structure. We offer a more detailed discussion next of why the solution conditions and primary structures had little effect on the peptide immobilization.

3.6 Discussion of Antimicrobial Peptide Surface Structure, Orientation, and Conformation

The work described in this chapter is one part of an on-going collaboration with the Dr. Charlene Mello of the US Army Natick Soldier Center in an effort to develop biosensors containing antimicrobial peptide arrays. Our efforts focused on determining the surface structure of the immobilized antimicrobial peptides and the effects of solution conditions, and it serves as one of the first studies to investigate naturally occurring antimicrobial peptides. We investigated the surface structure three peptides, cecropin P1, pleurocidin, and PGQ, in effort to expand the information obtained from an earlier whole cell binding assay performed by the Mello group.[23] The three peptides form linear amphipathic α-helices in their active configuration, and differ in charge (CP1 +5, PL +7, PGQ +3) and hydrophobicity (CP1 35%, PL 44%, PGQ 45%). The native peptides were slightly modified via the addition of a terminal cysteine residue to promote binding to gold substrates through the thiol moiety on the cysteine residue. The modification was shown to have minimal effect on the solution structure of the peptides as compared to the non-modified peptides. Below, we review the key results and provide a discussion of how the primary and secondary structures of the peptides had the largest influence in their surface structure.

The peptides PGQ, Pleurocidin, and Cecropin P1 all exhibited similar surface structures when immobilized to gold at physiological pH. In aqueous buffer, the peptides exhibit a random

coiled secondary structure, which is characteristic of amphiphilic peptides because hydrogen bonding to polar solvent molecules is more favorable than intermolecular hydrogen bonding. When the peptides are folded in to α-helices, the non-polar amino acid residues are placed in close proximity to each other, which is an energetically unfavorable configuration. In order to overcome this barrier, the non-polar residues must have other intramolecular interactions that are more energetically favorable. Upon binding with a lipid-containing bacterial membrane, the peptides fold into α-helices because the non-polar residues interact with the lipid membrane while the polar residues interact with the polar constituents of the membrane as well as the polar solvent molecules. The introduction of a non-polar solvent, such as trifluoroethanol, to the peptide buffer can induce the peptides to fold into α-helices because of the favorable interactions between the non-polar residues and the non-polar trifluoroethanol molecules.

Cysteine-terminated PGQ, Pleurocidin, and Cecropin P1 were all adsorbed to gold substrates with and without trifluoroethanol present in the pH 7.4 phosphate buffer. The random coil and α-helical secondary structures of CP1_c in solution were confirmed by circular dichroism measurements and similar conformation changes for PGQ and Pleurocidin have been demonstrated previously in the literature.[187, 188] All three peptides exhibited similar secondary conformation and surface densities after immobilization to gold, irrespective of the secondary structure in solution. In all cases, based on assignment of the frequency of the amide I absorbance mode, the peptides were α-helical on the surfaces in atmosphere. Even when the peptides were immobilized as random coils, they folded into α-helices upon removal from the buffer. Without the non-polar solvent molecules present, intermolecular hydrogen bonding occurs, which drives the peptide conformational change. The conformational change driven by the removal of solvent has been observed previously.[189]

All of the peptides formed a random distribution of tilted α-helices on the surface. The calculated tilt angles were independent of solution secondary structure and were typically between 50 and 55° according to the molecular coordinate system described in Figure 3-5. However, almost all of the peptide films had a calculated amide intensity ratio between 1.5 and 2.0, which is characteristic of randomly oriented peptides as observed in bulk phases.[168-170] Based on the intensity of the amide I modes and the carbon-gold ratios as measured with XPS, the surfaces immobilized as α-helices in solution had slightly higher surface densities than did

the peptides immobilized as random coils. The α-helical peptides in solution are more compact and occupy less volume than do the random coil peptides. Because of their smaller volume, the helical peptides might be able to diffuse to the surface at a faster rate than the random coil peptides, and once immobilized, they occupy a smaller surface area per molecule. The combination of the two factors is most likely responsible for the observed slightly higher surface density for the peptides adsorbed as α-helices.

Peptide	Conc.	pH	TFE (%)	TCEP (mM)	Amide I (x 10^{-3})	Amide II (x 10^{-3})	Ratio	Tilt
CP1_c	9.7	7.4	0	0	1.64 ± 0.18	0.96 ± 0.16	1.79 ± 0.34	50.7 ± 4.2
CP1_c	9.7	7.4	25	0	1.44 ± 0.37	0.95 ± 0.18	1.52 ± 0.24	54.2 ± 3.8
CP1_c	9.7	7.4	0	5	2.75 ± 1.66	1.66 ± 0.18	1.66 ± 0.03	52.2 ± 0.3
CP1_c	9.7	7.4	25	5	3.34 ± 1.74	1.74 ± 0.52	1.95 ± 0.20	48.6 ± 2.2
CP1_c	29.1	7.4	0	0	1.65 ± 0.08	1.03 ± 0.06	1.60 ± 0.01	52.9 ± 0.2
CP1_c	29.1	7.4	25	0	2.07 ± 0.15	1.31 ± 0.09	1.59 ± 0.09	53.2 ± 1.3
CP1_c	9.7	9.2	0	0	1.57 ± 0.04	1.05 ± 0.01	1.49 ± 0.05	54.6 ± 0.9
CP1_c	9.7	9.2	25	0	1.44 ± 0.42	1.05 ± 0.27	1.52 ± 0.24	54.2 ± 3.8
CP1_c	9.7	11	0	0	1.63	1.00	1.63	51.69
CP1_c	9.7	11	25	0	1.92	1.12	1.71	51.37
CP1_c	9.7	11	0	5	2.00	1.17	1.71	51.37
CP1_c	9.7	11	25	5	1.85	1.23	1.5	54.25

Table 3-5: Summary table of the amide peak data from the RAIR spectra recorded under the various solution conditions.

Peptide	Conc.	pH	TFE (%)	TCEP (mM)	C: Au Ratio
CP1_c	9.7	7.4	0	0	1.40
CP1_c	9.7	7.4	25	0	1.42
CP1_c	9.7	9.2	0	0	1.73
CP1_c	9.7	9.2	25	0	1.66
CP1_c	29.1	7.4	0	0	1.57
CP1_c	29.1	7.4	25	0	1.94
CP1_c	9.7	7.4	0	5	2.44
CP1_c	9.7	7.4	25	5	3.00

Table 3-6: Summary table of the C1s:Au4d$^{5/2}$ ratios determined from XP multiplex spectra recorded under the various solution conditions

Cecropin P1 was chosen for a more detailed study into the effects of solution factors on surface structure. The effects of the solution concentration on the peptide structure were investigated by increasing the CP1_c concentration from 9.7 to 29.1 μM. The increased concentration of peptides led to surface structures similar to those observed at the lower concentration. Whether immobilized as random coils or α-helices, the peptides again formed a highly tilted layer on the gold surface. The amide I intensities were higher for both the random coil and α-helical spectra at the higher concentration relative to the corresponding lower concentration spectra, which is indicative of higher surface densities. The carbon-gold ratios determined from XPS supported the RAIRS data as both higher concentration ratios were larger than the corresponding low concentration ratios. In addition, at higher peptide solution concentration the RAIR and XP spectra data again suggested a slightly higher surface density for the α-helical peptides. The higher concentration of peptides in solution does appear to have a small effect on the adsorption rate, but despite the slightly larger surface density, the orientation of the peptides were still highly titled on the surface and independent of conformation in solution.

Circular dichroism measurements revealed that the solution pH influences the secondary structure of CP1_c in solution. At a basic pH of 9, the α-helicity was reduced by over 20 percent relative to physiological pH of 7.4 and the effect can be attributed to a disruption of the electrostatic interactions of the peptides with the environment. At physiological pH, the cecropin P1 helix contains five positively charged residues along the polar face. The formation of a stable α-helix requires a delicate balance between hydrophobic and electrostatic forces and the change in pH causes an imbalance of these forces. CP1_c was immobilized to gold using phosphate buffer at pH 9.2 and CAPS buffer at pH 11 to determine if the surface structure was affected by the disruption of the electrostatic forces felt by the peptides in solution. We hypothesized that the peptides may be able to create a denser layer on the surface if the cationic residues were fully or partially neutralized due to deprotonation of the ammonium groups on the lysine residues. The hypothesized charge reduction/elimination would diminish electrostatic repulsion of neighboring peptides and allow them to come into closer proximity.

The RAIR spectra recorded at basic pH were very similar to those recorded at physiological pH. The peptides again formed a highly tilted layer irrespective of conformation

in solution. The carbon-gold ratios determined via XPS, however, did not follow the same trend observed at physiological pH. At pH 9.2, the ratio for the α-helical peptides was only slightly larger than the random coil ratio, and at pH 11 the ratio was larger for the random coil peptides. While both the α-helical and random coil peptides formed highly titled layers on the gold, at higher pH the surface density was independent of the solution conformation. This is most likely caused by the fact that at higher pH the peptides do not fold into α-helices as effectively as at physiological pH. In essence, at substantially basic pH, the peptides are immobilized as random coils irrespective of the presence of TFE in the buffer. However, when the surfaces are removed from solution, the peptides fold into α-helices because hydrogen bonding with solvent molecules is no longer possible.

The effect of the oxidation state of the terminal cysteine residues of CP1_c on the surface structure was investigated by adding the disulfide specific reducing agent tris 2-(carboxylethyl) phosphine to the phosphate buffer. If oxidation is favorable, disulfide bonds can form between neighboring thiol moieties. The disulfide bond links two peptide molecules to form a dimer and the larger size of the dimer compared to the monomer can affect the adsorption kinetics and peptide diffusivity. The addition of TCEP to the peptide solution had a large effect on the peptide surface density. Both the solution random coil and α-helical peptides had higher surface densities as shown by RAIRS, XPS, and SPR. The α-helical peptides form a denser layer than the random coil peptides as evidenced by both the amide I mode intensities and carbon-gold ratios. The SPR sensorgrams provided the most convincing evidence of the increased surface density due to the reducing effects of the TCEP. The reduced peptides had an average surface density of 814 pg/mm^2 compared to the non-reduced peptides that had an average density of 453 pg/mm^2. However, even with a near 80 percent increase in surface density, the peptide layers formed under reducing conditions were highly tilted with an average tilt angle again near 50°. None of the solution conditions investigated here resulted in a close-packed vertical layer of peptides.

An important question stemming for the results presented is why did the peptides adopt a very similar surface structure independent of solution conditions? Cysteine-terminated PGQ, pleurocidin, and cecropin P1 all formed highly titled layers independent of secondary structure in solution, and the secondary structure of the immobilized peptides was always α-helical. The

cecropin P1 peptides also showed very similar surface structures independent of pH, solution concentration, or the presence of peptide dimers linked via a disulfide group. The only significant difference observed was an increased surface density when the disulfide-containing peptide dimers were reduced to monomers. The key to explaining the surface structures is the primary and secondary structures of the peptides.

As was explained above, the antimicrobial peptides contain, in addition to other types, both hydrophobic and cationic amino acids that occupy different faces of the α-helix. An important structural requirement of a well-ordered high density surface is that the immobilized molecules are packed tightly enough that intramolecular forces are felt. Favorable intramolecular forces, such as the van der Waals attractive forces that are shown to drive the organization of alkanethiol SAMs into a well ordered crystalline-like structure,[190] are necessary to form a well-ordered close-packed surface. When two antimicrobial α-helical peptides are in a vertical orientation and close enough for intramolecular forces to be important, the two distinct faces of the helix gives rise to three possible intramolecular interactions, shown schematically in Figure 3-31, and only one of them is favorable. First, the hydrophobic face can interact with the cationic polar face, which is an unfavorable interaction. Second, the cationic polar faces of two peptides can interact, but this is also unfavorable due to electrostatic repulsion at pH below the isoelectric point. The third interaction is from the close contact of two hydrophobic faces, which is favorable. Hydrophobic interactions have been used to form a peptide layer of close-packed all vertical helices, but those peptides were designed to contain *only* non-polar hydrophobic amino acids.[135, 148, 152] If present in α-helical conformation, close-packed amphipathic antimicrobial peptides cannot interact solely through hydrophobic interactions. If the hydrophobic face of one peptide is interacting with the hydrophobic face of another peptide, the opposite polar faces of the neighboring peptides cannot interact favorably with other close-packed peptides. The amphipathic nature of the peptides prevents them from being able to close pack on a surface, and without favorable interactions with nearby surface-bound peptides the molecules "lay down" on the surface. The peptides investigated in our study all adopted a highly titled arrangement of α-helices, which suggest that they were not close-packed.

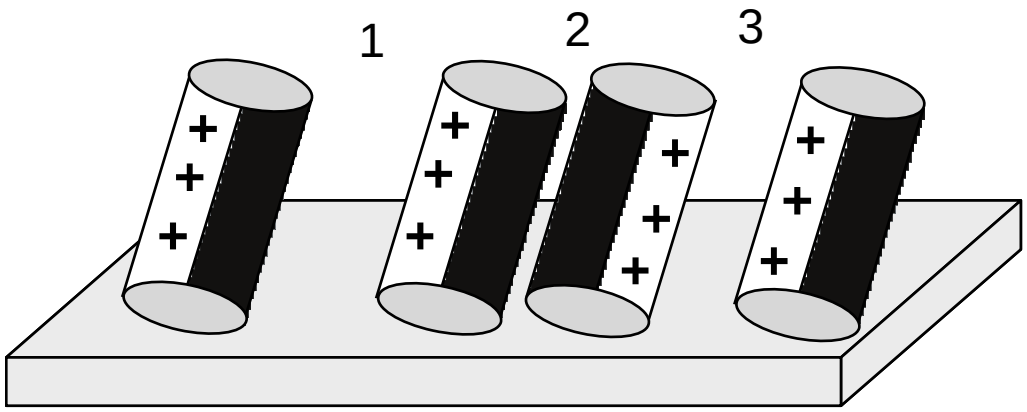

Figure 3-31: Schematic drawing of the possible intramolecular interactions of the immobilized peptides: 1) Hydrophobic-polar (non-favorable), 2) Hydrophobic-hydrophobic (favorable), 3) polar-polar (non-favorable due to electrostatic repulsion).

In addition to the peptide molecular structures preventing close-packing, there is a peptide-surface interaction that also promotes the formation of highly titled immobilized peptide layers. Cationic residues, such as glycine and lysine, have an affinity for gold and can direct the peptides to predominantly flat orientations in order to maximize the contact area between the gold surface and the polar face of the peptides. The pH of the peptide solution was increased to 11, which is above the isoelectric point of cecropin P1, using CAPS buffer in an attempt to deprotonate the cationic amino acids and diminish or even eliminate the influence of the cationic charges on surface structure. The basic pH, however, had little effect on the surface structure as the peptides were again highly titled and randomly packed on the surface regardless of secondary structure in solution. The minimal effects of the high pH can probably be attributed to the loss of helical content. Circular dichroism spectra showed an over 20 percent loss of helicity at pH 9.2, which is still below the pI of CP1_c. At pH 11 all the cationic residues are deprotonated, which should have a very significant effect on the ability of the peptides to fold into α-helices. With a diminished ability to form α-helices, the peptides adsorb to the gold as random coils regardless of the presence of TFE in the buffer. The immobilized random coil peptides do not close pack on the surface due to the lack of favorable intramolecular interactions. The high pH may eliminate electrostatic effects, but the peptides lose the ability to fold into α-helices in solution which prevents the ability to form a mostly vertical close-packed surface layer.

The majority of the solution conditions investigated, including pH, peptide concentration, and solution secondary conformation, had very little effect on the resulting peptide surface structure. Only minor differences in peptide surface density were. One final condition, the dimerization state of the peptides, was investigated and it did have a significant effect on binding characteristic of cecropin P1. The elimination of peptide dimers via the reduction of intramolecular disulfide bonds by introducing TCEP into the buffer led to a large increase in the surface density of the peptides, however even at an increased surface density the peptide layer was still highly tilted with respect to surface normal. While the same prohibitive intramolecular forces, such as electrostatic repulsion, exist for the peptides adsorbing as pure monomers, the SPR data provided quantitative surface density measurements which help demonstrate another reason the peptide layers were mostly horizontal. The non-reduced peptide had an average SPR response of 453 RU which is equivalent to 453 pg/mm^2 and a surface concentration of 0.0132 nmol/cm^2. The average radius of an α-helix is 2.3 Å and the length of per amino acid of an α-helical peptide is 1.5 Å. For cysteine-terminated CP1, the helix has dimensions of 4.6 Å diameter by 48 Å length. In a totally flat orientation, each helical peptide occupies a surface area of 2.21 nm^2. For a peptide layer with a surface concentration of 0.0132 nmol/cm^2, each peptide occupies a surface area of 12.53 nm^2 which puts the peptides too far away from each other to be close packed even in flat configuration. The reduced peptides formed a layer with surface density of 814 pg/mm^2, equivalent to a surface concentration of 0.0236 nmol/cm^2. Each peptide at that surface concentration occupies a surface area of 7.02 nm^2 which is over three times larger than the surface area of close-packed flat peptides. These calculations demonstrate that the immobilized peptides, even under reducing conditions, are spread too far apart on the surface to organize into a well-packed layer.

3.7 Conclusions and Future Work

Our work has demonstrated that the antimicrobial peptides PGQ, Pleurocidin, and Cecropin P1 immobilized on gold are α-helical and highly tilted relative to surface normal. The same average orientation and secondary conformation was observed for all the solution conditions investigated. The surface structures were determined for the peptides in atmosphere or a dry air environment, which is much different than the environment often found when the peptides interact with bacteria. The structure of the immobilized peptides *in solution* may be

much different than those observed out of solution. Another group at the University of Michigan that is part of our collaboration with the Mello Group, has performed some preliminary Sum Frequency Generation Spectroscopy (SFGS) experiments on the immobilized peptides. SFGS is a spectroscopic technique that can record the vibrational spectra of molecules at interfaces in the presence of bulk phases. The new results indicate that our hypothesis is correct: the structure of the immobilized peptides while in the aqueous buffer is different than what we have observed in air. Future experiments will continue to investigate the surface structures in solution.

In addition to studying the structure of the immobilized peptides in a liquid environment, other solution parameters such as ionic strength will be explored in future work. Earlier studies of *E. coli* binding to immobilized peptides showed a dependence on ionic strength,[23] but little is known about the effects on the surface structure. Perhaps an increased ionic strength in the peptide buffer may shield the effects of electrostatic repulsion and allow the α-helical peptides to pack closer at pH's below the pI. The amino acid sequence of the peptides might be changed to increase or decrease the number cationic groups or the helix may be extended away from the surface by introducing spacer glycine groups between the cysteine and first helix residue. The increased space from the gold substrate may eliminate the non-covalent interaction between the lysine groups and the gold surface.

Our work here has helped to initiate the study of immobilized antimicrobial peptide structure. Future experiments will help to increase our understanding of peptide adsorption to surfaces and might eventually allow for control over the surface structure. The ability to control peptide surface structure will have tremendous application for biosensing platforms such as discriminatory pathogen sensing or immunoassays.

Chapter 4

Design and Construction of an Ultrahigh Vacuum Surface Analysis Instrument with Triple Gas Dosing Capabilities

4.1 Background and Motivation

In this next part of our infrared spectroscopic based investigation of surfaces pertinent to chemical and biological warfare agent defense, we shift our focus to the study of chemical agents. The strategy currently used by the Army for chemical warfare agent decontamination uses vaporous hydrogen peroxide and chlorine dioxide to oxidize surface-bound agents. Studies exist demonstrating the efficacy of the oxidizing agents in solution,[25, 27, 191-193] however very few studies exist that explore surface chemistry that occurs when the vaporous decontamination formulas interact with both the warfare agents and the militarily-relevant substrates. The reaction products, both in the gas phase and remaining on the surface, are unknown, and the products maybe deleterious to both personal and sensitive equipment. Further understanding of the chemistry that occurs when an oxidizing gas interacts with both bare and simulant covered surfaces is necessary to develop the best and safest chemical warfare agent decontamination and protection strategies.

The study of fundamental chemistry that occurs in gas-surface reactions has two important stipulations that must be satisfied. First, the molecular structure of the surface prior to any reaction must be well characterized. Typically, the structure of the surface under investigation is controlled or chosen beforehand to contain desired properties. Self-assembled monolayers comprised of alkanethiols immobilized on gold substrates are used extensively to control surface structure, however many other techniques are available as well.[194] In addition to controlling the surface structure, the most important requirement for studying a gas-surface reaction is that the surface remains clean by careful control of the external environment. Maintaining a clean surface is not easy because of the incredibly fast adsorption process that is dependent on pressure. To study a gas-surface reaction *in situ*, proper conditions must exist so

that the time it takes for a monolayer to form is longer than the time of the experiment. A typical gas-surface reaction study requires many hours to complete, therefore experiments are performed in the ultrahigh vacuum pressure regime where the monolayer formation time is excess of 10,000 seconds.

Pressure (torr)	**Mean Free Path** (m)	**Gas Density** Molecules / m^3	**Monolayer Formation** (sec)
760	7.0E-08	2.0E+25	1.0E-08
1	5.0E-05	3.0E+22	1.0E-06
1.0E-03	5.0E-02	3.0E+19	1.0E-03
1.0E-06	5.0E+01	3.0E+16	1.0E+00
1.0E-10	5.0E+05	3.0E+12	1.0E+04

Table 4-1: Pressure ranges and the corresponding gas properties. The monolayer formation time assumes a sticking probability of unity.

In addition to monolayer formation time, the mean free path of gas molecules, which is the average distance a gas molecule travels before colliding with another gas molecule, is very important. It is also crucial that probe particles, such as ions and electrons, interact only with the surface of interest before reaching the detector. The largest mean free path should be larger than the dimensions of the analysis chamber, and for most chambers this requires pressures at least in the high vacuum regime. Obtaining a consistent pressure in the ultrahigh vacuum range is not a trivial endeavor and requires specialized equipment and instrument design. This chapter describes the design and construction of a new ultrahigh vacuum surface analysis instrument built in our lab that has the capability of directing up to three gases or vapors simultaneously to a surface of interest.

4.2 Description of the Triple Gas Dosing Surface Analysis Chamber

4.2.1 Overview of the Chamber Design

In designing the surface analysis chamber, we had four key goals in mind. Figure 4-1 shows a schematic of the general design of the surface analysis chamber and helps describe graphically how we accomplished our design goals. For the first goal, we needed the ability to control the sample position and temperature. This was accomplished by including a precision sample manipulator and mount containing both heating and cooling elements. Second, we

desired the ability to characterize the surfaces before, after, and during the reaction with gas phase species. We incorporated three analytical instruments into our design to accomplish the second goal. Reflection infrared spectroscopy is used to monitor the surface bound reaction products, mass spectrometry is used to monitor the desorbed gas phase reaction products, and X-ray photoelectron spectroscopy is used to acquire elemental analysis before and after the surface reactions. The third key goal was the ability to dose the surface with multiple gas phase reactants *simultaneously*. This was accomplished by including three capillary array dosers in addition to a precision gas leak valve. The fourth goal was the ability to transfer new samples into the UHV environment rapidly without the need to break vacuum. This was accomplished via the use of a load lock system which isolates the sample introduction chamber from the main chamber. In the following sections, each part of the chamber design is explained in greater detail.

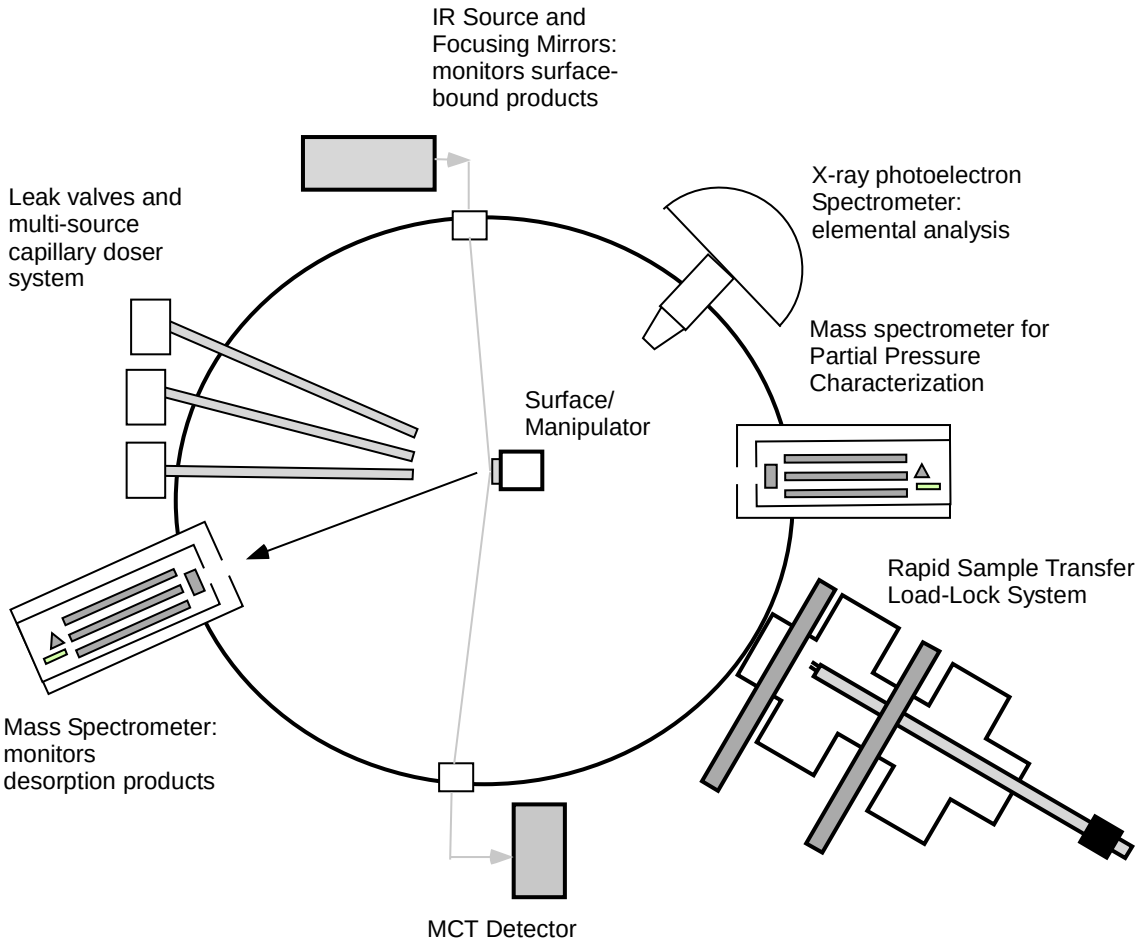

Figure 4-1: Schematic drawing highlighting the features and overall design of the new surface analysis chamber.

4.2.2 Chamber Construction

When designing an ultrahigh vacuum surface analysis chamber, careful attention must be paid to avoid possible leak sources. The chamber material must have a very small outgassing rate, and it must be mechanically strong enough to withstand the force of atmospheric pressure (14.7 pounds/inch^2). A common material with the desired properties is 304 stainless steel, which is what we selected for our chamber. After initial fabrication, the inner surfaces are electropolished to remove adsorbed species prior to the chamber being sealed and pumped down. Connecting the chamber to external components, like pumps and pressure gauges, is done using a ConFlat^{TM} seal. Each the two flanges to be connected are sharpened to a knife edge and a copper gasket is placed between the two knife edges. Bolting the two flanges together causes the knife edges to cut into the copper gasket creating a seal that can maintain pressures down to 10^{-12} Torr. The copper also "flows" to fill in small defects in the knife edge to further help seal the edges between two flanges.

The surface analysis chamber consists of three main components: the main chamber, the mass spectrometry chamber, and the load lock. The main chamber is composed of 1/8" 304 stainless steel cylindrical dome that contains 21 flanges of various sizes located along the surface. Figure 4-2 shows the locations of the various flanges and Table 4-2 describes the diameter and physical location of the flanges with respect to an azimuthal angle referenced to flange 1 and a polar angle referenced to a vertical surface normal.

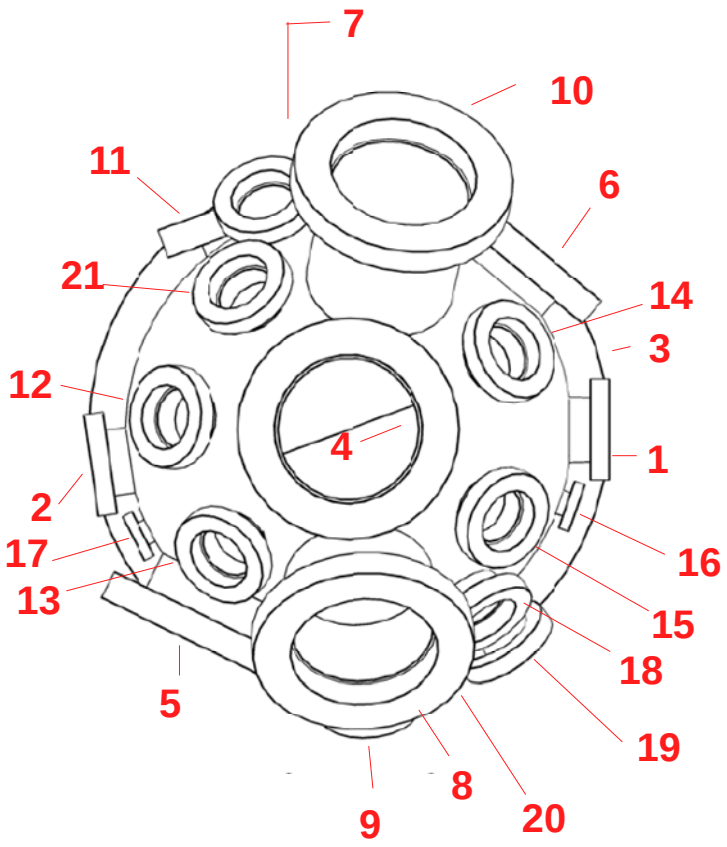

Figure 4-2: Schematic diagram of the top view of the main chamber showing the locations of the 21 flange ports. See Table 4-2 for flange sizes and locations.

Flange Number	Azimuth Angle	Polar Angle	Flange OD Inches	Focal Length Inches
1	0	90	2.75	7.00
2	188	90	2.75	7.00
3	0	180	14	9.50
4	0	0	6	7.00
5	244	90	8	7.00
6	50	90	6	7.00
7	110	90	6	6.78
8	274	45	6	8.50
9	274	122	2.75	9.00
10	78	45	6	10.00
11	110	45	2.75	9.50
12	176	45	2.75	7.00
13	225	45	2.75	7.00
14	26	45	2.75	7.00
15	330	45	2.75	7.00
16	341	90	1.33	6.50
17	207	90	1.33	6.50
18	290	90	2.75	7.00
19	306	114	2.75	8.00
20	306	66	2.75	7.00
21	127	45	2.75	7.00

Table 4-2: The size, location, and orientation of the 21 flanges of the surface analysis chamber.

4.2.3 Chamber Pressure Reduction: Vacuum Pump Selection

Obtaining pressures in the ultrahigh vacuum range requires a specialized pumping setup. Normally the chamber is initially "roughed out" using a mechanical or sorption pump that reduces the pressure from atmosphere (760 Torr) to approximately 10^{-4} Torr . At that point, the primary pump, which include diffusion, ion, cryogenic, titanium sublimator, and turbo molecular pumps, is initiated and used to obtain even lower pressures. On our chamber we use the latter tubromolecular pumps that are backed by mechanical roughing pumps. We have chosen magnetically-levitated turbo pumps because they offer high pumping speeds (2000 L/s), are extremely reliable, effectively pump all gases, can be operated in corrosive environments, have very low vibrations, are oil-free, can be mounted in many configurations, and are normally maintenance free for up to ten years.

The main turbo pump, attached beneath the chamber through flange number 3 in Figure 4-2, is a magnetically levitated HiMag® 2400 from Pfeiffer Vacuum that has a maximum pumping speed of 2000L/s. The turbo pump is backed by an oil-free scroll pump from Ulvac Vacuum (model DIS-250). The main turbo pump and the mechanical backing pump are separated by a pneumatic right angle valve (Kurt J. Lesker, Model SA0100PVQF) that is controlled via a custom written software program that will be described later. Pressure in the chamber is monitored with a Full Range Gauge from Pfeiffer Vacuum (model PKR 251). The full range gauge is a combination Pirani and cold cathode gauge that uses the Pirani gauge in the pressure range from atmosphere (760 Torr) to 10^{-4} Torr, and the cold cathode gauge at at pressures below 10^{-4} Torr . The pressure at the mechanical pump foreline is monitored with a pirani gauge.

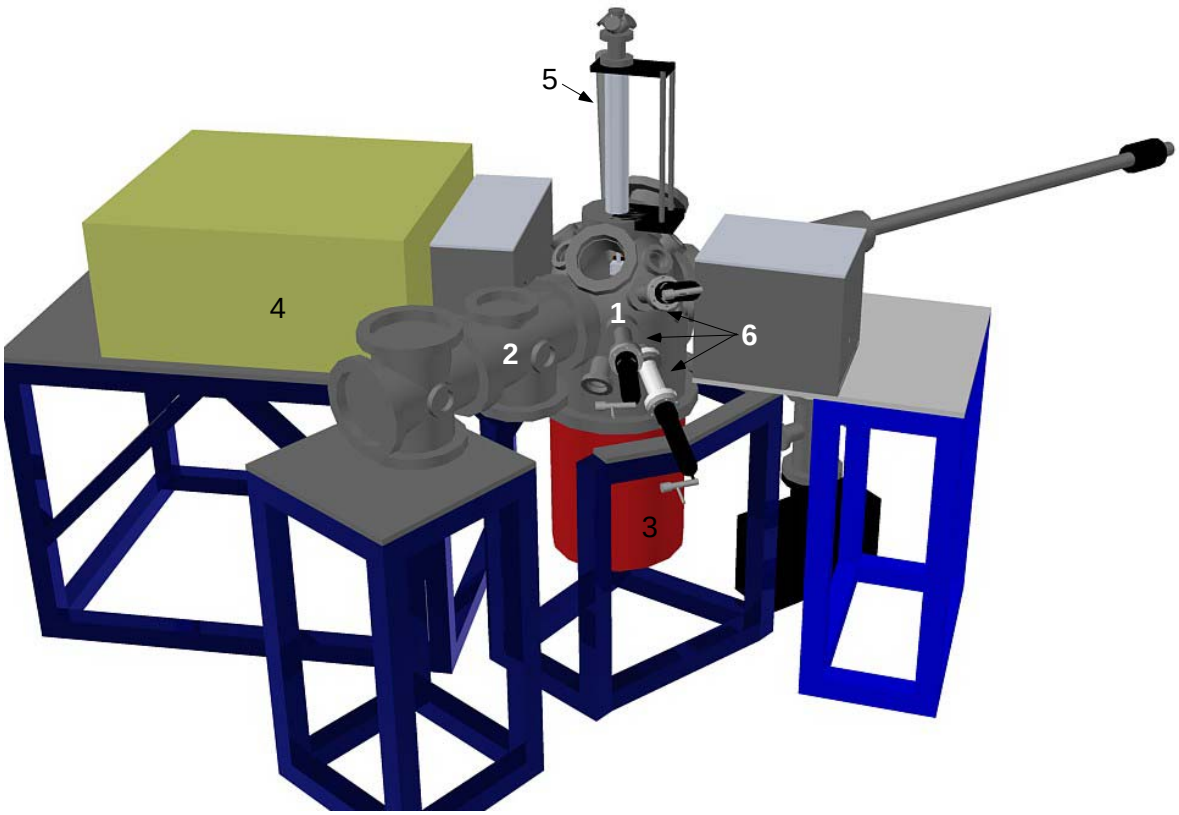

Figure 4-3: Schematic drawing of front view of the entire chamber setup. The following components are labeled: (1) Main chamber, (2) mass spec detector chamber, (3) main chamber turbo pump, (4) FTIR spectrometer, (5) sample manipulator, (6) capillary array dosers.

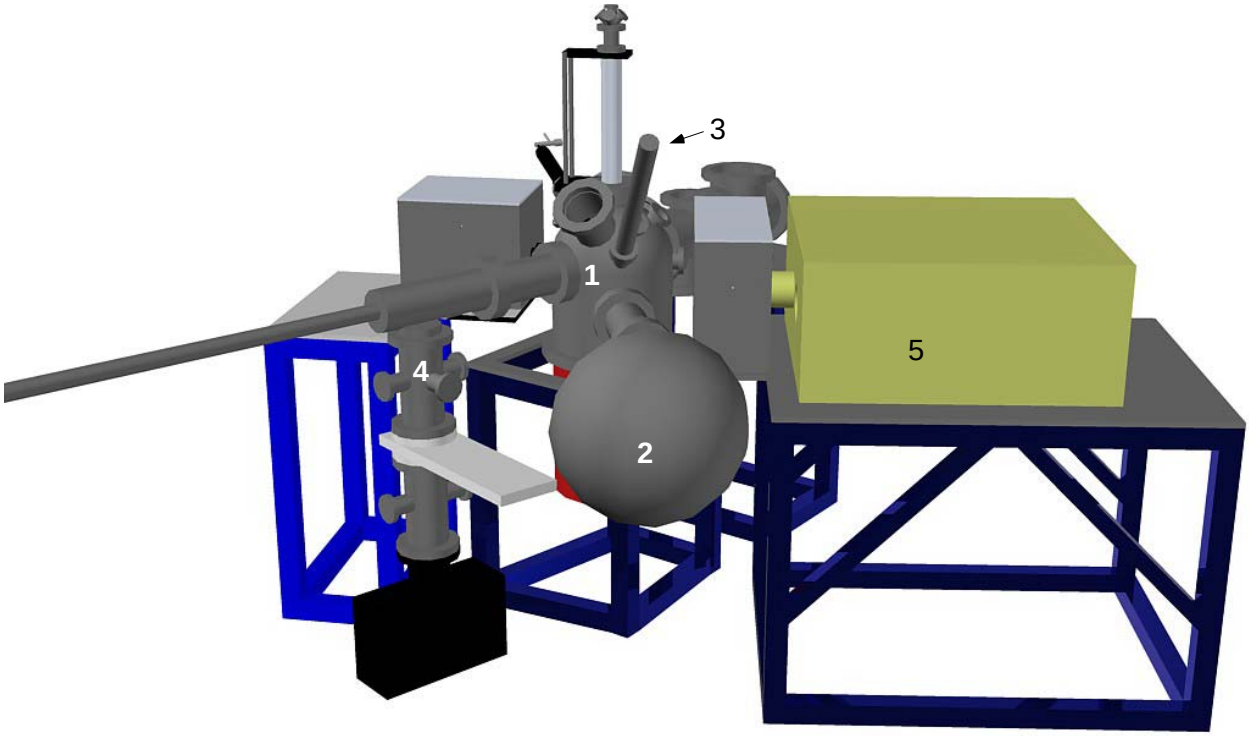

Figure 4-4: Schematic diagram of the back view of the entire chamber. The following components are labeled: (1) main chamber, (2) XPS hemispherical analyzer, (3) X-ray source, (4) load lock, (5) FTIR spectrometer.

4.2.4 Sample Position and Temperature Control

Proper positioning and alignment of the sample is of crucial importance when studying gas-surface reactions because the analytical instruments used to monitor the reactions require precise orientation. Our chamber contains a precision sample manipulator from McCallister Technical Services that allows for specific translation in the X, Y, and Z direction as well as rotation angle manipulation. The nearly 360° rotation capability stems from the differentially pumped seals that are connected separately to low and high vacuum parts of the chamber. The manipulator is attached to the top of the chamber at flange 4 (see Figure 4-2) and contains a custom five-flanged top hat that feed into a six-inch long bellows. A precision ground stainless steel rod that attaches into the chamber to secure the sample mount is attached to the upper 1

1/3” flange of the manipulator. The other four mini flanges in the top hat serve as feedthroughs for the various components needed for sample temperature control.

The test surfaces are secured to a multi-piece sample mount that is based on a similar design developed by a former member of our group, Larry Fiegland.[195] The setup of the sample stage assembly is shown in Figure 4-5. A copper block serves as the mounting piece of the stage and it is secured to the precision ground rod with a stainless steel clamp. The copper block has a ¾” diameter threaded mounting dock machined to one side. The main copper block was also designed to allow for a liquid nitrogen dewar and UHV button heater to be connected, which enables temperature control of the surfaces over a large range. The sample mount is secured to the copper block via the use of a linear/rotary precision magnetic manipulator (Transfer Engineering and Manufacturing, Inc., model DBLRP). Attached to the magnetic manipulator is a transfer key that is designed to maintain a tight connection with the sample mount until it is firmly secured to the stage. A diagram of the transfer key along with the sample mount are shown in Figure 4-6, which demonstrates the locking mechanism. The posts on the sample mount only fit into the transfer key in one orientation. When the transfer key is rotated, the bolt heads of the sample mount posts cannot be removed which ensures the security of the mount.

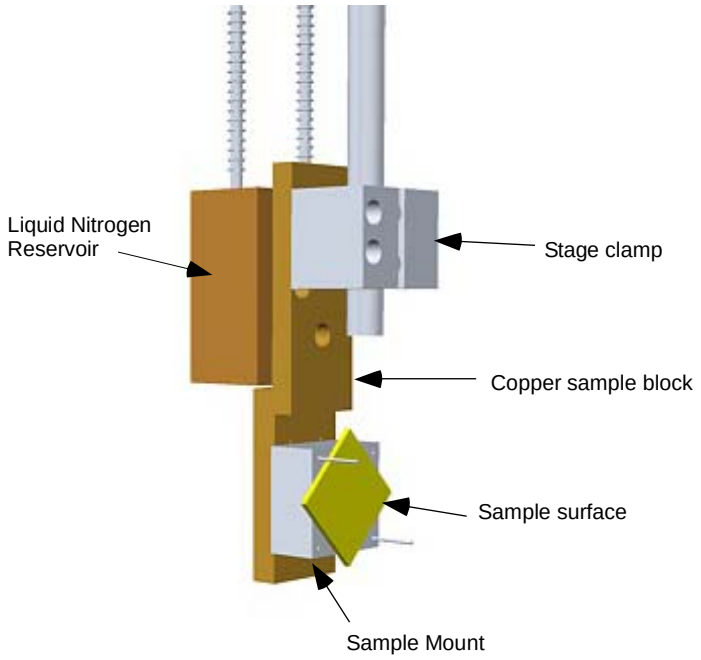

Figure 4-5: A CAD drawing of the sample mount setup. The sample mount is secured to the copper sample block by screwing it on to a threaded knob.

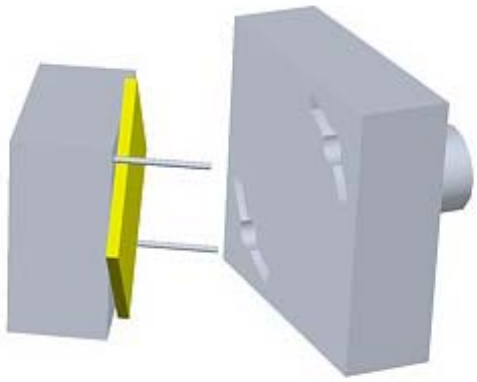

Figure 4-6: A CAD drawing of the sample mount and transfer key. The posts of the mount fit into the holes on the transfer key. When the key is rotated, the sample mount is locked in place.

4.2.5 Sample Introduction: Load Lock Chamber

When operating an ultrahigh vacuum chamber, it is of crucial importance that the UHV pressure level be constantly maintained. Many surface samples are prepared in atmosphere and any attempt to transfer the samples directly into the UHV chamber would cause catostrophic damage to the chamber and the turbo pumps. In addition, if the installation of a new sample required a total chamber vent each time, it would take an unacceptable amount of time to reach the UHV pressure range ($<10^{-9}$ Torr). In order to facilitate fast, safe transfer of samples from atmosphere into the UHV chamber, a load lock system is employed. The UHV chamber is isolated from the load lock using a manual 6" gate valve from Kurt J.Lesker (model SG0400MCCF) and the pressure in the load lock is maintained at 10^{-7} Torr via the use of a 60 L/s ion pump from Duniway Stockroom (rebuilt Varian model 911-5034). To introduce a sample from atmosphere, the ion pump is first isolated by closing a 2 ¾ inch pnematic gate valve from Kurt J. Lesker (model SG0150PCCF). The load lock is then vented to atmospheric pressure with house nitrogen after which the load lock door can be opened followed by sample introduction. After securing the sample and closing the load lock door, the chamber is initally evacuated using a liquid nitrogen cooled molecular sorption pump. Pressure in the load lock is monitored using a Full Range Gauge from Pfeiffer Vacuum, and once the pressure has reached 10^{-4} Torr, the 2 ¾ inch pneumatic gate valve is opened to the ion pump on the high vacuum side of the load lock. The sorption pump is then isolated from the load lock by closing a pneumatic right angle valve

(Kurt J. Lesker Model SA0100PVQF) and the entire load lock is further evacuated by the ion pump. When the load lock pressure has reaced 5 x 10^{-7} Torr , the manual gate valve is opened slowly and the sample is transferred into the chamber as described earlier. When the gate valve is opened, the pressure in the main chamber typically rises to 1 x 10^{-8} Torr. After sample transfer, the transer arm is withdrawn and the manual gate valve is closed.

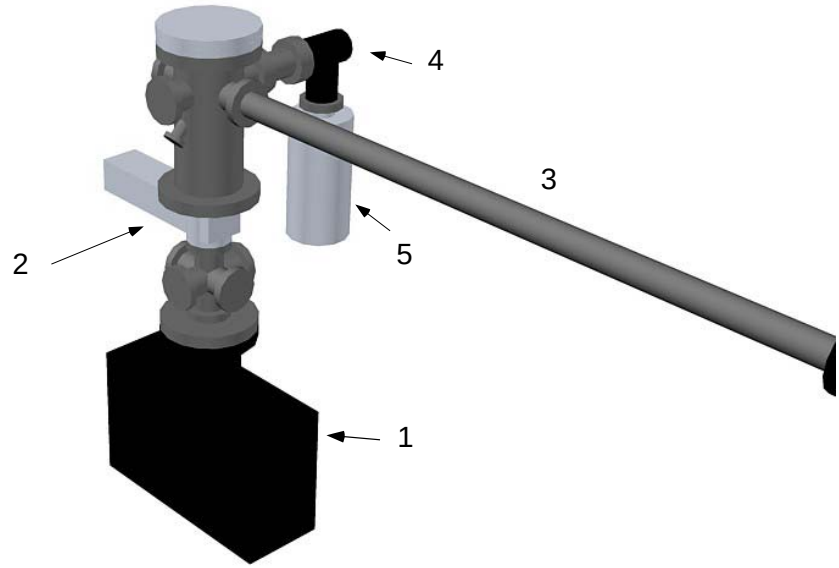

Figure 4-7: Schematic diagram of the load lock setup. The following components are labeled: (1) ion pump, (2) 2 ¾ inch pneumatic gate valve, (3) transfer arm, (4) pneumatic right angle valve, (5) sorption pump

4.2.6 Gas Phase Reactant Introduction

The reactant gases are introduced into the chamber using two different effusive methods, where effusion is defined as the emergence of a gas from a small hole. The first method uses a variable saphire-plate precision leak valve from Duniway Stockroom (model VLVE-1000) that

allows for gas leak rates down to 10^{-10} Torr L/s. The leak valve is located at flange 15 and is heated with heat tape controlled with a Variac unit to ensure low vapor pressure liquid samples properly volitalized. The second gas effusion method uses a custom capillary array doser.[195] The most important advantage of our chamber is that it allows for the simultaneous use of three capillary array dosers which are located at flages 18, 19, and 20 (see Figure 4-2). The dosers can be used to control the flux of reactant gas molecules at the surface.

The capilary array doser design was based off the work of Zhukov[196] and Yates,[197] and a schematic is shown in Figure 4-8.[198] The doser contains a Pyrex capillary with an internal diameter of 0.08 mm and a total length of 20 mm. When dosing, the high pressure side of the doser can be controlled by opening a teflon-sealed glass valve; typically the pressure is near 50 Torr. The doser is connected to the chamber with a glass-to-stainless steel ConFlat flange. The end of the doser contains a baffle plate which randomizes the motions of the gas molecules before they escape through a glass array containing 120 holes 0.5 mm in diameter. The baffle ensures that the gas molecules leave the doser in a uniform directed flux which allows for calculation of the number of reactant molecules contacting the surface.

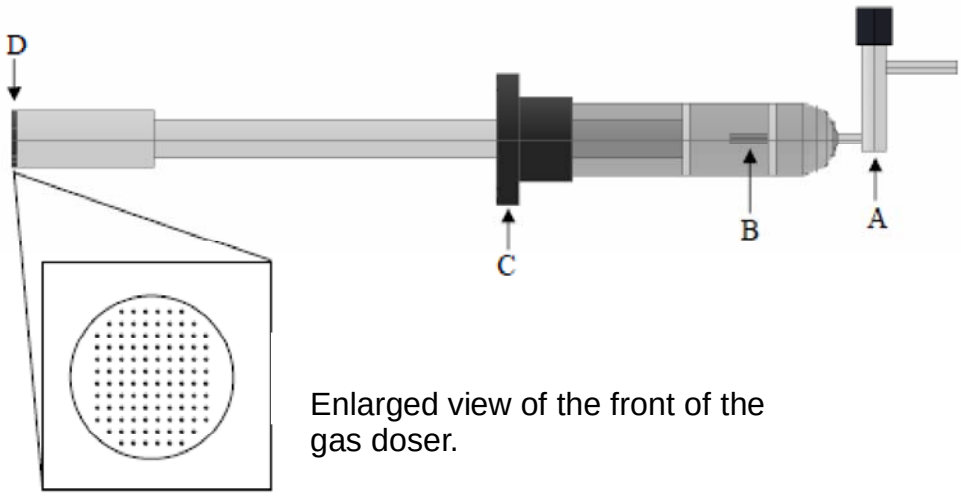

Figure 4-8: Schematic drawing of the capillary array dosers. The following components are located at (A) Teflon-sealed glass valve, (B) 0.08 mm diameter glass capillary (C) 2.75" conflate flange with glass-to-metal seal, (D) glass doser head containing the 120 hole array, which is shown in detail in the inset.

4.2.7 Chlorine Dioxide Generation

The oxidizing gases that comprise the decontamination formulas are highly reactive and potentially unstable, and storage of concentrated hydrogen peroxide and chlorine dioxide is dangerous because the gases can be explosive if stored under pressure. Because of this, the compounds are never shipped and the reagents are always made on-site. A large number of strategies have been investigated for chlorine dioxide generation, however many of them are suited for large scale industrial applications.[199] One of the first objectives in our study of the decontamination of surface-bound CWA simulants was to develop a safe, easy, and reproducible method of generating chlorine dioxide.

The method we employed to generate vaporous ClO_2 was originally revealed in US patent 4,292,292. The reaction is a simple acidification of aqueous sodium chlorite as shown below:

$$5NaClO_2 + 4\ HCl \rightarrow ClO_2 + 5NaCl + 2H_2O$$

Typically a 15% molar excess of HCl is used and the reaction requires approximately 30 minutes to reach completion. A significant benefit of the selected procedure is that the reaction bi-products are non hazardous and easy to dispose.

With a simple procedure in hand to generate the ClO_2, the next step was developing a way to introduce the reactive gas into the chamber where it could interact with the surface of interest. A modified glass gas bubbler was designed and constructed in order to facilitate the generation of ClO_2, and a schematic drawing of the modified bubbler is shown in Figure 4-9. The primary modification is the addition of a port and glass straw that reaches the bottom of the bubbler. The ClO_2 generation is started by placing 3-5 milliliters of a 0.1-2.0 M aqueous solution of $NaClO_2$ in the bottom of the bubbler. The system is then evacuated and purged with ultrahigh purity nitrogen. 0.1-1.0 mL of 1-10 M HCl is then added to the $NaClO_2$ by syringe injection through a rubber septum placed on the glass port, labeled HCl in Figure 4-9. The reaction begins immediately when the first drop of HCl hits the solution and the reaction progress can be monitored by observing the color of the solution. The $NaClO_2$ is colorless but ClO_2 is a yellow-greenish color. When the gas is dissolved, the solution turns yellow to brown, depending on the concentration. The concentration of ClO_2 in the gas phase can be controlled via temperature due

to solubility, because below 10 °C, ClO_2 is completely soluble in water and over 10 times more soluble than chlorine. The dissolved ClO_2 is also very stable, as it undergoes hydrolysis 7 to 10 million times slower than chlorine gas. The gas can then be desolvated by increasing the temperature via the use of a water circulation bath. The evolved gas is then directed to the chamber by the flow of the nitrogen carrier gas through Teflon tubing and into the glass capillary array doser described in Chapter 4.

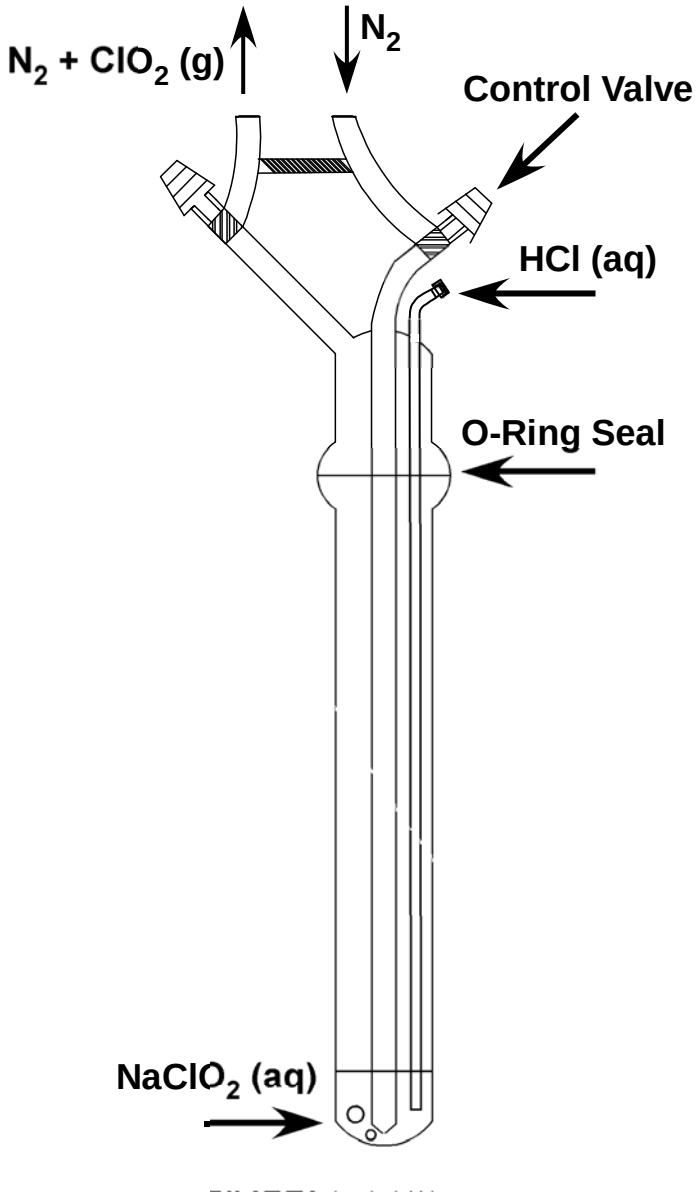

Figure 4-9: A schematic diagram of the modified gas bubbler used for to generate and introduce chlorine dioxide vapor into the surface analysis chamber.

4.2.8 Analytical Instrumentation

The ability to monitor gas-surface reactions performed in ultrahigh vacuum requires that various analtyical instruments are interfaced with the chamber. Our instrument is interfaced with an FTIR spectrometer, a mass spectrometer, and an X-ray photoelectron spectrometer which enables us to gather complimentary data before, during, and after the gas-surface reactions. This section describes each instrument and how it is interfaced with the UHV chamber.

The chamber is interfaced with a dry air purged Nicolet Nexus 670 Fourier Transform Infrared Spectrometer via two nitrogen-purged aluminum mirror optics enclosures. Figure 4-10 shows a schematic diagram that outlines the path of the IR light through the chamber. The infrared light exits the spectrometer and is reflected off a gold-coated flat mirror (Bruker Optics IM190-GH) towards a gold-coated parabolic focusing mirror (Bruker Optics IM137-GH, focal length 250 mm). The parabolic mirror focuses the light through a differentially pumped potassium bromide window located at flange 2, towards the surface where it reflects at precisely 86° towards another KBr window located at flange 1. After passing through the window, the diverging IR light reflects from another focusing mirror (Bruker Optics IM137-GH, focal length 250 mm) that directs the light towards another 90° flat mirror (Bruker Optics IM190-GH). The flat mirror directs the light towards one final focusing mirror (Bruker Optics IM151-GH ,focal length 69 mm) that focuses the light into the mecury cadmium telluride (MCT-A) detector.

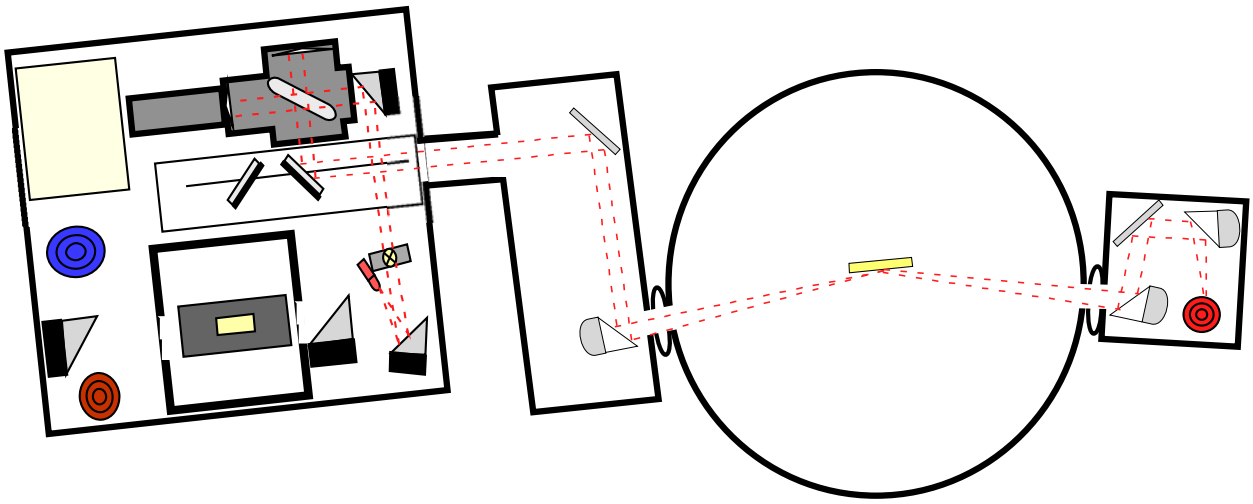

Figure 4-10: Schematic drawing of the infrared light path originating in the Nexus 670 FTIR and ending at the external MCT-A detector.

The mass spectrometer is an ABB Extrel (model: MEXM 1000) from EXTREL and has a 2-1000 amu range with 1 amu resolution. Maintaining pressures lower than 10^{-7} Torr is crucial when operating the mass spectrometer to minimize the interference of background gases when monitoring products from a particular gas-surface reaction. To ensure that the low pressure is constantly maintained, the mass spectrometer analyzer is housed in a doubly-differentially pumped chamber located separate from the chamber (flange 5). The first stage of the mass spec chamber is pumped by a 200 L/s turbo pump and the second stage by a 400 L/s turbo pump, both from Pfeiffer Vacuum (models TMH 200M and TMH 400M, resepectively). Both turbo pumps are backed by a mechanical pump from Garver Vacuum (model 1101006401). As with the main chamber turbo pump, the mass spec turbos are separated from the mechanical pump foreline by a pnematic right angle valve (Kurt J. Lesker, model SA0100PVQF). The detector chamber stages are separated from each other and from the main chamber by apertures that control the flux of gas molecules which, in turn, limits the pressure. The main chamber and first detector stage are separated by a 4.7 mm aperture and the first stage and second detector stage are separated by a 4.3 mm aperture. The presure in the dector chamber is monitored with a cold cathode gauge from Pfeiffer Vacuum.

Unlike infrared and mass spectrometry, X-ray photoelectron specroscopy is not typically performed *in situ*. Because of this, we designed our chamber to include a second focal point, used only for XPS, positioned away from the gas doser focal points. The second focal point is located exactly four inches below the primary focal point. The sample is rotated 66° clockwise and lowered with the precision maniuplator where the surface rests only 0.25 inches from the tip of the X-ray source. The X-ray source, detector, and electronics are part of a 5400 system from Phi. The X-ray source, positioned at flange number 7, is a dual source Mg/Al anode (model 04-500). The ejected photolelectrons are detected in a 30 cm diameter hemispherical energy analyzer (model 10-360) located at flange 11.

4.2.9 Ultrahigh Vacuum Interlock Program

The operation of an ultrahigh vacuum system requires that system is constantly safe from events that may cause catostrophic damage. A very significant problem that can occur is if

power is suddenly interupted and both the turbo and backing mechanical pumps shut down. In this situation, a pressure gradient exisits between the ultrahigh and low vacuum regions of the two pumps. The pressure will naturally try to equalize by flowing from the high pressure area to the low pressure area, and the problem herein stems from the fact that mechanical pumps use oil as a lubicant. If the pressure suddenly tries to equalize, the flow from high to low pressure areas will bring the pump oil along with it which will contaminate the ultrahigh vacuum chamber. In order to guard against such castrophic events as well as to allow for control over the entire UHV chamber with one computer system, an interlock system was designed and built for the instrument.

The interlock system is a home-written computer program that monitors the pressure at the various locations of the chamber and compares them to preset set points. If satisfactory pressure conditions are not met, through a series of home built electronics, the program instructs the pneumatic gate valves to close and the turbo pumps to shut down. This section describes the entire inlerlock program design, including the interlock relay electronics, the pressure gauge electronics, and the interlock program that runs the system.

Interlock Program and Electronics

The interlock program was created with Lab View Software, Version 8.2, available from National Instruments. The software uses a graphical programming language called *G* that greatly simplifies the necessary code writing for creating programs. The program communicates with a series of Field Point relays that are stationed in the interlock electronics box though a 15 pin serial cable. The FP relays contain a master relay (National Instruments: model FP-RLY-420) that sends and receives signals from the sub relays, each of which contain eight indidual circuits. Our system has three sub relays, therefore with our setup we have the capability to control up to 24 sepearate devices. Each of the twenty four relays are assigned a communication channel within the Interlock Lab View program. For example, the pneumatic right angle valve separating the main turbo pump and the foreline is assigned to relay position 1. The open or closed status of the valve is determined by the open or closed status of the relay in position 1. When the interlock program determines that potentially dangerous conditions exist, such as loss of power or unacceptable pressures, the relay receives a signal to open which in turn closes the pneumatic

right angle valve. The entire logic of the interlock program will be explained in more detail below.

The interlock electronics unit consits of a series of 20 relays interfaced with the Field Point relay circuits that supply 110 VAC to a plug located at the back of the box. Each relay is controlled by a three-position manual switch located at the front of the box that allows for each circuit to be turned on, off, or set to allow for computer control via Field Point. If the switch is set to on or off, the commands sent from the computer are ignored. The logic of one of the twenty circuits is shown in Figure 4-11. The interlock box is connected to standard a 110 VAC power supply. After passing through a 20 amp fuse, the current flows through a momentary switch. This switch is connected to a latching relay that closes only when the momentary switch is depressed. With this setup, in case of total power failure, the electronics can only be restarted manually which allows the user to ensure that all appropriate set points and chamber conditions are satisfied before resuming operation.

If the latching relay is closed, the AC current is supplied to 20 three-position switches in parallel and an AC-DC converter power supply. The converter changes the voltage from 110 VAC to 30 VDC, which is used to power the Field Point relays as well as the indicator LED's located above the three-position switches on the outside of the electronics unit. The three-position switches are each connected to a mechanical relay that is designed to close if 110 VAC is supplied. If the three-way switch is in the on position or in the computer controlled position, and the Field Point is relaying an 'on' signal, the mechanical relay switches to the closed position, which routs 110 VAC to the associated plug as well as 30 VDC throuh a 22 kΩ resistor to a 5 V DC green LED. If the mechanical relay is open, 110 VAC is not sent to the plug and the 30 VDC is sent to a red LED. The 110 VAC plugs are used to control the pneumatic gate and right angle valves located at varioius positions of the chamber. By using the interlock system, the status of the valves can be controlled automatically with a PC.

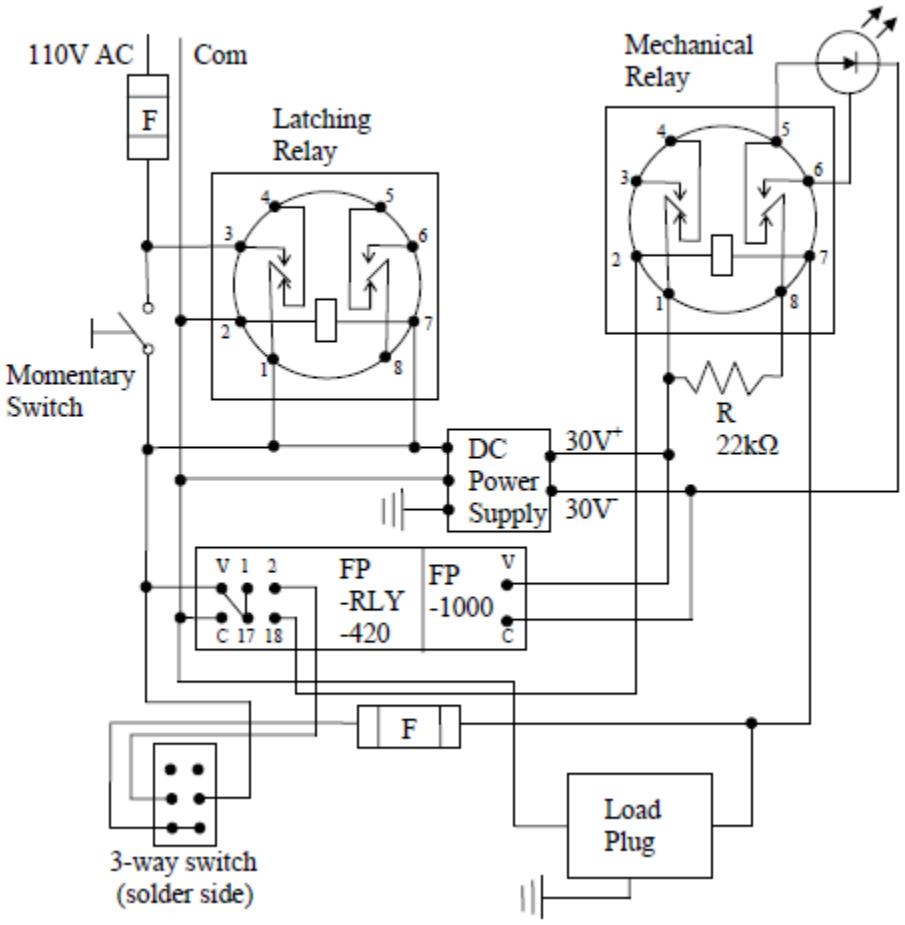

Figure 4-11: Schematic diagram of the wiring of the interlock electronics box. The box contains twenty individual circuits containing a mechanical relay and LED.

The entire logic of the interlock program is based on the comparison of the live chamber pressures to pre-determined setpoints. In order to simultanously read the pressure from multiple locations throughout the chamber, a custom made pressure gauge electronics box was home built and is interfaced to the interlock computer. The gauge box consisits of ten identical cirucuits that both supply power to and relay the signal voltages from the gauges. An example of the gauge box circuits is shown in Figure 4-12. The main power supply is 110 VAC from the wall which connects to an AC-DC converter, which changes the voltate to 24 VDC. The hot suppply voltage is run in parallel to pin 4 on each of the gauge pins. The common voltage is connected to pin 5 on each gauge and terminates at the DC supply. The gauge signal voltage is carried on pins 4 (hot) and 5 (supply). The signal voltage lines are connected to specific positions on a 68-pin digital and trigger input/output terminal block (National Instruments, model CB68-LP), which

simultaneously relays the signals from all ten gauges to a PCI data acquisition (DAQ) board located in the operating PC. The DAQ board (National Instruments model PCI-6014) converts the input analog votages into digital signals which are then used in the interlock program.

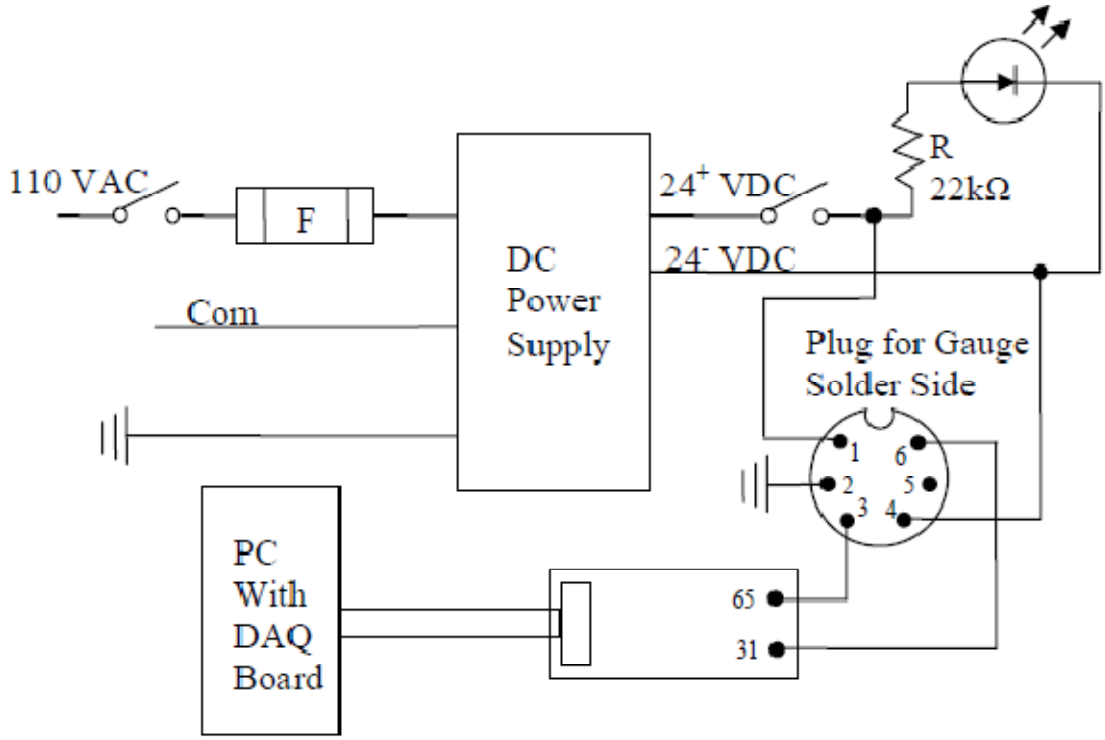

Figure 4-12: Schematic diagram of the wiring of the gauge box. The box contains ten circuits, but the DAQ board can accommodate up to eight simultaneous analog signals.

Interlock Program

The interlock program was writtin with Labview Version 8.2 and is based on similar interlock programs that monitor other UHV chambers in our lab. The program consists of two main parts; the front panel and the block diagram. The front panel is essentially the user interface where the chamber pressures can be read, the set points can be selected, valve statuses can be changed, and the turbo pumps can be turned on or off. Figure 4-13 shows an image of the front panel. On the left side is a table that provides live readings of the chamber pressures at the indicated locations. Above the pressure readings are the pressure set points as well as a pull down menu that has preset set point values for a number of possible chamber conditions. For example, when not in use, the 'Standby UHV' option is selected which then assigns approriate set points. During a sample transfer, the setpoints need to be typically higher than during

standby. If a user selects 'Sample Transfer' from the pull down menu, the setpoints change automatically. There is a 'Manual' option that can be selected to allow the operator to choose the setpoints, however all other settings available in the pull down menu do not let the operator change the set ponts. This was done to ensure that set points could not acidentally be set incorrectly.

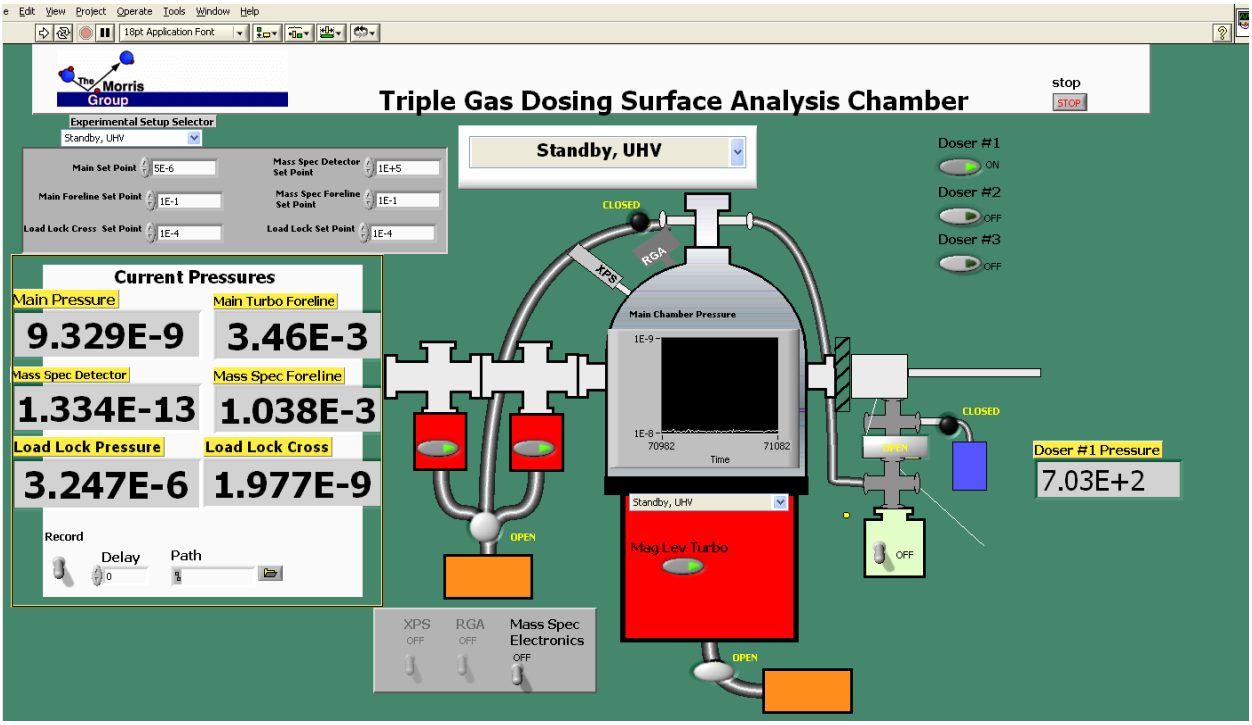

Figure 4-13: Image recorded of the front panel of the interlock program written with LabView 8.2 that protects the chamber form catastrophic failure and allows the user to control the various valves and vacuum pumps of the surface analysis chamber.

The bottom left of the front panel contains pressure recording options. The switch turns the recording function on or off and the delay sets the recording intervals. The 'path' option allows the user to selecte a text file to record the pressures. After the passage of each delay period, the pressures of each part of the chamber are recorded along with a time stamp in chronological order in the text file. The recording continues until the switch is turned off. The recording feature was included to view the pressure history of the chamber in case of a failure.

In the middle of the front panel is a schematic of the chamber layout, which contain graphical two-way switches that control the pneumatic valves and turbo pump. When a valve switch is pressed, a 5 VDC signal is sent to a corresponding Field Point relay position, which

then allows the 110 VAC mechanical relay to open sending 110 VAC to the specific mechanical gate valve. If a turbo pump switch is pressed, a corresponding Field Point relay switch is closed; however, unlike the pneumatic valves, the field point relay does not open a 110 VAC mechanical relay. The three turbo pumps are configured for remote operation, and to achieve this, a 24 VDC and 15 VDC output signal is sent from the large and two smaller turbo pumps, respectively. These signals are connected separately to a Field Point relay switch, and when the front panel switch is turned on, the circuit closes and the 24 or 15 VDC signal is sent to another pin on the remote plug of the turbo pump. When these pins receive the approriate DC voltage, the pump is started and when the DC signal is terminated, the pump shuts down. By controlling the operation of the turbo pumps remotely, we can ensure that in case of a pressure burst or other malfunction, pumps, as well as pneumatic gate valves, turn off approriately.

The block diagram contains the actual "code" of the program written in Labview's G programming language. The images of each part of the program are provided in Appendix B. The program "flows" from left to right through a series of conditional cases that are connected with wires. The entire program is contained in a while loop that continues indefinitely until the 'stop' button on the front panel is pressed. Within the while loop are a series of case structures that the program process in numerical order beginning with case #1 on the left. The experimental setup options and corresponding set points are determined in case #1. Within the case is another case structure where the set points of each experimental condition are found. The user can change the set points manually for all conditions in this part of the block diagram.

In case 2, the signal voltages are read from the gauge box using the DAQ Assistant express VI, which greatly simplifies the coding needed to read from the many gauges. Within the DAQ assistant, the physical DAQ board addresses are defined for each gauge as well as the sampling rates and voltage signal ranges. The DAQ assistant VI sends a combined signal out as dynamic data which is converted to a cluster. The cluster is unbundled and the individual gauge voltages are sent through sub VI's that convert the raw voltage signal into a pressure reading in units of Torr. Each gauge type has a corresponding voltage-pressure conversion equation that was supplied in the gauge instruction manual. The converted pressure readings are then connected to the front panel displays and stored as individual variables.

Case 3 is the first example of the comparison of current pressures to their respective set points. Here, the ability to turn on the mass spectrometer electronics is dependent on the pressures of the main and mass spectrometer detector chambers. In the case structure, the mass spectrometer detector and main chamber pressures are compared to their set points. If neither pressure is above their set points, a '0' is returned by the selector and the mass spectrometer electronics can be turned on. If either the main or mass spectrometer detector chamber pressures are above their set points, a '1' is returned by the selector. On the next pass through case #3, the '1' case is selected and the mass spectrometer electronics variable is set to 'False", which corresponds to the off position of the mass spectrometer electronics switch on the front panel. The '1' selection is then changed to a '0' and the pressure comparison is made again on the next lap of the while loop.

In Case 4, the foreline pressures are compared to their set points. If neither foreline is above the set point, nothing is done. If either foreline pressure is above the set point, all the pneumatic right angle valves are closed to isolate the foreline from the chambers, and the three turbo pumps are turned off. An increase in the foreline pressure may be caused by a malfunction of the mechanical backing pumps, and if they are not running, oil may back stream into the chambers. This potentially catastrophic situation is prevented by closing the foreline pneumatic valves. Case 5 operates similar to case 4 with the main chamber and mass spectrometer detector chamber pressures being compared to their respective set points. As with case 4, if either pressure exceeds the set point, the valves are closed and the turbo pumps are shut down.

Case 6 compares the load lock pressure to its set point. If the set point is exceeded, only the load lock gate valve is closed which protects the ion pump from being damaged. This also helps keep the high vacuum area of the load lock constantly evacuated and saves significant pumping time when the rest of the load lock is re-evacuated. Case 7 similarly compares the load lock cross pressure (the high vacuum side) to its respective set point.

In Case 8, all of the set points are compared to the live pressures. If any of the set points are exceeded, a false signal is sent to every Field Point relay switch and the status of every valve and switch on the front panel is turned to off, which effectively shuts down the chamber. If none of the set points are exceeded, the original value of the valve and switch values are sent to the Field point relays. This case was installed as a failsafe double check to ensure that at no time

will the chamber be able to operate at full capacity if any set point pressure is exceeded. Frame 9 reads the status of every Field Point relay switch and returns the signal to the corresponding variable. The variable update ensures that the switch representations on the front panel are indeed representative of the actual state of the Field Point relay switches. Frame 10 performs the pressure recording as was described earlier. Future users can add more recording options by simply extending the array and wiring in new items similarly to those currently present.

4.3 Concluding Remarks

In this chapter, we described the design and construction a new ultrahigh vacuum surface analysis chamber in order to study the reactions of bare and chemical warfare agent simulant-covered surfaces with vaporous decontamination formulas currently used by the Army. The study of gas-surface reactions is not a simple endeavor and requires specialized equipment. To help us determine how the vaporous decon gases interact with militarily-relevant surfaces, we designed and constructed a new surface analysis chamber. In designing the chamber, we had four key goals; 1) the ability to manipulate and control the sample surface in vacuum, 2) the ability to monitor surface reactions before, during, and after the introduction of a reactant gas with multiple surface analysis techniques, 3) the ability to introduce up to three reactant gases to the surface simultaneously, and, 4) the ability to introduce new samples into the chamber rapidly without the need to break vacuum. Our surface analysis chamber allows us to carefully control many aspects of the gas-surface reactions of interest including the background pressure, the sample surface temperature, and the flux of gas molecules interacting with the surface of interest. In the following chapter, we describe the initial experiments performed in the new chamber which demonstrate the utility of the system and the success of our design.

Chapter 5

Adsorption of Chemical Warfare Agent Simulants to Silica Nanoparticulate Films

5.1 Introduction

The primary objectives of this work are the study of the interaction of chemical warfare agent simulant molecules with militarily-relevant surfaces and the decomposition pathways of surface-bound simulants by well-known decontamination gases currently in use by the military. Vaporous formulas containing either hydrogen peroxide or chlorine dioxide along with concomitant vapors such as ammonia have been used by the military to decontaminate locations and objects exposed to chemical warfare agents. While the decontamination strategies have been effective in destroying the harmful agents, very little is known about the overall reaction mechanisms and the role of the underlying surface. Examples of such surfaces include paint coatings, certain plastics, or even the surfaces of microelectronics. There is a strong need to determine how these surfaces are affected by CWA's and the highly oxidizing molecules used in their decomposition. The ultimate goal of this work is to provide rules for predicting the fate of surface-adsorbed agents, which will enable scientists to develop more effective strategies for decontamination.

Our study presented here, along with the majority of CWA research, focuses on chemical warfare agent *simulant* molecules because of the highly dangerous nature of the real agents. The real CWA's are classified according to their physiological effect and include the blood agents, asphyxiates (choking agents), vesicants (blister agents), and nerve agents. The latter category has further been designated as G or V-type agents according to when they were developed. The G agents were discovered by German scientists beginning in the 1930's after work with organophosphate insecticides revealed that certain formulae were harmful to mammals. Figure 5-1 and the subsequent table show the molecular structure and some physical properties of the well-known chemical warfare agents.

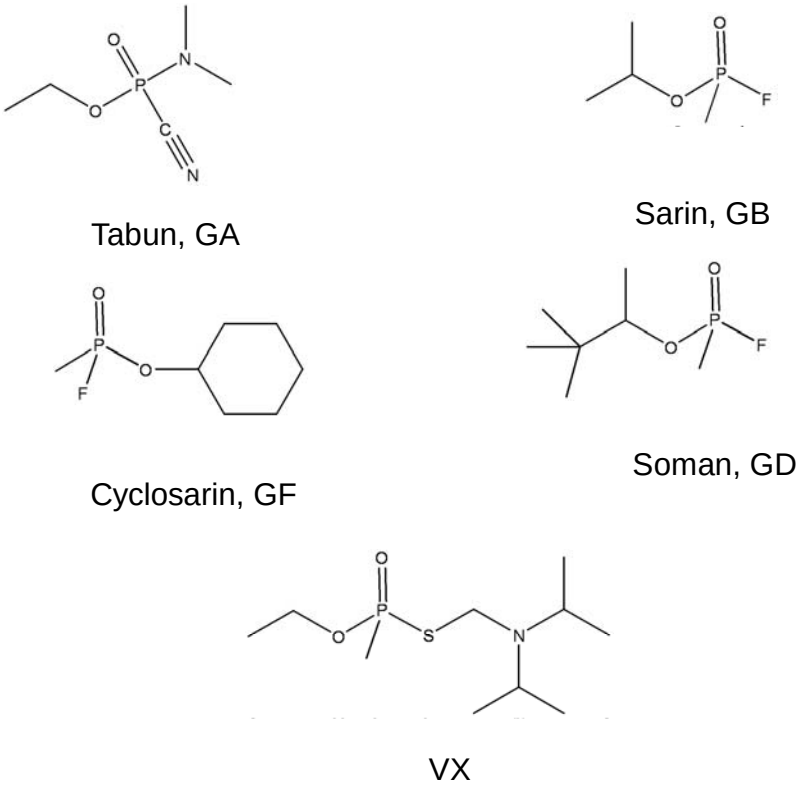

Figure 5-1: The molecular structures of some chemical warfare agents.

Name	Molecular Weight	Melting Point (K)	Boiling Point (K)	Vapor Pressure (Torr)	Decomposition Temperature (K)
GA, *ethyl dimethylphosphoramidocyanidate*	162.1	223	493	0.037 @ 293 K	423
GB, *isopropyl methylphosphonofluoridate*	140.1	217	431	2.1 @ 293 K	423
GD, *3,3-dimethylbutan-2-yl methylphosphonofluoridate*	182.2	231	471	0.4 @ 298 K	403
GF, , *cyclohexyl methylphosphonofluoridate*	180.2	261	512	0.07 @ 298 K	---
VX, *S-(diisopropylamino)methyl O-ethyl methylphosphonothioate*	253.3	222	571	0.0007 @ 293 K	423

Table 5-1: Physical properties of the chemical warfare agents shown in Figure 5-1.[200]

The nerve agents shown above all impart physiological havoc by disrupting the reuptake of the neurotransmitter acetylcholine by binding to the acetylcholinesterase enzyme. Acetylcholine is crucial in regulating nerve impulses in the body, and if excess acetylcholine molecules are not broken down by the enzyme after an impulse, the nerves will continue to fire

indefinitely and without voluntary control. The ultimate effect is paralysis of the muscles, including the diaphragm, which eventually leads to asphyxiation and death. The agents are extremely potent in low doses both through inhalation and percutaneous entry into the body.[200] The use of agents of these types in a terrorist or warfare capacity is a pressing concern to military and civilian sectors alike, and the study of decontamination and decomposition methods has received much attention.

CWA Simulant Molecules

Due to the extreme health risks and strict safety regulations associated with live chemical warfare agents, very few studies using live agents exist. The vast majority of studies undertaken outside of regulated laboratories into the decomposition of CWA's have been done with simulant molecules. These molecules are chosen because they possess many of the same chemical structures and functional groups found in the live CWA's without the extremely dangerous health risks. Figure 5-2 and the following table provide the molecular structures and physical properties of six of the most commonly used CWA simulant molecules.

The CWA simulants have many structural and chemical similarities to the live agents. Trying to correlate the reactions of simulant molecules with the live agents requires using multiple simulants because there is no single simulant that contains the same properties as a live agent molecule. The choice of simulant depends on what part of the live agent molecule one is trying to investigate. For example, DMMP contains two bulky ester groups attached to the central phosphorus, and the reactivity of the ester groups could be used to predict the reactivity of the ester groups of GA or VX. The simulant DIMP contains two isopropyl groups, which are similar to isopropyl groups of GB and VX. The chlorinated simulant molecules, TMP and MDCP, may have similar reactivity to the fluorinated live agents GB, GD, and GF. In fact, MDCP contains three components similar to GB; the ester, phosphoryl, and chlorophosphate groups. Ultimately, the choice of simulant depends on the part of the live agent that is under study.

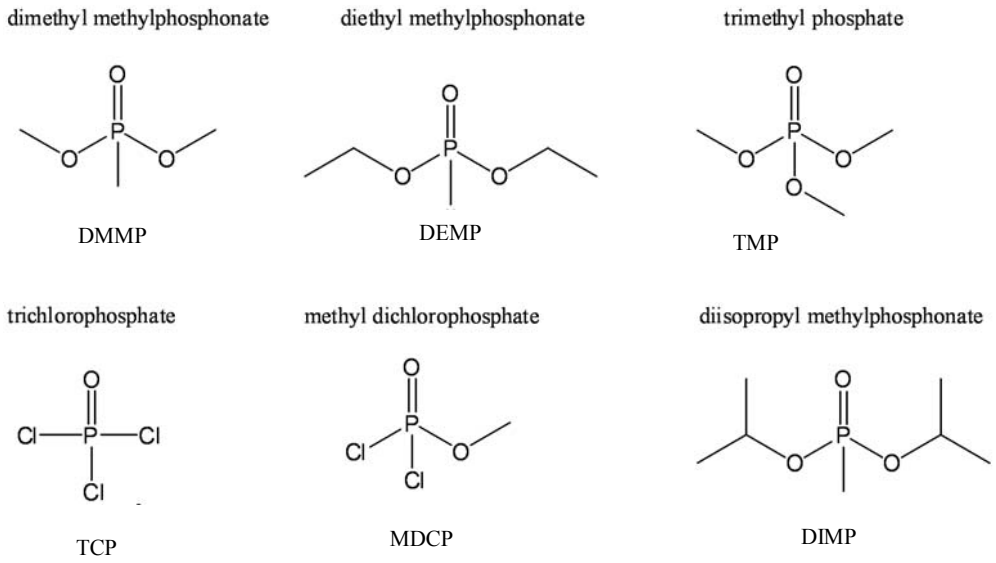

Figure 5-2: The molecular structures of commonly used chemical warfare agent simulants.

Name	Molecular Weight	Melting Point (K)	Boiling Point (K)	Vapor Pressure (Torr)
DMMP	124.08	225	454	0.962
DEMP	152.13	---	467	5.2 (343 K)
TMP	140.08	227	470	0.85
TCP	153.33	272	378	---
MDCP	148.91	---	336	---
DIMP	180.18	298	394	0.277

Table 5-2: Physical properties of the chemical warfare agent simulants shown in Figure 5-2.

Previous CWA Decomposition Studies

Solution Phase Decontamination Strategies

The solution phase decomposition of the selected nerve agents has been investigated. Under basic conditions (pH > 10), it was found that GB, GD, and VX all undergo hydrolysis with water; however the solubility of VX in water decreases as a function of increasing pH,[192] making complete reaction of the agent difficult in highly basic solutions. Solutions containing either sodium chlorite ($NaClO_2$) or calcium chlorite ($Ca(OCl)_2$) can hydrolyze the P-S bond of VX after initial oxidation of the sulfur.[191] In addition, basic solutions of hydrogen peroxide have been shown to decompose GB,[27] VX,[193] and HD via the generation of the peroxy anion (OOH^-). While the solution phase decontamination strategies shows promise, it is not plausible to apply them in most situations. For example, decontaminating an entire building or even one water-sensitive piece of equipment is unreasonable. In order to address complex decontamination

challenges, focus has shifted to the study and development of surfaces that contain inherent CWA decomposition properties as well as decontamination gases.

CWA Decomposition on Metal Oxides

The adsorption and subsequent decomposition of chemical warfare agents and simulants on metal oxide surfaces has been studied for a number of systems including WO_3,[31, 34, 35] TiO_2,[31, 35, 37-41] Al_2O_3,[31] Fe_2O_3,[33] HfO_2,[36] and Y_2O_3.[32] Metal oxides are better sorbents and are more reactive towards CWA's than are pure metal surfaces.[201-203] The increased activity has been attributed to the larger number of defect sites found in the oxides. Nanomaterial metal oxides show an even larger activity enhancement that is accredited to the much larger surface area nanoparticle, and the defect sites show even higher reactivity. Each of the oxides listed above showed similar simulant adsorption and decomposition mechanisms. DMMP and its analogues initially adsorb to the oxides through both Lewis acid (metal atom) and Brønsted base (hydroxyl) sites.[42, 43]

After adsorbing to the surface, both the agent and simulant molecules can undergo an oxidation or hydrolysis decomposition reaction. The typical resulting species are a surface-bound O-P-O bridging species and a gas phase methoxy, or often the methoxy group remains bound to the surface as well.[32] After decomposition, however, the remaining surface-bound species often require very high temperatures to thermally desorb form the surface. The surface-bound reaction products essentially inactivate their occupied metal oxide binding site from further reaction with additional CWA or simulant molecules. Eventually, the metal oxide surface will become saturated and inert to continuous exposure to the adsorbate molecules. While the metal oxides that react with CWA's at room temperature are promising, the search is still on for a more catalytic decontamination material that does not require extreme measures to regenerate the reactive sites.

Silicon Dioxide as a Sorbent

In addition to studying reactive metal oxide nanoparticulate films, investigation of non-reactive films is also important. The non-reactive films could potentially serve as a sorbent material for CWA simulants and live agents. A material that adsorbs the CWA's without reaction would be ideal for the study of the reaction of simulants and live agents with

decontamination gases. Silicon dioxide (SiO_2) nanoparticulate films are a good potential sorbent material for CWA's because they can be easily loaded with silanol (Si-OH) groups that can hydrogen bond well to the phosphoryl (P=O) and methoxy (O-CH_3) found in the simulant molecules.

Silica films have been investigated as a possible sorbent material for CWA's.[33, 44] In contrast to the other metal oxide systems discussed above, SiO_2 does not react with adsorbed DMMP and other simulants. At near atmospheric pressures, the simulant molecules adsorbed to the surface and desorbed molecularly, even at elevated temperatures. The work by Tripp et al. revealed the adsorption mechanism of DMMP and its analogues.[44] SiO_2 forms surface hydroxyl species that populate the surface, and these groups are capable of extensive hydrogen bonding.[204] DMMP and its analogues adsorb to the surface of silica via the formation of hydrogen bonds with the free silanol groups. Tripp's work showed that the strength of the interaction between the simulants and the silica surface was dependent on both the type and number of hydrogen bonding groups found within the simulant molecules. TMP, with three methoxy hydrogen bonding groups, had the strongest interaction followed by DMMP, MDCP, and finally trichlorophosphate (TMP), which can only bind through weak phosphoryl group hydrogen bonding. All of the simulants desorbed in vacuum at elevated temperatures.

SiO_2 has also been investigated as a part of a substrate for the UV induced photooxidation of a mustard gas simulant. Panayotov and Yates created bulk films containing a 50% mixture of SiO_2 and TiO_2 which were saturated with the mustard simulant, 2-chloroethyl ethyl sulfide (2-CEES).[205] They found that 2-CEES can be completely decomposed by the photooxidation process, and that the reaction products are completely desorbed by heating to 400 K. The product desorption regenerates the active surfaces that can further decompose additional 2-CEES molecules. The SiO_2 by itself, however, was unreactive, and the SiO_2-TiO_2 mixture was more reactive than the TiO_2 alone. It is thought that the addition of SiO_2 generates more surface sites that may enhance the reactivity.

The fact that the SiO_2 surface does not decompose CWA and CWA simulant molecules can be advantageous. For example, the motivation for Tripp's work was to develop a sensor that can selectively measure CWA vapors in a gas mixture to use as an early warning system for possible contamination. The strong adsorption characteristics of SiO_2 films can also be

exploited. As was stated earlier, the motivation for constructing our triple gas dosing surface analysis chamber was to investigate the surface reactions of vaporous decontamination formulas with both bare and simulant-doped surfaces. Understanding the reaction of the CWA simulants with the decon vapors is difficult if there are competing surface reactions occurring simultaneously. The inactivity of silica towards CWA decomposition makes it a good candidate to use as a highly sorbent material to study the reaction between the decon vapors and the simulant molecules.

The reactivity of the military-relevant surfaces with the gases used in chemical warfare agent decomposition is not well understood. Understanding the fate of surfaces, adsorbates, and gases after interaction with the highly oxidizing decontamination gases is very important to both the military and civilian sectors. For example, the reaction products of surface-bound CWA's, both on the surface and desorbed into the gas phase, may themselves be hazardous. The reaction of military-relevant surfaces with the oxidizing gases may also cause unwanted damage and compromise the integrity of the material. The ultimate goal of this project is to develop a detailed understanding of the chemistry that occurs when oxidizing neat and modified vapors impinge on both bare and simulant-covered surfaces of military relevance. The acquired knowledge will help military scientists develop improved and safer chemical warfare agent decontamination strategies. Silica is an excellent model system that we chose to use as our initial test surface.

Prior to studying the reactions of the decon vapors with the surface-bound CWA simulants, the adsorption to the silica surface requires a more detailed study. The study of the gas-surface reactions with the decon vapors will include pressures below atmosphere and a better understanding of the simulant-silica interaction at the lower pressures is needed. The adsorption of DMMP and its analogues at saturation pressures has been studied, but relatively few studies exist of DMMP adsorption at lower pressures. By determining the dependence of the simulant surface coverage on pressure or a large range, insight into the adsorption mechanism can gained. The focus of the first part this next study was to, for the first time, determine adsorption isotherms of DMMP, TMP, and MDCP on thin silica nanoparticle films. The isotherms will help reveal the adsorption mechanism as well as the relative simulant-silica interaction strength at lower pressures.

The study of adsorption of the CWA simulant to the silica nanoparticulate films also served as an excellent test system for the new surface analysis instrument described in Chapter 4. The work described here verified that the following systems worked: 1) the sample introduction via the load lock system 2) the chamber pressure could be accurately measured and controlled, 3) the RAIRS system and associated optics worked properly, 4) a background flux of a choice vapor could be introduced into the chamber in a controlled manner.

5.2 Experimental Setup

Chemicals and Reagents

Aerosil silica nanoparticles, with average surface area of 200 m^2/g and 12 nm particle diameter, were purchased from Spectrum Chemical. Dimethyl methylphosphonate (DMMP, 97%), trimethylphosphate (TMP, 99+%), and methyl dichlorophosphate (MDCP, 85%) were purchased from Sigma-Aldrich. 2-propanol was purchased from Fisher Scientific and used as received. Sodium chlorite (85%) was purchased from Aldrich and used as received. Hydrochloric acid (12M) was purchased from EM Industries. Deionized water (18.2 MΩ) was prepared using a Millipore Purification system. Gold slides were purchased form Evaporated Metal Films and contain 1000 Å gold on top of a glass substrate with a 100 Å titanium or chromium adhesion layer in between.

Sample Preparation

The silica films were prepared by a solution cast film technique. A suspension of silica nanoparticles was prepared in which approximately 60 mg of nanoparticles were mixed with 10 mL of isopropanol. The mixture was sonicated for up to an hour to disperse the nanoparticles. Freshly cleaned gold slides were placed into the nanoparticle mixtures for 10-30 minutes. The slides were then removed carefully to ensure that they remained level and covered with liquid from the nanoparticle mixture and placed into a covered glass petri dish. The dish was placed into a vacuum desicator that was attached to a diaphragm pump, and the chamber was evacuated to one Torr to increase the evaporation rate of the isopropanol. After 15 minutes, the pump was turned off and the desicator was vented to atmosphere. At this point, the gold slides had a film of silica on the surface. The slides were immediately removed and placed into the load lock of the surface analysis chamber.

Simulant Vaporization and Delivery

To deliver the simulant molecules to the silica films positioned in the surface analysis chamber, a gas bubbler system was employed. The bubbler is made of glass and consists of a long round bottom cylinder clamped to a gas inlet-outlet manifold. A glass straw extends from the gas inlet port into the simulant liquid and the exit port is attached to stainless steel tubing that runs to the chamber. Both the inlet and exit ports contain manual o-ring valves that allow the inlet and outlet gas flow to be controlled. A schematic of the bubbler is shown in Figure 5-3. The simulant liquid is placed into the glass tube and the entire system is evacuated with a diaphragm pump to remove air from the system. The system is then backfilled with ultrahigh purity nitrogen which is used as a carrier gas. The nitrogen enters the system through the inlet straw where it bubbles through the simulant liquid. The bubbling causes a small fraction of the liquid simulant to vaporize and the carrier gas and vaporized simulant exit the bubbler through the exit port.

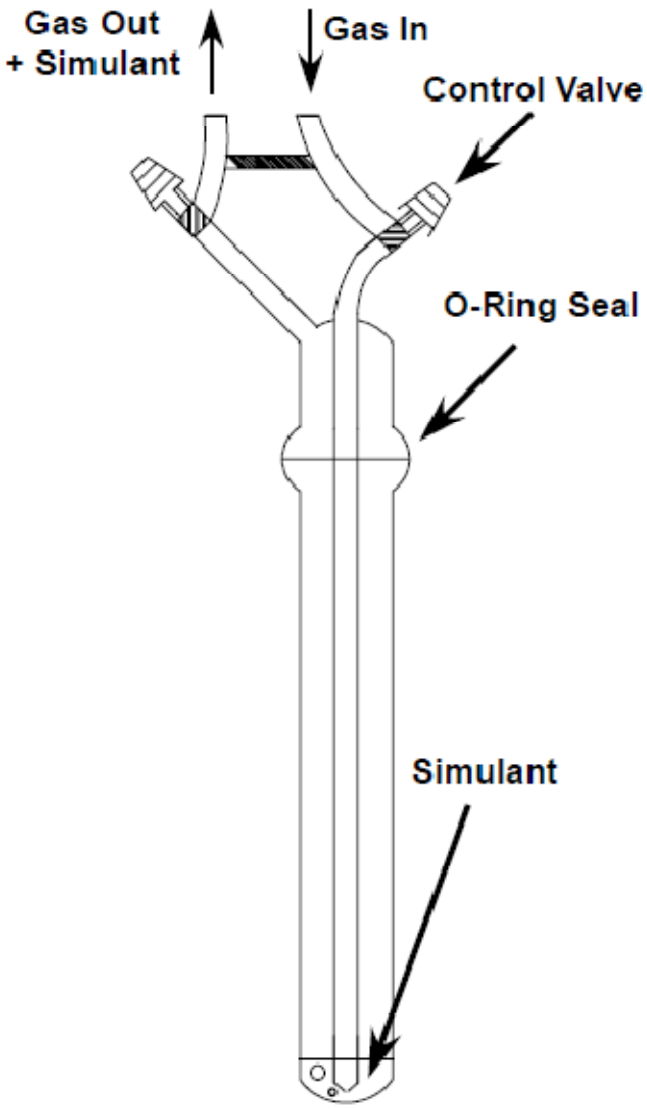

Figure 5-3: A schematic diagram of the gas bubbler used for introducing simulant molecules into the surface analysis chamber.

The bubbler is connected to the chamber with ¼" diameter stainless steel tube and the other end of the tube is connected to a sapphire precision leak valve which can control leak rates down to 10^{-10} Torr L/s. The leak valve and steel tubing are wrapped in resistive heating wire to increase the temperature of their surfaces and diminish the adsorption of simulant molecules. The temperature is controlled using Variac transformers that regulate the output current to the heating tape. To increase the vaporization rate of the simulants during dosing, the glass bubbler was placed into a temperature controlled sand bath or a water/ethylene glycol circulator to maintain a temperature of 75 °C.

RAIRS

Reflection-absorption infrared spectroscopy (RAIRS) was performed by using a Nicolet Nexus 670 FTIR spectrometer configured for external optics, as was described in Chapter 4. Briefly, p-component of the linearly polarized light is selected by passing through a ZnSe polarizer. The light is focused onto the surface at the optimal 86° grazing angle where it reflects and is focused into an MCT-A detector. Each spectrum is the average of 512 scans collected at a resolution of 4 cm^{-1}.

Data Collection for the Preparation of Pressure Isotherms

The isotherm experiments were performed by collecting RAIR spectra as a function of pressure. The total pressure was regulated by adjusting the gas entrant rate of a sapphire plate precision leak valve. The pressure in the chamber was measured using a combination Full Range gauge that uses a cold cathode gauge to measure pressures below 10^{-4} Torr, and a Pirani gauge to measure pressures above 10^{-4} Torr. The experiment was started by collecting a spectrum of a clean gold slide which was used as a reference. Next, a fresh silica film formed on a gold slide was transferred into the chamber and a spectrum was recorded using the clean gold spectrum as a reference. Next, a background spectrum of the silica film was collected to use as the reference for the isotherm spectra. With this configuration, spectral peaks that have negative intensity indicate the reduction or elimination of surface vibration modes and positive peaks indicate the appearance and growth of surface vibration modes.

Prior to recording the isotherm RAIR spectra, the leak valve was opened to the heated simulant bubbler for a minimum of four hours to saturate the dosing lines with the simulant vapor. Because DMMP and TMP have low vapor pressures, the molecules are prone to condense on surfaces until saturation is reached. After the saturation period was complete, the isotherm experiment was started. To maintain pressures below 10^{-3} Torr, the turbo pumps were left on at 50 percent of maximum rotation speed. The first spectrum was recorded with the leak valve opened far enough to provide a total chamber pressure of 1×10^{-6} Torr. The pressure was then incrementally increased by further opening the leak valve. When the pressure reached 1×10^{-4} Torr, the turbo pumps were shut down, which resulted in the pressure increasing to 1×10^{-3} Torr. The pressure was increased incrementally again until the final spectra were recorded at a

pressure of 25 Torr. After the final spectrum was collected, the pumps were restarted and the chamber was evacuated.

5.3 Data Analysis: Isotherm Models

Several models have been developed in the past century to predict surface coverage as a function of pressure, and many of them have been derived from kinetic, thermodynamic, and statistical mechanistic methods.[206] One of the most commonly used isotherm models used for surface adsorption is the Langmuir isotherm which was developed by Irving Langmuir in 1918.[207] The Langmuir equation is shown as equation 5-1 where p is the adsorbate partial pressure, q^* is the sorbate concentration at equilibrium, q_s is the saturation limit of the sorbate concentration, and b is the Langmuir constant, which is a ratio of the adsorption and desorption rates.

$$q^* = \frac{q_s b p}{1 + bP}$$

Equation 5-1

An example of a Langmuir isotherm system is shown schematically in Figure 5-4. The model contains a number of assumptions regarding the surface and the adsorbate molecules. First, the sorbent surface is assumed to be perfectly flat and every adsorption site on the surface is considered equivalent. The adsorbed molecules have no influence on remaining free binding sites. The adsorbate molecules are also assumed to have no interactions with each other. The final assumption is that the adsorption is complete upon the formation of a monolayer and that no further adsorption can take place. While the equation has been applied to a great number of systems, the necessary assumptions rarely represent reality. However, for systems that exhibit Langmuirian type properties, the model provides a great deal of insight into the mechanism of adsorption.

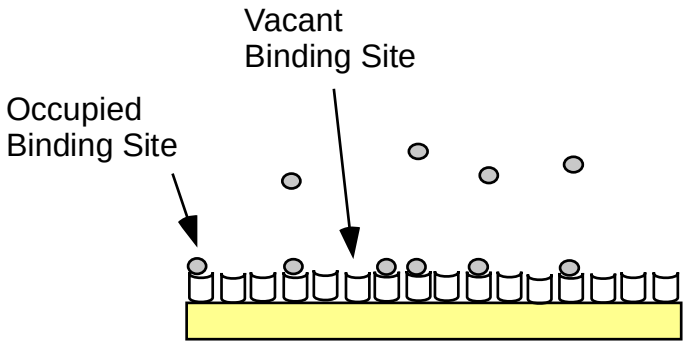

Figure 5-4: Schematic of the adsorption process assumed in the Langmuir isotherm model. The gas phase molecules adsorb to the vacant binding sites until monolayer saturation is reached.

Another common isotherm is the Freundlich isotherm developed by Herbert Freundlich in 1926.[208] The Freundlich equation is shown below where q* is the equilibrium sorbate concentration, p is the adsorbate partial pressure, K is the Freundlich constant and n is an empirical exponent. The Freundlich isotherm, like the Langmuir, has a few important assumptions. First, an infinite number of adsorption sites are assumed, which means the isotherm equation has no upper limit. During adsorption, the most favorable binding sites are filled first and as the adsorbed amount increases, the free energy of adsorption decreases, which means that adsorption becomes less energetically favorable. While the Freundlich isotherm has been used to successfully model adsorption in several systems,[209-212] the assumptions limit its applicability to many processes.

$$q^* = Kp^n$$

Equation 5-2

The Langmuir and Freundlich isotherms have been combined to from the Langmuir-Fruendlich isotherm, also known as the Sips model.[213] The isotherm has been shown to successfully model a wide variety of sorption data, and the equation is shown below. The equation variables are the same as the Langmuir equation along with the empirical parameter, n. While many empirical parameters are not manifested in physical reality, the Langmuir-Freundlich isotherm parameter has been used to describe the number of molecules in one adsorption site, which can represent the surface heterogeneity.[214] This breaks the Langmuir isotherm assumption that every surface binding site is homogeneous.

$$q^* = \frac{q_s b p^n}{1 + b p^n}$$

Equation 5-3

The best isotherm models are those that are thermodynamically consistent, meaning that they can be reduced to follow Henry's Law (shown in Equation 5-5), which shows a linear dependence of adsorbate equilibrium concentration on the pressure at low concentration.[215] One of the most popular isotherms that follows thermodynamic consistency is the Toth isotherm. The Toth model equation is shown below and contains the same variables as the Langmuir-Freundlich isotherm.[216]

$$q^* = \frac{q_s p}{\left(b + p^n\right)^{1/n}}$$

Equation 5-4

$$q^* = Kp$$

Equation 5-5

In our study, we employed the Langmuir and Toth models to fit our isotherm data because they both are considered to be thermodynamically consistent, and they contain different assumptions about the system. The Langmuir model assumes homogenous binding sites and monolayer saturation, whereas the Toth model allows for heterogenous bindings sites and multilayer binding. By determining how well each model fits the isotherm data, we will gain insight into the adsorption mechanism of the CWA simulant molecules to silica nanoparticulate films.

Preparation of Isotherm Data and Model Fitting Procedure

Isotherms were prepared by plotting the integrated intensity of selected infrared vibration modes versus the calculated partial pressure of the simulant of interest. The IR mode intensities were calculated using OPUS software from Bruker Optics and the calculated partial pressures were determined by multiplying the measured main chamber total pressure by the mole fraction of the simulant of interest at the experimental temperature. The mole fractions were determined

by first calculating the simulant vapor pressure at an elevated temperature, which for TMP and DMMP was 75°C. The vapor pressures can be calculated at higher temperatures using the Antoine equation and the associated constants. Equation 5-6 is the Antoine equation and Table 5-3 gives the constants and calculated vapor pressures for DMMP and TMP at 75°C.

$$\log P = A - \left(\frac{B}{T + C} \right)$$

Equation 5-6

Simulant	A	B	C	P (Torr)	X_j
DMMP	1.82239	444.796	-224.556	12.55	0.0165
TMP	4.96817	2249.287	-12.294	13.999	0.0184

Table 5-3: Antoine equation coefficients for DMMP and TMP.

The mole fraction of each simulant was determined by dividing the calculated vapor pressure by standard atmospheric pressure, 760 torr. For the isotherm plots, the partial pressures listed are the product of the calculated mole fractions and the measured total pressure.

The isotherm models were fit to the experimental data using the nonlinear curve fitting program found in OriginPro 8 software from Origin Labs (Podunk, USA). The program uses the Levenberg-Marquardt algorithm to perform the iterative least squares fitting of the equation parameters.

5.4 Results

5.4.1 Characterization of Silica Nanoparticulate Films

The silica films were characterized prior to simulant exposure using RAIRS and ICP-ES. The RAIR spectra were used to indentify surface-bound functional groups including the free silanols (SiOH), which are capable of hydrogen bonding to adsorbate molecules. Monitoring the silanol sites is important because by doing so, we can learn about their importance in simulant adsorption. ICP-ES was used to determine the mass of silicon on the surface, from which a surface density can be calculated. If the silicon surface density is known, along with the total surface area and free-silanol-groups-per-area of the nanoparticles (as reported by the

manufacture), it is possible to determine the number and density of possible adsorption sites on the surface. These parameters are important to know when analyzing adsorption isotherms.

RAIRS of a Silica Nanoparticulate Film on Gold

Figure 5-5 shows the RAIR spectra of a solution cast silica nanoparticulate film. The largest adsorption mode, found at 1190 cm^{-1}, is from the asymmetric stretching vibration of the bulk Si-O-Si groups, and the corresponding symmetric stretch of the group is found at 810 cm^{-1}.[217] The stretching mode of the free, non-hydrogen bonded silanol groups is found at 3747 cm^{-1} and the hydrogen bonded moieties (Si-O-H--O-Si) are found as a broad peak at 3200 cm^{-1}. The appearance of the free silanol modes is important because it is these groups that participate in hydrogen bonding with the simulant molecules. In the RAIR spectra recorded during simulant exposure, spectra of the clean silica films similar to that of Figure 5-5 are used as the background reference spectrum. In this particular setup, peaks that are negative with respect to the baseline are indicative of the disappearance of a functional group, whereas a positive peak indicates the appearance of new functional groups. The RAIR spectrum of the clean silica nanoparticle films clearly shows signature vibrations of bulk silica particles as well as the free silanol species, which are capable of hydrogen bonding to the phosphoryl (P=O) and methoxy (OCH_3) groups of the impinging stimulant.

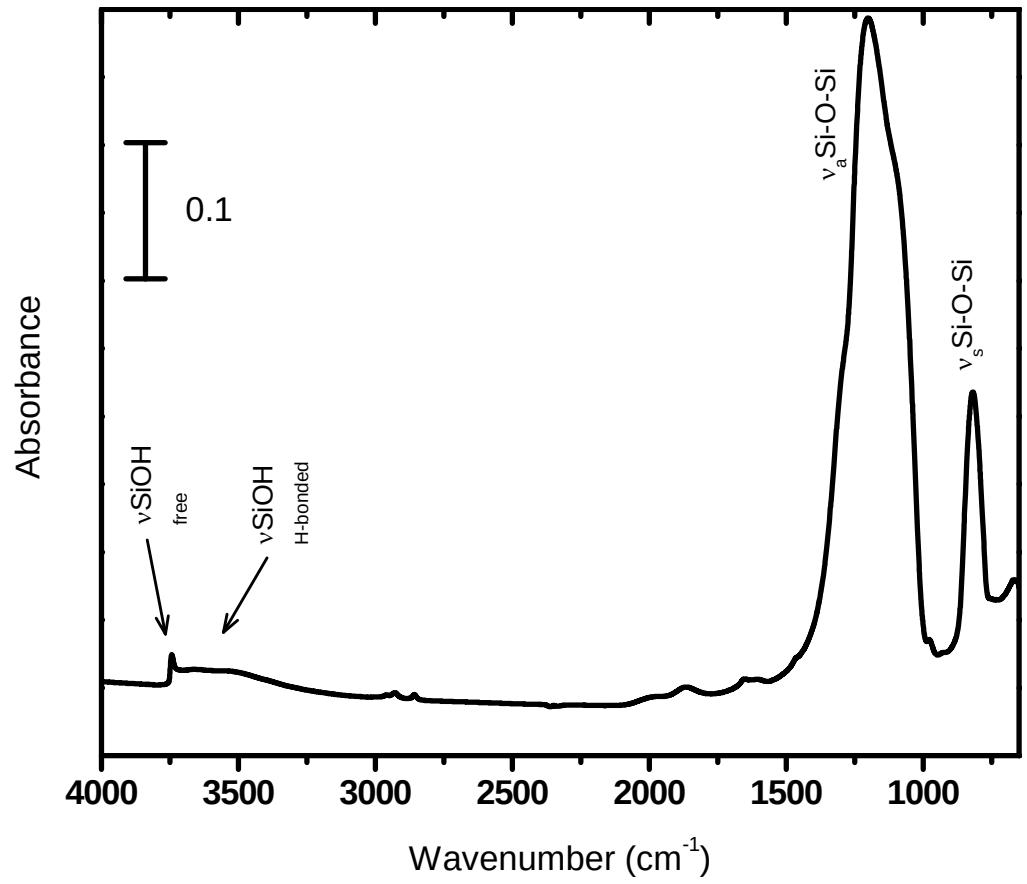

Figure 5-5: RAIR spectrum of a silica nanoparticle film on gold prepared by the solution deposition method.

5.4.2 Simulant Dosing of Silica Nanoparticulate Films

RAIR spectra of the silica nanoparticulate films were recorded while dosing with the CWA simulants DMMP, TMP, and MDCP at increasing total pressures in order to ascertain the adsorption mechanism of each molecule. A plethora of information about the adsorption mechanism can be gained from a single RAIR spectrum. Each of the simulant molecules contain functional groups that can potentially hydrogen bond with the silanol groups found on the silica surface. The functional groups have characteristic vibrational modes that can shift or even disappear completely if the molecule adsorbs to the silica film via hydrogen bonding interactions. The key hydrogen-bonding groups that are found in all three of the simulant molecules investigated here are the phosphoryl group (P=O) and the methoxy group (OCH_3). The most important difference between TMP, DMMP, and MDCP are the number of potential hydrogen bonding groups (see Figure 5-2); TMP has four groups (1 P=O and 3 OCH_3), DMMP has three (1 P=O and 2 OCH_3), and MDCP has two (1 P=O and 1 OCH_3). As we will show

shortly, the number of hydrogen bonding groups was crucial to the strength of the interaction between the simulant molecules and the silica films.

Our analysis of the RAIR spectra was performed based on the work of Kanan and Tripp.[44] The vibrational mode assignments are from the literature, and comparisons to gas phase spectra are made to the spectra published by Tripp.[44] Tripp also recorded the RAIR spectra of adsorption of the simulants of interest to thin silica films at saturation pressure. We present the mode assignments of the gas phase spectra, Tripp's silica spectra, and our silica spectra in Table 5-4. We next present the RAIR spectra of the three simulants DMMP, TMP, and MDCP.

RAIRS of DMMP Adsorbed to a Silica Nanoparticulate Film

The RAIR spectrum of DMMP adsorbed to a silica nanoparticulate film, shown in Figure 5-6, was recorded at a total pressure of nine Torr. The mode assignments are provided in Table 5-4 along with the values from the gas phase spectrum. The interaction of the DMMP with the free silanol groups is evidenced by change of the silanol stretching mode. The negative peak at 3747 cm^{-1} is accompanied by a broad positive peak at 3238 cm^{-1}. The change in position of the silanol stretching mode suggests that it is interacting with the adsorbate species. Characteristic peaks of DMMP can also be identified. The symmetric and asymmetric C-H stretching modes of the methoxy groups can be seen at 2958 and 2859 cm^{-1}, respectively, along with the symmetric deformation modes of the methoxy and P-CH_3 groups at 1454 and 1420 cm^{-1}, respectively. The asymmetric P-CH3 deformation is found at 1317 cm^{-1}.

None of the preceding vibrational modes are shifted from their gas phase assignments (see Table 5-4), however the following modes have shifted or disappeared completely. The phosphoryl (P=O) stretching mode has shifted from the gas phase value of 1275 cm^{-1} to 1240 cm^{-1}, and the O-C stretching modes of the methoxy groups, found in the gas phase at 1075 and 1049 cm^{-1}, have disappeared. The change of the latter two modes suggests that they are interacting with the silica surface, specifically through hydrogen bonding. A hydrogen bonding interaction changes the electron density of a covalent bond resulting in a slightly weaker bond. A weaker bond results in an infrared absorption at a lower energy. The silanol stretching mode

and the phosphoryl mode red shift to slightly lower energies, which suggests that they may interact through a hydrogen bond.

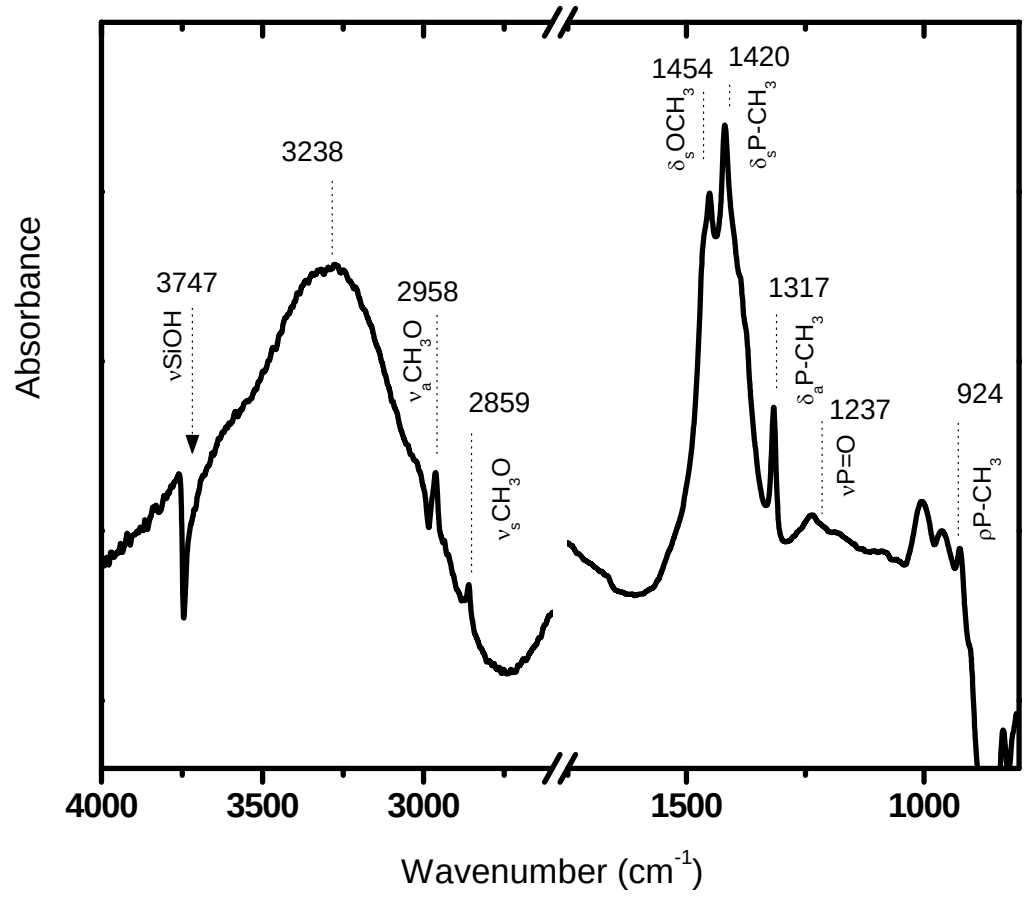

Figure 5-6: RAIR spectrum of DMMP adsorbed to a silica nanoparticulate film. The reference spectrum was of the silica film prior to exposure to DMMP.

The shift of the phosphoryl stretch and the disappearance of the O-C methoxy stretching modes suggests two possible hydrogen bonding arrangements of DMMP with the silanol groups. A schematic of the possible bonding arrangements is shown in Figure 5-7. First, both methoxy groups and the phosphoryl group can hydrogen bond with three silanol groups, and second, the two methoxy groups can hydrogen bond with two silanol groups with the phosphoryl group pointing in the opposite direction.

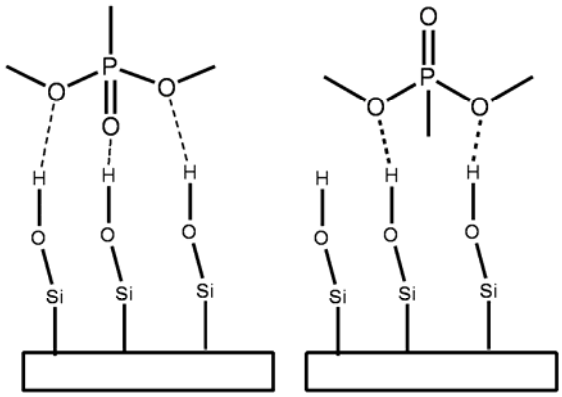

Figure 5-7: Schematic of the possible hydrogen bonding configurations of DMMP to silica.

This helps ascertain the correct hydrogen bonding configuration of DMMP, the RAIR spectra of TMP and MDCP adsorbed to the silica nanoparticulate films were recorded. TMP has an additional methoxy group in place of the P-CH3 group, and MDCP contains only one methoxy group and two P-Cl groups, which are not capable of hydrogen bonding.

RAIRS of TMP Adsorbed to a Silica Nanoparticulate Film

The RAIR spectra of TMP adsorbed to the silica film, shown in Figure 5-8, was recorded at a total pressure of nine Torr. The interaction of the silanol groups with the adsorbed molecules is again evidenced by the negative peak at 3747 cm^{-1} along with the broad positive peak at 3292 cm^{-1}. Characteristic modes of TMP are also evident in the spectrum. The asymmetric and symmetric C-H stretching modes of the methoxy groups are present at 2963 and 2863 cm^{-1}, respectively, and these values are not shifted from their gas phase counterparts. In contrast to the C-H stretching modes, and as was seen in the DMMP spectrum, both the phosphoryl and O-C methoxy stretching modes are different than the gas phase spectrum. The phosphoryl stretch has shifted from the gas phase value of 1290 cm^{-1} to 1268 cm^{-1}, and the methoxy deformation modes are absent in the RAIR spectrum. This suggests, like with DMMP, that TMP adsorbs to the silica via hydrogen bonding of the phosphoryl and/or methoxy groups with the silanol groups.

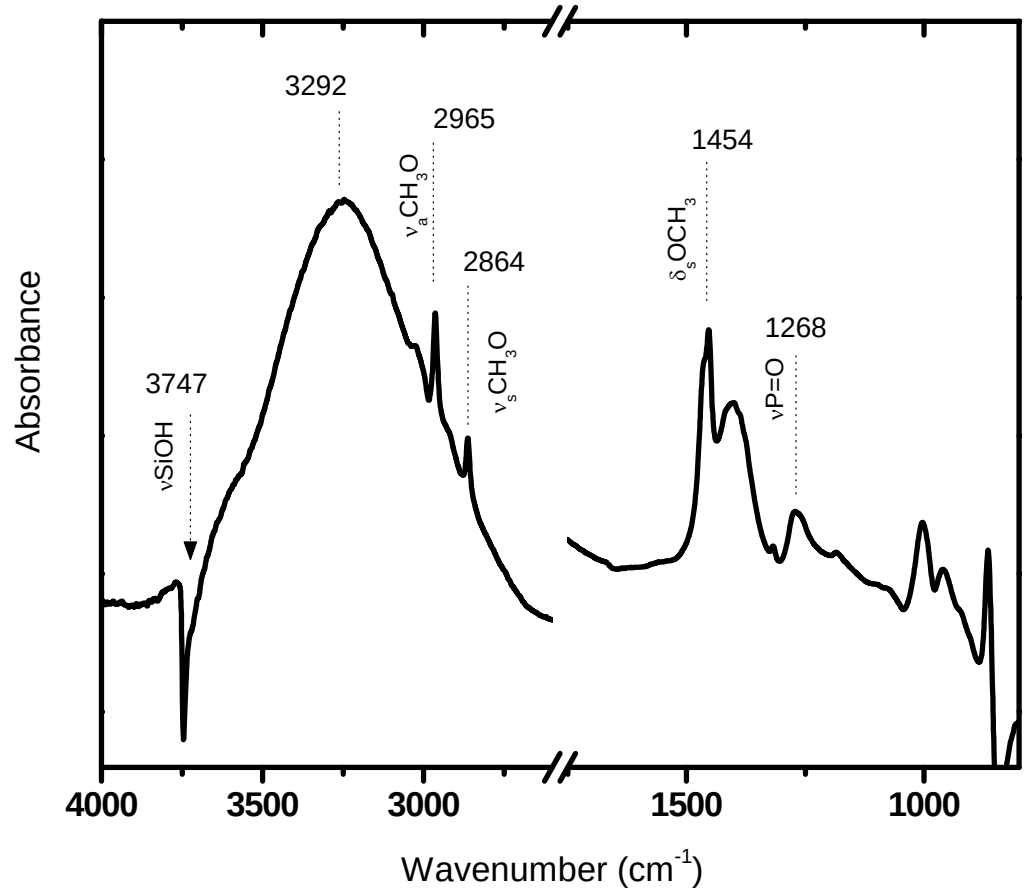

Figure 5-8: RAIR spectrum of TMP adsorbed to a silica nanoparticulate film. The reference spectrum was of the silica film prior to exposure to TMP.

The most probable bonding configuration of TMP with silica can be explained by the molecular structure of TMP. In the structure, the phosphoryl bond is opposite of the methoxy groups, and if the phosphoryl group and the three methoxy groups are hydrogen bonded with silanol groups, the TMP molecule would have a very constrained and energetically unfavorable configuration. On the other hand, if the TMP interacts with the silica via hydrogen bonding of the three methoxy groups only, a more favorable and unconstrained configuration results. Examples of the two possible hydrogen bonding configurations are shown in Figure 5-9.

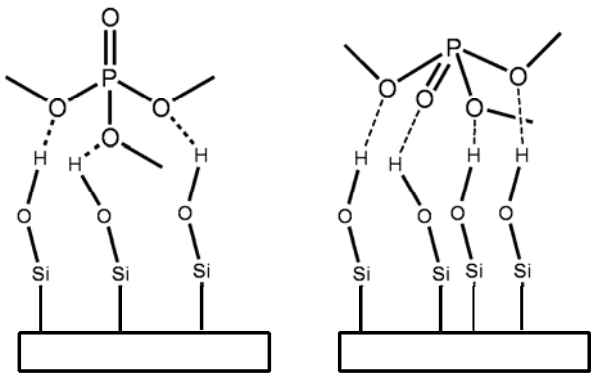

Figure 5-9: Schematic of the possible hydrogen bonding configurations of TMP with the silanol groups of a nanoparticulate silica film. The right schematic is highly improbable as the TMP is in a highly constrained and energetically unfavorable configuration.

RAIRS of MDCP Adsorbed to a Silica Nanoparticulate Film

The RAIR spectrum of MDCP, shown in Figure 5-10, was recorded at a total pressure of 30 Torr. The interaction of the silanol groups with MDCP is evidenced by the negative peak at 3747 cm^{-1} and positive broad peak at 3397 cm^{-1}. The asymmetric and symmetric C-H stretching modes of the methoxy groups are present as well at 2967 and 2863 cm^{-1}, respectively. However, in contrast our spectra of TMP and DMMP as well as to Tripp's MDCP spectra, neither the phosphoryl stretching nor the O-C methoxy stretching modes shift from their gas phase values. This suggests that the majority of the MDCP in the chamber has not adsorbed to the silica and remains in the gas phase. The possible reasons for our observations will be explained in more detail in the discussion section.

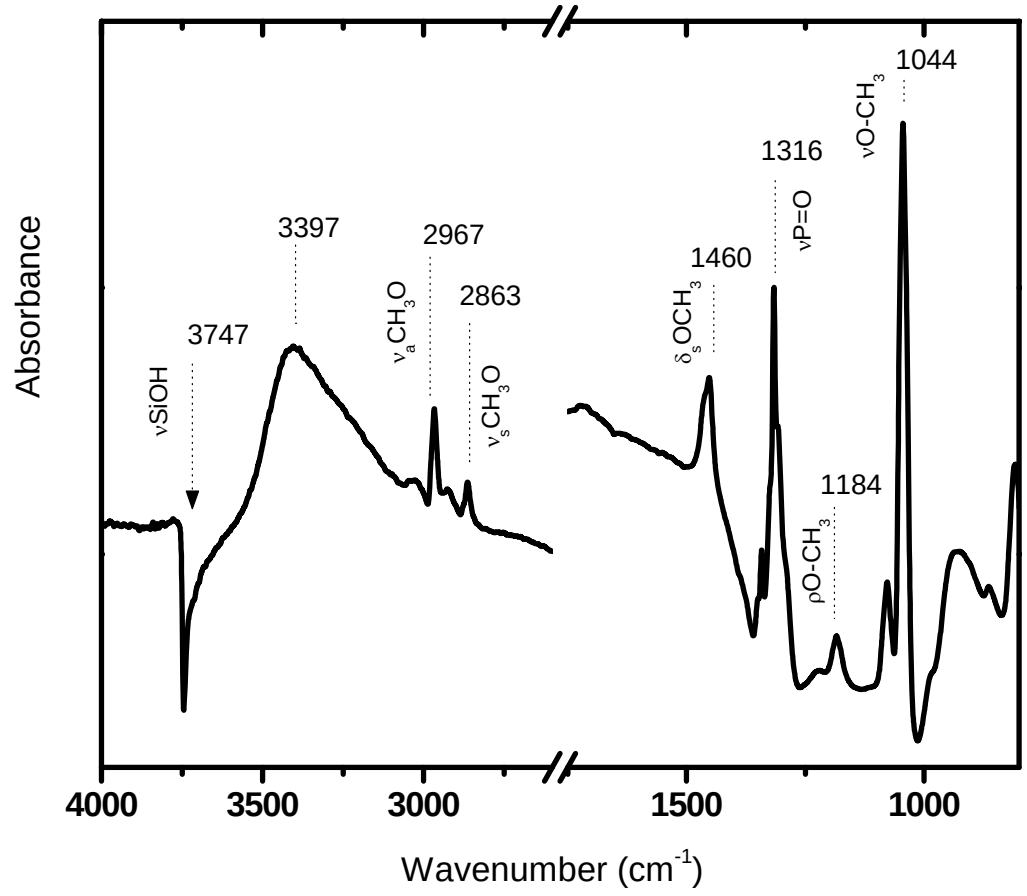

Figure 5-10: RAIR spectrum of TMP adsorbed to a silica nanoparticulate film. The reference spectrum was of the silica film prior to exposure to TMP

RAIRS Summary

The RAIR spectra recorded for the adsorption of DMMP, TMP, and MDCP helped reveal how the simulants interact with the silica nanoparticulate films. The DMMP interacts through hydrogen bonding interactions between the surface silanol groups and the two DMMP methoxy groups, and the TMP interacts through the hydrogen bonding of its three methoxy groups. The hydrogen bonding interaction of the phosphoryl groups of DMMP and TMP was ruled out primarily due to the constrained and energetically unfavorable molecular configurations that would arise if it too participated in hydrogen bonding. Further support for the lack of the phosphoryl-silanol interaction comes from the forthcoming isotherm data.

The MDCP spectrum was quite different than the DMMP and TMP spectra. Although there was some evidence of adsorption due to the change of the silanol stretching modes, the

vibrations of gas phase MDCP dominated the spectrum. A thorough discussion of this seemingly strange result is offered in the discussion section.

While the RAIR spectra recorded at relatively high total pressure allowed us to determine how the simulant molecules interacted with the surface groups, a single spectrum cannot help determine the adsorption mechanism. By recording an adsorption isotherm of surface coverage versus partial pressure, information about the adsorption process can be discovered. The adsorption isotherms of the three simulants, DMMP, TMP, and MDCP are presented next.

	DMMP			TMP			MDCP		
Mode	**Gas**	**Tripp**	**Ours**	**Gas**	**Tripp**	**Ours**	**Gas**	**Tripp**	**Ours**
Si-OH H bond		3223	3238		3262	3292		3433	3397
$\nu_a(CH_3)$, $\nu(CH_3O)$	3006			3006			2999		
$\nu_a(CH_3O)$	2958	2958	2963	2963	2963	2965	2968	2968	2967
$\nu_s(CH_3)$, $\nu(CH_3O)$	2917			2920					
$\nu_s(CH_3)$	2859	2859	2859	2863	2863	2864	2866	2866	2863
$\delta_a(P\text{-}CH_3)$	1471								
$\delta_s(O\text{-}CH_3)$	1459		1452	1457		1454	1460		1453
$\delta_s(P\text{-}CH_3)$	1420	1420	1418						
$\delta_a(P\text{-}CH_3)$	1319	1319	1317						
$\nu(P{=}O)$	1275	1256	1240	1290	1268	1268	1316	1291	1316
$\rho(O\text{-}CH_3)$	1190			1195	---	---	1192	---	1184
$\nu(O\text{-}CH_3)$	1075/1049	---	---	1061	---	---	1078/1046	---	1078/1044
$\rho(P\text{-}CH_3)$	914	914		914					
$\nu(P\text{-}O\text{-}(C))$	816			858		866	811		806
vs(P=Cl)							617		
va(P=Cl)							593		

Table 5-4: The mode assignments and frequencies of the RAIR spectra of DMMP, TMP, and MDCP adsorbed to silica nanoparticulate films in the gas phase, as reported by Tripp et al.[44], and reported here.

5.4.3 Adsorption Isotherms

The adsorption isotherms were prepared by plotting the integrated intensity of select IR modes as a function of the calculated partial pressure of the impinging simulant molecules. The data was then fit with two adsorption isotherm models, the Langmuir and the Toth models. These two models considered thermodynamically consistent and do not contain empirical fitting parameters. The two models differ in their assumptions about the adsorption system. The Langmuir model assumes monolayer saturation, equivalent adsorption sites, and no interaction between adsorbate molecules, whereas the Toth model allows for multilayer adsorption,

inequivalent adsorption sites, and for interaction between adsorbate molecules. By fitting the adsorption isotherm data with the two different models, additional information about the adsorption the simulants to the silica nanoparticulate films revealed.

Adsorption Isotherm of DMMP

The RAIR spectra used to determine the adsorption isotherm of DMMP on the silica nanoparticulate film are shown in Figure 5-11. The vibrational mode assignments and their relevance to the adsorption mechanism of DMMP were explained in the preceding section. What is important to note for Figure 5-11 is that the intensity of the absorption modes increase as a function of total pressure, which demonstrates that the amount of adsorbed DMMP is a function of pressure. The initial pressure where DMMP adsorption can be detected is also important because it is related to the relative interaction strength of DMMP with the silica. In Figure 5-11, the first observable absorption peaks appear at a pressure of 1×10^{-4} Torr.

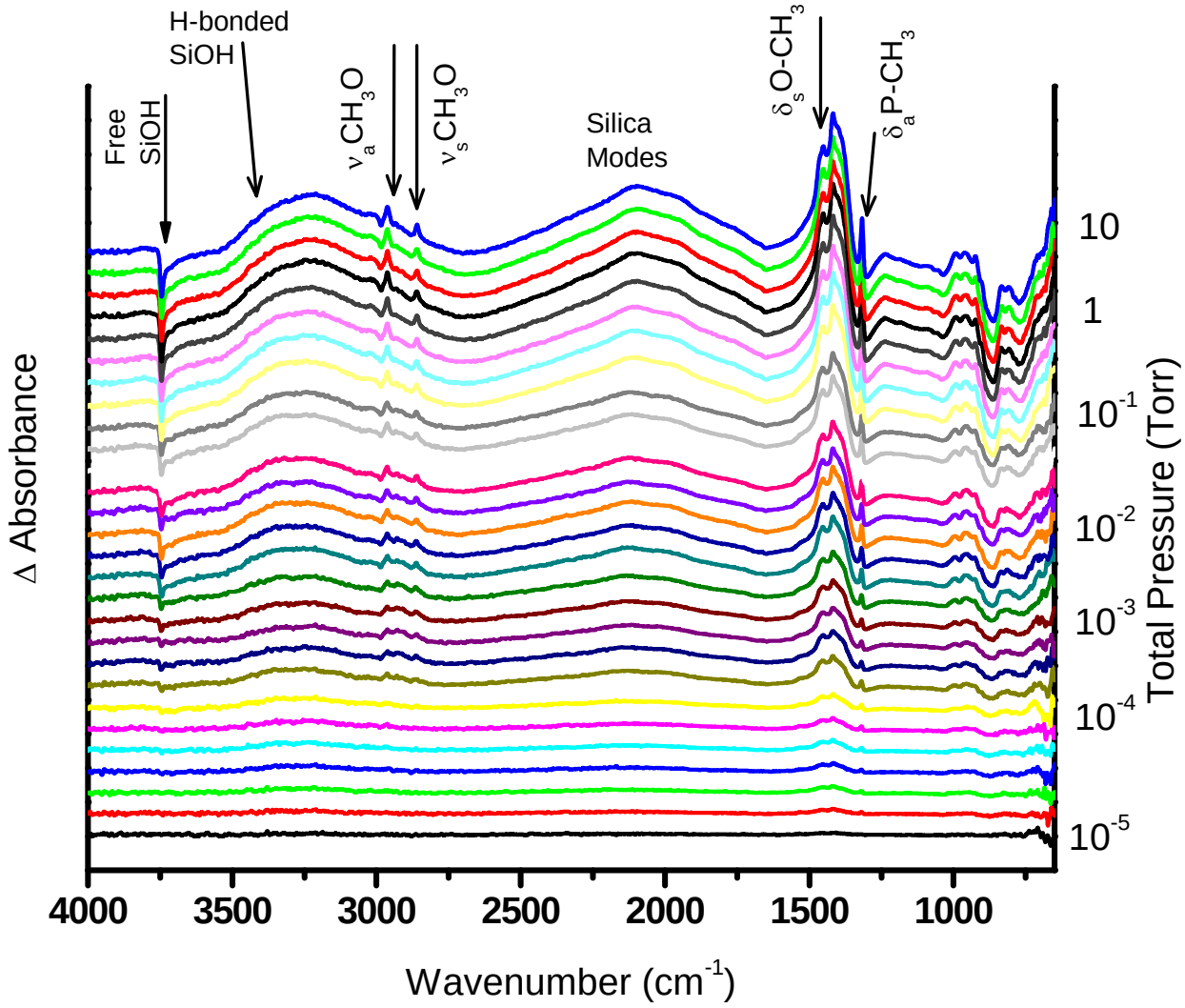

Figure 5-11: RAIR difference spectra of DMMP adsorbed to a silica nanoparticulate film on gold as a function of total chamber pressure.

The adsorption isotherm of DMMP was prepared by integrating the peak intensities of the following modes: $\delta_s OCH_3$ at 1452 cm^{-1}, $\nu_a CH_3O$ at 2958 cm^{-1}, and νsCH_3O at 2859 cm^{-1}. The isotherm plots along with the fits of the Langmuir and Toth models are shown in Figure 5-12. The fitting parameters of the two isotherm models are provided in Appendix C. There appeared to be a sudden change in the isotherm data near a partial pressure of 0.025 Torr. After beginning to level off up to 0.025 Torr, the pressure increased significantly at the next pressure measurement. At 0.025 Torr, the turbo pumps were stopped, which most likely changed the flux of simulant molecules within the chamber. The adsorption of the simulants at the low pressure regime, where the turbo pumps are running, may be different than the adsorption at higher

pressures. To test our hypothesis, we fit the isotherm data with the Langmuir and Toth models for the absorbance data recorded below partial pressures of 1 x 10^{-5} Torr.

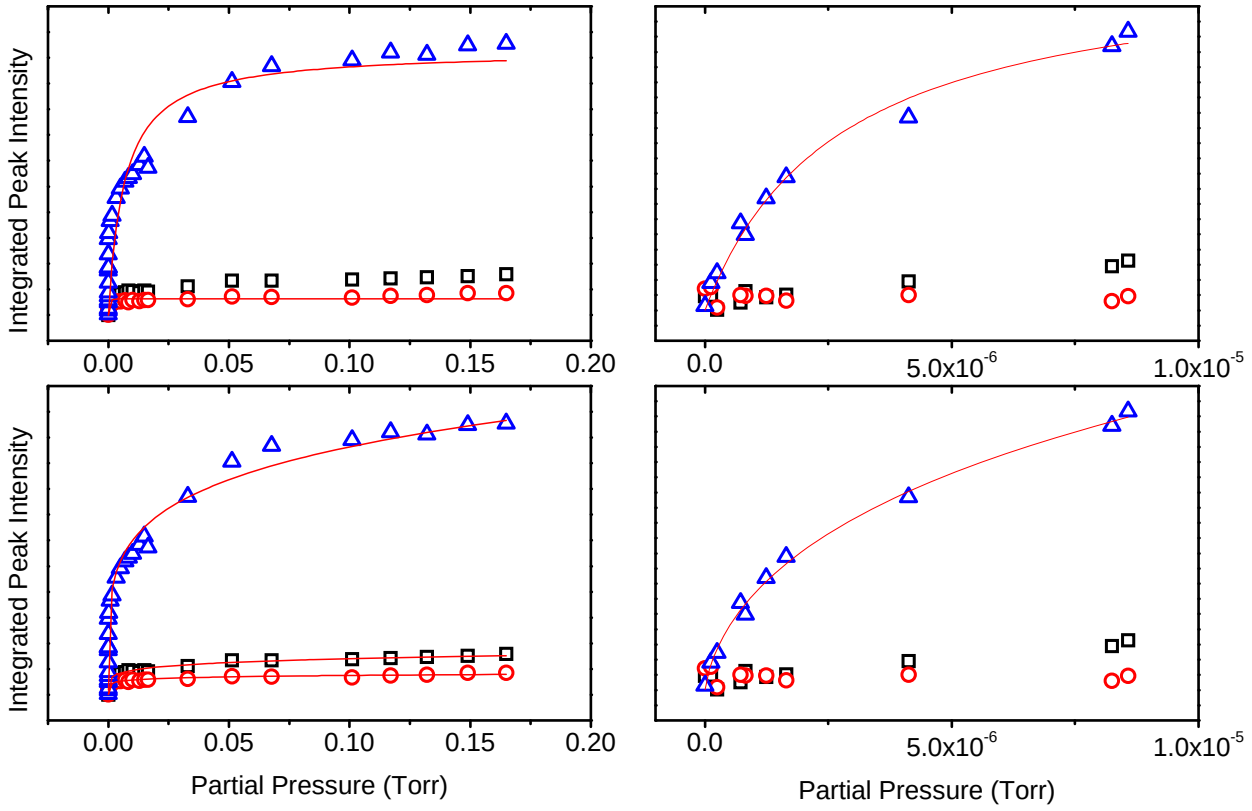

Figure 5-12: The adsorption isotherms of DMMP. The left panels are the full pressure range, the right panels are the low pressure range, the top row are the Langmuir isotherm fits, and the bottom row are the Toth isotherm fits.

For the entire pressure range investigated, the Toth model results in a much superior fit than does the Langmuir model. However, at the low pressure regime, both the Langmuir and Toth models fit extremely well, which implies that the adsorption of DMMP at low partial pressures is different that the adsorption over the entire pressure range. A possible explanation for this hypothesis is that at lower pressures, the assumptions of the Langmuir model are valid, but at the higher pressures, the assumptions fail and the Toth model, which considers heterogeneous surfaces, multilayer adsorption, and adsorbate-adsorbate interactions, results in the better fit. A further explanation of the isotherm observations and adsorption mechanism is presented in the discussion section.

Adsorption Isotherm of TMP

The RAIR spectra used to determine the adsorption isotherm of TMP on the silica nanoparticulate film are shown in Figure 5-13. The vibrational mode assignments and their relevance to the adsorption mechanism of TMP were explained previously. The total pressure where TMP adsorption was initially detected was 5.0 x 10^{-5} Torr, which is two times less than that of DMMP. This suggests that the TMP has a stronger interaction with the silica than does DMMP, and this agrees with the work of Tripp who observed that DMMP desorbed from a silica film at a lower temperature than TMP.[44]

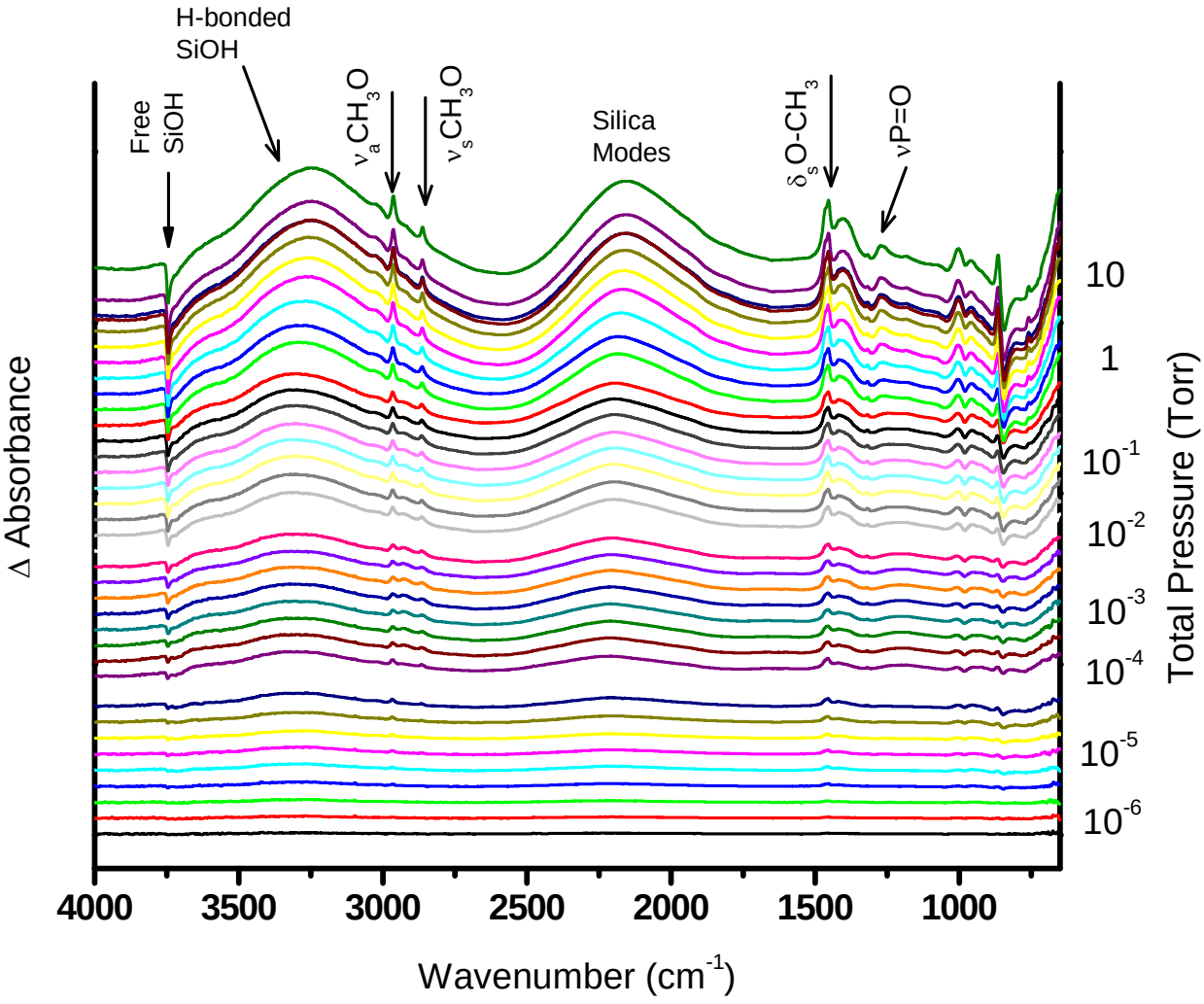

Figure 5-13: RAIR difference spectra of TMP adsorbed to a silica nanoparticulate film on gold as a function of total chamber pressure.

The integrated intensities of the same modes used for the DMMP isotherms were used to create the TMP isotherms. The isotherms were similar in appearance to the DMMP isotherms in the fact that at a partial pressure of 0.025, the absorbance intensities increase abruptly. As was done with DMMP, the turbo pumps were stopped when the total chamber pressure exceeded 5×10^{-4} Torr, and the change in the isotherm data appears at this pressure. The data was fit with the Langmuir and Toth models for both the total pressure range investigated, and at total pressures less than 10^{-4} Torr. The fitting parameters and correlation coefficients are provided in Appendix C.

The adsorption of TMP to the silica nanoparticulate films appears very similar to that of DMMP, which should be expected because both molecules interact with the silica via hydrogen bonding of the methoxy groups. The isotherms of the total and low pressure regimes for TMP followed the same trends as the DMMP; the Toth model provided a superior fit over the whole pressure range, but both the Langmuir and Toth models provided good fits at the low pressure regime. As was explained for DMMP, at the low pressure regime, the assumptions of the Langmuir isotherm are most likely valid, but at the higher pressures, the assumptions fail and the Toth model becomes valid.

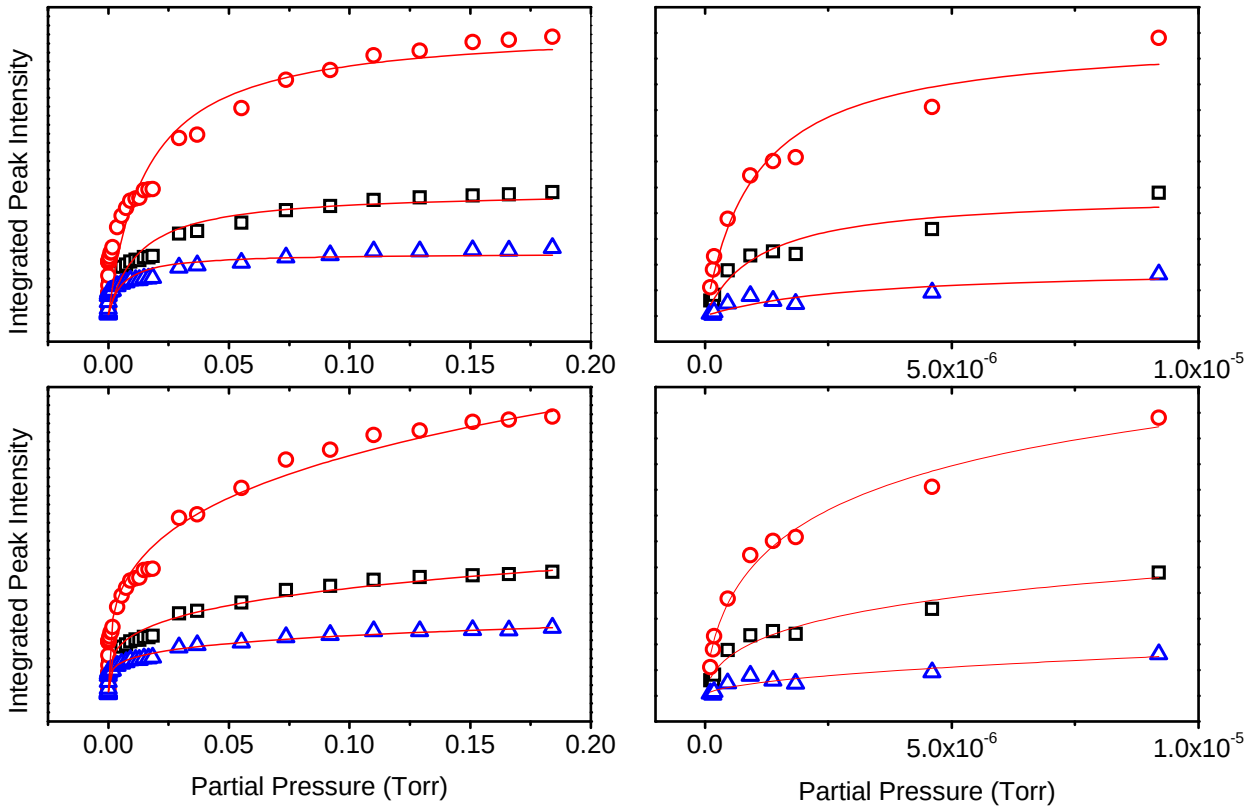

Figure 5-14: The adsorption isotherms of TMP. The left panels are the full pressure range, the right panels are the low pressure range, the top row are the Langmuir isotherm fits, and the bottom row are the Toth isotherm fits.

Adsorption Isotherm of MDCP

The RAIR spectrum of MDCP adsorbed to silica at 30 Torr revealed significant differences compared to the TMP and DMMP spectra. Even though there was evidence for adsorption, the MDCP spectrum was dominated by features consistent with gas phase MDCP. Because there was less adsorption of MDCP to the silica, we expected the adsorption isotherms of MDCP to also be different than those of DMMP and TMP. The RAIR spectra of MDCP recorded as a function of total pressure are shown in Figure5-15. The interaction strength of MDCP with silica relative to TMP and MDCP can be ascertained by determining the lowest pressure where adsorption could be detected. The first evidence for adsorption occurred at a pressure of 1 x 10^{-2} Torr, which is 100 times greater than that for DMMP, and 200 times greater than TMP. The weaker interaction of MDCP agrees with Tripp's study where they observed the

desorption of MDCP via evacuation at room temperature.[44] The isotherm data, prepared from the integrated peak intensities of the RAIR spectra of Figure 5-15, is shown in Figure 5-16.

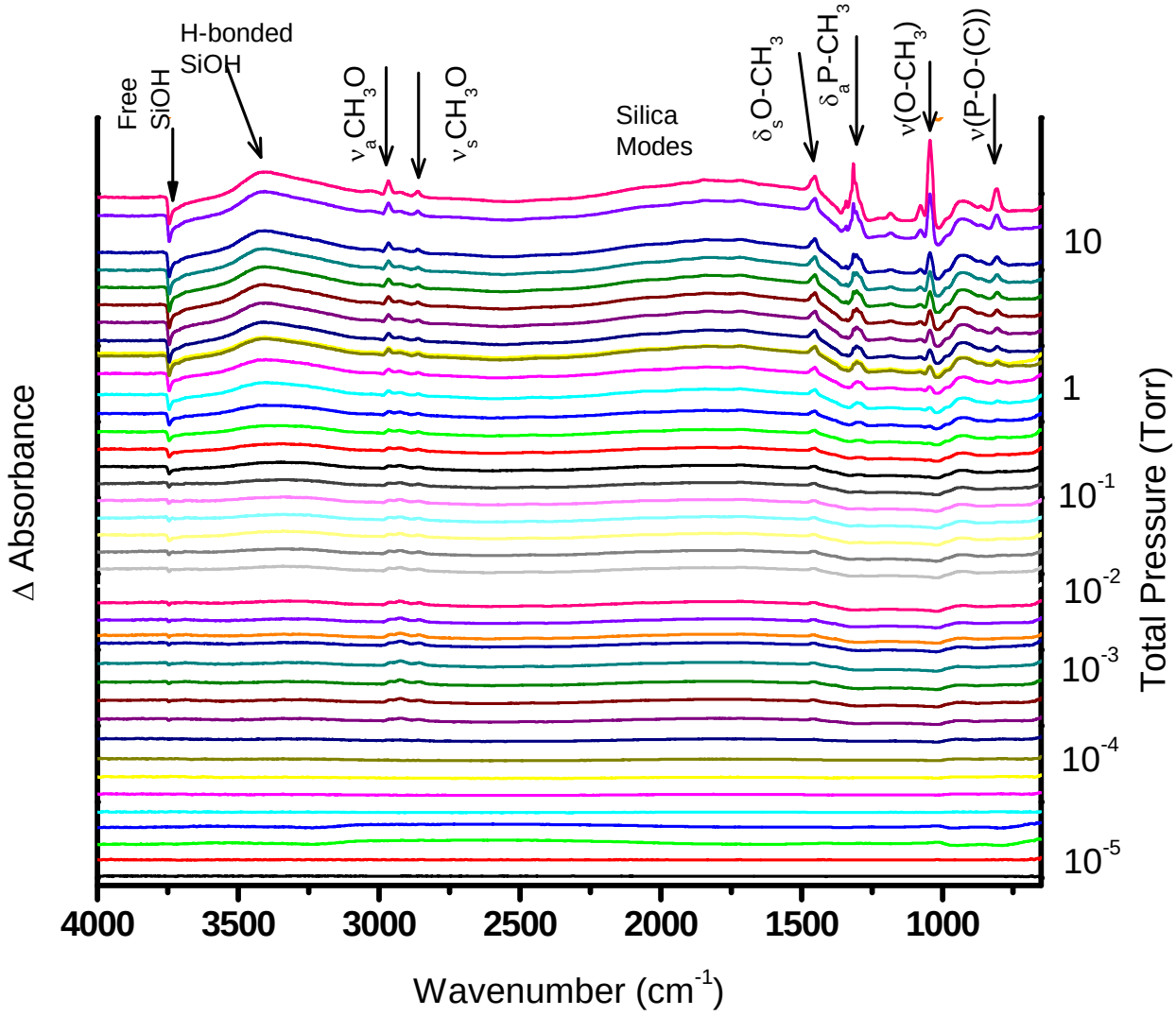

Figure 5-15: RAIR difference spectra of MDCP adsorbed to a silica nanoparticulate film on gold as a function of total chamber pressure.

The adsorption isotherm data of MDCP is much different that corresponding DMMP and TMP data, which is consistent with the differences observed in the single RAIR spectra collected at higher pressure (> 10 Torr). The isotherm data for MDCP cannot be modeled by any of the well-known adsorption models as the correlation coefficients were all below 0.70, and because of the poor fits, we do not display the fitting lines or the model parameters. Both the persistence of gas phase vibrational modes and the poor isotherm data of MDCP can likely be explained by the weak interaction between the MDCP and the silanol groups of the silica nanoparticulate film.

The residence time of the adsorbed MDCP molecules is very short at the relatively low pressures studied (relative to atmospheric).

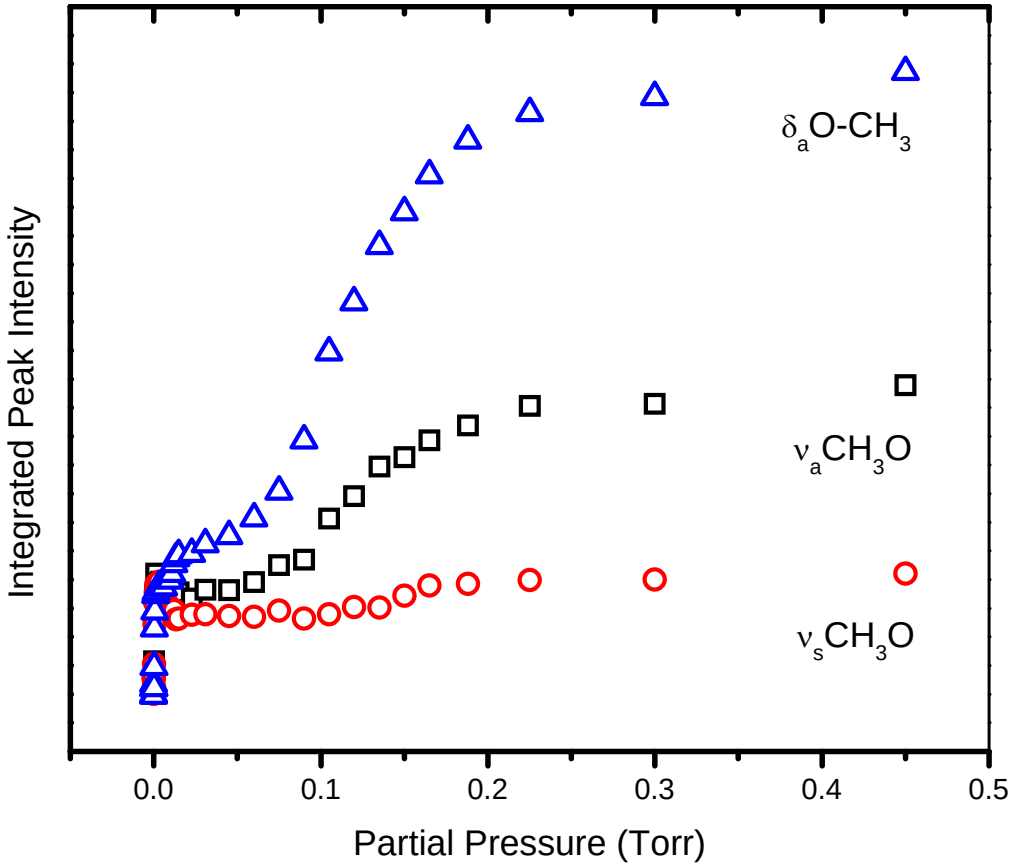

Figure 5-16: The isotherm data of MDCP.

5.5 Discussion of the Adsorption of DMMP, TMP, and MDCP to Silica Nanoparticulate Films

In the work presented here, we investigated the adsorption of three chemical warfare agent simulants, dimethyl methylphosphonate (DMMP), trimethyl phosphate (TMP), and methyl dichlorophosphate (MDCP), to silica nanoparticulate films. The goals of our study were to determine the structure of the adsorbed simulant molecules, to determine the adsorption mechanism, and to evaluate silica a sorbent material for further study of CWA simulant decomposition. We used RAIRS in our study to determine both the structure of the adsorbed simulant molecules, and to prepare adsorption isotherms that presented the IR absorbance intensity as a function of partial pressure. In this section, we discuss the key results of our study.

The RAIR spectra of the simulants recorded at higher pressure (10-30 Torr) helped reveal the structure of the adsorbed simulant molecules. When a molecule binds to a surface, the absorption frequency of certain vibrational modes shift as a result of the newly formed surface bonds. The vibrational modes of both the sorbent and adsorbate species can shift, and by correlating the shifts, one can determine how the adsorbate molecule interacts, or bonds, with the sorbent surface molecules. The frequency shift of the vibrational modes of the simulant molecules relative to the gas phase spectra, along with the shift of the silanol modes, helped reveal the structure of adsorbed DMMP and TMP.

DMMP contains three groups that are capable of hydrogen bonding with the surface silanol moieties: the phosphoryl group and the two methoxy groups. If the functional groups interact with the surface, the absorption frequency red shifts because the original dipole moment strength is diminished as a result of the interaction with the surface. DMMP showed a shift in the phosphoryl stretching frequency (νP=O) from 1275 cm^{-1} in the gas phase to a weak, broad peak centered near 1240 cm^{-1}. In addition, the O-C stretching modes of the two methoxy groups (νO-CH_3), found at 1075 and 1049 cm^{-1} in the gas phase spectra disappear completely in the RAIR spectra. In addition, the stretching mode of the silanol groups (νSiO-H) shifts from 3747 cm^{-1} to 3238 cm^{-1}. The combination of the red shifts of the stretching modes of silanol and the DMMP groups capable of hydrogen bonding indicates that the DMMP adsorbs to the silica via hydrogen bonding interactions between the phosphoryl and methoxy groups and the surface silanol species. This gave rise to two possible bonding configurations as shown in Figure 5-7.

The shift of the phosphoryl stretch of DMMP adsorbed to silica is much less than that observed for metal oxides. We observed a phosphoryl group shift on silica of around 30 cm^{-1} to 1240 cm^{-1}, but on other metal oxides the shifts were much larger. On TiO_2/Nb,[31] the P=O mode shifted to 1210 cm^{-1}, on Pt(111)[203] to 1215 cm^{-1}, on Al_2O_3[31] and MgO[43] to 1190 cm^{-1}, on La_2O_3[43] to 1224 cm^{-1}, and on Fe_2O_3[43] to 1077 cm^{-1}. If the DMMP were interacting with the silica via a hydrogen bonding interaction of the phosphoryl group, we would expect the frequency to be much larger than what was observed. Because the shift is small compared to the other metal oxide systems, we conclude that the most probable structure of adsorbed DMMP is the hydrogen bonding interaction of the two methoxy groups with two surface-bound silanol groups.

The RAIR spectra of TMP adsorbed to silica appeared similar to DMMP. The phosphoryl stretching mode red shifted from 1290 cm^{-1} to 1268 cm^{-1}, and the O-C methoxy stretching modes are absent. The silanol stretching mode shifted as well, from 3747 cm^{-1} to 3292cm^{-1}, which, like DMMP, indicates that the TMP interacts with the free silanol groups of the silica via hydrogen bonding interactions of the methoxy and phosphoryl groups, and possible bonding structures were shown in Figure 5-9 However, the proposed structure where all three methoxy groups and the phosphoryl group hydrogen bond with a silanol is unlikely because the TMP molecule would adopt a highly constrained and energetically unfavorable conformation. As a result, it is unlikely that the phosphoryl group participates in hydrogen bonding with the surface silanol groups and the adsorption is dominated by the surface interaction of the methoxy groups only. The shift of the phosphoryl stretching frequency has been observed previously, and is most likely due to the sensitivity of functional groups attached to a central phosphorus atom.[218]

The RAIR spectrum of MDCP adsorbed to silica at 30 Torr was much different than the spectra of DMMP and TMP. The phosphoryl stretching mode did not shift from its gas phase value, and the O-C methoxy stretching modes are clearly visible. The static appearance of the RAIR spectrum relative to the gas phase spectrum indicates that the MDCP does not adsorb to silica as strongly as the other two simulants. The low concentration of adsorbed MDCP (compared to the gas phase) is likely caused by two factors.

First, the interaction strength of MDCP with the silica is probably much lower than the DMMP and MDCP. This was shown previously by Tripp who observed that a silica surface saturated with MDCP completely desorbed in vacuum at room temperature.[44] The gas-phase dominated RAIR spectrum was recorded at low pressure relative to atmosphere At low pressure, the interaction between the hydrogen bonding groups of the MDCP and the surface silanol groups is relatively weak, resulting in a shorter residence time for the adsorbed MDCP. This hypothesis is further supported by the isotherm data and will be discussed shortly.

The second factor that may limit the adsorbed concentration of MDCP is the reactivity of the MDCP molecule. MDCP differs from TMP and DMMP because it contains two P-Cl bonds, which are prone to undergo hydrolysis reactions.[34] The MCDP can react with both silica-adsorbed water, and minute water contaminates found in the MDCP liquid. As shown in Figure 5-17, the hydrolysis reaction results in the replacement of a chlorine atom with a hydroxyl group

along with the formation of a hydrogen chloride (HCl) molecule. The remaining P-Cl bond can also be hydrolyzed to form a dihydroxy-containing species. The hydrolysis of MDCP by surface-adsorbed water molecules is likely because the silica nanoparticulate films were not heated prior to the adsorption experiments, and the films were prepared in an ambient environment without effort to eliminate water vapor.

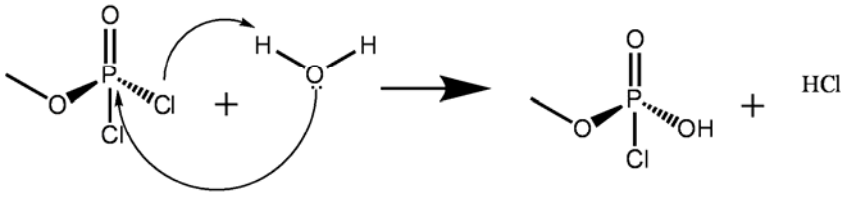

Figure 5-17: Schematic of the hydrolysis reaction of MDCP.

The adsorption of the simulant molecules to silica was further investigated by forming adsorption isotherms. The isotherms were formed by first recording the RAIR spectra of the adsorbed simulant as a function of total pressure. The absorbance intensity of selected vibrational modes were integrated and plotted against the partial pressure. The data was then fit with two thermodynamically consistent isotherm models to help ascertain the adsorption mechanism. In addition, the relative interaction strength with silica of the three simulants was determined from the RAIR spectra.

The explicit calculation of the binding energy of an adsorbed molecule is typically determined by plotting the surface coverage as a function of exposure time at constant pressure. The binding energy is related to the residence time by the following equation:

$$\tau \approx \frac{h}{kT} e^{E_a / kT}$$

Equation 5-7

where τ is the residence time, h is the Planck's constant, k is the Boltzmann constant, T is the absolute temperature, and E_a is the binding energy. In our experimental setup, we were unable to directly measure the surface coverage of the adsorbed simulants, however we were able to measure the infrared absorbance intensity, which is related to surface coverage in the following way:

The quantity of adsorbed simulant is in equilibrium with the amount of simulant in the gas phase, as represented in the following equilibrium equation:

$$[S]_g \rightleftharpoons [S]_s$$

Where $[S]_g$ and $[S]_s$ are the concentration of simulant in the gas phase and adsorbed to the surface, respectively. The equilibrium constant of the adsorption process is given by:

$$K = \frac{[S]_S}{[S]_g}$$

Equation 5-8

and the equilibrium constant, K, is directly proportional to the residence time, τ. In our measurements, the IR absorbance intensity of the surface bound vibrational modes is proportional to the surface concentration, which related to the equilibrium constant and the residence time, and therefore the binding energy (or interaction strength) of the simulant.

The relative interaction strengths with silica of the three simulants can be determined from the RAIR spectra in two ways. The first way is by comparing the shift from 3747 cm^{-1} of the silanol stretching mode. A stronger hydrogen bonding interaction of the silanol groups with the simulants will result in a larger red shift of the absorbance frequency. The MDCP had the smallest shift of 350 cm^{-1} to 3397 cm^{-1}, followed by TMP with a shift of 455 cm^{-1}, and DMMP at 509 cm^{-1}. The data indicates that DMMP had the strongest interaction with the silica, however this contradicts the expected interactions strengths predicted by the number of hydrogen bonds each molecule makes with the surface. The TMP forms a hydrogen bond with each of its three methoxy groups data indicates that DMMP had the strongest interaction with the silica, however this contradicts the expected interaction strengths predicted by the number of hydrogen bonds each molecule makes with the surface. The TMP forms a hydrogen bond with each of its three methoxy groups, and the DMMP can form up to three hydrogen bonds as well, via interaction with the two methoxy groups and the phosphoryl group. However, we earlier concluded that the phosphoryl group does not hydrogen bond to the surface because the shift of the phosphoryl stretch was much lower than what would be expected if hydrogen bonding did occur. That conclusion is further supported by observing the shift of the silanol stretch for the adsorbed

DMMP. If the DMMP adsorbed through both the methoxy groups and the phosphoryl group, then there should be two observed shifted silanol modes. We only observed one shift from the more strongly interacting methoxy groups; therefore the bifunctional binding of DMMP through the two methoxy groups is the most probable adsorbed structure.

The relative interaction strengths of the adsorbed simulants were also revealed by determining the lowest total pressure upon which adsorption could be detected. The more strongly interacting species should be detected a relatively lower pressure. The three simulants followed the trend of TMP > DMMP >> MDCP. Evidence for TMP adsorption was observed at a pressure of 5×10^{-5} Torr, followed by DMMP at 1×10^{-4} Torr, and MDCP at 1×10^{-2} Torr. The trend follows the expected order based on the number of hydrogen bonding interactions each molecule makes with the silica surface. The TMP interacts trifunctional via hydrogen bonding of three methoy groups, the DMMP interacts bifunctionaly via hydrogen bonding of two methoxy groups, and the MDCP interacts bifunctionally via the hydrogen bonding of one methoxy group and one relatively weaker hydrogen bonding phosphoryl group. This is in agreement with a previous adsorption study that found the simulant desorption temperature decreased in the same order, TMP > DMMP > MDCP.

5.6 Discussion of Isotherm Data

The adsorption isotherms of both DMMP and TMP revealed that the system behaved differently at different pressures. The isotherms at both pressure ranges were fit with the Langmuir and Toth isotherm models, which are both thermodynamically consistent, but differ in their assumptions about the system. The Langmuir model assumes that the surface is flat, each adsorption site is equivalent, and the highest possible surface coverage is a monolayer. In contrast to the Langmuir assumptions, the Toth model allows for non-planar surfaces, hetergenous adsorption sites, and the formation of multilayers. By fitting both the low and total pressure regimes with the two isotherm models, we observed different adsorption behaviors.

For both DMMP and TMP, at low pressure, both the Langmuir and Toth models fit well, but over the entire pressure range, only the Toth model provided a good fit. These observations suggest that the adsorption mechanism is different for the low and high pressure regimes, and we

hypothesize that the heterogeneity of the silica surface is the factor most responsible for the adsorption behavior. The schematics shown in Figure 5-18 aid in the discussion of the adsorption at the two different pressure ranges.

If the silica surface is heterogeneous, some adsorption sites will be more favorable than others. In the case of simulant adsorption to silica, the most favorable sites may be those that contain free silanol groups spaced far enough apart to match the distance between the simulant methoxy groups. At low pressure, the adsorption equilibrium favors the gas phase simulant, which results in a low simulant surface coverage. The molecules that do adsorb at low pressure will adsorb to the preferential binding sites. In the top panel of Figure 5-18, the preferential binding sites are colored grey, and only the grey silanol groups are bound to the green circles, which represent the simulant molecules. If only the preferential binding sites interact with simulant molecules, the isotherm data should conform to the Langmuir model because only one type of binding site is interacting with the adsorbates. This is precisely what was observed for both DMMP and TMP.

At higher pressures, which are represented by the bottom panel schematic of Figure 5-18, the adsorption is different. At this point, all of the preferential binding sites are occupied, which, according to the Langmuir isotherm, means that the surface coverage should be at a maximum. Clearly the saturation of the preferential binding sites was not the end of adsorption as the absorbance intensities continued to increase beyond the low pressure regime. Beyond preferential binding site saturation, the Langmuir model should no longer produce a good fit. After the initial saturation of the preferred binding sites, the secondary binding sites begin to interact with adsorbed simulant molecules. In the bottom schematic of Figure 5-18, the secondary binding sites are indicated by the black silanol groups, and the simulant molecules adsorbed to those sites are represented by the red circles. The Toth model, which accounts for surface heterogeneity and different types of binding sites, fit the data beyond the low pressure regime very well.

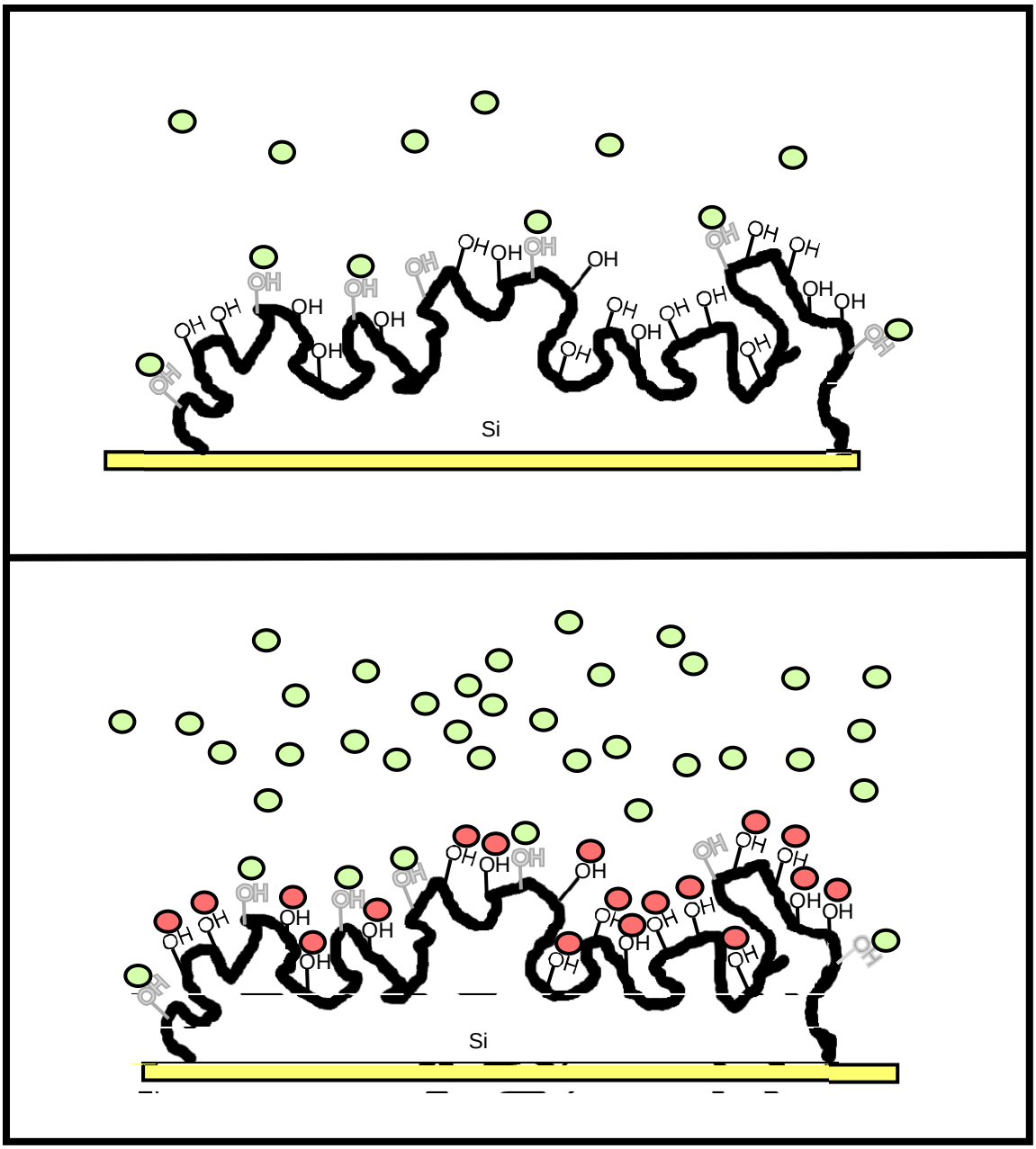

Figure 5-18: Schematic of the adsorption of simulant molecules to a heterogeneous silica nanoparticulate film at low (top panel) and high pressure (bottom panel).

5.7 Conclusions

The goal of this part of our study was to determine the structure, relative interaction strengths, and adsorption mechanism of the adsorption of the chemical warfare agent simulants DMMP, TMP, and MDCP, to silica nanoparticulate films. To accomplish our goals, we utilized RAIRS in two different ways: 1) the structure of the adsorbed molecules was determined via

analysis of the shifts of certain vibrational modes of the RAIR spectra and, 2) the adsorption mechanism was deduced via the formation of adsorption isotherms displaying the integrated intensity of selected vibration modes as a function of simulant partial pressure. Our results led to the following conclusions:

1) DMMP and TMP adsorb to the silica via the formation of two and three hydrogen bonds, respectively, between the methoxy groups of the simulants and the free silanol groups of the silica. Our conclusions were based on the red shift of the silanol stretching vibration and the disappearance of the methoxy stretching modes relative to the gas phase spectra. Interaction via hydrogen bonding of the phosphoryl groups was ruled out because the shift of the phosphoryl stretching mode was much lower than those reported in the literature.

2) The interaction of MDCP and the silica was too weak for significant adsorption to occur at the relatively (compared to atmosphere) pressures used in our study. The RAIR spectra were dominated by vibrational modes characteristic of gas phase MDCP, which indicated that very little MDCP had adsorbed to the surface.

3) The relative interaction strength of the simulants with silica followed the trend of TMP > DMMP >> MDCP. We determined the trend by determining the lowest total pressure where spectral evidence of adsorption could be observed. The trend correlates with the number of hydrogen bonding interactions each simulant can make with the silica; TMP has three methoxys, DMMP has two methoxys, and MDCP has one methoxy and one phosphoryl group.

4) The adsorption mechanism of DMMP and TMP to the silica nanoparticulate films is dependent on the pressure and the different types of binding sites that are found on the heterogeneous silica sorbent. At low pressures, the adsorption occurs to preferential binding sites only and the isotherms follow the Langmuir model. At higher pressures, the preferential binding sites are saturated, and further adsorption occurs and secondary binding sites. The Toth model accounts for surface

heterogeneity and fit the data much better than the Langmuir model at higher pressures.

5.8 Future Work

Our work presented here revealed the surface structure, relative interaction strengths, and adsorption mechanism of the adsorption of DMMP and TMP to silica nanoparticulate films. In future experiments, emphasis should be placed on a third important measurement. First, a mass spectrometer should be included to get an accurate measurement of the partial pressure of the simulants during the collection of isotherm data. Second, the quantity of adsorbed simulant should be monitored, and third, the number of binding sites should be determined. By obtaining each of the three parameters, the thermodynamics of the adsorption process, such as the free energy of adsorption and simulant binding energy, can be calculated. Obtaining the thermodynamic parameters will further reveal the surface chemistry of chemical warfare agents simulants, and in the future, the study can be extended to the live chemical warfare agents.

Chapter 6

Summary and Concluding Remarks

6.1 Summary of Results

The work presented here investigated the synthesis and characterization of surfaces relevant to chemical and biological warfare agent defense. The overall goals were divided into three projects: 1) the development of a surface synthesis strategy to create alkanethiol self-assembled monolayers that contained long-chain quaternary ammonium groups, 2) the characterization of immobilized antimicrobial peptides, and 3) the design and construction of a new surface science instrument designed to study the reaction of oxidizing gases with bare and simulant covered surfaces of military relevance. Common to each project was the use of reflection-absorption infrared spectroscopy, which demonstrates its power and versatility when applied to study of surface reactions and structure. The following section summarizes the results and conclusions obtained from each of the three projects.

6.1.1 Surface Synthesis of Quaternary Ammonium Self-Assembled Monolayers

A surface synthesis strategy was employed to create an alkanethiol monolayer containing long chain quaternary ammonium groups. Long-chain QAC groups are well known antimicrobial agents, however little is known about the relationship between the function and structure of antimicrobial monolayers. The surface synthesis strategy was adopted to eliminate the labor intensive thiol protection and deprotection steps, as well as numerous separations steps that are encountered using traditional solution phase synthesis. The surface synthesis followed a general scheme. First, a carboxylic acid terminated self-assembled monolayer was formed on a gold substrate. The carboxylic acid groups were then converted to an amide species that contained a terminal tertiary amine group. The resulting tertiary amine groups then reacted with long chain 1-bromo-2-ketone molecules to form the quaternary ammoniums. The second and third steps of the reaction were optimized by investigating the effects of solvent, temperature, concentration, catalyst, and time. RAIRS and XPS were the primary analysis tool used to determine the success or failure of each reaction.

The conversion of the carboxylic acid groups into amide groups was best achieved by using an intermediate species. The acid groups were reacted pentafluorophenol in the presences of a carbodiimide catalyst to form a pentafluorophenol ester species. The PFP ester then served as an excellent leaving group during the reaction with a primary diamine. RAIRS confirmed the successful formation of the amide groups due to the disappearance of the acid carbonyl stretching mode at 1741 cm^{-1} and the appearance of the amide I and II modes at 1650 and 1545 cm^{-1}, respectively. XPS helped confirm that 90 percent of the carboxylic acid groups had reacted to form a tertiary amine group.

The optimal conditions for the reaction of the 1-bromo-2-ketone molecules with the tertiary amine groups were at room temperature using a 0.025 M solution in toluene. The reaction occurred slowly, taking over three weeks to reach completion. RAIR spectra confirmed the reaction was successful as the methylene stretching vibrations increased more than two-fold intensity, and a new peak was observed at 1732 cm^{-1}, which was characteristic of the carbonyl moiety on the ketone molecules. XP spectra further supported the formation of the quarternary ammonium groups. The N1s region of the XP spectra showed the formation of a new nitrogen oxidation state at 402 eV, which is characteristic of a quaternary nitrogen. The intensity of the quaternary nitrogen peak increased as a function of time. The relative concentration of quaternary ammonium groups was determined by measuring the intensity ratio of the quaternary and tertiary N1s peaks. At completion, 84 percent of the tertiary amine had reacted to form quaternary ammoniums. The resulting surface density of quaternary ammonium groups was calculated to be 3.4×10^{14} groups/cm^2.

The QAC-containing SAMs were tested for antimicrobial activity, and it was found that less than 15 percent of the bacteria challenged by the surfaces were killed. The low antimicrobial activity of the QAC SAMs was attributed to the surface density of the accessible quaternary ammonium groups being below the threshold necessary to cause membrane destabilization and subsequent death. Despite the low antimicrobial activity, our work successfully demonstrated that long chain quaternary ammonium monolayer can be formed using only surface reactions. Future work should focus on increasing the surface density of the quaternary ammonium groups, and suggested strategies include using branched thiols or gemini dithiols.

6.1.2 Surface Structure of Immobilized Antimicrobial Peptides

Recently a series of antimicrobial peptides were tested for their ability to selectively bind the pathogenic bacteria *E. coli* O157:H7. The peptides cecropin P1, PGQ, and pleurocidin were immobilized to gold substrates via the attachment of a terminal thiol-containing cysteine residue. By using surface plasmon resonance detection, cecropin P1 and PGQ showed a binding preference for the pathogenic bacteria strain relative to the non-pathogenic. The results were noteworthy, however the immobilized peptides were not characterized, and therefore the effects of peptide conformation and surface concentration upon binding were unknown. The focus of our work was to characterize the peptides after immobilization to gold substrates using RAIRS and XPS as the primary surface analysis tools.

The peptides cecropin P1, PGQ, and Pleurocidin all adopted a mostly flat and random orientation on the gold substrates. In atmosphere, the peptides folded into α-helical conformation as verified by the frequency of the amide I absorbance mode of the RAIR spectra. The surface structure of the peptides was found to be independent of the peptide conformation in solution. In an aqueous environment, the peptide molecules adopt a random coil conformation. Upon the addition of a non-polar solvent, such as trifluoroethanol, the peptides fold into their active α-helical conformation. The peptides were immobilized to gold from aqueous solutions with and without trifluoroethanol. RAIR spectra confirmed that the surface structures obtained under the two solution conditions were remarkably similar.

Cecropin P1 was selected for a more detailed investigation of the effects of solution parameters on the surface structure and density. The effects of pH, solution concentration, and peptide aggregation state were studied. Under all conditions, the peptides formed a mostly random, tilted layer of α-helices. The peptide aggregation state was the only condition to show an effect on peptide density. SDS-PAGE experiments showed that many of the peptides had formed dimers in solution due to the formation of a disulfide bond between two peptide molecules. By adding the disulfide reducing agent TCEP to the peptide solution, the dimerized peptides were all converted into monomers. The resulting peptide surface had a nearly two-fold larger surface density compared to the non-reduced peptide surface.

The results of our investigation into the structure of immobilized antimicrobial peptides have set the foundation for future studies focused towards creating peptide arrays to use for pathogen sensing. Future work will focus peptide structure on pre-modified substrates as well as modification of the peptide structures.

6.1.3 Chemical Warfare Agent Simulant Adsorption on Silica Nanoparticulate Films

The first part of our final project focused on designing and constructing a new surface science instrument that will allow us to study the interaction of the decontamination vapors hydrogen peroxide and chlorine dioxide with bare and chemical-warfare-agent-simulant covered surfaces of military relevance. The instrument couples an ultrahigh vacuum chamber with three capillary array gas dosers that allow various mixtures of gases to be directed toward the surface-of-interest simultaneously. The surface reactions are monitored by three analytical instruments that are coupled to the chamber: 1) a RAIR spectrometer used to monitor surface-bound products, 2) a mass spectrometer to monitor gas phase products, and, 3) an X-ray photoelectron spectrometer that allows for surface elemental analysis before and after a reaction.

The initial study using the new surface science chamber investigated adsorption of three chemical warfare agent simulants, DMMP, TMP, and MDCP, to silica nanoparticulate films formed on gold substrates. Silica is an excellent adsorbent material that binds but does not decompose CWA's or simulants, and the adsorption of the simulant molecules to silica films was investigated to elucidate the structure of the adsorbed molecules as well as the adsorption mechanism.

At pressures below 30 Torr, RAIR spectra revealed that DMMP and TMP adsorb to the silica via the formation of hydrogen bonds via methoxy groups. TMP bound through its three methoxy groups and DMMP through two. We determined that hydrogen bonding through the phosphoryl groups did not occur because of a relatively small frequency shift of the phosphoryl stretching mode compared to the gas phase spectra. MDCP showed some evidence of adsorption to the silica, however at 30 Torr the RAIR spectra was dominated by modes characteristic of gas phase MDCP. We hypothesized that the single methoxy and weak phosphoryl hydrogen bonding interactions were not strong enough to cause significant binding at the relatively low pressure of 30 Torr (compared to 760 Torr atmospheric pressure).

Adsorption isotherms of DMMP and TMP were prepared by recording RAIR spectra at increasing simulant partial pressure. The integrated intensities of select vibrational modes were then plotted as a function of partial pressure to form the isotherm plots. The data were fit with two isotherm models, the Langmuir and the Toth. The two models contain different assumptions about the adsorption system which can be used to determine an adsorption mechanism. The Langmuir model assumes a flat, homogeneous adsorbent layer that reaches saturation at monolayer coverage, and the Toth model allows for heterogeneous adsorption sites, porous material, and the formation of multilayers. At total pressures less than 5×10^{-4} Torr, the adsorption followed the Langmuir model, but over the entire pressure range (up to 30 Torr), the adsorption followed the Toth model. The different behavior observed at different pressure ranges was the result of heterogeneous binding sites on the silica surface. At low pressures, there are most likely a significant number of vacant preferential binding sites. Because the preferential binding sites are not totally occupied at low pressure, the isotherm follows Langmuirian behavior. At higher pressures, the preferential binding sites become saturated, and further adsorption must occur at secondary and tertiary binding sites. These sites may by different than the primary binding sites, and the occurrence of non-homogeneous binding sites violates the assumptions of the Langmuir model. The Toth model allows for heterogeneous binding sites, and at high pressures, it fit the data with greater than 0.95 correlation.

6.2 Concluding Remarks

The search for effective and safe means to detect, decontaminate, and destroy bacteria and chemical warfare agents remains a crucial endeavor to military and civilian authorities. Surface chemistry remains on the frontier of the investigation because the initial interaction of the harmful agents with potential detection and decontamination materials is via interfacial contact. Our work here has helped further the understanding of the design and structure of surfaces designed to kill, capture, and decompose both bacterial and chemical agents. In addition, we demonstrated the tremendous power and versatility of reflection-absorption infrared spectroscopy to a number of surface chemistry related problems. Continuing to increase the fundamental knowledge of the interfacial chemistry of warfare agents might someday lead the minimization of the threats caused by chemical and biological attacks.

Appendices

Appendix A

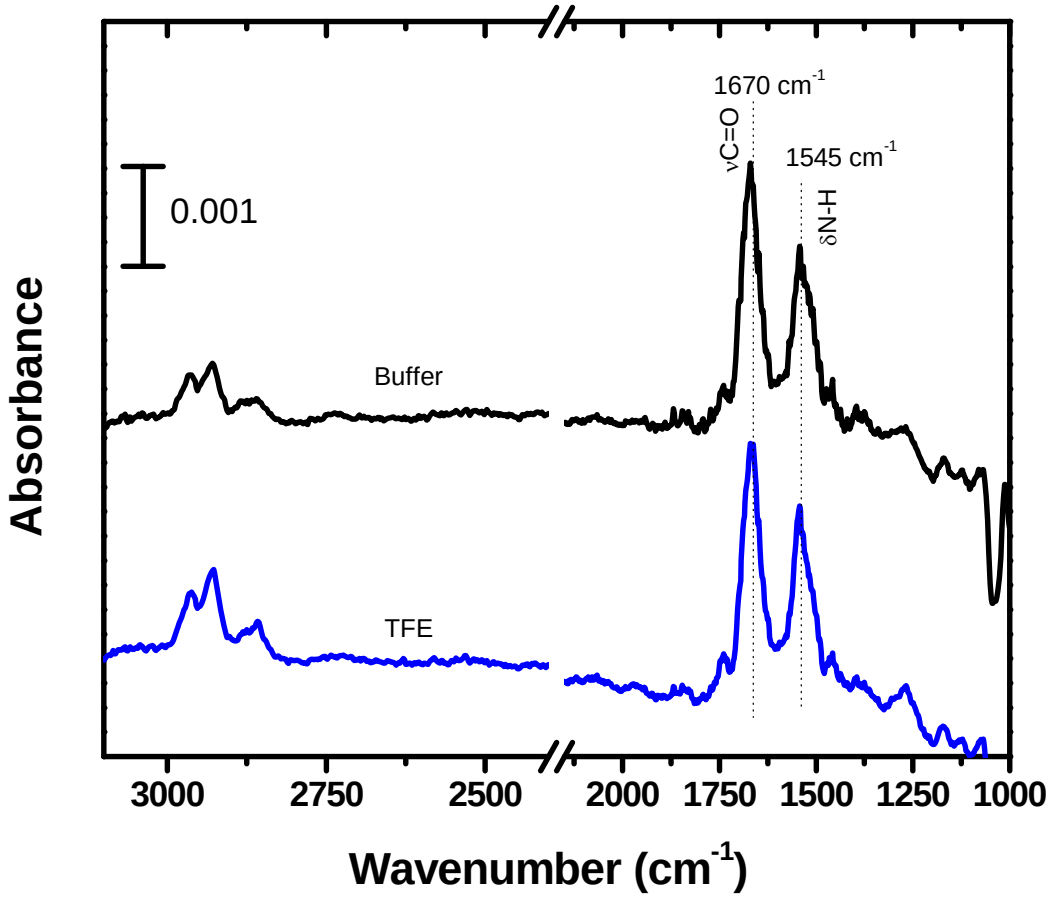

Figure A-1: RAIR spectra of cecropin P1 immobilized with and without 25% TFE in the buffer. The peptide solution concentration was 9.7 µM in pH 7.4 phosphate buffer.

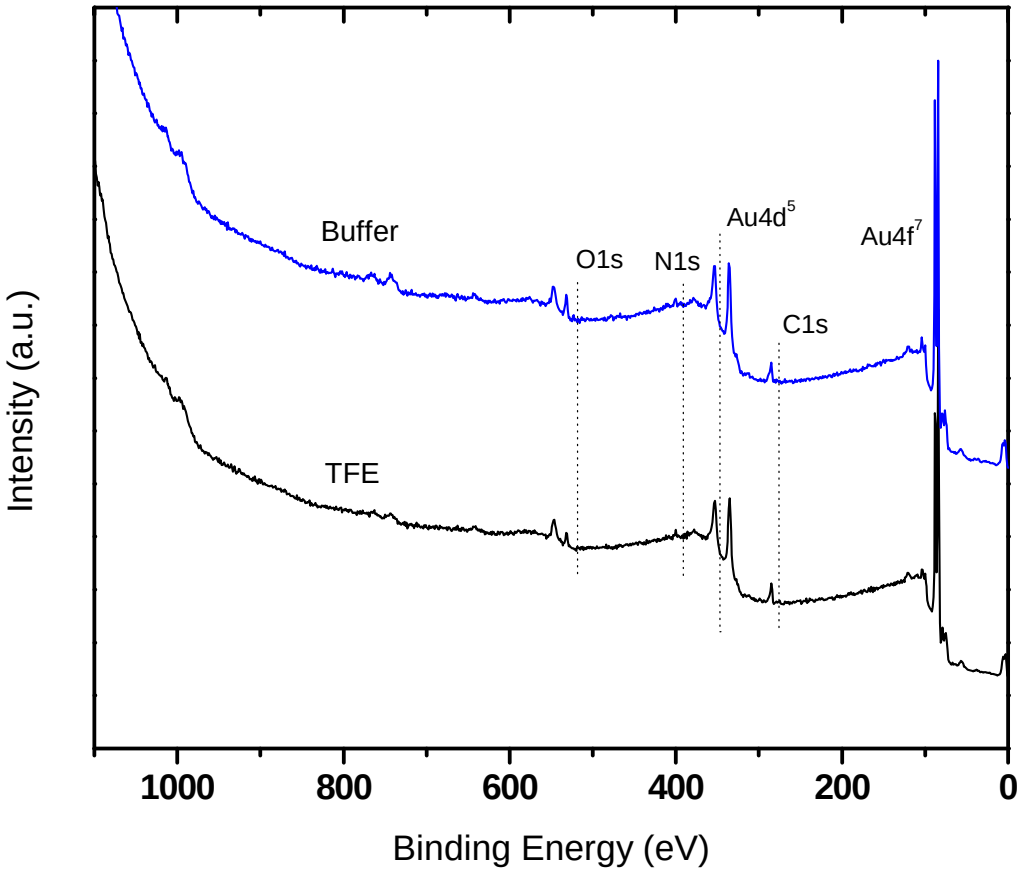

Figure A-2: X-ray photoelectron survey spectra of cecropin P1 immobilized with and without 25% TFE.

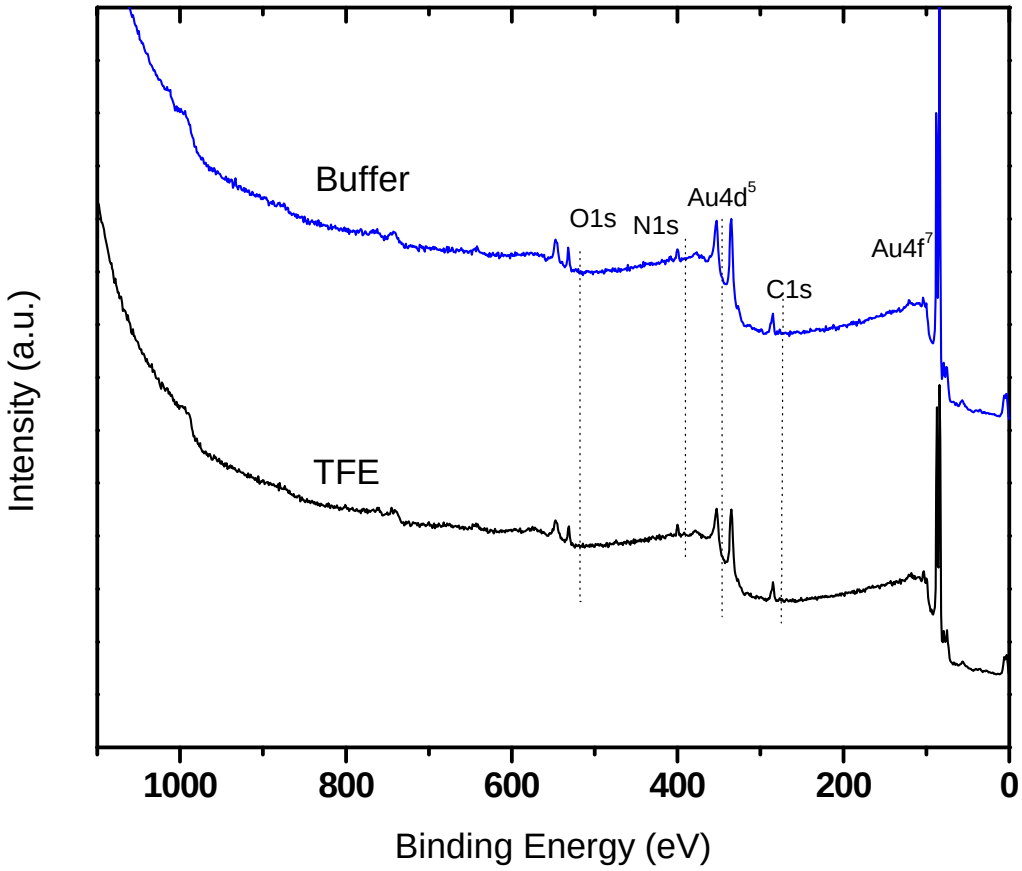

Figure A-3: XP survey spectra recorded for cecropin P1 immobilized with and without 25% TFE at a peptide solution concentration of 29.1 μM in pH 7.4 phosphate buffer.

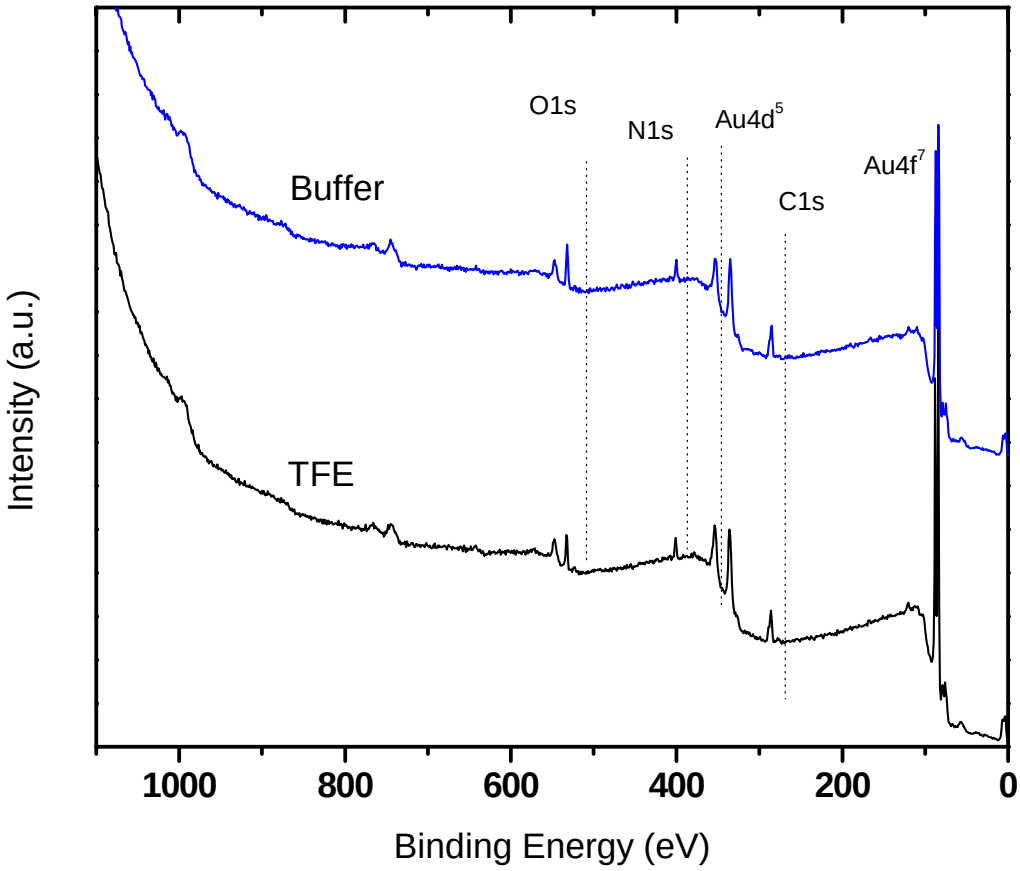

Figure A-4: XP survey spectra recorded for cecropin P1 immobilized with and without 25% TFE and 5 mM TCEP at a peptide solution concentration of 9.7 µM in pH 7.4 phosphate buffer.

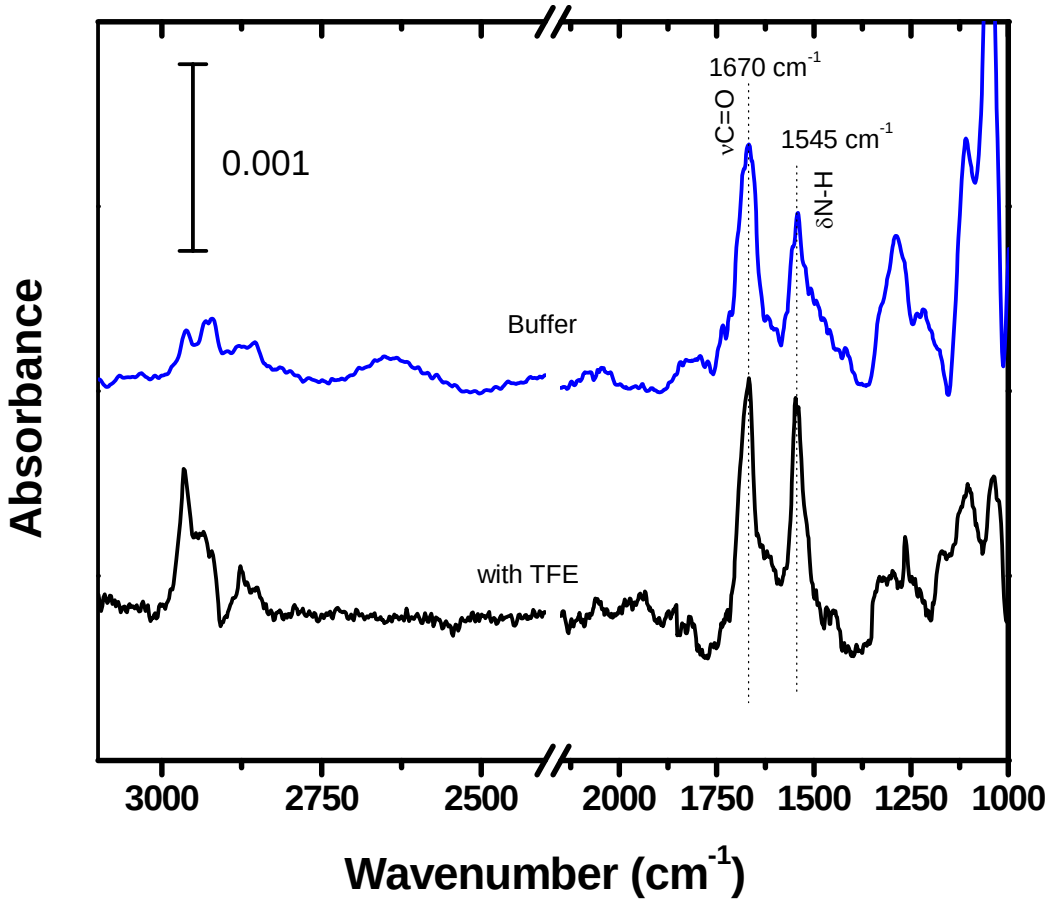

Figure A-5: RAIR spectra of PGQ immobilized with and without 25% TFE in the buffer. The peptide solution concentration was 13.0 μM in pH 7.4 phosphate buffer.

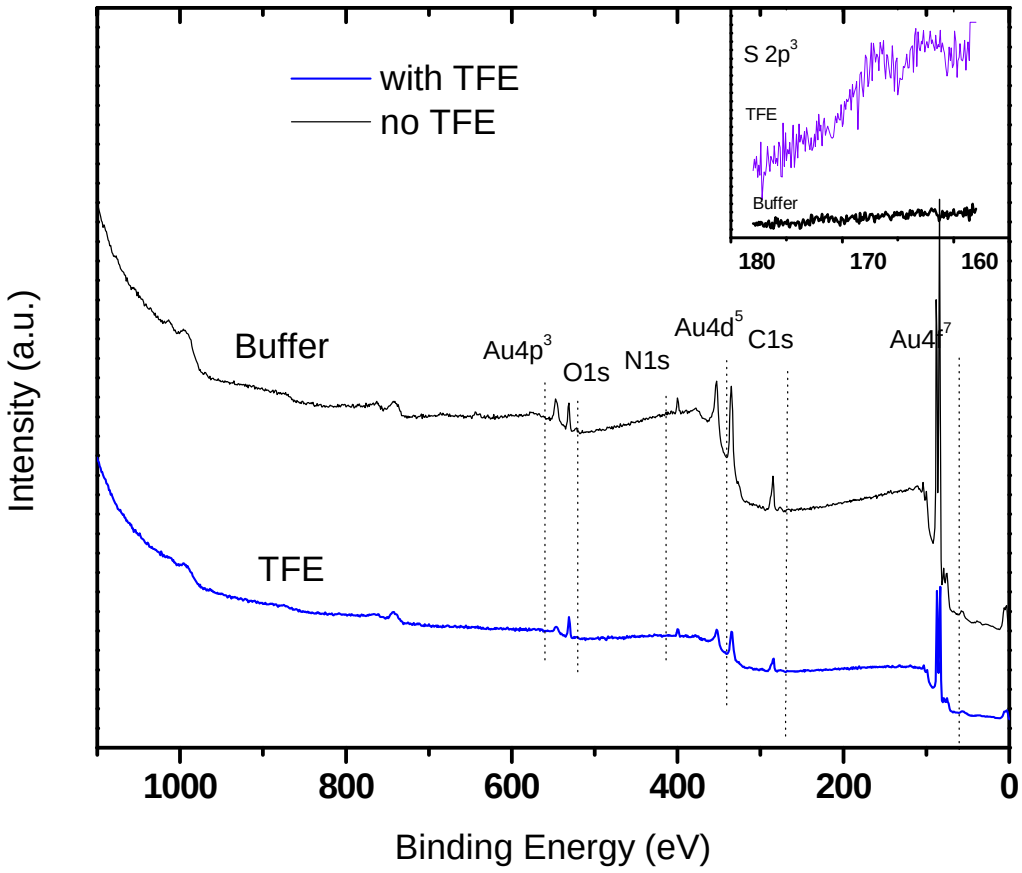

Figure A-6: X-ray photoelectron survey spectra of PGQ immobilized with and without 25% TFE along with the multiplex spectra of the S $2p^3$ region.

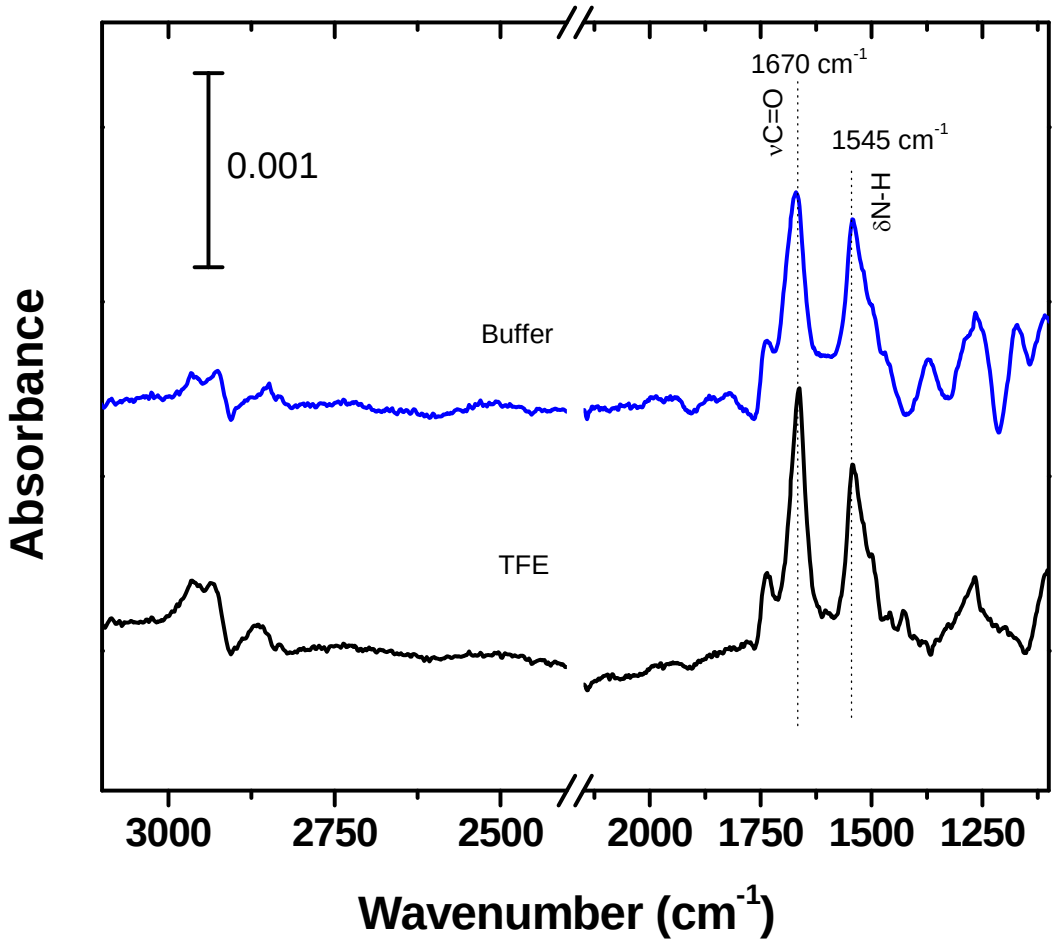

Figure A-7: RAIR spectra of pleurocidin immobilized with and without 25% TFE in the buffer. The peptide solution concentration was 11.0 µM in pH 7.4 phosphate buffer.

Appendix B

The following figures are from the block diagram of the interlock program used to run the surface analysis chamber.

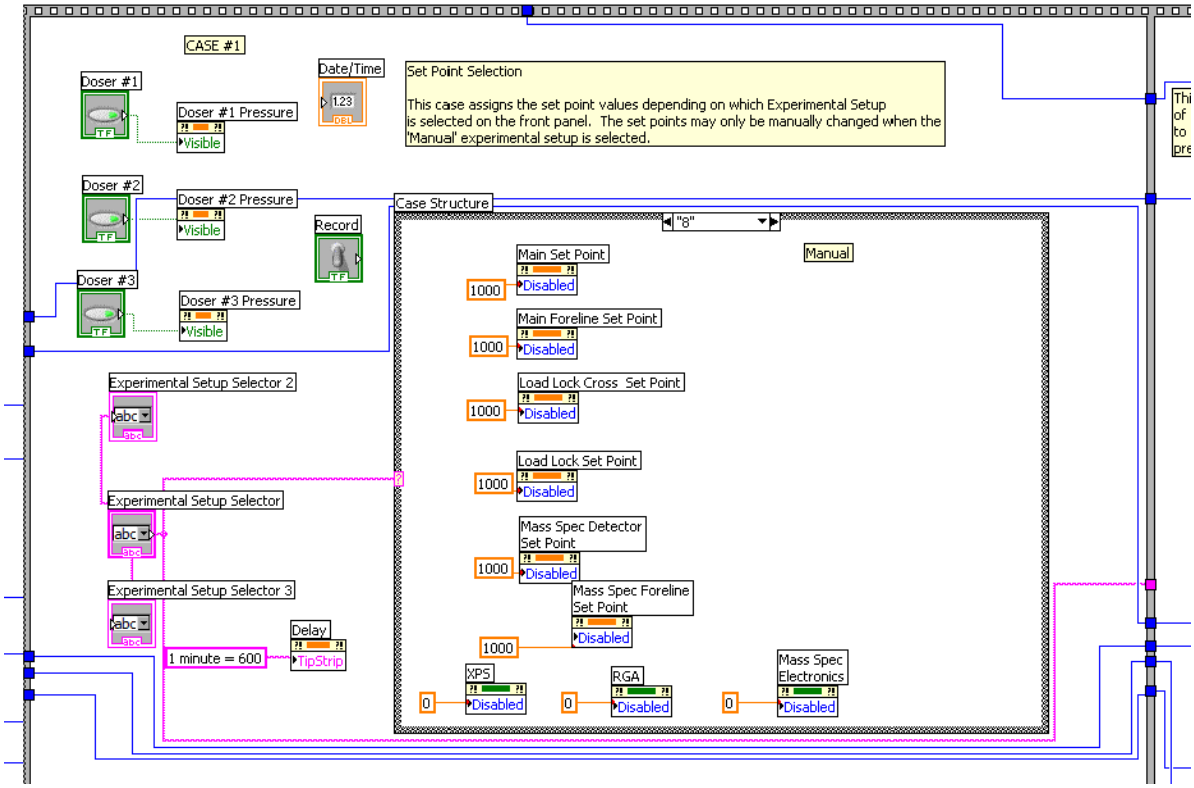

Figure B-1: Case 1 of the Chamber Interlock Program. The pressure set point conditions are defined

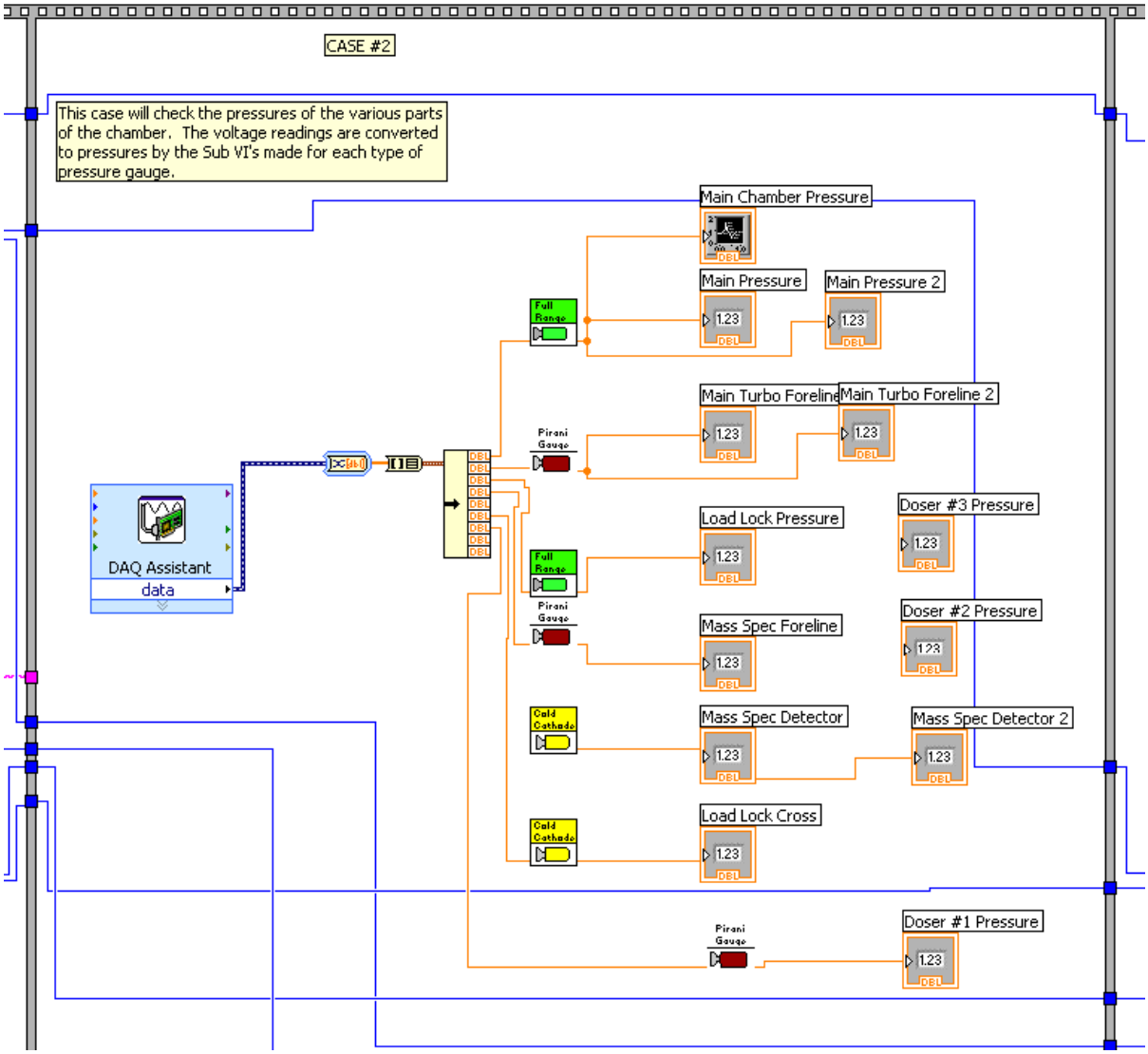

Figure B-2: Case 2 of the Chamber Interlock Program. The analog voltages are read from the gauge box, converted to a digital signal, converted to pressure, and displayed on the front panel.

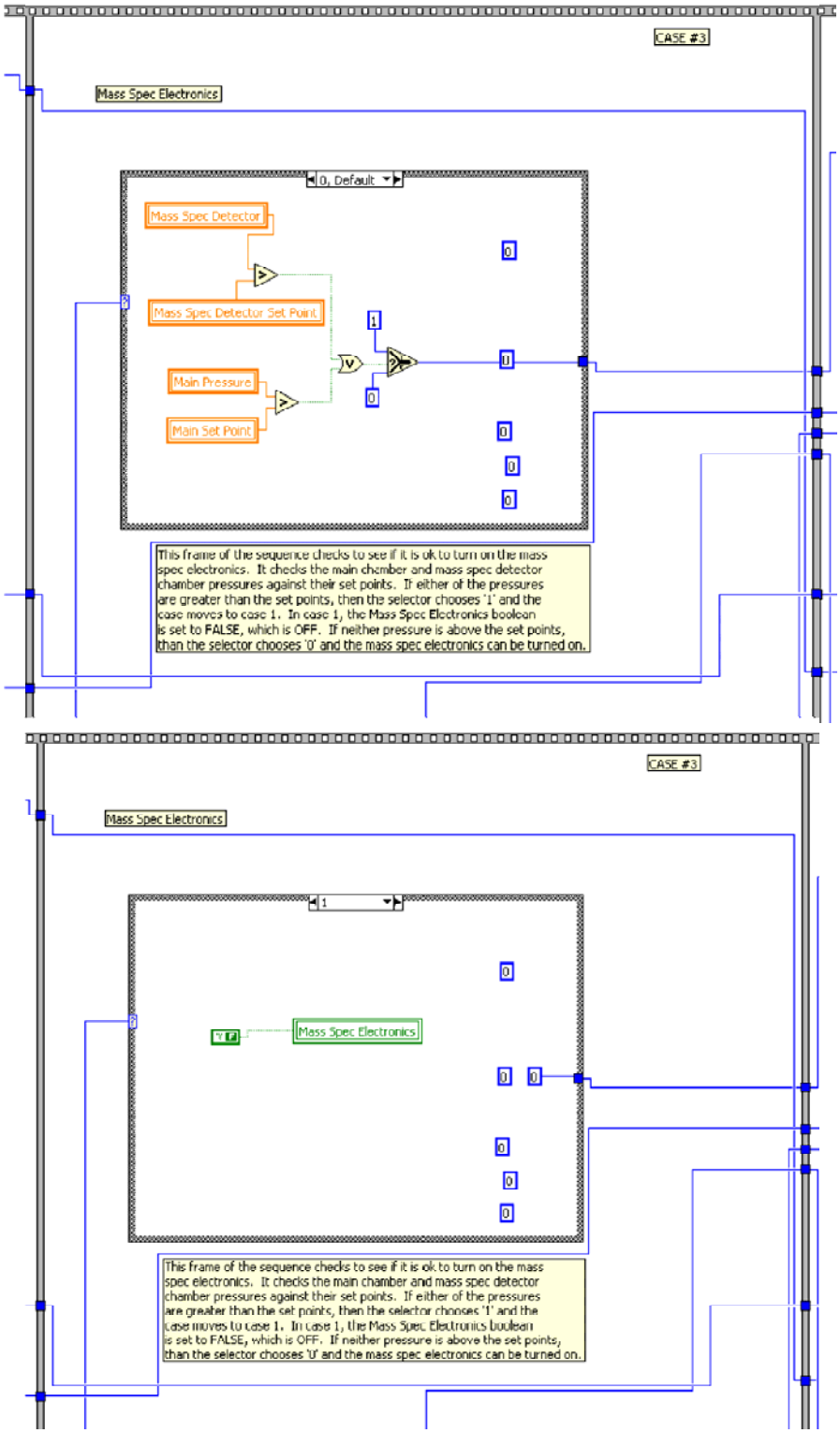

Figure B-3: Case 3 of the Chamber Interlock Program. The mass spec detector and main chamber pressures are checked against the set points. If either pressure is above the set point, the mass spec electronics cannot be turned on.

Figure B-3:

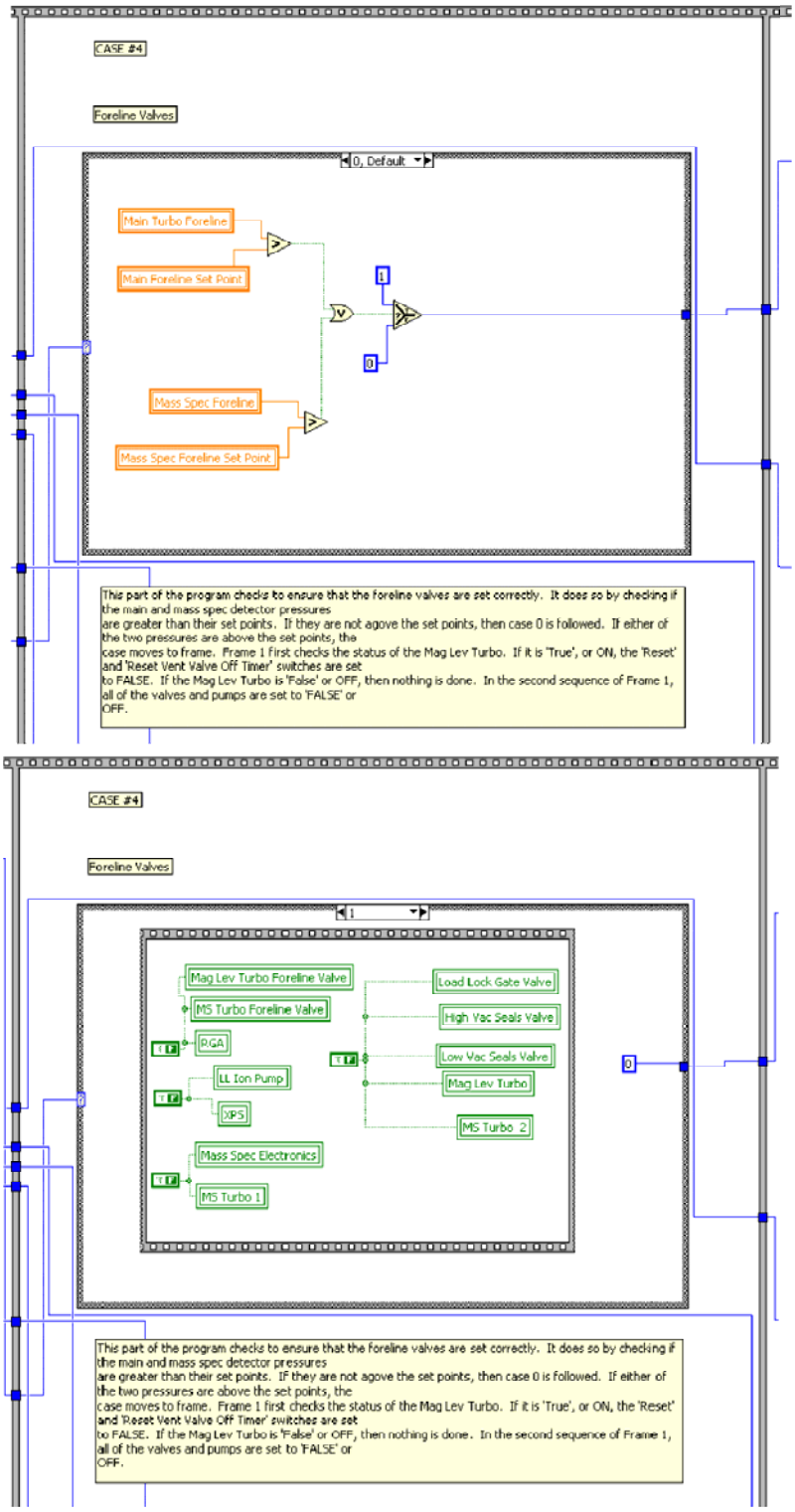

Figure B-4: Case 4 of the Chamber Interlock Program. The main and mass spectrometer turbo foreline pressures are checked against their set points.

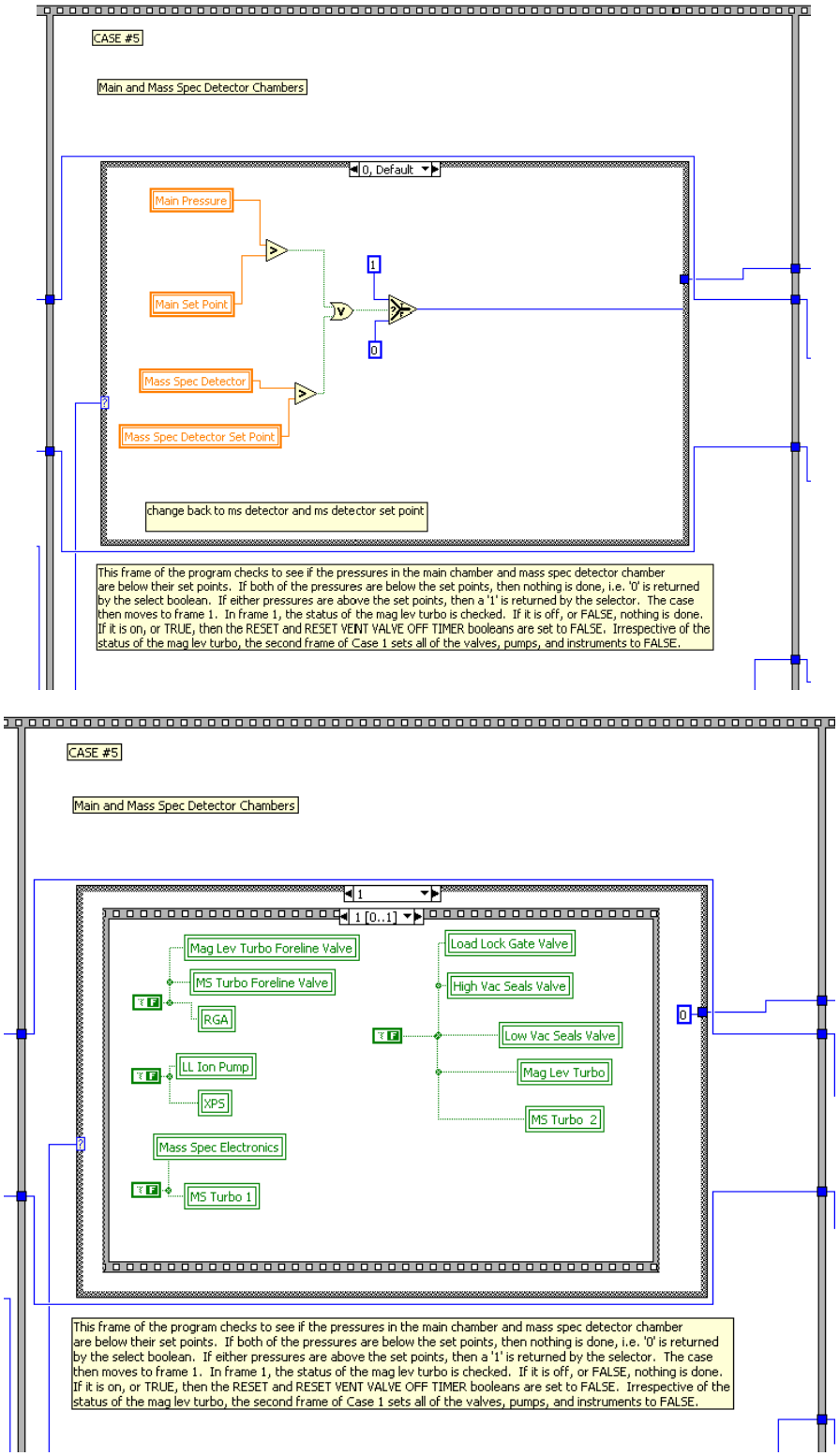

Figure B-5: Case 5 of the Chamber Interlock Program. The main chamber and mass spec detector pressures are checked against their set points. If either pressure is above the set point, the turbo pumps are shut down and all pneumatic valves are closed.

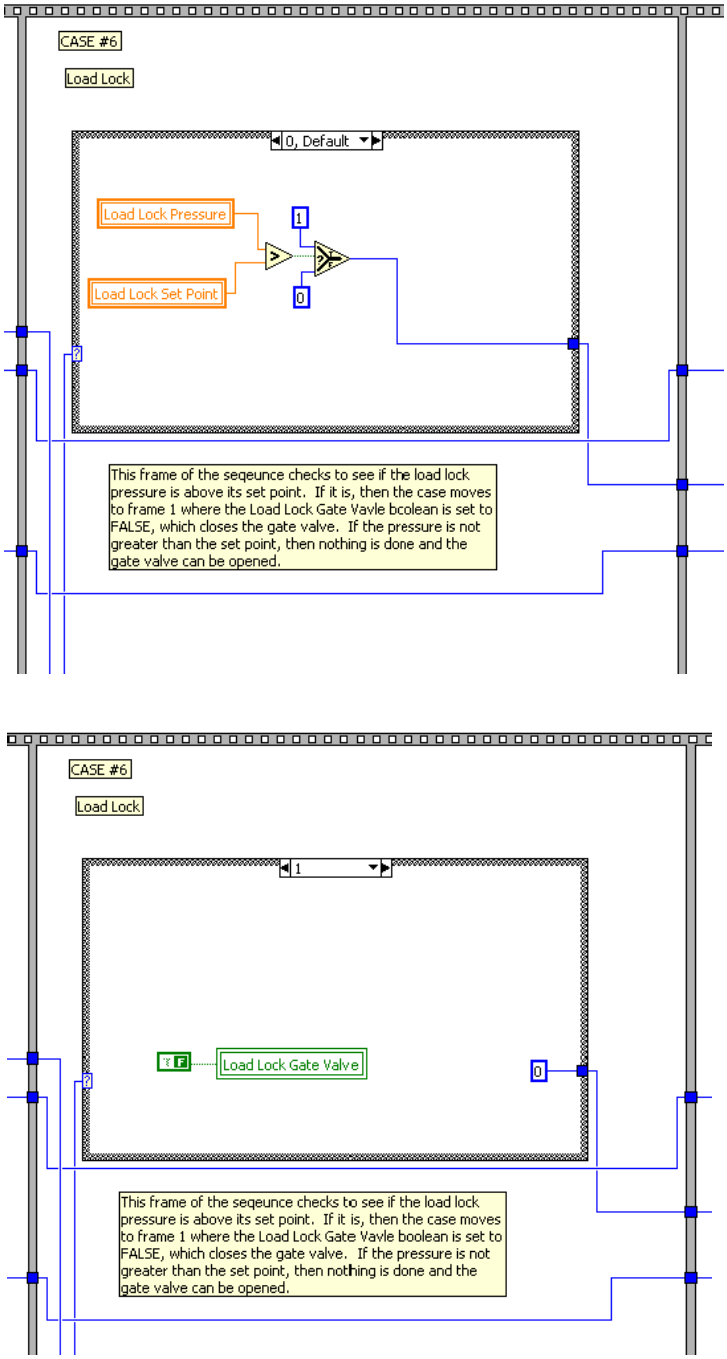

Figure B-6: Case 6 of the Chamber Interlock Program. The load lock pressure is checked against the set point. If the pressure exceeds the set point, the load lock gate valve is closed.

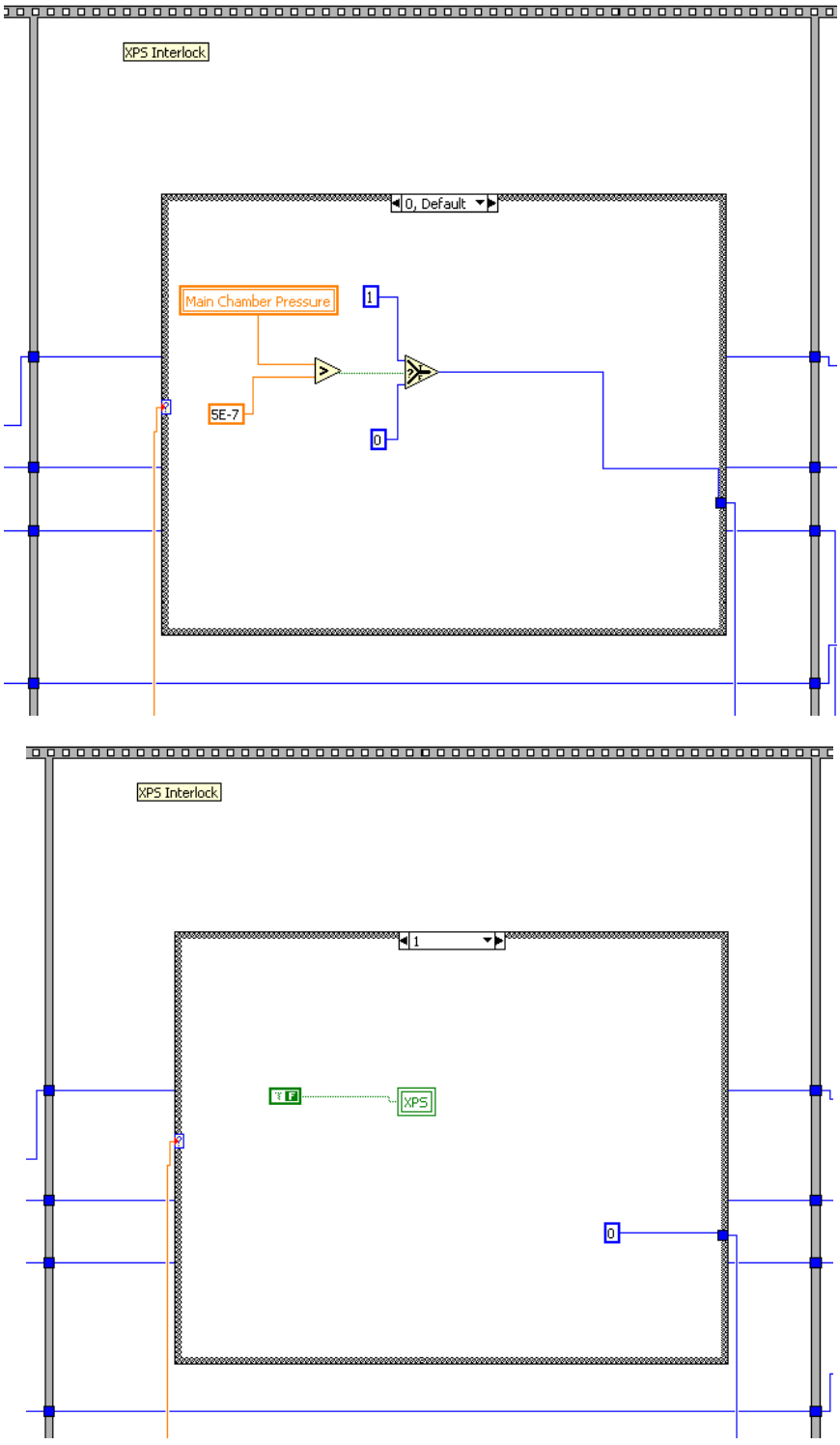

Figure B-7: Case 7 of the Chamber Interlock Program. If the main pressure is larger than 5 x 10-7Torr, the XPS source cannot be turned on.

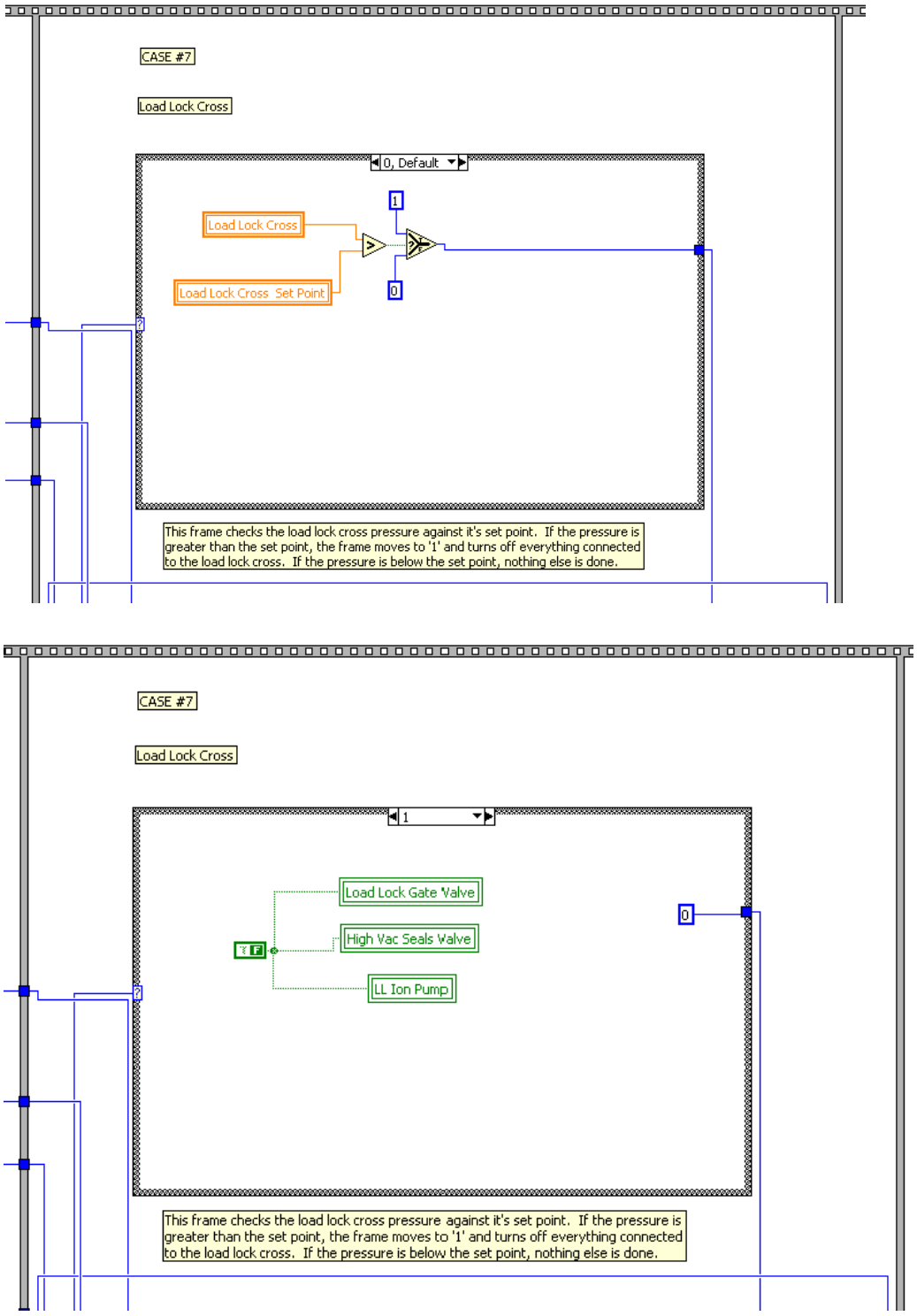

Figure B-8: Case 11 of the Chamber Interlock Program. The load lock cross pressure is checked against the set point. If the set point is exceeded, the high and low vacuum seals of the sample manipulator and are closed and the ion pump is

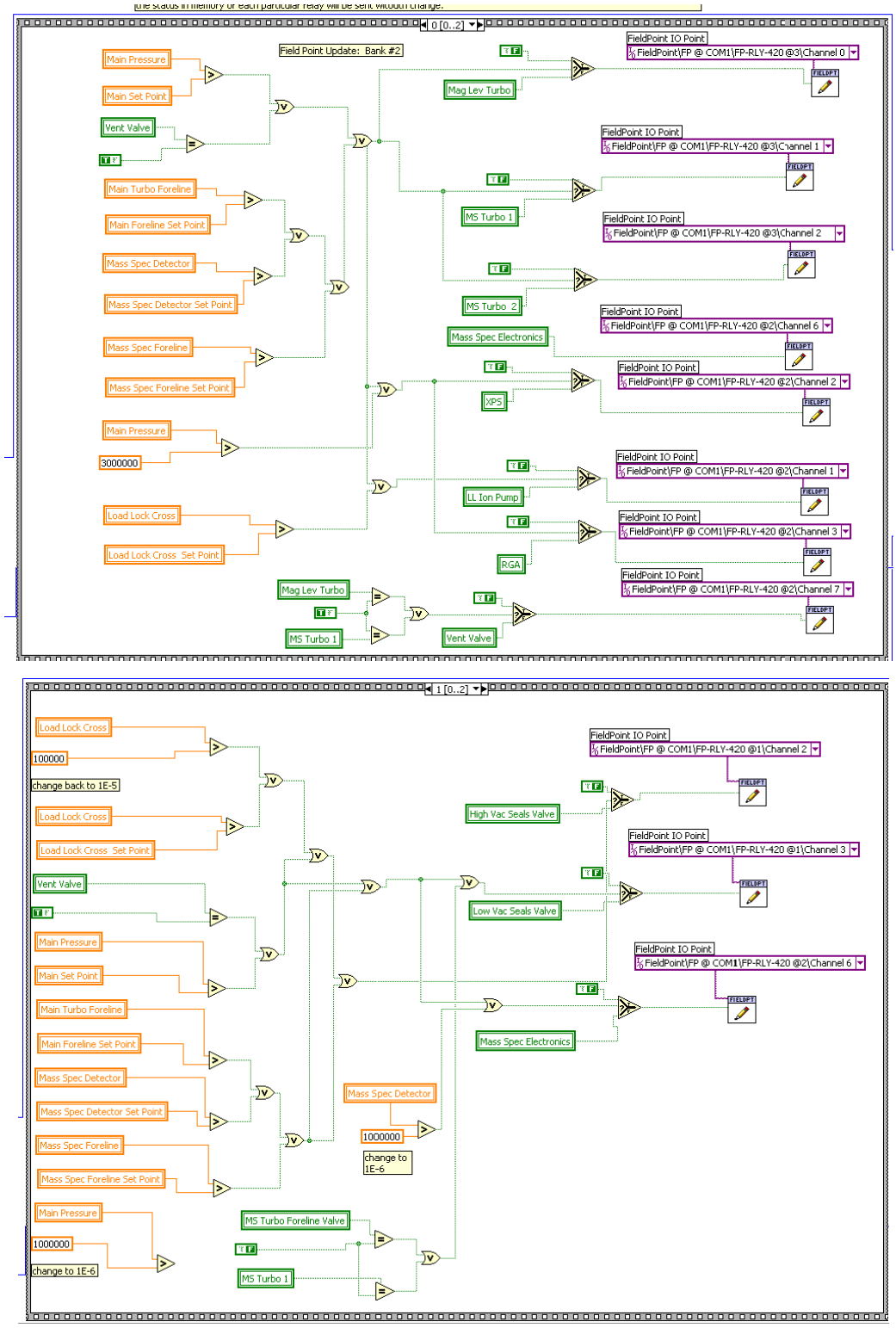

Figure B-9: Case 9a of the Chamber Interlock Program. In cases 9a-b, all of the pressures are rechecked against their set points.

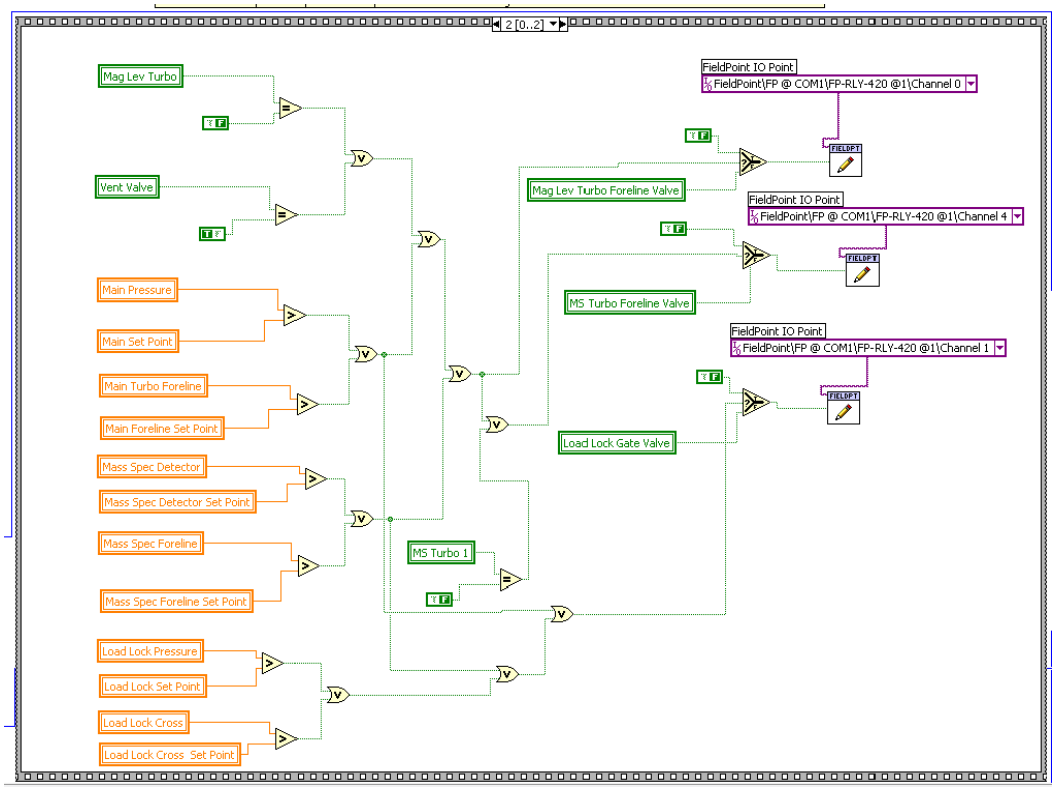

Figure B-10: Case 9b of the Chamber Interlock Program

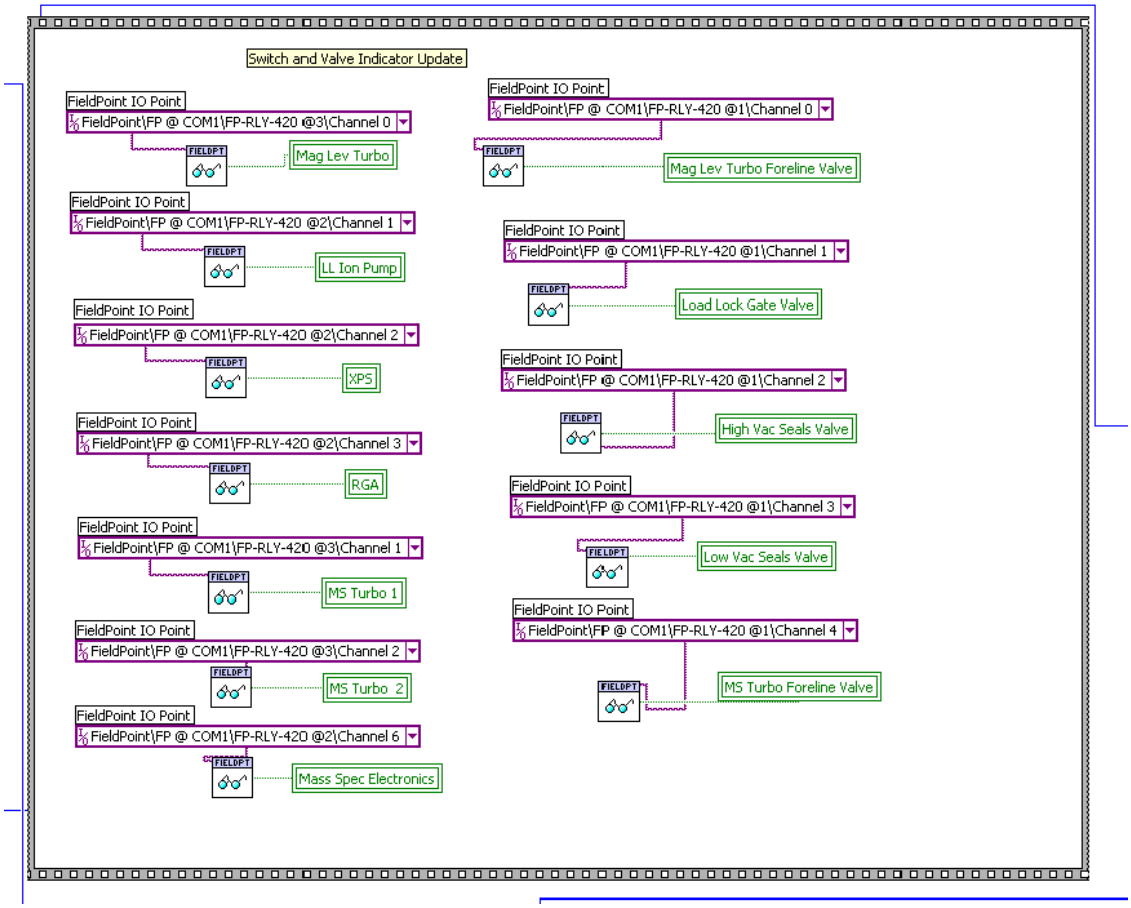

Figure B-11: Case 10a of the Chamber Interlock Program. The status of each program variable is checked against its real status as determined by the Field Point Relay modules.

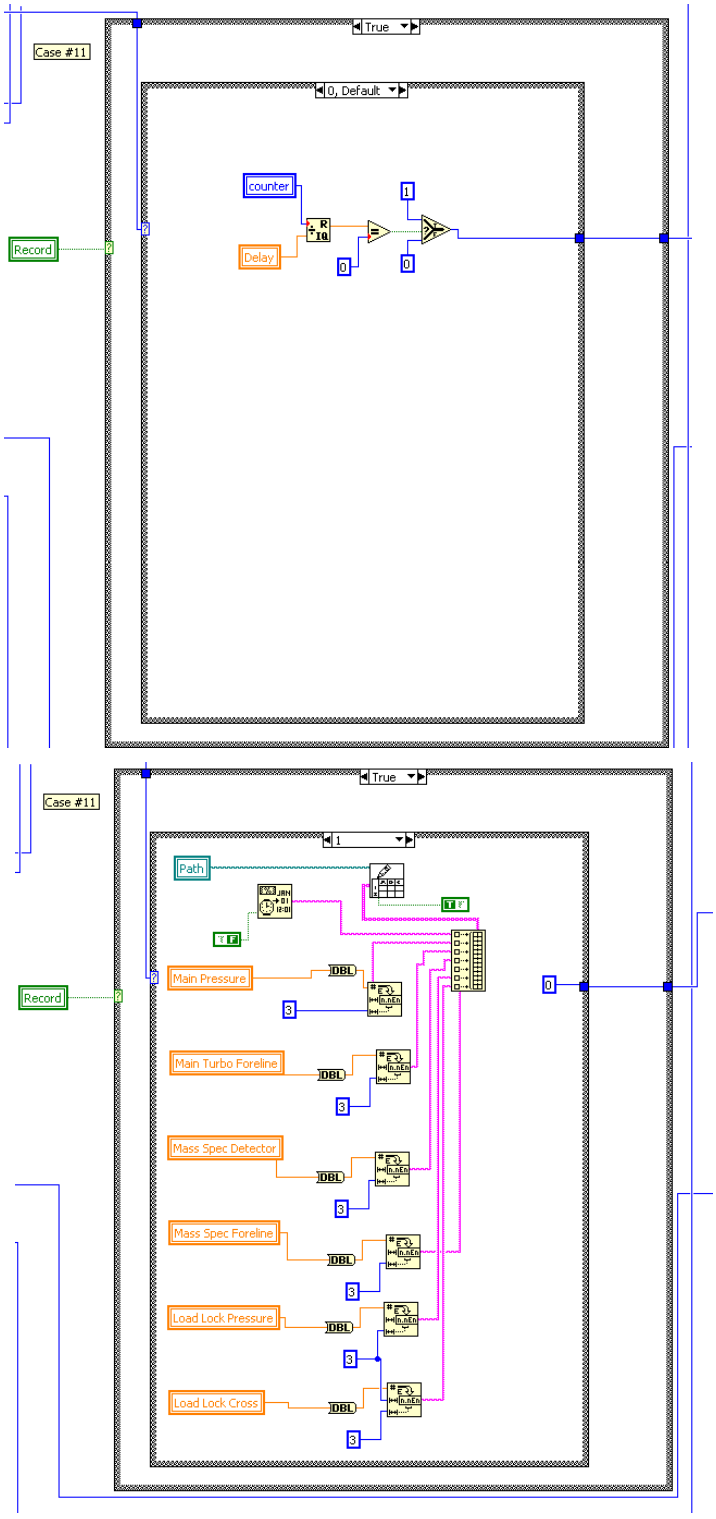

Figure B-12: Case 11 of the Chamber Interlock Program. The front panel pressures are recorded to a text file in selected time intervals

Appendix C

ICP-ES

Inductively coupled plasma emission spectroscopy (ICP-ES) is a trace elemental analysis technique that was used to quantify the amount of silicon present in the nanoparticle films. The technique is based on the production of an argon gas plasma generated by the interaction of a flow of argon gas with a high-frequency alternating electromagnetic field. The plasma forms when the electrons collide with the gas molecules resulting in ionization. At the plasma torch location, temperatures can reach higher than 10,000 K, which is high enough in energy to vaporize and atomize sample elements of interest. The large thermal energy can also excite and promote the outer energy level electrons of the atoms to a higher energy level. The excited electrons can then fall back into the lower energy level while simultaneously emitting a photon energy characteristic of the element from which it was generated. A high-resolution spectrometer is used to detect the emitted photons, and the resulting atomic emission spectra lines are extremely narrow (<2 pm).

The ICP-ES instrument used was Perkin-Elmer Optima 4300 DV spectrometer. For experiments here, the standard and unknown solutions were quantitatively mixed with an internal standard of 1 ppm Yttrium via a mixing block, and then conveyed at 1.5 mL/min with a peristaltic pump through a Meinhard nebulizer with a gas flow rate of 0.7 L/min. After passing through a cyclonic spin chamber to eliminate large droplets, ionization was performed with a 40 MHz RF generator operated at 1250 Watts. For quantitation, data was collected for five spectral regions characteristic of Si. For each data point, five measurements were collected in series to give a mean value of integrated area. Simultaneous measurements of the Y internal standard were performed to confirm the absence of error due to clogging, flow changes, or solution viscosity effects. A 1000 ppm commercial Si standard solution was diluted in series to produce five standards in the 1-30 ppm range. The resulting linear calibration curve had a 0.9998 or greater correlation coefficient.

Unknown samples were prepared by immersing the silicon films on gold substrates into 5.0 mL of 10 mM KOH followed by gentle agitation at room temperature. After 10 minutes, all of the visible silica had dissolved from the surface via the formation of silicates.[219] Silicate production from the glass backing of the slide was minimized by using mild conditions and short

times coupled with the much smaller surface area of the glass substrate. The 5.0 mL silicate solution was then transferred to a 50 mL volumetric flask and diluted to volume. Control experiments using blank slides and Teflon® labware confirmed that any contribution to the solution phase Si from either the glass slide or glass volumetric labware was less than 0.10 ppm or 1% of the unknown concentrations. All solutions were diluted with 3% Omnitrace ultra nitric acid (EMD) in 16 MΩ deionized water. The diluted samples were then analyzed directly with ICP.

ICP Results

Figure C-1 shows the standard curve obtained from the silicon standards measured at a wavelength 251 nm. The correlation coefficient, 0.99999, was excellent. The sample data, fit to the standard curve equation and recorded from the average of three samples, had a mean silicon concentration of 5.44 mg/L. This value, when corrected for dilution and surface area, corresponds to a mass of 0.257 ± 0.03 mg Si per sample.

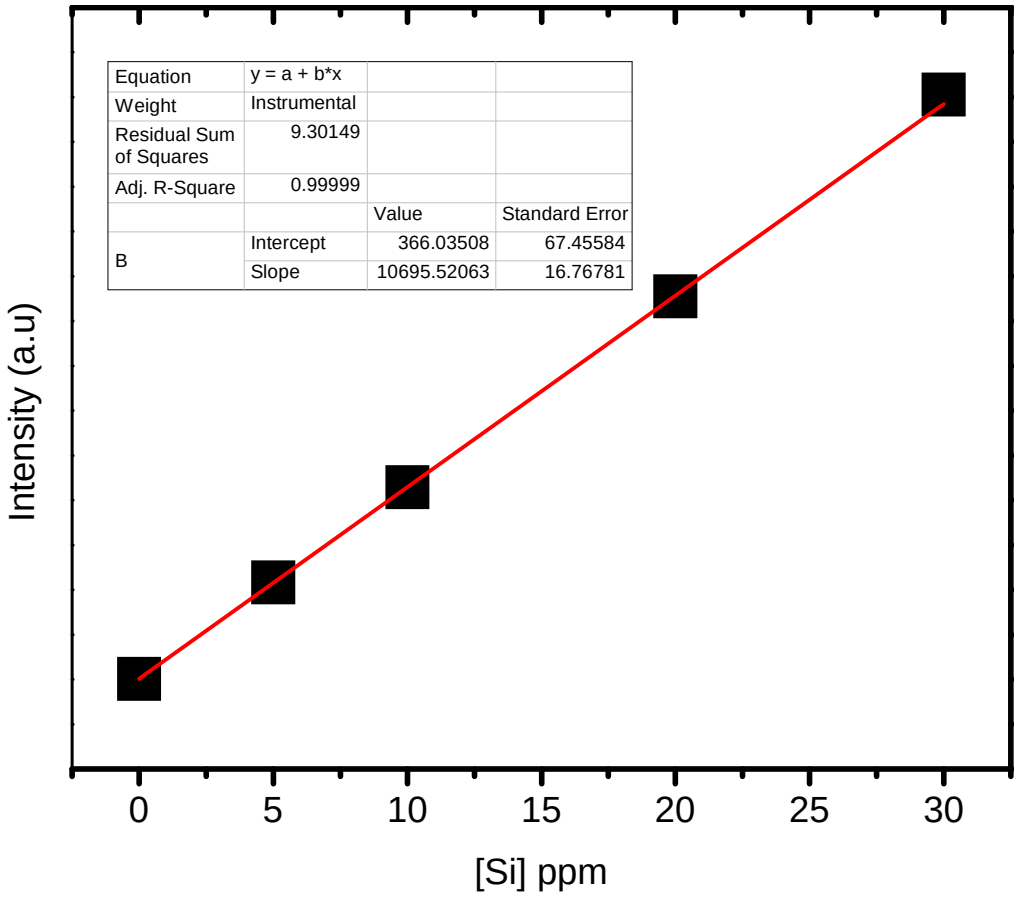

Figure C-1: The experimental calibration curve used for ICP analysis

Isotherm Fitting Parameters

The isotherm data collected for DMMP and TMP were analyzed at both low pressure and full pressure ranges by fitting the data with Langmuir and Toth isotherms. The equation parameters and correlation coefficients were determined by using the nonlinear fitting feature of OriginPro 8 software. The following tables show the fitting parameters of each model.

Langmuir All	R^2	q_s	b	n
$\nu_a CH_3O$	---	---	---	---
$\nu_s CH_3O$	0.85	6.37E-03 ± 2.6E-04	1.19E+05 ± 5.09E+03	---
$\delta_s O\text{-}CH_3$	0.86	1.03E-01 ± 6.0E-03	1.49E+02 ± 3.39E+01	---
Langmuir Low	R^2	q_s	b	n
$\nu_a CH_3O$	---	---	---	---
$\nu_s CH_3O$	---	---	---	---
$\delta_s O\text{-}CH_3$	0.98	2.31E-02 ± 1.2E-03	3.68E+05 ± 4.78E+04	---
Toth All	R^2	q_s	b	n
$\nu_a CH_3O$	0.98	6.15E+00 ± 3.3E-01	1.82E-01 ± 2.8E-02	2.93E-02 ± 2.30E-02
$\nu_s CH_3O$	0.95	2.17E-02 ± 1.26E-02	9.29E-02 ± 2.54E-02	1.05E-01 ±3.9E-02
$\delta_s O\text{-}CH_3$	0.98	1.63E+08 ± 7.79E+09	2.50E-01 ± 3.9E-02	1.07E-02 ± 2.21E-02
Toth Low	R^2	q_s	b	n
$\nu_a CH_3O$	---	---	---	---
$\nu_s CH_3O$	---	---	---	---
$\delta_s O\text{-}CH_3$	0.99	1.11E-01 ± 2.57E-01	2.48E-02 ± 5.47E-02	2.85E-01 ± 1.73E-01

Table C-1: The fitting parameters of the Langmuir and Toth models applied to the isotherms of DMMP adsorbed to a silica nanoparticulate film.

Langmuir Total	R^2	q_s	b	n
$\nu_a CH_3O$	0.88	3.41E-02 ± 2.0E-03	7.82E+01 ± 1.21E+01	---
$\nu_s CH_3O$	0.83	1.70E-02 ± 1.0E-03	1.67E+02 ± 4.58E+01	---
$\delta_s O\text{-}CH_3$	0.90	7.97E-02 ± 4.4E-03	6.30E+01 ± 1.21E+01	---
Langmuir Low	R^2	q_s	b	n
$\nu_a CH_3O$	0.92	4.74E-03 ± 4.6E-04	8.92E+05 ± 2.51E+05	---
$\nu_s CH_3O$	0.80	1.90E-03 ± 4.7E-04	3.32E+05 ± 1.87E+05	---
$\delta_s O\text{-}CH_3$	0.96	1.09E-02 ± 1E-03	9.90E+05 ± 2.04E+05	---
Toth All	R^2	q_s	b	n
$\nu_a CH_3O$	0.98	1.22E+06 ± 4.86E+07	2.56E-01 ± 4.28E-01	1.29E-02 ± 2.63E-02
$\nu_s CH_3O$	0.97	1.14E+08 ± 6.58E+09	3.76E-01 ± 7.9E-02	1.55E-02 ± 3.90E-02
$\delta_s O\text{-}CH_3$	0.98	1.84E+12 ± 2.07E+14	3.36E-01 ± 6.4E-02	9.29E-03 ± 2.89E-02
Toth Low	R^2	q_s	b	n
$\nu_a CH_3O$	0.95	1.62E-02 ± 2.71E-02	1.75E-02 ± 6.04E-02	2.71E-01 ± 2.62E-01
$\nu_s CH_3O$	0.84	3.37E+04 ± 8.87E+06	6.30E-01 ± 5.48E+00	4.16E-02 ± 5.93E-01
$\delta_s O\text{-}CH_3$	0.98	2.05E-02 ± 1.06E-02	3.11E-03 ± 7.76E-03	3.95E-01 ± 1.90E-01

Table C-2: The fitting parameters of the Langmuir and Toth models applied to the isotherms of TMP adsorbed to a silica nanoparticulate film.

References

1. Yates, J. T., *Experimental Innovations in Surface Science*. AIP Press: 1997.
2. Barth, E.; Myrvik, Q. M.; Wagner, W.; Gristina, A. G., *In Vitro* and *vivo* comparative colonization of *Staphylococcus aureus* and *Staphylococcus epidermidis* orthopedic implant materials. *Biomaterials* **1989,** *10*, 325-328.
3. Oga, M.; Sugioka, Y.; Hobgood, C. D.; Gristina, A. G.; Myrvik, Q. N., Surgical biomaterials and differential colonizationby *Stapylococcus epidermidis. Biomaterials* **1988,** *9*, 285-289.
4. Hogt, A. H.; Dankert, J.; Feijen, J., Adhesion of *Staphylococcus epidermidis* and *Staphylococcus saprophyticus* to a hydrophobic biomaterials. *J. Gen. Microbiol.* **1985,** *131*, 2485-2491.
5. Pringle, J. H.; Fletcher, M., Influence of sustratum hydration and adsrobed macromolecules on bacterial attatchment to surfaces. *Appl. Environ. Microbol.* **1986,** *51* (1321-1325).
6. Reynolds, E. C.; Wong, A., Effect of adsorbed protein on hydroxyapatite zeta potential and *Streptococcus mutans* adherence. *Infect. Immunol.* **1983,** *39*, 1285-1290.
7. An, Y. H.; Friedman, R. J.; Draughn, R. A.; Smith, E. A.; Nicholson, J.; John, J. F., Rapid Quantification of staphylococci adhered to titanium surfaces usuing image analyzed epifluorescence microscopy. *J. Microbiol. Methods* **1995,** *24*, 29-40.
8. Locci, R.; Peters, G.; Pulverer, G., Microbial colonization of prosthetic devices. I. Microtopographical characteristics of intravenous catheters as detected by scanning electron microscopy. *Zbl. Bakt. Hyg. I. Abt. Orig. B* **1981,** *173*, 285-292.
9. Gristina, A. G., Biomaterial-centered infection: microbial adhesion versus tissue integration. *Science* **1987,** *237*, 1595.
10. Gristina, A. G.; Hobgood, C. D.; Barth, E., Biomaterial specificity, molecular mechansims, and clinical relevance of *S. epidermidis* and *S. aureus* infections in surgery. In *Pathogenesis and Clinical Significance of Coagulaes-Negative Staphylococci*, Pulverer, G.; Quie, P. G.; Peters, G., Eds. Fisher Verlag: Stuttgart, 1987; pp 143-157.
11. Duran, L. W.; Pietig, J. A.; Driemeyer, J. E.; al., e., Prevention of micribial colonization on medical devices by photochemical immobilization of antimicrobial peptides. *Trans. Soc. Biomater.* **1993,** *16*, 35.
12. Bridgett, M. J.; Davies, M. C., Control of staphylococcal adhesion to polystyrene surfaces by polymer surface modification with surfactant. *Biomaterials* **1992,** *13*, 411-416.
13. Farber, B. F.; Wolff, A. G., The use of nonsteroidal antiinflammatory drugs to prevent the adherence of *Staphylococcus epidermidis* to medicinal polymers. *J. Infect. Dis.* **1992,** *166*, 861-865.
14. Speier, J. L.; Malek, J. R., Destruction of microorganisms by contact with solid surfaces. *J. Colloid Interface Sci.* **1982,** *89* (68-76).
15. Harder, P.; Grunze, M.; Dahint, R.; Whitesides, G. M.; Laibinis, P. E., Molecular Conformation in Oligo(ethylene glycol)-Terminated Self-Assembled Monolayers on Gold and Silver Surfaces Determines Their Ability To Resist Protein Adsorption. *J. Phys. Chem. B* **1998,** *102* (2), 426-436.
16. Qian, X.; Metallo, S. J.; Choi, I. S.; Wu, H.; Liang, M. N.; Whitesides, G. M., Arrays of Self-Assembled Monolayers for Studying Inhibition of Bacterial Adhesion. *Anal. Chem.* **2002,** *74* (8), 1805-1810.

17. Walker, S. L.; Hill, J. E.; Redman, J. A.; Elimelech, M., Influence of Growth Phase on Adhesion Kinetics of Escherichia coli. *Appl. Environ. Microbiol.* **2005,** *71* (6), 3093-3099.
18. Tiller, J. C.; Lee, S. B.; Lewis, K.; Klibanov, A., Polymer Surfaces Derivatized with Poly(Vinyl-N-Hexylpyridinium) Kill Airborne and Waterborne Bacteria. *Biotechnology and Bioengineering* **2002,** *79* (4), 465-471.
19. Tiller, J. C.; Liao, C.-J.; Lewis, K.; Klibanov, A., Designing surfaces that kill bacteria on contact. *PNAS* **2001,** *98* (11), 5981-5985.
20. Cooper, M. A.; Victoria T. Singleton, A survey of the 2001 to 2005 quartz crystal microbalance biosensor literature: applications of acoustic physics to the analysis of biomolecular interactions. *Journal of Molecular Recognition* **2007,** *20* (3), 154-184.
21. Tanious, F. A.; Nguyen, B.; Wilson, W. D.; Dr. John, J. C.; Dr. H. William Detrich, III, Biosensor[Surface Plasmon Resonance Methods for Quantitative Analysis of Biomolecular Interactions. In *Methods in Cell Biology*, Academic Press: 2008; Vol. Volume 84, pp 53-77.
22. Zhang, S.; Wright, G.; Yang, Y., Materials and techniques for electrochemical biosensor design and construction. *Biosensors and Bioelectronics* **2000,** *15* (5-6), 273-282.
23. Soares, J. W.; Kirby, R.; Morin, K. M.; Mello, C. M., Antimicrobial Peptide Preferential Binding of E. coli O_{157}:H_7. *Protein and Peptide Letters* **2008,** *15* (10), 1086-1093.
24. Kanu, A. B.; Haigh, P. E.; Hill, H. H., Surface detection of chemical warfare agent simulants and degradation products. *Analytica Chimica Acta* **2005,** *553* (1-2), 148-159.
25. Talmage, S. S.; Watson, A. P.; Hauschild, V.; Munro, N. B.; King, J., Chemical Warfare Agent Degredation and Decontamination. *Current Organic Chemistry* **2007,** *11*, 285-298.
26. Munro, N. B.; Talmage, S. S.; G.D.Griffin; Waters, L. C.; Watson, A. P.; J.F.King; Hauschild, V., The Sources, Fate, and Toxicity of Chemical Warfare Agent Degradation Products. *Eviron. Healt. Persp.* **1999,** *107*.
27. Wagner, G. W.; Yang, Y.-C., Rapid Nucleophilic/Oxidative Decontamination of Chemical Warfare Agents. *Industrial & Engineering Chemistry Research* **2002,** *41* (8), 1925-1928.
28. Hovanec, J. W.; Albizo, J. M.; Henderson, V. D.; Yang, Y., C. Agent Neutralization Study IV. VX-Caustic Peroxide Reactions. Arenal, E., Ed. Aberdeen Proving Ground, MD, 1994; Vol. ERDEC-TR^{-1}72.
29. Cassagne, T.; Criseau, H. J.; Delmas, G.; Desgranges, M.; Lion, C.; Magnaud, G.; Torreilles, E.; Virieux, D., *Heter. Chem.* **2001,** *12*, 485.
30. Brickhouse, M.; Wagner, G.; Procell, L.; Sorrick, D.; MacIver, B.; Turetsky, A.; Schwartz, L.; McVey, I.; Wiget, P., Large Scale Tests of Vaporous Hydrogen Peroxide (VHP) for Chemical and Biological Weapons Decontamination. Center, E. C. B., Ed. Aberdeen Proving Ground, MD, 2005; p ADA 433058.
31. Aurian-Blajeni, B.; Boucher, M. M., Interaction of dimethyl methylphosphonate with metal oxides. *Langmuir* **1989,** *5* (1), 170-174.
32. Gordon, W. O. Metal Oxide Nanoparticles: Optical Properties and Interaction with Chemical Warfare Agent Simulants. Dissertation, Virginia Polytechnic Institute and State University, Blacksburg, VA, 2006.
33. Henderson, M. A.; Jin, T.; White, J. M., A TPD/AES study of the interaction of dimethyl methylphosphonate with iron oxide (α-Fe_2O_3) and silicon dioxide. *The Journal of Physical Chemistry* **1986,** *90* (19), 4607-4611.

34. Kanan, S. M.; Lu, Z.; Tripp, C. P., A Comparative Study of the Adsorption of Chloro- and Non-Chloro-Containing Organophosphorus Compounds on WO_3. *The Journal of Physical Chemistry B* **2002,** *106* (37), 9576-9580.
35. Kim, C. S.; Lad, R. J.; Tripp, C. P., Interaction of organophosphorous compounds with TiO_2 and WO_3 surfaces probed by vibrational spectroscopy. *Sensors and Actuators B: Chemical* **2001,** *76* (1-3), 442-448.
36. Milojevich, A. Hafnium Dioxide Nanoparticle Thin Film Morphology and Reactivity with Dimethyl Methylphosphonate. Master's Thesis, Virginia Polytechnic Institutde and State University, Blacksburg, VA, 2006.
37. Moss, J. A.; Szczepankiewicz, S. H.; Park, E.; Hoffmann, M. R., Adsorption and Photodegradation of Dimethyl Methylphosphonate Vapor at TiO_2 Surfaces. *The Journal of Physical Chemistry B* **2005,** *109* (42), 19779-19785.
38. Rusu, C. N.; Yates, J. T., Photooxidation of Dimethyl Methylphosphonate on TiO_2 Powder. *The Journal of Physical Chemistry B* **2000,** *104* (51), 12299-12305.
39. Rusu, C. N.; Yates, J. T., Adsorption and Decomposition of Dimethyl Methylphosphonate on TiO_2. *The Journal of Physical Chemistry B* **2000,** *104* (51), 12292-12298.
40. Trubitsyn, D. A.; Vorontsov, A. V., Experimental Study of Dimethyl Methylphosphonate Decomposition over Anatase TiO_2. *The Journal of Physical Chemistry B* **2005,** *109* (46), 21884-21892.
41. Zhou, J.; Varazo, K.; Reddic, J. E.; Myrick, M. L.; Chen, D. A., Decomposition of dimethyl methylphosphonate on TiO_2(1 1 0): principal component analysis applied to X-ray photoelectron spectroscopy. *Analytica Chimica Acta* **2003,** *496* (1-2), 289-300.
42. Li, Y. X.; Koper, O.; Atteya, M.; Klabunde, K. J., Adsorption and decomposition of organophosphorus compounds on nanoscale metal oxide particles. In situ GC-MS studies of pulsed microreactions over magnesium oxide. *Chemistry of Materials* **1992,** *4* (2), 323-330.
43. Mitchell, M. B.; Sheinker, V. N.; Mintz, E. A., Adsorption and Decomposition of Dimethyl Methylphosphonate on Metal Oxides. *The Journal of Physical Chemistry B* **1997,** *101* (51), 11192-11203.
44. Kanan, S. M.; Tripp, C. P., An Infrared Study of Adsorbed Organophosphonates on Silica: A Prefiltering Strategy for the Detection of Nerve Agents on Metal Oxide Sensors. *Langmuir* **2001,** *17* (7), 2213-2218.
45. Hartmann, M.; Kaig, H., Saure Seifen. *Z. agnew. Chem.* **1928,** *41*, 127-130.
46. Kuhn, R.; Bielig, H., Uber Inversteifen. I. Die. Einwirkkung von Invertseifen aus Eiweiss-Stoffe. *Berichte der Deutschen Chemischen Gesellschaft* **1940,** *73*, 1080-1091.
47. Hotchkiss, R. D., Gramicidin, tyrocidin and tyrothricin. *Advances in Ezymology* **1944,** *4*, 153-199.
48. Denyer, S. P.; Hugo, W. B., Biocide-induced damgae to the cytoplasmic membrane. *Soc. Appl. Bacteriol. Tech. Ser.* **1991,** *27*, 171-187.
49. Chen, X.; Ferrigno, R.; Yang, J.; Whitesides, G. M., Redox Properties of Cytochrome c Adsorbed on Self-Assembled Monolayers: A Probe for Protein Conformation and Orientation. *Langmuir* **2002,** *18* (18), 7009-7015.
50. El Kasmi, A.; Wallace, J. M.; Bowden, E. F.; Binet, S. M.; Linderman, R. J., Controlling Interfacial Electron-Transfer Kinetics of Cytochrome c with Mixed Self-Assembled Monolayers. *J. Am. Chem. Soc.* **1998,** *120* (1), 225-226.

51. Martins, C. L.; Ratner, B. D.; Barbosa, M. A., Protein adsorption on mixtures of hydroxyl- and methyl-terminated alkanethiols self-assembled monolayers. *Journal of Biomedical Materials Research Part A* **2003,** *67A* (1), 158-171.
52. Mrksich, M.; Grunwell, J. R.; Whitesides, G. M., Biospecific Adsorption of Carbonic Anhydrase to Self-Assembled Monolayers of Alkanethiolates That Present Benzenesulfonamide Groups on Gold. *J. Am. Chem. Soc.* **1995,** *117* (48), 12009-12010.
53. Ostuni, E.; Grzybowski, B. A.; Mrksich, M.; Roberts, C. S.; Whitesides, G. M., Adsorption of Proteins to Hydrophobic Sites on Mixed Self-Assembled Monolayers. *Langmuir* **2003,** *19* (5), 1861-1872.
54. Ostuni, E.; Yan, L.; Whitesides, G. M., The interaction of proteins and cells with self-assembled monolayers of alkanethiolates on gold and silver. *Colloids and Surfaces B: Biointerfaces* **1999,** *15* (1), 3-30.
55. Halik, M.; Klauk, H.; Zschieschang, U.; Schmid, G.; Dehm, C.; Schutz, M.; Maisch, S.; Effenberger, F.; Brunnbauer, M.; Stellacci, F., Low-voltage organic transistors with an amorphous molecular gate dielectric. *Nature* **2004,** *431* (7011), 963-966.
56. Salomon, A.; Cahen, D.; Lindsay, S.; Tomfohr, J.; Engelkes, B.; C.D. Frisbie, Comparison of Electronic Transport Measurements on Organic Molecules. *Advanced Materials* **2003,** *15* (22), 1881-1890.
57. Dubois, L. H.; Nuzzo, R. G., Synthesis, Structure, and Properties of Model Organic Surfaces. *Annual Review of Physical Chemistry* **1992,** *43* (1), 437-463.
58. Valiokas, R.; Svedhem, S.; Svensson, S. C. T.; Liedberg, B., Self-Assembled Monolayers of Oligo(ethylene glycol)-Terminated and Amide Group Containing Alkanethiolates on Gold. *Langmuir* **1999,** *15* (10), 3390-3394.
59. Nuzzo, R. G.; Dubois, L. H.; Allara, D. L., Fundamental studies of microscopic wetting on organic surfaces. 1. Formation and structural characterization of a self-consistent series of polyfunctional organic monolayers. *J. Am. Chem. Soc.* **1990,** *112* (2), 558-569.
60. Love, J. C.; Estroff, L. A.; Kriebel, J. K.; Nuzzo, R. G.; Whitesides, G. M., Self-Assembled Monolayers of Thiolates on Metals as a Form of Nanotechnology. *Chem. Rev.* **2005,** *105*, 1103-1169.
61. Terena P. Sullivan, W. T. S. H., Reactions on Monolayers: Organic Synthesis in Two Dimensions. *European Journal of Organic Chemistry* **2003,** *2003* (1), 17-29.
62. Uzarski, J. R. Investigations of Bacteria Viability on Surfaces Using ω-functionalized Alkanethiol Self-Assembled Monolayers. Master's Thesis, Virginia Polytechnic Institute and State University, Blacksburg, 2006.
63. Endo, Y.; Tani, T.; Kodama, M., Antimicrobial activity of tertiary amine covalently bonded to a polystyrene fiber. *Appl. Environ. Microbiol.* **1987,** *53* (9), 2050-2055.
64. Bragg, P. D.; Rannie, D. J., *Can. J. Microbiol.* **1973,** *20*, 883-889.
65. Yudkin, J., *Enzymogia* **1937-1938,** *2*, 161-170.
66. Hugo, W. B., Handbuch der Antiseptik. In *Band I, Teil 2*, Weuffen, W.; Kramer, A.; Groschel, D.; Berensci, G.; Bulka, E., Eds. Volk und Gesundheit: Berlin, 1981; pp 361-409.
67. Rose, A. H., An Introduction to Microbial Physiology. In *Chemical Microbiology*, 2nd. Edn ed.; Butterworths: London, 1976; pp 119-120.
68. Daune, M.; Dekker, C. A.; Schachman, H. K., Complexes of silver ion with natural and synthetic polynucleotides. *Biopolymers* **1966,** *4* (1), 51-76.

69. Izatt, R. M.; Christensen, J. J.; Rytting, J. H., Sites and thermodynamic quantities associated with proton and metal ion interaction with ribonucleic acid, deoxyribonucleic acid, and their constituent bases, nucleosides, and and nucleotides. *Chem. Rev.* **1971,** *71* (5), 439-481.
70. Jensen, R. H.; Davidson, N., Spectrophotometric, potentiometric, and density gradient ultracentrifugation studies of the binding of silver ion by DNA. *Biopolymers* **1966,** *4* (1), 17-32.
71. Richard, H.; Schreiber, J. P.; Daune, M., Interactions of metallic ions with DNA. V. DNA Renaturation Mechanism in the Presence of Cu. *Biopolymers* **1973,** *12* (1), 1-10.
72. Zavriev, S. K.; Minchenkova, L. E.; Vorlícková, M.; Kolchinsky, A. M.; Volkenstein, M. V.; Ivanov, V. I., Circular dichroism anisotropy of DNA with different modifications at N_7 of guanine. *Biochimica et Biophysica Acta (BBA) - Nucleic Acids and Protein Synthesis* **1979,** *564* (2), 212-224.
73. Greenler, R. G., Infrared Study of Adsorbed Molecules on Metal Surfaces by Reflection Techniques. *The Journal of Chemical Physics* **1966,** *44* (1), 310-315.
74. Greenler, R. G., *Journal of Chemical Physics* **1969,** *50*, 1963-1968.
75. Moulder, J. F.; Stickle, W. F.; Sobol, P. E.; Bomben, K. D., *Handbook of X-ray Photoelectron Spectroscopy*. Physical Electronics, Inc.: Eden Prairie, MN, 1995.
76. Ferguson, M. K.; Low, E. R.; Morris, J. R., Well-Ordered Self-Assembled Monolayers Created via Vapor-Phase Reactions on a Monolayer Template. *Langmuir* **2004,** *20* (8), 3319-3323.
77. Duevel, R. V.; Corn, R. M., Amide and ester surface attachment reactions for alkanethiol monolayers at gold surfaces as studied by polarization modulation Fourier transform infrared spectroscopy. *Anal. Chem.* **1992,** *64* (4), 337-342.
78. Troughton, E. B.; Bain, C. D.; Whitesides, G. M.; Nuzzo, R. G.; Allara, D. L.; Porter, M. D., Monolayer films prepared by the spontaneous self-assembly of symmetrical and unsymmetrical dialkyl sulfides from solution onto gold substrates: structure, properties, and reactivity of constituent functional groups. *Langmuir* **1988,** *4* (2), 365-385.
79. Uchida, E.; Ikada, Y., Introduction of quaternary amines onto a film surface by graft polymerization. *Journal of Applied Polymer Science* **1996,** *61* (8), 1365-1373.
80. Engquist, I.; Lestelius, M.; Liedberg, B., Microscopic Wettability of Ester$^-$ and Acetate-Terminated Self-Assembled Monolayers. *Langmuir* **1997,** *13* (15), 4003-4012.
81. Fox, M. A.; Whitesell, J. K.; McKerrow, A. J., Fluorescence and Redox Activity of Probes Anchored through an Aminotrithiol to Polycrystalline Gold. *Langmuir* **1998,** *14* (4), 816-820.
82. Arnold, R.; Azzam, W.; Terfort, A.; Woll, C., Preparation, Modification, and Crystallinity of Aliphatic and Aromatic Carboxylic Acid Terminated Self-Assembled Monolayers. *Langmuir* **2002,** *18* (10), 3980-3992.
83. Dannenberger, O.; Weiss, K.; Himmel, H. J.; Jäger, B.; Buck, M.; Wöll, C., An orientation analysis of differently endgroup-functionalised alkanethiols adsorbed on Au substrates. *Thin Solid Films* **1997,** *307* (1-2), 183-191.
84. Nuzzo, R. G.; Fusco, F. A.; Allara, D. L., Spontaneously organized molecular assemblies. 3. Preparation and properties of solution adsorbed monolayers of organic disulfides on gold surfaces. *J. Am. Chem. Soc.* **1987,** *109* (8), 2358-2368.
85. Frey, B. L.; Corn, R. M., Covalent Attachment and Derivatization of Poly(L-lysine) Monolayers on Gold Surfaces As Characterized by Polarization-Modulation FT-IR Spectroscopy. *Anal. Chem.* **1996,** *68* (18), 3187-3193.

86. Anderson, M. R.; Baltzersen, R., Reductive desorption of 11-mercaptoundecanoic acid monolayers modified by covalent attachment of 1,3- and 1,4-phenylenediamine. *Journal of Colloid and Interface Science* **2003,** *263*, 516-521.
87. Cabrita, J. F.; Abrantes, L. M.; Viana, A. S., N-Hydroxysuccinimide-terminated self-assembled monolayers on gold for biomolecules immobilisation. *Electrochimica Acta* **2005,** *50* (10), 2117-2124.
88. Voicu, R.; Boukherroub, R.; Bartzoka, V.; Ward, T.; Wojtyk, J. T. C.; Wayner, D. D. M., Formation, Characterization, and Chemistry of Undecanoic Acid-Terminated Silicon Surfaces: Patterning and Immobilization of DNA. *Langmuir* **2004,** *20* (26), 11713-11720.
89. Lahiri, J.; Isaacs, L.; Tien, J.; Whitesides, G. M., A Strategy for the Generation of Surfaces Presenting Ligands for Studies of Binding Based on an Active Ester as a Common Reactive Intermediate: A Surface Plasmon Resonance Study. *Anal. Chem.* **1999,** *71* (4), 777-790.
90. Dordi, B.; Schonherr, H.; Vancso, G. J., Reactivity in the Confinement of Self-Assembled Monolayers: Chain Length Effects on the Hydrolysis of N-Hydroxysuccinimide Ester Disulfides on Gold. *Langmuir* **2003,** *19* (14), 5780-5786.
91. Murata, H.; Koepsel, R. R.; Matyjaszewski, K.; Russell, A. J., Permanent, non-leaching antibacterial surfaces--2: How high density cationic surfaces kill bacterial cells. *Biomaterials* **2007,** *28* (32), 4870-4879.
92. Ohrt, T.; Merkle, D.; Birkenfeld, K.; Echeverri, C. J.; Schwille, P., In situ fluorescence analysis demonstrates active siRNA exclusion from the nucleus by Exportin 5. *Nucl. Acids Res.* **2006,** *34* (5), 1369-1380.
93. Wang, D.; Visser, N. V.; Veenhuis, M.; van der Klei, I. J., Physical Interactions of the Peroxisomal Targeting Signal 1 Receptor Pex_5p, Studied by Fluorescence Correlation Spectroscopy. *J. Biol. Chem.* **2003,** *278* (44), 43340-43345.
94. Kovacs, J.; Mayers, G. L.; Johnson, R. H.; Cover, R. E.; Ghatak, U. R., Racemization of amino acid derivatives. III. Rate of racemization and peptide bond formation of cysteine active esters. *J. Org. Chem.* **1970,** *35* (6), 1810-1815.
95. Lahiri, J.; Ostuni, E.; Whitesides, G. M., Patterning Ligands on Reactive SAMs by Microcontact Printing. *Langmuir* **1999,** *15* (6), 2055-2060.
96. Tam-Chang, S.-W.; Biebuyck, H. A.; Whitesides, G. M.; Jeon, N.; Nuzzo, R. G., Self-Assembled Monolayers on Gold Generated from Alkanethiols with the Structure $RNHCOCH_2SH$. *Langmuir* **1995,** *11* (11), 4371-4382.
97. Tsuboi, M., Infrared dichroism and molecular conformation of -form poly--benzyl-L-glutamate. *J. Polym. Sci.* **1962,** *59*, 139-153.
98. Kubelka, J.; Keiderling, T. A., Ab Initio Calculation of Amide Carbonyl Stretch Vibrational Frequencies in Solution with Modified Basis Sets. 1. N-Methyl Acetamide. *The Journal of Physical Chemistry A* **2001,** *105* (48), 10922-10928.
99. Clegg, R. S.; Hutchison, J. E., Control of Monolayer Assembly Structure by Hydrogen Bonding Rather Than by Adsorbate-Substrate Templating. *Journal of the American Chemical Society* **1999,** *121* (22), 5319-5327.
100. Clegg, R. S.; Reed, S. M.; Hutchison, J. E., Self-Assembled Monolayers Stabilized by Three-Dimensional Networks of Hydrogen Bonds. *Journal of the American Chemical Society* **1998,** *120* (10), 2486-2487.
101. Clegg, R. S.; Reed, S. M.; Smith, R. K.; Barron, B. L.; Rear, J. A.; Hutchison, J. E., The Interplay of Lateral and Tiered Interactions in Stratified Self-Organized Molecular Assemblies. *Langmuir* **1999,** *15* (26), 8876-8883.

102. Bomben, K. D.; Dev, S. B., Investigation of poly(L-amino acids) by x-ray photoelectron spectroscopy. *Analytical Chemistry* **1988,** *60* (14), 1393-1397.
103. Mendoza, S. M.; Arfaoui, I.; Zanarini, S.; Paolucci, F.; Rudolf, P., Improvements in the Characterization of the Crystalline Structure of Acid-Terminated Alkanethiol Self-Assembled Monolayers on Au(111). *Langmuir* **2007,** *23* (2), 582-588.
104. Bertilsson, L.; Liedberg, B., Infrared study of thiol monolayer assemblies on gold: preparation, characterization, and functionalization of mixed monolayers. *Langmuir* **1993,** *9* (1), 141-149.
105. Pan, S.; Castner, D. G.; Ratner, B. D., Multitechnique Surface Characterization of Derivatization Efficiencies for Hydroxyl-Terminated Self-Assembled Monolayers. *Langmuir* **1998,** *14* (13), 3545-3550.
106. Wong, Y.-L.; Hubieki, M. P.; Curfman, C. L.; Doncel, G. F.; Dudding, T. C.; Savle, P. S.; Gandour, R. D., A structure-activity study of spermicidal and anti-HIV properties of hydroxylated cationic surfactants. *Bioorganic & Medicinal Chemistry* **2002,** *10* (11), 3599-3608.
107. Kelemen, S. R.; Afeworki, M.; Gorbaty, M. L.; Kwiatek, P. J.; Solum, M. S.; Hu, J. Z.; Pugmire, R. J., XPS and 15N NMR Study of Nitrogen Forms in Carbonaceous Solids. *Energy Fuels* **2002,** *16* (6), 1507-1515.
108. Kugler, R.; Bouloussa, O.; Rondelez, F., Evidence of a charge-density threshold for optimum efficiency of biocidal cationic surfaces. *Microbiology* **2005,** *151* (5), 1341-1348.
109. Yokokawa, S.; Tamada, K.; Ito, E.; Hara, M., Cationic Self-Assembled Monolayers Composed of Gemini-Structured Dithiol on Gold: A New Concept for Molecular Recognition Because of the Distance between Adsorption Sites. *J. Phys. Chem. B* **2003,** *107* (15), 3544-3551.
110. Kertes, A. S., Solubility and Activity of High-molecular Amine Hydrochlorides in Organc Solvents. *J. Inorg. Nucl. Chem.* **1964,** *27* (1), 209-217.
111. Isquith, A. J.; Abbott, E. A.; Walters, P. A., Surface-Bonded Antimicrobial Activity of an Organosilicon Quaternary Ammonium Chloride. *Appl. Environ. Microbiol.* **1972,** *24* (6), 859-863.
112. Matias, V. R.; Terry J. Beveridge, Cryo-electron microscopy reveals native polymeric cell wall structure in *Bacillus subtilis* and the existence of a periplasmic space. *Molecular Microbiology* **2005,** *56* (1), 240-251.
113. Matias, V. R. F.; Al-Amoudi, A.; Dubochet, J.; Beveridge, T. J., Cryo-Transmission Electron Microscopy of Frozen-Hydrated Sections of Escherichia coli and Pseudomonas aeruginosa. *J. Bacteriol.* **2003,** *185* (20), 6112-6118.
114. Meroueh, S. O.; Bencze, K. Z.; Hesek, D.; Lee, M.; Fisher, J. F.; Stemmler, T. L.; Mobashery, S., Three-dimensional structure of the bacterial cell wall peptidoglycan. *Proceedings of the National Academy of Sciences of the United States of America* **2006,** *103* (12), 4404-4409.
115. Yokokawa, S.; Hara, M.; Tamada, K.; Ito, E., Cationic self-assembled monolayers composed of gemini-structured sulfur compounds on gold: a new approach to control ionic functions on surfaces. *Molecular Crystals and Liquid Crystals* **2003,** *407*, 115 - 120.
116. Chechik, V.; Schonherr, H.; Vancso, G. J.; Stirling, C. J. M., Self-Assembled Monolayers of Branched Thiols and Disulfides on Gold: Surface Coverage, Order and Chain Orientation. *Langmuir* **1998,** *14* (11), 3003-3010.
117. Romeo, D.; Skerlavaj, B.; Bolognesi, M.; Gennaro, R., Structure and bactericidal activity of an antibiotic dodecapeptide purified from bovine neutrophils. *J. Biol. Chem.* **1988,** *263* (20), 9573-9575.

118. Zasloff, M., Antimicrobial peptides of multicellular organisms. *Nature* **2002,** *415* (6870), 389-395.
119. Matsuzaki, K., Why and how are peptide-lipid interactions utilized for self-defense? Magainins and tachyplesins as archetypes. *Biochimica et Biophysica Acta (BBA) - Biomembranes* **1999,** *1462* (1-2), 1-10.
120. Shai, Y., Mechanism of the binding, insertion and destabilization of phospholipid bilayer membranes by α-helical antimicrobial and cell non-selective membrane-lytic peptides. *Biochimica et Biophysica Acta (BBA) - Biomembranes* **1999,** *1462* (1-2), 55-70.
121. Yang, L.; Weiss, T. M.; Lehrer, R. I.; Huang, H. W., Crystallization of Antimicrobial Pores in Membranes: Magainin and Protegrin. *Biophys. J.* **2000,** *79* (4), 2002-2009.
122. Westerhoff, H. V.; JuretiÄ‡, D.; Hendler, R. W.; Zasloff, M., Magainins and the disruption of membrane-linked free-energy transduction. *Proceedings of the National Academy of Sciences of the United States of America* **1989,** *86* (17), 6597-6601.
123. Bierbaum, G.; Sahl, H.-G., Induction of autolysis of staphylococci by the basic peptide antibiotics Pep 5 and nisin and their influence on the activity of autolytic enzymes. *Archives of Microbiology* **1985,** *141* (3), 249-254.
124. Kragol, G.; Lovas, S.; Varadi, G.; Condie, B. A.; Hoffmann, R.; Otvos, L., The Antibacterial Peptide Pyrrhocoricin Inhibits the ATPase Actions of DnaK and Prevents Chaperone-Assisted Protein Folding. *Biochemistry* **2001,** *40* (10), 3016-3026.
125. Kulagina, N. V.; Lassman, M. E.; Ligler, F. S.; Taitt, C. R., Antimicrobial Peptides for Detection of Bacteria in Biosensor Assays. *Anal. Chem.* **2005,** *77* (19), 6504-6508.
126. Kulagina, N. V.; Shaffer, K. M.; Anderson, G. P.; Ligler, F. S.; Taitt, C. R., Antimicrobial peptide-based array for Escherichia coli and Salmonella screening. *Analytica Chimica Acta* **2006,** *575* (1), 9-15.
127. Kulagina, N. V.; Shaffer, K. M.; Ligler, F. S.; Taitt, C. R., Antimicrobial peptides as new recognition molecules for screening challenging species. *Sensors and Actuators B: Chemical* **2007,** *121* (1), 150-157.
128. Arcidiacono, S.; Mello, C. M.; Pivarnik, P.; Senecal, A., Cy_5 Labeled Antimicrobial Peptides for Enhanced Detection of *Escherichia coli* O_{157}:H_7. *Accepted Biosensors and Bioelectronics* **2008**.
129. Gregory, K.; Mello, C. M., Immobilization of Escherichia coli Cells by Use of the Antimicrobial Peptide Cecropin P1. *Appl. Environ. Microbiol.* **2005,** *71* (3), 1130-1134.
130. Mello, C. M.; Soares, J. W., Membrane Selectivity of Antimicrobial Peptides. In *Microbial Surfaces: Structure, Interactions and Reactivity*, Camesano, T. A.; Mello, C. M., Eds. American Chemical Society: Washington, D.C., in press; Vol. ACS Symposium Series 984.
131. York, R. L.; Mermut, O.; Phillips, D. C.; McCrea, K. R.; Ward, R. S.; Somorjai, G. A., Influence of Ionic Strength on the Adsorption of a Model Peptide on Hydrophilic Silica and Hydrophobic Polystyrene Surfaces: Insight from SFG Vibrational Spectroscopy. *J. Phys. Chem. C* **2007,** *111* (25), 8866-8871.
132. Fujita, K.; Bunjes, N.; Nakajima, K.; Hara, M.; Sasabe, H.; Knoll, W., Macrodipole Interaction of Helical Peptides in a Self-Assembled Monolayer on Gold Substrate. *Langmuir* **1998,** *14* (21), 6167-6172.
133. Miura, Y.; Kimura, S.; Imanishi, Y.; Umemura, J., Oriented Helical Peptide Layer on the Carboxylate-Terminated Alkanethiol Immobilized on a Gold Surface. *Langmuir* **1999,** *15* (4), 1155-1160.

134. Baas, T.; Gamble, L.; Hauch, K. D.; Castner, D. G.; Sasaki, T., Characterization of a Cysteine-Containing Peptide Tether Immobilized onto a Gold Surface. *Langmuir* **2002,** *18* (12), 4898-4902.
135. Miura, Y.; Kimura, S.; Imanishi, Y.; Umemura, J., Formation of Oriented Helical Peptide Layers on a Gold Surface Due to the Self-Assembling Properties of Peptides. *Langmuir* **1998,** *14* (24), 6935-6940.
136. Strong, A. E.; Moore, B. D., Self-assembling monolayers of helical oligopeptides on gold with applications in molecular electronics. *J. Mater. Chem.* **1999,** *9*, 1097-1105.
137. Mermut, O.; Phillips, D. C.; York, R. L.; McCrea, K. R.; Ward, R. S.; Somorjai, G. A., In Situ Adsorption Studies of a 14-Amino Acid Leucine-Lysine Peptide onto Hydrophobic Polystyrene and Hydrophilic Silica Surfaces Using Quartz Crystal Microbalance, Atomic Force Microscopy, and Sum Frequency Generation Vibrational Spectroscopy. *J. Am. Chem. Soc.* **2006,** *128* (11), 3598-3607.
138. Vallieres, K.; Chevallier, P.; Sarra-Bournet, C.; Turgeon, S.; Laroche, G., AFM Imaging of Immobilized Fibronectin: Does the Surface Conjugation Scheme Affect the Protein Orientation/Conformation? *Langmuir* **2007,** *23* (19), 9745-9751.
139. Moore, K.; Bevins, C.; Brasseur, M.; Tomassini, N.; Turner, K.; Eck, H.; Zasloff, M., Antimicrobial peptides in the stomach of Xenopus laevis. *J. Biol. Chem.* **1991,** *266* (29), 19851-19857.
140. Cole, A. M.; Weis, P.; Diamond, G., Isolation and Characterization of Pleurocidin, an Antimicrobial Peptide in the Skin Secretions of Winter Flounder. *J. Biol. Chem.* **1997,** *272* (18), 12008-12013.
141. Sipos, D.; Andersson, M.; Ehrenberg, A., The structure of the mammalian antibacterial peptide cecropin P_1 in solution, determined by proton-NMR. *European Journal of Biochemistry* **1992,** *209* (1), 163-169.
142. Jun Yao, L. T., Fei Wang, Hui-Lun Chen, Chao-Qian Xu, Chun-Li Su, Ming-Fa Cai, Thomas Maskow, Gyulad Zaray, Yan-Xin Wang,, Microcalorimetric Study on Effect of Chromium(III) and Chromium(VI) Species on the Growth of *Escherichia coli*. *Chinese Journal of Chemistry* **2008,** *26* (1), 101-106.
143. Krimm, S.; Bandekar, J., Vibrational Spectroscopy and Conformation of Peptides, Polypeptides, and Proteins. *Advances in Protein Chemistry* **1986,** *38*, 181-364.
144. Yen, Y. S.; Wong, J. S., Infrared reflectance properties of surface thin films. *J. Phys. Chem.* **1989,** *93* (20), 7208-7216.
145. Cantor, C. R.; Schimmel, P. R., Table 8-6. In *Biophysical Chemistry*, W.H. Freeman: San Francisco, 1980; Vol. 2, p 471.
146. Fringeli, U. P.; Gunthard, H. H., Infrared membrane spectroscopy. In *Membrane Spectrocopy*, Grell, E., Ed. Springer Verlag: New York, 1981.
147. Goormaghtigh, E.; Cabiaux, V.; Ruysschaert, J. M., Determination of soluble and membrane protein structure by FTIR spectroscopy. I. Assignments and model compounds. In *Subcelluar Biochemistry*, Ralston, G. B.; Hilderson, H. J., Eds. Plenum Press: New York, 1994; Vol. 23, pp 329-362.
148. Boncheva, M.; Vogel, H., Formation of stable polypeptide monolayers at interfaces: controlling molecular conformation and orientation. *Biophys. J.* **1997,** *73* (2), 1056-1072.
149. Enriquez, E. P.; Gray, K. H.; Guarisco, V. F.; Linton, R. W.; Mar, K. D.; Samulski, E. T. In *Behavior of rigid macromolecules in self-assembly at an interface*, 38th National Symposium

of the American Vacuum Society, Seattle, Washington (USA), AVS: Seattle, Washington (USA), 1992; pp 2775-2782.
150. Gremlich, H. U.; Fringeli, U. P.; Schwyzer, R., Conformational changes of adrenocorticotropin peptides upon interaction with lipid membranes revealed by infrared attenuated total reflection spectroscopy. *Biochemistry* **1983,** *22* (18), 4257-4264.
151. Jackson, M.; Mantsch, H. H., The Use and Misuse of FTIR Spectroscopy in the Determination of Protein Structure. *Critical Reviews in Biochemistry and Molecular Biology* **1995,** *30* (2), 95 - 120.
152. Toshihiko Sakurai; Oka, S.; Kubo, A.; Nishiyama, K.; Taniguchi, I., Formation of oriented polypeptides on Au(111) surface depends on the secondary structure controlled by peptide length. *Journal of Peptide Science* **2006,** *12* (6), 396-402.
153. Worley, C. G.; Linton, R. W.; Samulski, E. T., Electric-Field-Enhanced Self-Assembly of α-helical polypeptides. *Langmuir* **1995,** *11* (10), 3805-3810.
154. Frutos, A. G.; Corn, R. M., SPR of ultrathin organic films. *Anal. Chem.* **1998,** *70*, 449A-455A.
155. Boussaad, S.; Pean, J.; Tao, N. J., High-Resolution Multiwavelength Surface Plasmon Resonance Spectroscopy for Probing Conformational and Electronic Changes in Redox Proteins. *Anal. Chem.* **2000,** *72* (1), 222-226.
156. Jung, L. S.; Campbell, C. T.; Chinowsky, T. M.; Mar, M. N.; Yee, S. S., Quantitative Interpretation of the Response of Surface Plasmon Resonance Sensors to Adsorbed Films. *Langmuir* **1998,** *14* (19), 5636-5648.
157. Wang, S.; Boussaad, S.; Wong, S.; Tao, N. J., High-Sensitivity Stark Spectroscopy Obtained by Surface Plasmon Resonance Measurement. *Anal. Chem.* **2000,** *72* (17), 4003-4008.
158. Zacher, T.; Wischerhoff, E., Real-Time Two-Wavelength Surface Plasmon Resonance as a Tool for the Vertical Resolution of Binding Processes in Biosensing Hydrogels. *Langmuir* **2002,** *18* (5), 1748-1759.
159. Beychok, S., Circular Dichroism of Biological Macromolecules. *Science* **1966,** *154* (3754), 1288-1299.
160. Greenfield, N. J., Using circular dichroism spectra to estimate protein secondary structure. *Nat. Protocols* **2007,** *1* (6), 2876-2890.
161. Martin, S. R.; Schilstra, M. J.; Dr. John, J. C.; Dr. H. William Detrich, III, Circular Dichroism and Its Application to the Study of Biomolecules. In *Methods in Cell Biology*, Academic Press: 2008; Vol. Volume 84, pp 263-293.
162. Morrow, J. A.; Segall, M. L.; Lund-Katz, S.; Phillips, M. C.; Knapp, M.; Rupp, B.; Weisgraber, K. H., Differences in Stability among the Human Apolipoprotein E Isoforms Determined by the Amino-Terminal Domain. *Biochemistry* **2000,** *39* (38), 11657-11666.
163. Blondelle, S. E.; Lohner, K.; Aguilar, M.-I., Lipid-induced conformation and lipid-binding properties of cytolytic and antimicrobial peptides: determination and biological specificity. *Biochimica et Biophysica Acta (BBA) - Biomembranes* **1999,** *1462* (1-2), 89-108.
164. Buck, M., Trifluoroethanol and colleagues: cosolvents come of age. Recent studies with peptides and proteins. *Quarterly Review of Physics* **1998,** *31*, 297-355.
165. Lehrman, S. R.; Tuls, J. L.; Lund, M., Peptide .alpha.-helicity in aqueous trifluoroethanol: correlations with predicted α-helicity and the secondary structure of the corresponding regions of bovine growth hormone. *Biochemistry* **1990,** *29* (23), 5590-5596.

166. Sonnichsen, F. D.; Van Eyk, J. E.; Hodges, R. S.; Sykes, B. D., Effect of trifluoroethanol on protein secondary structure: an NMR and CD study using a synthetic actin peptide. *Biochemistry* **1992,** *31* (37), 8790-8798.
167. Uzarski, J. R.; Tannous, A.; Morris, J. R.; Mello, C. M., The effects of solution structure on the surface conformation and orientation of a cysteine-terminated antimicrobial peptide cecropin P1. *Colloids and Surfaces B: Biointerfaces* **2008,** *67* (2), 157-165.
168. Enander, K.; Aili, D.; Baltzer, L.; Lundstrom, I.; Liedberg, B., Alpha-Helix-Inducing Dimerization of Synthetic Polypeptide Scaffolds on Gold. *Langmuir* **2005,** *21* (6), 2480-2487.
169. Miura, Y.; Kimura, S.; Imanishi, Y.; Umemura, J., Self-Assembly of α-Helix Peptide/Crown Ether Conjugate upon Complexation with Ammonium-Terminated Alkanethiolate. *Langmuir* **1998,** *14* (10), 2761-2767.
170. Koenig, J. L.; Tabb, D. L., In *Analytical Applications of FT-IR to Molecular and Biological Systems*, Durig, J. R., Ed. D. Riedel: Dordrecht, 1980; p 241.
171. Butt, H.-J.; Graf, K.; Kappl, M., *Physics and Chemistry of Interfaces*. Wiley-VCH GmbH & Co.: KGaA, Weinham, 2003.
172. Wang, Z.; Wang, G., APD: the antimicrobial peptide database. *Nucleic Acids Res.* **2004,** *35*, 92.
173. Chi, E. Y.; Krishnan, S.; Randolph, T. W.; Carpenter, J. F., Physical Stability of Proteins in Aqueous Solution: Mechanism and Driving Forces in Nonnative Protein Aggregation. *Pharmaceutical Research* **2003,** *20* (9), 1325-1336.
174. McKee, T.; McKee, J. R., *Biochemistry: An Introduction*. Times Mirror Higher Education Group, Inc.: Dubuque, IA, 1996.
175. Shapiro, A. L.; Viñuela, E.; V. Maizel, J., Molecular weight estimation of polypeptide chains by electrophoresis in SDS-polyacrylamide gels. *Biochemical and Biophysical Research Communications* **1967,** *28* (5), 815-820.
176. Burns, J. A.; Butler, J. C.; Moran, J.; Whitesides, G. M., Selective reduction of disulfides by tris(2-carboxyethyl)phosphine. *J. Org. Chem.* **1991,** *56* (8), 2648-2650.
177. Tyndall, G. S.; Ravishankara, A. R., Atmospheric oxidation of reduced sulfur species. *International Journal of Chemical Kinetics* **1991,** *23* (6), 483-527.
178. Bain, C. D.; Biebuyck, H. A.; Whitesides, G. M., Comparison of self-assembled monolayers on gold: coadsorption of thiols and disulfides. *Langmuir* **1989,** *5* (3), 723-727.
179. Nuzzo, R. G.; Zegarski, B. R.; Dubois, L. H., Fundamental studies of the chemisorption of organosulfur compounds on gold(111). Implications for molecular self-assembly on gold surfaces. *Journal of the American Chemical Society* **1987,** *109* (3), 733-740.
180. Joseph, Y.; Besnard, I.; Rosenberger, M.; Guse, B.; Nothofer, H.-G.; Wessels, J. M.; Wild, U.; Knop-Gericke, A.; Su, D.; Schlogl, R.; Yasuda, A.; Vossmeyer, T., Self-Assembled Gold Nanoparticle/Alkanedithiol Films: Preparation, Electron Microscopy, XPS-Analysis, Charge Transport, and Vapor-Sensing Properties. *The Journal of Physical Chemistry B* **2003,** *107* (30), 7406-7413.
181. Ihs, A.; Liedberg, B., Chemisorption of -cysteine and 3-mercaptopropionic acid on gold and copper surfaces: An infrared reflection-absorption study. *Journal of Colloid and Interface Science* **1991,** *144* (1), 282-292.
182. Liedberg, B.; Lundstrom, I.; Wu, C. R.; Salaneck, W. R., Adsorption of glycine on hydrophilic gold. *Journal of Colloid and Interface Science* **1985,** *108* (1), 123-132.

183. Craig, N. L.; Harker, A. B.; Novakov, T., Determination of the chemical states of sulfur in ambient pollution aerosols by X-ray photoelectron spectroscopy. *Atmospheric Environment* **1974,** *8* (1), 15-21.
184. Warner, M. G.; Reed, S. M.; Hutchison, J. E., Small, Water-Soluble, Ligand-Stabilized Gold Nanoparticles Synthesized by Interfacial Ligand Exchange Reactions. *Chem. Mater.* **2000,** *12* (11), 3316-3320.
185. Liedberg, B.; Ivarsson, B.; Hegg, P. O.; Lundstrom, I., On the adsorption of β-lactoglobulin on hydrophilic gold surfaces: Studies by infrared reflection-absorption spectroscopy and ellipsometry. *Journal of Colloid and Interface Science* **1986,** *114* (2), 386-397.
186. Liedberg, B.; Ivarsson, B.; Lundstrom, I., Fourier Transform Infrared Reflection Absorption Spectroscopy (FT-IRAS) of fibrinogen adsorbed on metal and metal oxide surfaces. *Journal of Biochemical and Biophysical Methods* **1984,** *9*, 233-243.
187. Maurizio Simmaco, G. M., Donatella Barra,, Antimicrobial peptides from amphibian skin: What do they tell us? *Peptide Science* **1998,** *47* (6), 435-450.
188. Yoshida, K.; Mukai, Y.; Niidome, T.; Takashi, C.; Tokunaga, Y.; Hatakeyama, T.; Aoyagi, H., Interaction of pleurocidin and its analogs with phospholipid membrane and their antibacterial activity: Authors' affiliations. In *Journal of Peptide Research*, Blackwell Publishing Limited: 2001; Vol. 57, pp 119-126.
189. Kerth, A.; Erbe, A.; Dathe, M.; Blume, A., Infrared Reflection Absorption Spectroscopy of Amphipathic Model Peptides at the Air/Water Interface. *Biophys. J.* **2004,** *86* (6), 3750-3758.
190. Nuzzo, R. G.; Dubois, L. H.; Allara, D. L., Fundamental studies of microscopic wetting on organic surfaces. 1. Formation and structural characterization of a self-consistent series of polyfunctional organic monolayers. *Journal of the American Chemical Society* **1990,** *112* (2), 558-569.
191. Yang, Y.-C., Chemical Detoxification of Nerve Agent VX. *Accounts of Chemical Research* **1999,** *32* (2), 109-115.
192. Yang, Y. C.; Baker, J. A.; Ward, J. R., Decontamination of chemical warfare agents. *Chemical Reviews* **1992,** *92* (8), 1729-1743.
193. Yang, Y. C.; Szafraniec, L. L.; Beaudry, W. T.; Bunton, C. A., Perhydrolysis of nerve agent VX. *The Journal of Organic Chemistry* **1993,** *58* (25), 6964-6965.
194. Ulman, A., Formation and Structure of Self-Assembled Monolayers. *Chemical Reviews* **1996,** *96* (4), 1533-1554.
195. Fiegland, L. R. Ultrahigh Vacuum Studies of the Reaction Mechansims of Ozone with Saturated and Unsaturated Self-Assembled Monolayers. Dissertation, Virginia Polytechnic Institute and State University, Blacksburg, VA, 2008.
196. Zhukov, V.; Popova, I.; Yates, J. J. T., Delivery of pure ozone in ultrahigh vacuum. *Journal of Vacuum Science & Technology A: Vacuum, Surfaces, and Films* **2000,** *18* (3), 992-994.
197. Yates, J. J. T., *Experimental Innovations in Surface Science*. Springer-Verlag: New York, 1998.
199. Gates, D. J., *The Chlorine Dioxide Handbook*. AWWA Publishing: Denver, CO, 1998.
200. Ellison, D. H., *Handbook of Chemical and Biological Warfare Agents*. CRC Press: New York, NY, 2000.
201. Guo, X.; Yoshinobu, J.; Yates, J. T., Decomposition of an organophosphonate compound (dimethylmethylphosphonate) on the nickel(111) and palladium(111) surfaces. *The Journal of Physical Chemistry* **1990,** *94* (17), 6839-6842.

202. Hegde, R. I.; Greenlief, C. M.; White, J. M., Surface chemistry of dimethyl methylphosphonate on rhodium(100). *The Journal of Physical Chemistry* **1985,** *89* (13), 2886-2891.
203. Henderson, M. A.; White, J. M., Adsorption and decomposition of dimethyl methylphosphonate on platinum(111). *Journal of the American Chemical Society* **1988,** *110* (21), 6939-6947.
204. Papirer, E., *Adsorption on Silica Surfaces*. Marcel Dekker, Inc.: New York, NY, 2000.
205. Panayotov, D.; Kondratyuk, P.; Yates, J. T., Photooxidation of a Mustard Gas Simulant over TiO_2-SiO_2 Mixed-Oxide Photocatalyst: Site Poisoning by Oxidation Products and Reactivation. *Langmuir* **2004,** *20* (9), 3674-3678.
206. Valenzuela, D. P.; Myers, A. L., *Adsorption Equilibrium Data Handbook*. Prentice-Hall: Englewood Cliffs, NJ, 1989.
207. Langmuir, I., THE ADSORPTION OF GASES ON PLANE SURFACES OF GLASS, MICA AND PLATINUM. *Journal of the American Chemical Society* **1918,** *40* (9), 1361-1403.
208. Freundlich, H., *Colloidal and capillary chemistry*. Methuen: London, 1926.
209. Proctor, A.; Toro-Vazquez, J., The Freundlich isotherm in studying adsorption in oil processing. *Journal of the American Oil Chemists' Society* **1996,** *73* (12), 1627-1633.
210. Allen, S. J.; McKay, G.; Khader, K. Y. H., Multi-component sorption isotherms of basic dyes onto peat. *Environmental Pollution* **1988,** *52* (1), 39-53.
211. Fraust, S. D.; Aly, O. M., In *Adsorption processes for water treatment*, Butterworth: Stoneham, MA, 1987; pp 1-23.
212. Mittal, A. K. Biosorption of cationic dyes and the dead macro fungus, *Fomitopsis carnea*. Dissertation, Indian Institute of Technology, Bombay, India, 1997.
213. Sips, R., On the Structure of a Catalyst Surface. *The Journal of Chemical Physics* **1948,** *16* (5), 490-495.
214. Helminen, J.; Helenius, J.; Paatero, E.; Turunen, I., Comparison of sorbents and isotherm models for NH_3 gas separation by adsorption. *AIChE Journal* **2000,** *46* (8), 1541-1555.
215. Tóth, J., Thermodynamical Correctness of Gas/Solid Adsorption Isotherm Equations. *Journal of Colloid and Interface Science* **1994,** *163* (2), 299-302.
216. Toth, J., *Acta Chim. Acad. Sci. Hung.* **1971,** *69*.
217. Tripp, C. P.; Hair, M. L., Reaction of chloromethylsilanes with silica: a low-frequency infrared study. *Langmuir* **1991,** *7* (5), 923-927.
218. Thomas, L. C., *Interpretation of the Infrared Spectra of Organophosphorus Compounds*. Heyden & Sons Ltd.: London, 1974.
219. Niibori, Y.; Kunita, M.; Tochiyama, O.; Chida, T., Dissolution rates of Amorphous Silica in Highly Alkaline Solution. *Journal of Nuclear Science and Technology* **2000,** *37* (4), 349-357.